

Raman-Differenzspektroskopie mit zwei  
verschiedenen Anregungswellenlängen zur  
untergrundfreien und bildgebenden Untersuchung  
von biologischen Proben



# FRIEDRICH-SCHILLER- UNIVERSITÄT JENA

**Dissertation (kumulativ)**

zur Erlangung des akademischen Grades

*doctor rerum naturalium (Dr. rer. nat.)*

vorgelegt dem Rat der Chemisch-Geowissenschaftlichen Fakultät

der Friedrich-Schiller-Universität Jena von

*Diplom Chemiker (Dipl.Chem.)* Florian Carsten Andreas Korinth,

geboren am 16.02.1980 in Hamburg

Gutachter:

1. Prof. Dr. Jürgen Popp

Institut für Physikalische Chemie, Friedrich-Schiller-Universität Jena

2. Prof. Dr. Iwan Schie

Fachbereich Medizintechnik und Biotechnologie, Ernst-Abbe-Hochschule Jena

Tag der öffentlichen Verteidigung: 9. Juni 2021





## Inhaltsverzeichnis

Inhaltsverzeichnis .....	i
Abkürzungsverzeichnis .....	iii
Abbildungsverzeichnis .....	iv
1. Einleitung .....	11
1.1. Motivation .....	11
1.2. Raman-Spektroskopie und –Bildgebung .....	14
1.2.1. Vorbehandlung von Raman–Daten .....	17
1.2.2. Chemometrie und multivariate Datenanalyse .....	19
1.3. Stand der Technik der Fluoreszenzkorrektur in Raman-Spektroskopie .....	23
1.4. „interlaced nod and shuffle“ in der Astrophysik .....	29
1.5. Anwendung .....	31
1.5.1. Pollen .....	31
1.5.2. Tierische Gewebeprobe .....	32
1.5.3. Synthetische Polymere .....	33
1.6. Zielsetzung der Dissertation .....	34
2. Eigene Forschungsergebnisse .....	35
2.1. Evaluierung von SERDS und Vergleich mit der mathematischen Basislinienkorrekturmethode EMSC .....	35
2.2. Klassifizierung von SERDS-Daten ohne vorherige Rekonstruktion .....	41
2.3. Weitfeld-SERDS-Bildgebung mit Hilfe der „nod and shuffle“ Technologie .....	47
3. Zusammenfassung .....	55
4. Summary .....	60
5. Literaturverzeichnis .....	65
6. Publikationen .....	74
6.1. Evaluation of Shifted Excitation Raman Difference Spectroscopy and Comparison to Computational Background Correction Methods Applied to Biochemical Raman Spectra [FK1] .....	77
6.2. New methodology to process shifted excitation Raman difference spectroscopy data: a case study of pollen classification [FK2] .....	95
6.3. Wide Field Spectral Imaging with Shifted Excitation Raman Difference Spectroscopy Using the Nod and Shuffle Technique [FK3] .....	116
7. Wissenschaftliche Beiträge .....	136
Danksagung .....	139

## Inhaltsverzeichnis

---

Erklärungen .....	141
Anhang – publizierte Version von [FK3] .....	143

**Abkürzungsverzeichnis**

3D	dreidimensional (engl. <i>3 dimensions</i> )
CCD	ladungsgekoppeltes Bauteil (engl. <i>charge-coupled device</i> )
EMSC	erweiterte multiplikative Signalkorrektur (engl. <i>extended multiplicative signal correction</i> )
FWHM	Halbwertsbreite (engl. <i>full width at half maximum</i> )
HCA	hierarchische Clusteranalyse (engl. <i>hierarchical cluster analysis</i> )
HTRS	Hochdurchsatz-Raman-Spektrometer (engl. <i>high throughput Raman spectrometer</i> )
IFS	Integralfeld-Spektroskopie
IFU	Integralfeld-Einheit (engl. <i>integral field unit</i> )
LDA	Lineare Diskriminanzanalyse (engl. <i>linear discriminant analysis</i> )
MSC	multiplikative Signalkorrektur (engl. <i>multiplicative signal correction</i> )
NIR	Nahinfrarot
PCA	Hauptkomponentenzerlegungsanalyse (engl. <i>principal component analysis</i> )
PMMA	Polymethylmethacrylat
PS	Polystyrol
SERDS	anregungswellenlängenverschobene Raman-Differenzspektroskopie (engl. <i>shifted excitation Raman difference spectroscopy</i> )
SNIP	empfindliche, nicht-lineare, iterative Bandenkorrektur (engl. <i>sensitive nonlinear iterative peak</i> )

## Abbildungsverzeichnis

Abbildung 1	Jablonski-Diagramm der elastischen und inelastischen Streuung .....	15
Abbildung 2	Zielscheiben mit Einschüssen für die Darstellung von Relevanz und Vertrauenswahrscheinlichkeit .....	21
Abbildung 3	SERDS ohne Photobleichen .....	25
Abbildung 4	SERDS mit Photobleichen .....	26
Abbildung 5	Schema der „ <i>interlaced nod and shuffle</i> “ Technik .....	30
Abbildung 6	Vergleich zwischen gemessenen Lipid-Spektren (a,d,g) und den Spektren von Protein A (b,e,h) und Protein B (c,f,i) .....	38
Abbildung 7	Score-Plots der drei PCA-LDA Klassifikationen, basierend auf den differenz-optimierten SERDS-Spektren der Testdatensätze .....	44
Abbildung 8	Filtern von Raumlichtbanden mittels Weitfeld-SERDS-Bildgebung in Kombination mit der „ <i>interlaced nod and shuffle</i> “ Technik .....	50
Abbildung 9	Beispiele für die Weitfeld-SERDS-Bildgebung in Kombination mit der „ <i>interlaced nod and shuffle</i> “ Technik an biologischen Proben .....	52







## 1. Einleitung

### 1.1. Motivation

Raman-Spektroskopie, eine Form der Schwingungsspektroskopie, findet immer häufiger Anwendung zur strukturellen Analyse chemischer und biochemischer Verbindungen [1–3]. Sie erfordert keine besondere Vorbereitung oder Markierung der Proben und ist nicht zerstörerisch. Selbst Proben mit hohem Wasseranteil oder komplexer chemischer Zusammensetzung wie Gewebeproben können mit Hilfe ihres Raman-spektroskopischen Fingerabdrucks untersucht werden [4–7]. Da Raumlicht zu intensiven Banden oder einem breiten Untergrund im Raman-Spektrum führen kann, finden Raman-Messungen idealerweise unter Ausschluss externer Lichtquellen statt. Dies erschwert den Einsatz von Raman-Spektroskopie während einer medizinischen Operation. Ferner erfolgt bei Raman-Messungen an biologischen Proben häufig eine gleichzeitige Anregung von Autofluoreszenz [8]. Dies kann, insbesondere bei sehr hoher Intensität des Autofluoreszenzuntergrunds, zu einer Maskierung der Raman-Banden führen, da diese im Schrotrauschen (engl. *shot noise*), das der Quadratwurzel der gemessenen Signalintensität entspricht [9], untergehen können. Bereits geringe Konzentrationen an fluoreszierenden Substanzen in einer Probe können zu einem merklichen Untergrund in den Raman-Spektren führen. Dieser Umstand wird auch verwendet, um mittels Autofluoreszenz die medizinisch relevante Region in einer Gewebeprobe zu bestimmen und anschließend gezielt diese Regionen mittels Raman-Spektroskopie zu messen [10,11], da die Autofluoreszenz alleine keine spezifischen Informationen über die biochemische Zusammensetzung der Probe gibt. Obwohl also nicht ausgeschlossen werden kann, dass der Autofluoreszenzuntergrund ebenfalls relevante Informationen über die Probe liefert [12], entspricht es dem Stand der Technik den Untergrund in Raman-Spektren biologischer Proben mittels Basislinienkorrekturmethode zu korrigieren [13–15]. Da der Autofluoreszenzuntergrund aufgrund von Ausbleichen oder Quenchen der Fluorophore während einer Messreihe variieren kann, ist keine ausreichende Reproduzierbarkeit gegeben. Durch Messung der Fluoreszenzlebensdauer kann die Reproduzierbarkeit aber deutlich verbessert werden, was für das bildgebende Verfahren FLIm (engl. *fluorescence life time imaging*) verwendet wird [16].

Um besagten Autofluoreszenzuntergrund zu korrigieren, wurden zahlreiche Methoden entwickelt. Diese können grob in zwei Kategorien eingeteilt werden [17]: Bei der ersten

Kategorie handelt es sich um die mathematischen, computerbasierten Korrekturmethode wie das Anpassen eines Polynoms [18], die Gummiband Methode (engl. *rubber band*) [19,20], die erweiterte multiplikative Signalkorrektur (engl. *extended multiplicative signal correction* – EMSC [21,22]) und die empfindliche, nicht-lineare, iterative Bandenkorrektur (engl. *sensitive nonlinear iterative peak* – SNIP [23,24]). Allen diesen Methoden ist gemein, dass sie rechenaufwendig sind und der Nutzer Erfahrung in der Korrektur von Raman-Spektren haben muss, um das richtige Maß an Korrektur des Untergrundes zu gewährleisten. Die zweite Kategorie stellen die instrumentellen Basislinienkorrekturmethode dar. Diese Methoden machen sich, gemäß der Regel Michael Kashas: "*The emitting level of a given multiplicity is the lowest excited level of that multiplicity.*" [25], die Anregungswellenlängenabhängigkeit der Raman-Streuung sowie den Geschwindigkeitsunterschied zwischen der schnellen Raman-Streuung und der langsameren Fluoreszenzemission zu Nutze. Beispiele hierfür sind die zeitgesteuerte Raman-Spektroskopie [26,27], die frequenz- und wellenlängenmodulierte Raman-Spektroskopie [28–31] und die anregungswellenlängenverschobene Raman-Differenzspektroskopie (engl. *shifted excitation Raman difference spectroscopy* – SERDS [32]), bei der an der gleichen Position auf der Probe zwei Raman-Spektren mit leicht verschobener Anregungswellenlänge gemessen und voneinander subtrahiert werden.

Das durch die SERDS-Methode erhaltene Differenzspektrum ist idealerweise untergrundfrei und wird normalerweise zu einem Raman-Spektrum rekonstruiert [33–37]. Dieses rekonstruierte Raman-Spektrum wird dann, wie in der Schwingungsspektroskopie üblich, anhand seines Bandenprofils interpretiert. Problematisch ist bei dieser Methode jedoch die Änderung der Intensität des Untergrundes z.B. durch Ausbleichen der Fluorophore, was zu einem Restuntergrund im Differenzspektrum führt. Ein weiterer Nachteil ist die Notwendigkeit, dass mehrere Spektren an der gleichen räumlichen Position gemessen werden müssen, was die Datenaufnahme verlangsamt. Insbesondere die beiden letztgenannten Nachteile führen dazu, dass nur Schmälzlin *et al.* bisher eine Bildgebung basierend auf der Raman-Differenzspektroskopie durchgeführt hat [38]. Üblicherweise wird die SERDS-Methode an Einzelspektren verwendet, die oft zur Reduzierung des Rauschens gemittelt werden [39,40]. Hinzu kommt, dass für die instrumentelle SERDS-Methode sehr häufig eine aufwendige Datenvorbehandlung (engl. *data preprocessing*) angewandt wird [41,42], was nach Ansicht des Autors der Idee einer instrumentellen Korrekturmethode zuwider läuft.

Ziel dieser Arbeit war die Untersuchung der SERDS-Technologie und deren Weiterentwicklung hin zu einer rein instrumentellen Methode mit einer stark verringerten Datenvorbehandlung. Hierbei lag ein besonderes Augenmerk auf einer schnellen Bildgebung mittels SERDS an biologischen Proben mittels der Weitfeld-Raman-Bildgebung. Durch die Integration der „*interlaced nod and shuffle*“ Technik aus der Astrophysik in einen Weitfeld-Raman-Bildgebungs Aufbau sollte die iterative Akkumulation kurzer Messzeiten ermöglicht werden, um das Photobleichen zu reduzieren. Ferner sollte die Fähigkeit von SERDS, Raumlicht aus einem Raman-Bild zu löschen, demonstriert werden. In den anschließenden Unterkapiteln werden die verwendeten Methoden kurz erläutert und auf den Stand der Technik in der SERDS-Technik eingegangen.

## 1.2. Raman-Spektroskopie und –Bildgebung

Trifft Licht auf ein Molekül, bewirkt das oszillierende, elektromagnetische Feld des Lichtes eine Auslenkung der Elektronenhülle aus dem Gleichgewichtszustand, also deren Polarisierung [9,43].

$$\begin{aligned}
 P = & \alpha_0 E_0 \cdot \cos[2\pi \cdot \nu_0 \cdot t] + \frac{1}{2} E_0 Q_j^0 \left( \frac{\delta\alpha}{\delta Q_j} \right) \cdot \cos[2\pi \cdot (\nu_0 - \nu_j) \cdot t] + \\
 & + \frac{1}{2} E_0 Q_j^0 \left( \frac{\delta\alpha}{\delta Q_j} \right) \cdot \cos[2\pi \cdot (\nu_0 + \nu_j) \cdot t]
 \end{aligned}
 \tag{1}$$

Die Größe dieser Polarisierung  $P$  der Elektronenhülle hängt nicht nur von der Stärke des elektromagnetischen Feldes  $E_0$  ab, sondern auch von der Polarisierbarkeit  $\alpha_0$  der Elektronenhülle. Die Oszillation des elektromagnetischen Feldes überträgt sich auf das dabei in dem Molekül induzierte Dipolmoment, wodurch das induzierte Dipolmoment mit der gleichen Frequenz  $\nu_0$  wie das eingestrahlte Licht oszilliert und selbst elektromagnetische Strahlung mit der gleichen Frequenz emittiert. Dies entspricht der voll-elastischen Streuung von Licht, welche als Rayleigh-Streuung bezeichnet wird (1. Term in Gleichung (1)). Durch das Oszillieren des Dipolmoments kann es zur Anregung von Normalmoden  $Q_j$  im Molekül kommen, wodurch sich die Schwingungsfrequenz des Dipolmoments und damit die Frequenz der emittierten elektromagnetischen Strahlung verändern. Diesen Vorgang bezeichnet man als inelastische Streuung [44], dessen Phänomen zum ersten Mal 1928 von Sir C. V. Raman gezeigt wurde. Hierbei wurde über einen langen Zeitraum mit Hilfe von gefiltertem Sonnenlicht ein Schwingungsspektrum einer Flüssigkeit aufgenommen, das erste Raman-Spektrum [45]. Für diese Arbeit wurde Sir C. V. Raman 1930 der Nobelpreis verliehen. Die inelastische Streuung wird ihm zu Ehren Raman-Streuung genannt. Wird ein höherer Schwingungszustand im Molekül angeregt, verringert sich die Schwingungsfrequenz des Dipolmoments um den Frequenzunterschied zwischen den beiden Eigenmoden  $\nu_j$  (Stokes-Raman-Streuung, 2. Term in Gleichung (1)). Wird ein tieferer Schwingungszustand im Molekül angeregt, erhöht sich die Schwingungsfrequenz des Dipolmoments um den Frequenzunterschied zwischen den beiden Eigenmoden  $\nu_j$  (Anti-Stokes-Raman-Streuung, 3. Term in Gleichung (1)). Durch inelastische Streuung können nur Normalmoden angeregt werden, bei denen sich die Polarisierbarkeit ändert bzw. bei denen der Polarisierbarkeitsgradient  $\frac{\delta\alpha}{\delta Q_j} \neq 0$  ist. Normalmoden auf die dies zutrifft,

heißen auch Raman-aktive Normalmoden. Da  $\alpha_0 \gg \frac{\delta\alpha}{\delta Q_j}$  gilt, tritt Raman-Streuung viel seltener auf als Rayleigh-Streuung. Da die Besetzung der Schwingungszustände in einem Molekül der Boltzmann-Verteilung folgt, befinden sich die meisten Moleküle bei Raumtemperatur im Schwingungsgrundzustand. Daraus folgt, dass bei Raumtemperatur die Wahrscheinlichkeit von Anti-Stokes-Raman-Streuung sehr viel geringer ist als von Stokes-Raman-Streuung. Die Intensität der Raman-Streuung  $I_R$  lässt sich auf klassischem Weg wie folgt berechnen:

$$I_R = \text{const} \cdot (\nu_0 \pm \nu_j)^4 \cdot \alpha^2 \cdot Q_j^2 \quad (2)$$

Oder vereinfacht ausgedrückt (siehe Gleichung (3)):

$$I_R \propto \nu^4 \quad \text{oder} \quad I_R \propto \frac{1}{\lambda^4} \quad (3)$$

Dies bedeutet, dass niedrigere Anregungswellenlängen  $\lambda$  eine höhere Raman-Intensität zeigen [46]. Bei vielen Molekülen nimmt die Wahrscheinlichkeit der Absorption der elektromagnetischen Strahlung bei niedrigeren Anregungswellenlängen unterhalb von 600 nm zu. Dies führt zu einer stärkeren Erwärmung der Probe und oft zu spontaner Emission von Fluoreszenz.

Betrachtet man die Raman-Streuung unter quantenmechanischen Gesichtspunkten, erfolgt eine kurzzeitige Anregung des Moleküls in einen virtuellen Schwingungszustand und eine Rückkehr in einen angeregten Schwingungszustand unter Emission von Licht. Dies kann am besten im Jablonski-Diagramm dargestellt werden (siehe Abbildung 1).

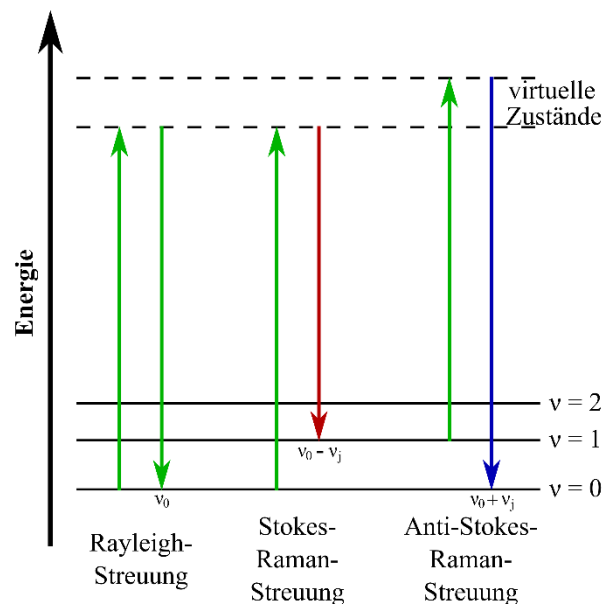


Abbildung 1: Jablonski-Diagramm der elastischen und inelastischen Streuung

Die Verwendung von Raman-Streuung für die spektroskopische Untersuchung einer Probe, um Aufschluss über ihre chemische Zusammensetzung zu erhalten, wird als Raman-Spektroskopie bezeichnet. Für einen Raman-spektroskopischen Aufbau wird in der Regel eine kohärente, monochromatische Lichtquelle (z. B. ein Laser) für die Anregung verwendet. Filter sorgen dafür, dass nur das inelastisch gestreute Licht in das Spektrometer gelangt. Dort wird das gemessene Licht mittels eines dispergierenden Elements (z.B. ein Gitter) zerlegt und von einer CCD-Kamera (ladungsgespeichertes Bauteil, engl. *charge-coupled device*) detektiert. Wird dieser Aufbau mit einem Mikroskop verbunden, bezeichnet man die Methode als Raman-Mikrospektroskopie. Registriert man während der Messung die räumliche Position der Messung, zum Beispiel durch Kombination des Raman-Mikroskop-Aufbaus mit einem motorisierten Tisch, kann die Raman-spektroskopische Bildgebung erfolgen. Die Vorteile der bildgebenden Raman-Spektroskopie sind die Möglichkeit einer orts aufgelösten Messung und eine hohe Konfokalität des Messsystems, wodurch ein stärkeres Raman-Signal gemessen und feinere Strukturen aufgelöst werden können. Für eine orts aufgelöste Messung [47] gibt es verschiedene Verfahren, die alle für jeden Messpunkt einen hyperspektralen Datenkubus generieren. In diesem Datenkubus sind zwei Dimensionen die x- und y-Position des Messpunktes. Die dritte Dimension entspricht der spektralen Intensität des gestreuten Lichtes an diesem Punkt, dem Raman-Spektrum an diesem Punkt. Folgende Verfahren werden angewendet:

- a) Punkt für Punkt Scan: Über die zu messende Probe wird ein Punktraster gelegt. An jedem Punkt dieses Rasters werden ein oder mehr Raman-Spektren aufgenommen, gespeichert und der nächste Punkt vermessen. Hierbei unterscheidet man zwischen zwei Messmodalitäten:
  - a. Einem Messvorgang, bei dem jeder Punkt zeilen- oder spaltenweise gemessen wird. Diese Methode ist am langsamsten, da der Messtisch am Ende jeder Zeile / Spalte an den Anfang der Zeile/Spalte zurückkehren muss, ohne dabei zu messen.
  - b. Einem schlangenartigen Messvorgang, bei dem man vom letzten Punkt der ersten Zeile zum letzten Punkt in der zweiten Zeile wechselt und diese Zeile dann von hinten nach vorne misst. Der letzte Messpunkt in der zweiten Zeile ist der erste Punkt der zweiten Zeile. Dann wird wieder der erste Punkt der dritten Zeile als erstes gemessen usw.



- b) Kontinuierlichen Scan: Man legt eine Geschwindigkeit fest, mit der der Laser in einem schlangenartigen Messvorgang über die Probe fährt. In einem vorher festgelegten Zeitintervall wird dann jeweils ein Spektrum aufgenommen und die Koordinaten des Messpunktes erfasst. Der Vorteil dieses Messvorgangs ist, dass die Messung schneller erfolgen kann. Der Nachteil ist, dass nicht mehrere Messungen am gleichen Punkt hintereinander erfolgen können.
- c) Weitfeld-Bildgebung: Ein komplettes spektrales Bild wird mit Hilfe der Integralfeld-Spektroskopie (engl. *integral field spectroscopy* – IFS) [48,49] auf einmal ohne ein Abrastern der Probe aufgenommen. Hierfür wird das Bild durch die sogenannte Integralfeld-Einheit (engl. *integral field unit* – IFU) optisch zerlegt und vor dem großen Eintrittsspalt des Weitfeld-Spektrographen aufgereiht. Die einfachste Umsetzung einer Integralfeld-Einheit ist die Verwendung eines Faserbündels. Probenseitig wird das Faserbündel dabei in einem zweidimensionalen Feld angeordnet, auf der Seite des Weitfeld-Spektrographen dagegen in Form einer Linie vor dem großen Spalt aufgereiht. Da mit dieser Methode viele Spektren auf einmal aufgenommen werden, ist eine große Detektorplatte mit einer entsprechend langen Auslesezeit notwendig [50,51]. Dies ist die schnellste Methode, benötigt jedoch einen starken Laser, hat einen hohen Energieeintrag in kurzer Zeit zur Folge und nur eine begrenzte Anzahl an Spektren pro Fläche.

### 1.2.1. Vorbehandlung von Raman-Daten

Vor der Analyse der Raman-Daten findet in der Raman-Spektroskopie eine Vorbehandlung (engl. *preprocessing*) der Daten statt, wobei Umfang und Art von der Datenqualität und der geplanten Analysemethoden abhängt. Diese kann die Entfernung von kosmischen Spitzen (engl. *cosmic spikes*), die Kalibrierung der Daten (Wellenlängen- und Intensitätskalibrierung), die Basislinienkorrektur, die Entfernung von Ausreißern (engl. *outlier*) aus dem Datensatz und die Normierung der Spektren beinhalten.

Durch kosmische Strahlung kann es zu Signalspitzen während einer Messung kommen. Die Entfernung dieser kosmischen Spitzen erfolgt entweder über entsprechende Algorithmen (durch Identifizieren von Ausreißern entweder in einem spektralen Fenster, in zwei, am gleichen Messpunkt aufgenommenen Spektren oder in einer Zeile in einem Raman-Bild) oder von Hand,

da die meisten Spitzen über eine sehr hohe Intensität verfügen und meist nur bis zu drei benachbarte Pixel betreffen.

Die Kalibrierung wird häufig mittels einer Kalibrierlampe durchgeführt. Hierbei wird eine Lampe mit einem schmalbandigen Emissionsprofil (z.B. Neon-Argon-Lampe) für die Wellenlängenkalibrierung und eine Lampe mit einem breiten Emissionsprofil (z.B. Wolfram-Halogen-Lampe) für die Intensitätskalibrierung verwendet. Zur Überprüfung der Wellenlängenkalibrierung werden zusätzlich Spektren von Substanzen mit einem scharfen Raman-Profil wie Paracetamol, Cyclohexan oder Polystyrol aufgenommen und die Wellenlängenchse gegebenenfalls nachjustiert [2,52].

In der Raman-Spektroskopie ist häufig eine Basislinienkorrektur aufgrund von probenabhängigen Variationen im Untergrund notwendig. Optional kann die Subtraktion eines geglätteten Spektrums einer Blindprobe erfolgen, um Puffer, Substrate und andere, systembedingte Untergründe zu korrigieren. Im einfachsten Fall kann eine Basislinienkorrektur mit Hilfe eines Polynoms niederen Grades vorgenommen werden. Bei komplexeren Untergründen wie z.B. Autofluoreszenz, kann auch die Korrektur mit Polynomen höheren Grades erforderlich werden. Es gibt viele verschiedene Algorithmen für die Basislinienkorrektur wie die multiplikative Signalkorrektur (engl. *multiplicative signal correction* – MSC [53]), EMSC [21,22], die Gummibandmethode [19], SNIP [23,24] und das Anfitten eines Polynoms [18]. In dieser Arbeit wurden die Korrekturalgorithmen EMSC und SNIP verwendet. Bei der EMSC werden Raman-Spektren möglicher Reinkomponenten oder vorbehandelte Mittelwertspektren der gemessenen Probe verwendet. Außerdem werden Spektren für den zu erwartenden Untergrund (z.B. ein Spektrum des Fluoreszenzverlaufs und/oder Polynome entsprechender Ordnung) angegeben. Die gemessenen Spektren werden an diese vorgegebenen Spektren mittels der Methode der kleinsten Quadrate angepasst und anschließend die Beiträge der Untergrundspektren subtrahiert. Beim SNIP Algorithmus wird ein Fenster vorgegeben, in dem die Intensitäten der Pixel an Anfang, Mitte und Ende gemittelt werden. Da die Unterschiede in den Intensitäten in einem Raman-Spektrum sehr hoch sein können, wird für die Berechnung des Mittelwertes der logarithmierte Quadratwurzeloperator auf das originale Spektrum angewandt. Durch Wiederholung dieser Prozedur für alle Pixel wird so eine Korrektur des Spektrums erreicht. Die Fenstergröße beeinflusst hierbei, wie sehr ein Spektrum korrigiert wird. Je kleiner das Fenster, desto kleiner der Bereich für die Anpassung und desto stärker die Basislinienkorrektur.

Für die Identifikation von Ausreißern wurde in dieser Arbeit eine Pearson-Korrelation [54] der gemessenen Spektren mit einem Mittelwertspektrum durchgeführt. Um sicher zu stellen, dass wirklich nur Ausreißer aus dem Datensatz entfernt werden, sollten die zu verwerfenden Spektren abschließend überprüft werden.

Auch für den letzten Schritt der Vorbehandlung von Raman-Daten, die Normierung, gibt es viele verschiedene Methoden, die alle eine Vergleichbarkeit der gemessenen Spektren gewährleisten soll. Beispiele hierfür sind die Flächennormierung (Gleichung (4)), z-score Normierung [42,55,56] (Gleichung (5)), die Vektornormierung (Gleichung (6)) und die Peak-Normierung, bei der entweder auf die Fläche unter einem Peak oder auf das Maximum eines Peaks normiert wird.

$$S_{\text{Fläche}}(\tilde{\nu}_i) = \frac{S(\tilde{\nu}_i)}{\sum_{i=1}^n S(\tilde{\nu}_i)} \quad (4)$$

$$S_{z\text{-score}}(\tilde{\nu}_i) = \frac{S(\tilde{\nu}_i) - \text{mean}(S)}{SD(S)} \quad (5)$$

$$S_{\text{vektor}}(\tilde{\nu}_i) = \frac{S(\tilde{\nu}_i)}{\sqrt{\sum_{i=1}^n (S(\tilde{\nu}_i))^2}} \quad (6)$$

Hierbei entspricht  $S(\tilde{\nu}_i)$  der Signalintensität der Wellenzahl  $i$ ,  $\text{mean}(S)$  dem Mittelwert und  $SD(S)$  der Standardabweichung der Signalintensität des gesamten Spektrums.

Die so vorbehandelten Raman-Daten können dann für die weitere Analyse verwendet werden.

### 1.2.2. Chemometrie und multivariate Datenanalyse

Die Chemometrie beschäftigt sich mit der Auswertung von chemischen Messdaten mit Hilfe der multivariaten, statistischen Datenanalyse. Hierbei entspricht die Anzahl der Messkanäle, d.h. im Falle von Raman-Spektren die Anzahl an Messpunkten pro Spektrum, der Anzahl an Variablen und damit der Dimensionalität des Datensatzes. Um die Analyse zu erleichtern, kann die Dimensionalität eines Datensatzes reduziert werden. Dies kann durch die Anwendung von Regressionsmethoden, durch Reduzierung der spektralen oder lateralen Auflösung mittels Binning, durch die Verwendung von gemittelten Spektren der verschiedenen Cluster einer Clusteranalyse oder durch eine Hauptkomponentenanalyse (engl. *principal component analysis* – PCA [57–59]) erreicht werden. Die in dieser Arbeit verwendete PCA stellt eine

Hauptachsentransformation des Datensatzes dar, wobei die neuen Hauptachsen den Eigenvektoren der Kovarianzmatrix des Datensatzes, auch Hauptkomponenten genannt, entsprechen. Die Eigenvektoren werden hierbei nach ihren Eigenwerten sortiert, wobei größere Eigenwerte mit einer größeren Varianz gleichzusetzen sind.

Für die Erkennung von geringsten Unterschieden in Raman-Spektren finden computerbasierte, mathematische Klassifikationsmethoden Anwendung. Diese können grob darin unterschieden werden, ob es sich um überwachte (engl. *supervised*) oder unüberwachte (engl. *unsupervised*) Methoden handelt.

Bei Letzteren werden die Daten nach bestimmten Kriterien gruppiert, ohne vorher Klassen vorzudefinieren. Beispiele für unüberwachte Klassifikationen sind die Clusteranalysen (z.B. hierarchische Clusteranalyse [60,61] und *k-means* [62]) und die bereits zuvor genannten PCA und Regressionsmethoden. Die hierarchische Clusteranalyse (engl. *hierarchical cluster analysis* – HCA) betrachtet jedes Spektrum als ein Cluster und berechnet den spektralen Abstand oder die spektrale Ähnlichkeit zwischen den Clustern nach einer vorgegebenen Formel, im Falle dieser Arbeit nach der Pearson-Distanz. Die Cluster werden dann Schritt für Schritt einem Fusionsalgorithmus folgend, z.B. dem Minimum Varianzkriterium nach Ward, bis zu einer vom Anwender vorbestimmten Anzahl vereinigt. Diese Methode ist rechenaufwendiger als andere Clustermethoden, resultiert aber bei gleichen Kriterien in der gleichen Clustereinteilung. Andere Clustermethoden müssen mehrfach iteriert werden, um eine stabile Einteilung in Cluster zu erhalten.

Bei der Verwendung von überwachten Methoden ist es notwendig, dass jedes Spektrum einer Klasse zugeordnet werden kann oder Referenzinformationen zur jeweiligen Probe vorliegen, welche beispielsweise mittels eines Goldstandards ermittelt wurden. Mit diesem Vorwissen wird ein mathematisches Modell entwickelt, nach welchem sich der Datensatz in die bereits bekannten Klassen einteilen lässt. Anschließend wird das entwickelte Klassifizierungsmodell dafür verwendet, um einen unbekanntem Datensatz zu klassifizieren. Wendet man das Modell auf einen Datensatz an, für den ebenfalls eine Klassenzuordnung vorliegt, kann eine Validierung des Modells erfolgen, indem die Daten mittels des Modells klassifiziert werden. Für die Güte einer Validierung gibt es verschiedene Klassifikatoren, wie Sensitivität (engl. *sensitivity*), Selektivität (engl. *specificity*), Relevanz (engl. *precision*) und Vertrauenswahrscheinlichkeit (engl. *accuracy*),

die aus der Konfusionsmatrix errechnet werden können. Die Sensitivität ist ein Maß dafür, wie viele Prozent der positiven Ergebnisse richtigerweise als positiv klassifiziert wurden. Die Spezifität hingegen ist ein Maß dafür, wie viele Prozent der negativen Ergebnisse richtigerweise als negativ klassifiziert wurden. Die Relevanz gibt an, wie stark die Ergebnisse streuen. Die Vertrauenswahrscheinlichkeit gibt an, wie viele Ergebnisse richtig klassifiziert wurden. Mit Hilfe von Abbildung 2 können Relevanz und Vertrauenswahrscheinlichkeit verdeutlicht werden.

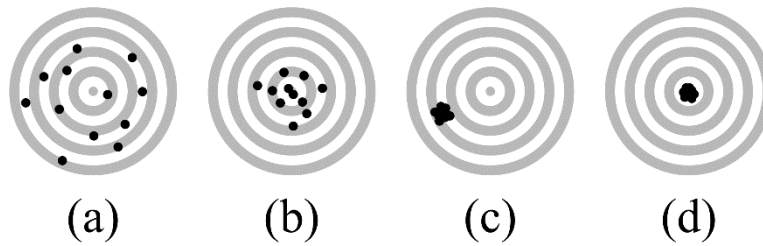


Abbildung 2: Zielscheiben mit Einschüssen für die Darstellung von Relevanz und Vertrauenswahrscheinlichkeit; **(a)** geringe Relevanz und Vertrauenswahrscheinlichkeit: Schüsse streuen und treffen nicht ins Ziel; **(b)** höhere Relevanz und Vertrauenswahrscheinlichkeit: Schüsse sind mittiger auf der Zielscheibe und streuen weniger; **(c)** hohe Relevanz, aber sehr geringe Vertrauenswahrscheinlichkeit: Schüsse treffen sehr dicht beieinander (geringe Streuung), aber am Rand des Ziels; **(d)** sehr hohe Relevanz und Vertrauenswahrscheinlichkeit: geringe Streuung der Schüsse und alle landen im Zentrum der Zielscheibe.

Um die Stabilität des Modells zu gewährleisten und die Gefahr einer Überanpassung des Klassifikationsmodells an den Trainingsdatensatz zu verringern, kann eine Kreuzvalidierung durchgeführt werden. Hierbei kann zwischen der internen und der externen Kreuzvalidierung unterschieden werden [63]. Bei der internen Kreuzvalidierung wird die Stabilität des Modells durch kleine Veränderungen im Trainingsdatensatz getestet. Bei der externen Kreuzvalidierung wird geprüft, wie sehr sich die Validierung eines Modells durch Änderung der Testdaten verändert, indem der Testdatensatz durch Auslassen von Daten variiert wird. Die häufigsten Techniken für eine Kreuzvalidierung sind die *k*-fach Kreuzvalidierung und die *leave-one-batch-out* Kreuzvalidierung. Bei der *k*-fach Kreuzvalidierung wird der Datensatz zufällig in *k* Teile unterteilt und jeweils ein Teil entweder für die Modellvalidierung verwendet oder, im Falle der externen Kreuzvalidierung, nicht für eine Validierung berücksichtigt. Dies wird dann *k*-fach wiederholt. Bei der *leave-one-batch-out* Kreuzvalidierung wird der Datensatz nicht zufällig, sondern gemäß seiner Probenchargen unterteilt. Alles Weitere erfolgt dann gemäß der *k*-fach Kreuzvalidierung.

Beispiele für überwachte, modellbasierte Klassifikationen sind die lineare Diskriminanzanalyse (engl. *linear discriminant analysis* – LDA [64,65]), die Stützvektor-Maschinen (engl. *support vector machines* – SVM [66]), die weiche, unabhängige Modellierung durch Klassenanalogie (engl. *soft independent modelling by class analogy* – SIMCA [67]) etc. Allen diesen Methoden ist gemein, dass sie aus Klassifikationen zwischen zwei Klassen aufgebaut sind. In dieser Arbeit wurde die LDA angewendet, die der PCA sehr ähnlich ist und auf der Maximierung der Varianz zwischen den Klassen basiert. Durch eine Koordinatentransformation wird die gemeinsame Kovarianzmatrix in eine sphärische Struktur überführt und durch die Normalenvektoren zwischen den Klassenmittelwerten die optimale Trennebene ermittelt. Durch eine Kostenfunktion kann eine Fehlklassifikation bestraft werden, um die Trennung der Klassen zu optimieren.

### 1.3. Stand der Technik der Fluoreszenzkorrektur in Raman-Spektroskopie

Raman-Streuung ist ein nur wenige Femtosekunden dauernder Prozess, während Fluoreszenz eine Lebensdauer von Nanosekunden besitzt. Im Vergleich zur Raman-Streuung ist Fluoreszenz folglich ein langsamer Prozess. Zeigt eine Probe Fluoreszenz, sind der Absorptionsquerschnitt der Fluoreszenz und damit die effektive Quantenausbeute häufig deutlich höher als der Streuquerschnitt und die Quantenausbeute der Raman-Streuung. Dies führt dazu, dass bereits geringe Konzentrationen einer fluoreszierenden Substanz, eines sogenannten Fluorophors, in der Probe zu einem sehr hohen spektralen Untergrund führen kann. Dadurch können bei Proben mit intrinsischen Fluorophoren nur kurze Expositionszeiten für die Raman-Spektroskopie verwendet werden, da sonst die Sättigung des Detektors durch Fluoreszenz erfolgen kann. Insbesondere in Metaboliten von Blut bzw. Häm und das Coenzym FAD (Flavin-Adenin-Dinukleotid) enthaltene Substanzen [8,68] können bei biologischen Proben ein Problem darstellen.

Eine deutliche Verringerung der Autofluoreszenz kann durch eine passende Wahl der Anregungswellenlänge erreicht werden. Je langwelliger das Anregungslicht ist, desto unwahrscheinlicher wird die Anregung von Fluoreszenz in biologischen Proben. Aus diesem Grund werden häufig Anregungswellenlängen aus dem Nahinfrarot-Bereich (NIR-Bereich) für die Raman-Spektroskopie verwendet. Jedoch verringert sich auch die Intensität der Raman-Streuung mit dem Inversen der vierfachen Potenz der Wellenlänge und die meisten Detektoren verlieren im NIR-Bereich stark an Sensitivität.

Eine andere Methode zur Verringerung des Fluoreszenzuntergrundes ist das Zerstören der Fluorophore, entweder durch reine Lichteinwirkung, das Photobleichen (engl. *photobleaching*) [69], oder durch Verwendung von Chemikalien wie Wasserstoffperoxid und anschließendes Bescheinen der Probe für einen längeren Zeitraum [70]. Der Nachteil ersterer Methode ist der erhöhte Wärmeeintrag in die Probe und das damit verbundene, erhöhte Risiko einer Beschädigung. Die zweite Form des Bleichens führt neben dem Wärmeeintrag auch zu Verunreinigung oder Veränderung der Probe durch Chemikalien.

Weitere Möglichkeiten für die Fluoreszenzkorrektur in der Raman-Spektroskopie sind Methoden der Basislinienkorrektur, welche sich in mathematische und instrumentelle Methoden unterteilen lassen. Für die mathematischen Methoden gibt es diverse Basislinienkorrekturalgorithmen (siehe Kapitel 1.2), welche auch für die Korrektur von Fluoreszenzuntergründen Anwendung finden.

Diese Software basierten Methoden sind kostengünstig, erfordern jedoch Erfahrung in der Datenanalyse. Bei den instrumentellen Verfahren zur Basislinienkorrektur macht man sich zu Nutze, dass die Fluoreszenz über einen größeren Anregungswellenlängenbereich konstant ist und durch die vibronische Relaxation nach der Anregung über eine deutlich längere Lebensdauer verfügt. Dadurch erfolgt die Fluoreszenzemission deutlich später als die Raman-Streuung. Die zeitabhängigen Methoden verwenden gepulste Laser-Anregung und schnell reagierende Detektoren mit niedrigen Verschlusszeiten (z.B. Kerr gates), die die Raman-Streuung detektieren und vor dem Eintreffen der Fluoreszenz die Blende schließen. Eine andere Möglichkeit stellt die Frequenzmodulation dar. Hierbei kann die schnelle Raman-Streuung der Frequenzmodulation folgen, während die langsamere Fluoreszenz der Anfangsfrequenz folgt. Dadurch ist es möglich, das Raman-Signal getrennt vom Fluoreszenzsignal zu detektieren. Modulation kann auch für die Wellenlänge verwendet werden, um die Fluoreszenz zu unterdrücken. Hierbei werden in festen Zeitintervallen einzelne Spektren aufgenommen, während die Anregungswellenlänge für mehrere Zyklen moduliert wird. Mittels einer PCA wird dann die Variation des Raman-Signals in den Spektren bestimmt. Das Differenzspektrum zeigt die Raman-Banden in Form von Differenzbanden, während der Untergrund wie Fluoreszenz, der der Veränderung der Anregungswellenlänge nicht folgen konnte und deshalb konstant bleibt, sich gegenseitig auslöscht.

Ein ähnliches Prinzip wird bei der Raman-Differenzspektroskopie mit leicht verschobener Anregungswellenlänge verwendet (engl. *shifted excitation Raman difference spectroscopy* – SERDS). Hierfür werden an der gleichen räumlichen Position zwei oder mehr Spektren mit leicht unterschiedlicher Anregungswellenlänge aufgenommen, wobei sich die Raman-Banden entsprechend der Anregungswellenlänge in den jeweiligen Spektren verschieben. Solange der Unterschied zwischen den Anregungswellenlängen so klein ist, dass die gleichen Fluorophore angeregt werden, ändert sich das Emissionsprofil der auftretenden Fluoreszenz nicht. Auch Instrument-inhärente Untergrundsignale, wie beispielsweise Filterprofile, und externe Störquellen, wie durch Leuchtstoffröhren emittiertes Raumlicht, ändern sich durch diese Verschiebung der Anregungswellenlänge nicht. Subtrahiert man zwei Spektren voneinander, erhält man ein Differenzspektrum oder SERDS-Spektrum, bei dem lediglich die Raman-Banden als Differenzbanden auftreten und diese sich vom übrigen Spektrum, das idealerweise überall sonst auf der Nulllinie liegt, deutlich abheben. In Abbildung 3 ist der simulierte, ideale SERDS-



Fall dargestellt. Durch Änderung der Anregungswellenlänge erhält man zwei Raman-Spektren mit leicht verschobenen Raman-Banden, die einen hohen, konstanten Fluoreszenzuntergrund aufweisen (a). Subtrahiert man die beiden Spektren voneinander erhält man ein Differenz- oder SERDS-Spektrum, welches ein charakteristisches Differenzprofil ohne Restuntergrund aufweist (b).

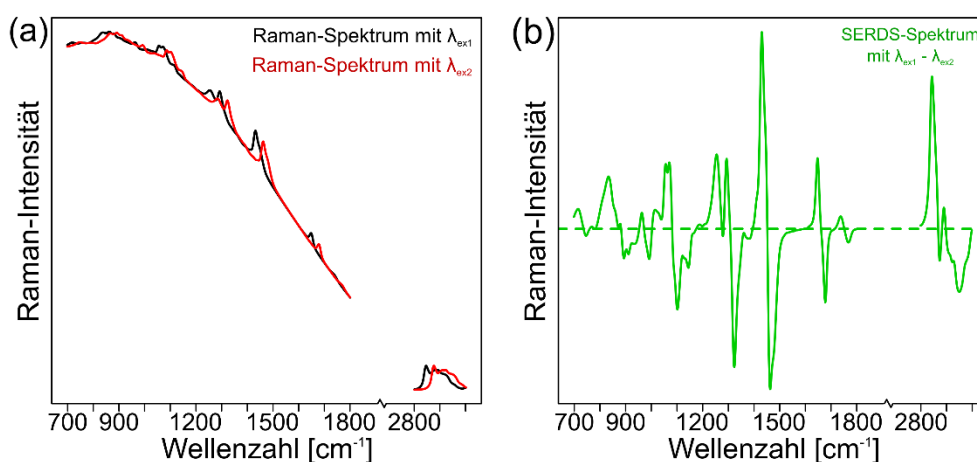


Abbildung 3: SERDS ohne Photobleichen; **(a)** simulierte Raman-Spektren mit zwei verschiedenen Anregungswellenlängen und konstantem Untergrund; **(b)** untergrundfreies Differenzspektrum, was durch Subtraktion der beiden Raman-Spektren aus (a) erhalten wird.

Ändert sich allerdings während einer Messung der Fluoreszenzuntergrund, bleibt nach der Subtraktion ein Restuntergrund im Differenzspektrum erhalten. Diese Änderungen basieren auf dem Ausbleichen der Fluorophore durch das Laserlicht, Intensitätsunterschiede in der Fluoreszenzemission aufgrund der geänderten Wellenlänge und eventuellen Intensitätsunterschieden des verwendeten Lasersystems bei den unterschiedlichen Anregungswellenlängen. In Abbildung 4 sind dieselben simulierten und verschobenen Raman-Spektren dargestellt. Der Fluoreszenzuntergrund verändert sich hierbei zwischen den Messungen, um Photobleichen zu simulieren (a). Im Differenzspektrum sind neben den Differenzbanden nun auch ein merklicher Restuntergrund sichtbar (b).

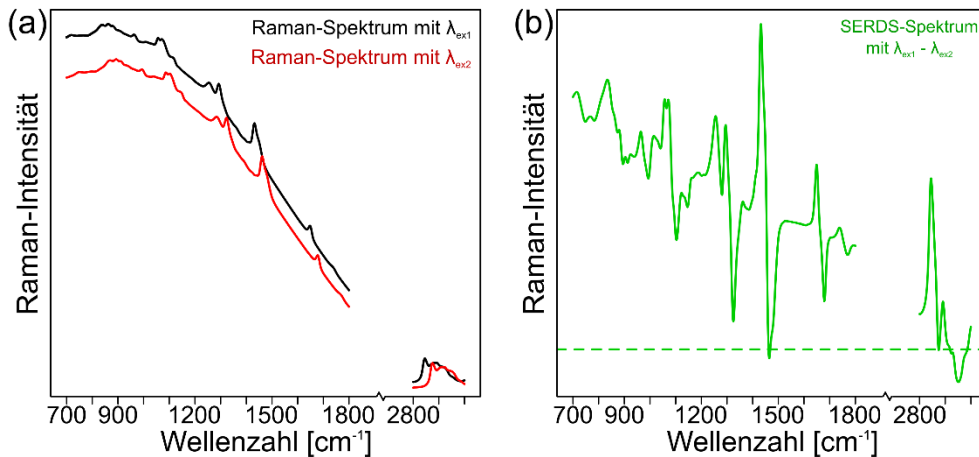


Abbildung 4: SERDS mit Photobleichen; **(a)** simulierte Raman-Spektren mit zwei verschiedenen Anregungswellenlängen und unterschiedlich intensivem Untergrund; **(b)** Differenzspektrum mit Restuntergrund, was durch Subtraktion der beiden Raman-Spektren aus (a) erhalten wird.

Da für die chemische Interpretation eines Raman-Spektrums die genauen Positionen der Raman-Banden benötigt werden, gibt es verschiedene Algorithmen zur Rekonstruktion eines Raman-Spektrums aus einem SERDS-Differenzspektrum. Da ein Differenzspektrum stark an die erste Ableitung eines Raman-Spektrums erinnert, kann eine Rekonstruktion des Raman-Spektrums durch Integration des Differenzspektrums, zum Beispiel durch eine schrittweise Aufsummierung der Intensitäten, erfolgen. Der Wendepunkt einer Differenzbande ist jedoch nur dann identisch mit der Position einer Raman-Bande, wie es in der ersten Ableitung eines Raman-Spektrums der Fall wäre, wenn der Versatz der Anregungswellenlänge genau der Halbwertsbreite (FWHM) der Raman-Bande entspricht. Weicht die Verschiebung der Anregungswellenlänge von dieser Halbwertsbreite ab, hinkt der Vergleich mit der ersten Ableitung eines Raman-Spektrums. Eine Rekonstruktion des Raman-Spektrums durch einfache Punkt-für-Punkt-Integration des Differenzspektrums ist dann zwar noch möglich, führt jedoch zu einer Verschiebung der Position der Raman-Banden. Es gibt eine Vielzahl an Rekonstruktionsalgorithmen wie beispielsweise Dekonvolutionsmethoden [32], das Anpassen von Gauss- oder Lorentzprofilen [29,31], lineare Datenmanipulation [31], Methoden der multiskalen Poisson-Intensitätsschätzungen [34,86], eine Rekonstruktion mittels einer Funktion ähnlich einer Kernel-Funktion [30], ein Anpassen nach der Methode der nicht-negativen kleinsten Quadrate [33] oder die bereits erwähnte Integration. Allen Rekonstruktionsmethoden ist gemein, dass sie zu Artefakten im rekonstruierten Spektrum führen können, da eine Verschiebung in benachbarte Banden oder die Subtraktion von sehr breiten Banden zu einem Differenzbandenprofil führen kann, das sehr stark von der ersten Ableitung eines Raman-Spektrums abweicht.

Entwickelt wurde SERDS von Shreve *et al.* [32,71] unter Verwendung eines durchstimmbaren Ti:Saphir Lasers. Cherepy *et al.* [72–75] verwendete denselben Aufbau mit nur leichten Modifikationen für SERDS Messungen an photosynthetischen Reaktionszentren. Die Verwendung von durchstimmbaren Lasern ermöglicht, dass unterschiedliche Wellenlängenverschiebungen aufgenommen werden können. Der Bereich für die Wellenlängenverschiebung wird häufig jedoch nicht durch die Durchstimbarkeit des Lasers, sondern üblicherweise durch die in einem Raman-Aufbau verbauten Laserlinien- und Bandpassfilter begrenzt. Eine spätere Entwicklung, die dem SERDS ähnlich ist, war die Verschiebung der Raman-Banden mittels einer Verschiebung des Gitters im Spektrographen [76,77]. Diese Methode ist kostengünstiger, weil kein durchstimmbarer Laser benötigt wird, aber die Korrektur des Untergrundes ist schlechter als bei SERDS.

Einige *proof-of-principle* Studien mit diversen Anregungswellenlängenkombinationen wurden durchgeführt, in denen Farbstoffe mit reinen Lösungsmitteln oder Lösungsmittelgemischen vermengt als Proben dienten [78–80]. Auch für die Untersuchung von biologischen Proben wurde die SERDS-Technik bereits eingesetzt [40,41,81–85]. Insbesondere die Untersuchungen von Gebrekidan *et al.* an tierischem Gewebe [42] und humanen Brustkrebsproben [86] zeigen, dass weiterhin eine aufwendige Prozessierung von SERDS-Daten notwendig ist, aufgrund der oben aufgeführten Verzerrung der Differenzspektren durch Restuntergrund oder der Rekonstruktion zu interpretierbaren Raman-Profilen. Dieser Aufwand steht im starken Gegensatz dazu, dass die SERDS-Methode als eine instrumentelle Basislinienkorrekturmethode eigentlich ohne großen Rechenaufwand auskommen sollte.

Die neuste Entwicklung auf dem Gebiet der SERDS-Technologie ist die Kombination von oberflächenverstärkter Raman-Spektroskopie (engl. *surface enhanced Raman spectroscopy* – SERS) und SERDS durch Strobbia *et al.* [87], um mit Hilfe eines mit einem Nanopartikel versehenen Sensormoleküls Mikro-Ribonukleinsäuremoleküle (engl. *micro ribonucleic acid* – miRNA) mit Hilfe von Raman-Spektroskopie zu detektieren. Die plasmonisch verstärkten Raman-Signale konnten hierbei mit Hilfe der SERDS-Methode durch ein Blatt hindurch bei angeschalteter Pflanzlampe gemessen werden.

Die bisherigen Publikationen über SERDS beschränken sich auf Einzelspektren oder auf Serien von Einzelspektren, die für ein besseres Signal-Rausch-Verhältnis gemittelt werden. Nach

anschließender, häufig sehr aufwendiger Datenprozessierung erfolgt die Rekonstruktion des Raman-Spektrums und die Interpretation und/oder Klassifikation. Lediglich die von Schmäzlin *et al.* durchgeführten Versuche [38] und die in Rahmen dieser Arbeit durchgeführten Experimente beschäftigten sich mit der SERDS-Bildgebung.

#### 1.4. „*interlaced nod and shuffle*“ in der Astrophysik

In der Astrophysik werden für spektroskopische Messungen von Himmelskörpern Teleskope mit großen CCD-Chips eingesetzt und sehr lange Belichtungszeiten benötigt. Da sich während der langen Messung der Hintergrund, also der Nachthimmel, ständig verändert und das Auslesen der großen CCD-Chips sehr viel Zeit kostet, wurde die „*nod and shuffle*“ Technik entwickelt [88]. Bei dieser Technik wird schnell zwischen dem zu messenden Himmelskörper und dessen Untergrund, dem benachbarten Nachthimmel, hin und her gewechselt. Diese Änderung des Messobjekts bezeichnet den „*nod*“, da das Teleskop dabei ursprünglich eine nickende Bewegung zwischen den zwei Positionen durchführt hat. Dies geht einher mit einer Verschiebung der Ladungen auf dem CCD-Chip, dem „*shuffle*“ in „*nod and shuffle*“. Auf diese Weise können in schnellen Messintervallen sowohl der sich ändernde Nachthimmel wie auch der Himmelskörper über einen langen Zeitraum spektroskopisch erfasst werden. Anfangs wurde hierfür der CCD-Chip in drei Bereiche aufgeteilt. Im mittleren Bereich wurden die Daten aufgenommen, während die obere und untere Bereich jeweils für Akkumulierung der Ladungen des Himmelskörpers und des Nachthimmels verwendet wurden. Werden die Ladungen für Himmelskörper und Nachthimmel nicht in extra Lagerbereiche auf dem CCD-Chip sondern in die Zwischenräume zwischen den Belichtungsregionen zweier Spektren verschoben, kann der Platz auf einem CCD-Chip effizienter genutzt werden [89,90]. Diese Art der Ladungsverschiebung wird als „*interlaced nod and shuffle*“ bezeichnet (siehe Abbildung 5) und hat den zusätzlichen Vorteil, dass Effizienzprobleme bei der Ladungsübertragung vermieden werden. Die in Abbildung 5 dargestellten Datenspuren, die auf der linken Seite mit (G) gekennzeichnet sind, repräsentieren Datenspuren des zu messenden Himmelskörpers, während die mit (N) versehenen denen des Nachthimmels entsprechen.

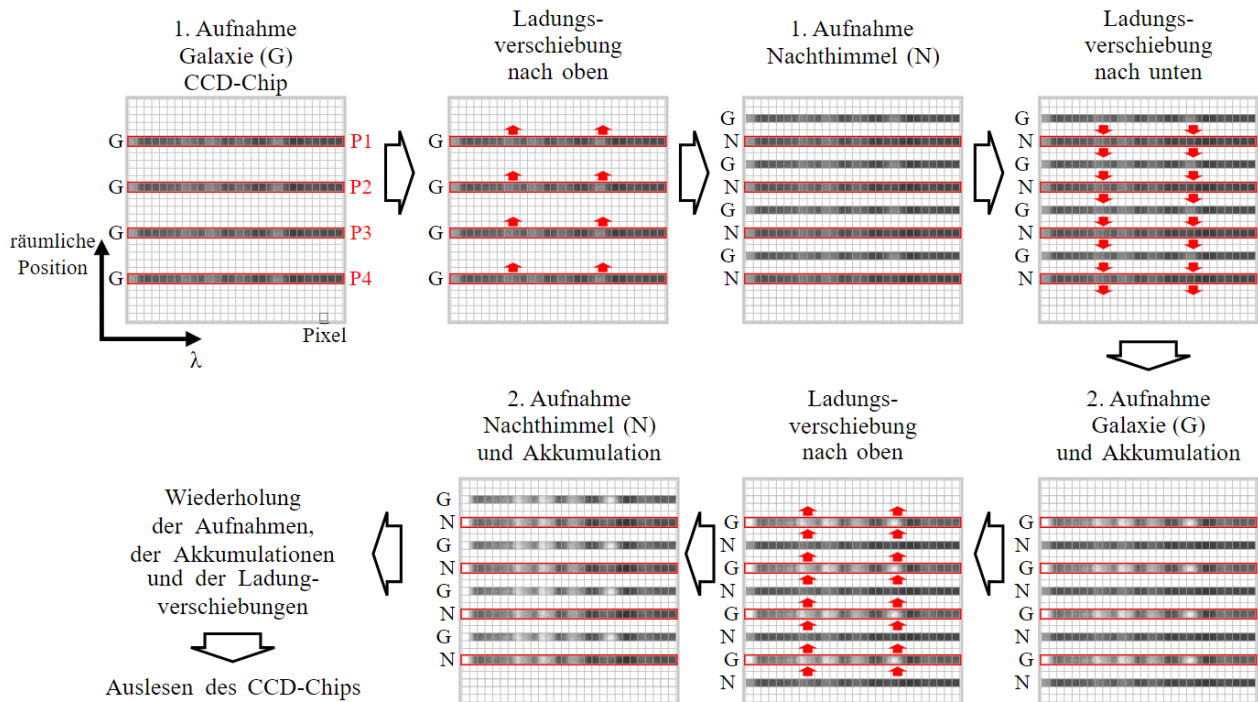


Abbildung 5: Schema der „interlaced nod and shuffle“ Technik; hierbei werden die Ladungsverschiebungen (rote Pfeile) auf einem CCD-Chip schematisch dargestellt, wobei ein Kästchen einem Pixel auf der CCD entspricht. Die horizontalen, schwarzen Linien symbolisieren die spektralen Signalspuren der Galaxie (G) bzw. des Nachthimmels (N). Die weißen Bereiche innerhalb der schwarzen Linien zeigen das gemessene Signal, welches sich über die Akkumulationen verstärkt, und somit heller wird. Die roten Rechtecke zeigen die Regionen auf dem CCD-Chip, welche während einer Aufnahme belichtet werden. Jedes rote Rechteck entspricht einer fixen, räumlichen Position im Weitfeldbild (P1, P2, P3 und P4). Zur Vereinfachung werden nur vier räumliche Positionen des Weitfeldbildes gezeigt.

Da der CCD-Chip nur einmal am Ende der Messung ausgelesen wird, addiert sich das elektronische Rauschen, was beim Auslesen des CCD-Chips entsteht, nur einmal auf den kompletten Datensatz. Außerdem enthalten beide Messungen, sowohl Nachthimmel als auch Himmelskörper, dieselben Messartefakte durch Sensitivitätsunterschiede der Pixel, da die Spektren-Paare jeweils auf den gleichen Pixeln des CCD-Chips gemessen werden.

## 1.5. Anwendung

### 1.5.1. Pollen

Die Palynologie beschäftigt sich mit der Analyse von Pollen, den männlichen Gametophyten, die für die Bestäubung und Befruchtung von Pflanzen und damit deren Fortpflanzung benötigt werden [91,92]. Pollen verfügen über eine Gestalt, die spezifisch für das jeweilige Pflanzengenus ist, und sind von einer stabilen Außenhülle umgeben [93]. Diese Außenhülle, das Sporoderm, besteht vor allem aus Pektin und Sporopollenin. Pollen können bei Menschen allergische Reaktionen hervorrufen [94–96]. Um die Pollenbelastung der Luft zu dokumentieren, wird ein Pollenflugkalender erstellt [97]. Dieser verändert sich aufgrund des Klimawandels und der damit verbundenen Verschiebung der Blütezeiten [98]. Mit Hilfe von Luftproben und der Analyse der in ihnen enthaltenen Blütenpollen wird die tägliche Pollenbelastung bestimmt, der Pollenkalender aktualisiert und die Veränderung des Klimas dokumentiert. Eine hohe Pollenbelastung kann durch Lüftungsanlagen, geöffnete Fenster oder Arbeiten unter freiem Himmel auch ein Problem für den Arbeitsschutz darstellen, da sich durch die Auswirkungen der Pollenallergie das Unfallrisiko bei der Arbeit erhöhen kann. In der Honigindustrie ist die Palynologie sehr wichtig, um die Herkunft eines Honigs und seine Reinheit mittels der Norm DIN 10760 zu bestimmen. Auch die Saatgutindustrie benötigt eine genaue Unterscheidung von Pollen, um reines Saatgut garantieren zu können. Der Goldstandard in der Palynologie ist die taxonomische Erfassung und Auszählung der Pollen basierend auf ihrer Morphologie [91,99,100]. Dies ist sehr zeitintensiv und benötigt gut ausgebildete Experten. Es gibt diverse Ansätze für eine Automatisierung und technische Verbesserungen der Pollenanalyse [99–106]. Auch Verfahren wie Fluoreszenz-Mikroskopie [107–109], Infrarot-Spektroskopie [92,98,107,110–114], Raman-Spektroskopie [96,98,113–124] und laserinduzierte Plasma-Spektroskopie [123,125] wurden bereits verwendet, um Pollen zu unterscheiden. Die in dieser Arbeit vorgestellte Untersuchung von 6028 Pollenproben unter Verwendung der SERDS-Methode zur Autofluoreszenzkorrektur stellt eine Neuheit dar. Die SERDS-Methode lässt sich außerdem gut in einen vollautomatisierten Aufbau integrieren, was für das Feld der Palynologie von großem Interesse sein kann.

### **1.5.2. Tierische Gewebeproben**

Jedes Gewebe verfügt über eine charakteristische, biochemische Zusammensetzung, welche mittels schwingungsspektroskopischer Methoden bestimmt werden kann [47]. Bei Erkrankungen kann es zu krankhaften Veränderungen im Gewebe kommen, wodurch sich auch die entsprechende biochemische Komposition verändert. In der Medizin gehören Sonographie, Röntgenstrahlung und Computertomographie, Positronen-Emissions-Tomographie und Magnetresonanztomographie zu den Standardverfahren für die Untersuchung von unterschiedlichem Gewebe [126,127]. Hierbei ist allen gemein, dass es sich bei ihnen um bildgebende Verfahren mit einer hohen Eindringtiefe und einer räumlichen Auflösung im mm-Bereich handelt und keine Auskunft über die biochemischen Veränderungen geben können. Für die pathologische oder intraoperative Diagnostik von Gewebe sind sowohl Informationen über die Morphologie und biochemische Zusammensetzung als auch eine Auflösung auf zellulärer Ebene notwendig. Diese Informationen können mit Hilfe der photonischen Methoden erhalten werden [128,129]. Beispiele hierfür sind die induzierte Fluoreszenz-Bildgebung [127] und die konfokale Endomikroskopie, welche jedoch den Einsatz von Markern notwendig macht. Weitere Methoden, die ohne Marker auskommen, sind die Autofluoreszenz-Bildgebung, optische Kohärenztomographie, die multimodale Multiphotonen-Bildgebung, die Raman-Spektroskopie, die Infrarot-Spektroskopie etc. Insbesondere mit Hilfe von Infrarot- und Raman-Spektroskopie [130–133] lassen sich biochemischen Veränderungen im Gewebe sehr gut beobachten, was bereits in zahlreichen Publikationen gezeigt werden konnte [1,2,4–7,12–14,43,134–137]. Auch die SERDS-Technik wurde bereits zur Untersuchung von tierischem und menschlichem Gewebe verwendet [38,39,41,42,81,83,86]. Die typischen Bestandteile von tierischem Gewebe sind Nukleinsäuren, Proteine, Lipide, Knochen, Blut und Wasser, welche über charakteristische Bandenstrukturen verfügen. Tierisches Gewebe stellt ein gutes Modell für Humangewebe dar und wurde deshalb im Zuge dieser Arbeit als Modellprobe für medizinische Proben verwendet. Die verwendeten Muskelgewebeproben stammten vom Schwein und enthielten vor allem Proteinstrukturen [138], die typisch für Muskelgewebe sind, und Lipidstrukturen [139], die typisch für Fettgewebe sind.



### 1.5.3. Synthetische Polymere

Synthetische Polymere sind Stoffe, die im Labor und nicht in einem Organismus hergestellt werden. Sie sind aus Makromolekülen aufgebaut sind, welche ihrerseits aus kleineren, sich wiederholenden Monomer-Einheiten bestehen. Ihre Herstellung erfolgt entweder durch Kettenpolymerisation, Polykondensation oder Polyaddition [140]. Ihr Vernetzungsgrad und ihre Kettenlänge können über die Reaktionsführung gesteuert werden, wodurch es möglich ist, wohl definierte Polymere zu erhalten. Aufgrund ihrer sehr regelmäßigen Struktur und ihrer großen Kettenlängen verfügen Polymere über einen großen Raman-Streuquerschnitt. Polymere finden in allen Bereichen des Lebens Anwendung und sind der Hauptbestandteil von Kunststoffen. Bei den in dieser Arbeit verwendeten Polymerkugeln handelt es sich um die beiden Polymere Polymethylmethacrylat (PMMA) [141,142] und Polystyrol (PS) [143–145], welche aufgrund ihres wohl definierten Durchmessers und ihrer intensiven, charakteristischen Raman-Spektren Anwendung fanden. Beide Polymere können vielfältig eingesetzt werden. PS wird beispielsweise in Verpackungen (z.B. CD-Hüllen und Kassetten oder, in aufgeschäumter Form, als Styropor) verwendet, während PMMA als Glasersatz in der Optik (z.B. Brillengläser, Lupen und Uhrgläser), im Bauwesen und in der Automobilindustrie Anwendung findet. Die wichtigsten Raman-Banden der beiden Polymere werden im Folgenden aufgeführt:

**Polystyrol** [146]:  $623\text{ cm}^{-1}$  (Ring Deformationsschwingung),  $1003\text{ cm}^{-1}$  (aromatische Ringatmungsschwingung),  $1034\text{ cm}^{-1}$  (in-plane CH Deformationsschwingung),  $1155\text{ cm}^{-1}$  (C-C Streckschwingung),  $1585\text{ cm}^{-1}$  und  $1603\text{ cm}^{-1}$  (Ring Streckschwingung),  $3066\text{ cm}^{-1}$  (aromatische CH Streckschwingung)

**Polymethylmethacrylat** [147]:  $604\text{ cm}^{-1}$  (C-C-O Streckschwingung),  $818\text{ cm}^{-1}$  (C-O-C Streck-schwingung),  $970\text{ cm}^{-1}$  ( $\text{CH}_3$  Schaukelschwingung)  $991\text{ cm}^{-1}$  (O- $\text{CH}_3$  Schaukelschwingung),  $1456\text{ cm}^{-1}$  ( $\text{CH}_3$  Deformationsschwingung),  $1736\text{ cm}^{-1}$  (C=O Streckschwingung),  $2957\text{ cm}^{-1}$  (CH Streckschwingung in  $\text{CH}_2$  und  $\text{CH}_3$ )

## 1.6. Zielsetzung der Dissertation

Ziel dieser Arbeit war die Evaluierung und Optimierung der instrumentellen Basislinienkorrekturmethode SERDS und deren Eignung für bildgebende Verfahren zur Untersuchung biologischer Proben. Als Beispiele für biologisches Gewebe wurden hierbei tierische Gewebeprobe und Pollen verwendet. Im ersten Schritt wurde eine tierische Gewebeprobe mittels eines Punkt-für-Punkt-Scans bei unterschiedlichen Anregungswellenlängen mit dem Ziel untersucht, die optimalen Parameter und entsprechende Datenverarbeitungsschritte für die SERDS-Technik zu ermitteln. In einem zweiten Schritt wurde ein Protokoll zur Verarbeitung und Klassifikation von SERDS-Daten erstellt, welches dann in einer Fallstudie erprobt und bewertet wurde. Für die Fallstudie wurden Einzelspektren von 6800 Pollen von acht verschiedenen Pflanzengenera gemessen. Das Protokoll sah eine direkte Klassifikation der SERDS-Spektren ohne vorherige Rekonstruktion von Raman-Spektren vor und wurde durch den Vergleich mit Klassifikationen basierend auf rekonstruierten Raman-Spektren und basislinienkorrigierten, gemessenen Raman-Spektren beurteilt. Im letzten Teil dieser Arbeit rückt erneut die Bildgebung mittels SERDS in den Vordergrund. Durch Adaption der „*interlaced nod and shuffle*“ Technik aus der Astrophysik wurden Messungen mit sehr kurzen Aufnahmezeiten (50 ms) für einen Weitfeld-SERDS-Bildgebungs Aufbau erstmals realisiert. Es sollte ferner gezeigt werden, dass durch die Verwendung kurzer Aufnahmezeiten eine kurze Störung der Messung durch Raumlicht und das Photobleichen in Weitfeld-SERDS-Bildern kompensiert werden kann. Zum Abschluss konnte durch die Untersuchung einer tierischen Gewebeprobe gezeigt werden, dass der Weitfeld-SERDS-Bildgebungs Aufbau mit integrierter „*interlaced nod and shuffle*“ Technik ein vielversprechender Ansatz für die Messung von medizinischen Proben darstellt.

## 2. Eigene Forschungsergebnisse

Im Folgenden werden die Ergebnisse zur Untersuchung und Bildgebung mittels SERDS vorgestellt. Zuerst werden verschiedene Anregungswellenlängenverschiebungen und Normalisierungsmethoden für die SERDS-Bildgebung betrachtet und mit der Basislinienkorrekturmethode EMSC verglichen [FK1]. Anschließend wird eine neue Methode der direkten Klassifizierung von SERDS-Daten ohne vorherige Rekonstruktion am Beispiel der Klassifizierung verschiedener Pflanzenpollen vorgestellt [FK2]. Der letzte Teil beschäftigt sich mit der Weitfeld-Bildgebung mittels SERDS und der Einführung der „*interlaced nod and shuffle*“ Technik für selbige [FK3]. Hierbei werden auch die Vorzüge von SERDS für die Raman-Bildgebung dargestellt und die Vorzüge der „*interlaced nod and shuffle*“ Technik für die Weitfeld-SERDS-Bildgebung demonstriert.

### 2.1. Evaluierung von SERDS und Vergleich mit der mathematischen Basislinienkorrekturmethode EMSC

([FK1] Cordero\*, Korinth\* et al. (2017) *Sensors* **17**: 1724, 1 – 17)

\* geteilte Erstautorenschaft

Autofluoreszenz ist ein häufig auftretendes Phänomen in der Raman-Spektroskopie [13–15,148]. Wie unter Kapitel 1.1 aufgeführt, kann Autofluoreszenz zur Maskierung von Raman-Banden führen, da diese aufgrund des hohen Untergrundes im Schrotrauschen untergehen können. Aus diesem Grund werden häufig Serien von Einzelspektren gemessen, um die Probe auszubleichen und so ein besseres Signal-Rausch-Verhältnis zu erhalten. Insbesondere bei Raman-bildgebenden Verfahren kann eine hohe Inhomogenität der Probe zu starken Schwankungen im spektralen Untergrund führen. Da alle Spektren eines Raman-Bildes mit dem gleichen Parametersatz korrigiert werden, kann eine große Probenheterogenität eine Herausforderung für eine mathematische Basislinienkorrektur bei der Untersuchung von Gewebe mittels Raman-Bildgebung, zum Beispiel für pathologische Fragestellungen, darstellen. Diese Problematik kann durch die Verwendung technisch aufwendigerer, instrumenteller Basislinienkorrekturmethode wie beispielsweise SERDS gelöst werden. In diesem Teil der Arbeit werden verschiedene Parameter für die SERDS-Methode untersucht, optimiert und mit den von E. Cordero theoretisch

ermittelten Werten verglichen. Durch den Vergleich zwischen SERDS und EMSC erfolgt eine Evaluierung der SERDS-Methode.

Da für die SERDS-Technik die richtige Wahl der Wellenlängenverschiebungen von Bedeutung ist, wurde im ersten Schritt untersucht, welches die optimale Wellenlängenverschiebung für SERDS-Untersuchungen an biologischen Proben darstellt. Damit die Bandenposition einer Bande eines SERDS-Spektrums dem Wendepunkt der Differenzbande entspricht, wie für die erste Ableitung zu erwarten wäre, muss die Verschiebung der Anregungswellenlänge, also die optimale Wellenlängenverschiebung, der Halbwertsbreite der Raman-Banden entsprechen (siehe Stand der Technik). Die Halbwertsbreite der Raman-Banden in einem Raman-Spektrum einer biologischen Probe kann jedoch stark variieren, weshalb dieses Kriterium für die optimale Anregungswellenlängenverschiebung nicht zielführend zu sein scheint. Da der größte Nachteil der SERDS-Methode die Erhöhung des Rauschens im SERDS-Spektrum durch die Subtraktion zweier Raman-Spektren voneinander ist, ist eine größtmögliche Signalintensität nach der Differenzbildung und daraus resultierend das beste Signal-Rausch-Verhältnis ein passenderes Kriterium für die optimale Verschiebung der Wellenlänge. Weitere limitierende Faktoren für die Größe der Verschiebung der Anregungswellenlänge sind die im verwendeten System verbauten Filter und die Bedingung, dass für das gleiche Fluoreszenzprofil die gleichen Fluorophore angeregt werden müssen.

Die Bestimmung der optimalen Wellenlängenverschiebung für biologische Proben erfolgte mittels eines Punkt-für-Punkt Rasterscans, mit dem eine Schweinefleischprobe Raman-spektroskopisch vermessen wurde. Der Einsatz eines durchstimmbaren Lasers (DLC DL pro 780, Toptica Photonics, Deutschland, durchstimmbarer Wellenlängenbereich: 765 nm – 850 nm) mit Verstärker (BoosTA Pro, Toptica Photonics, Deutschland) ermöglichte die mit fünf Anregungswellenlänge (784,0 nm / 784,5 nm / 785,0 nm / 785,5 nm / 786,0 nm mit einer Aufnahmezeit von jeweils 1 s) an jedem Punkt des Rasterscans, wobei durch die verwendeten Filter der mögliche Anregungsbereich auf 784 nm bis 786 nm limitiert wurde. Aus den so erhaltenen fünf Raman-Bildern wurden vier SERDS-Bilder mit unterschiedlicher Wellenlängendifferenzen zwischen 0,5 nm und 2,0 nm errechnet. Nach Anwendung einer HCA wurden drei Cluster, ein Lipid-Cluster und zwei Protein-Cluster, erhalten. In Abbildung 4 [FK1] sind gemittelten Raman-Differenzspektren für den Lipid-Cluster der Fleischprobe bei unterschiedlichen Verschiebungen der Anregungswellenlänge dargestellt.

Dabei fällt auf, dass sich mit der Anregungswellenlängenverschiebung auch das Bandenprofil der Differenzspektren verändert, wenn man die geringste mit der höchsten nm-Differenz vergleicht. Hier spielt die möglichen Subtraktion benachbarter Banden bei größeren Verschiebungen und die intrinsisch unterschiedlichen Halbwertsbreiten der Raman-Banden bei biologischen Proben eine Rolle, weshalb es für jede Raman-Bande eine bestimmte Anregungswellenlängenverschiebung für den Erhalt einer idealen Differenzbande gibt. Da jedoch für die Erzeugung eines SERDS-Spektrums nur eine Verschiebung verwendet wird, kann dies zu Abweichungen zwischen dem SERDS-Bandenprofil und dem idealen Differenzbandenprofil der ersten Ableitung eines Raman-Spektrums führen. Außerdem ist zu bemerken, dass ein Restuntergrund erhalten bleibt und eine simple Subtraktion der Rohspektren offensichtlich nicht ausreicht, um eine effektive Untergrundkorrektur zu bewerkstelligen. Dies ist vor allem auf die unterschiedliche, wellenlängenabhängige Laserleistung und das Ausbleichen der Probe (engl. *photobleaching*) während der Messung zurückzuführen. Ferner besitzt die größte Verschiebung die höchste absolute Signalintensität im SERDS-Spektrum, während die kleinste Verschiebung über die geringste absolute Signalintensität verfügt. Da eine größere Signalintensität im SERDS-Spektrum mit dem Erhalt von mehr Information nach der Differenzbildung verbunden ist, stellt die größtmöglich einstellbare Anregungswellenlängenverschiebung von 2 nm (entspricht  $32,46 \text{ cm}^{-1}$ ) die für diesen Aufbau optimale Verschiebung für SERDS an biologischen Proben dar. Dies bestätigt die Simulationen zum maximalen Signalerhalt in SERDS-Spektren mit verschiedenen Anregungswellenlängen für Protein- und Lipid-Spektren, die von E. Cordero [FK1] durchgeführt wurden. Diese Simulationen ergaben, dass sich der Signalerhalt mit einer Vergrößerung der Verschiebung bis zum Erreichen eines Maximums erhöht, wobei der maximale Signalerhalt im SERDS-Spektrum bei einer Anregungswellenlängenverschiebung von 7 nm ( $110 \text{ cm}^{-1}$ ) für Lipide und von 10 nm ( $160 \text{ cm}^{-1}$ ) für Proteine zu erwarten ist.

Aufgrund dieser Erkenntnisse wurden im weiteren Verlauf dieser Dissertation nur die Differenzspektren betrachtet, die aus der größtmöglichen Verschiebung der Anregungswellenlänge für die jeweiligen Aufbauten resultierten. Für die übrigen Ergebnisse von Kapitel 2.1 und Kapitel 2.2 entspricht dies einer Verschiebung der Anregungswellenlänge um 2 nm. In Kapitel 2.3 kamen zwei unterschiedliche Lasersysteme zum Einsatz: ein NIR-Laser mit einer Verschiebung von 1,05 nm (784,43 nm / 785,48 nm) und ein blauer Zwillings-Dioden-Laser mit einer Differenz von 1,1 nm (457,74 nm / 458,90 nm).

Für den Vergleich zwischen SERDS und der mathematischen Basislinienkorrekturmethode EMSC wurde das SERDS-Differenzbild der bereits erwähnten Schweinefleischprobe für die Anregungswellenlängen  $\lambda_{ex1} - \lambda_{ex2} = 786,0 \text{ nm} - 784,0 \text{ nm}$  gebildet und mittels der HCA wurden analog zu oben ein Lipid-Cluster und die zwei Protein-Cluster (Protein A und Protein B) enthalten. Um diese rohen Differenzspektren mit EMSC-korrigierten Spektren ( $\lambda_{ex} = 785,0 \text{ nm}$ ) vergleichen zu können, wurde die erste Ableitung der EMSC-korrigierten Spektren gebildet. Für die numerische Ableitung wurde ein kleines spektrales Fenster gewählt, um eine Verzerrung zu vermeiden, was aber auch ein hohes Rauschen in den Ableitungen der Proteinspektren zur Folge hat. Eine Gegenüberstellung der Spektren ist in Abbildung 6 (entspricht Abbildung 5 [FK1]) dargestellt.

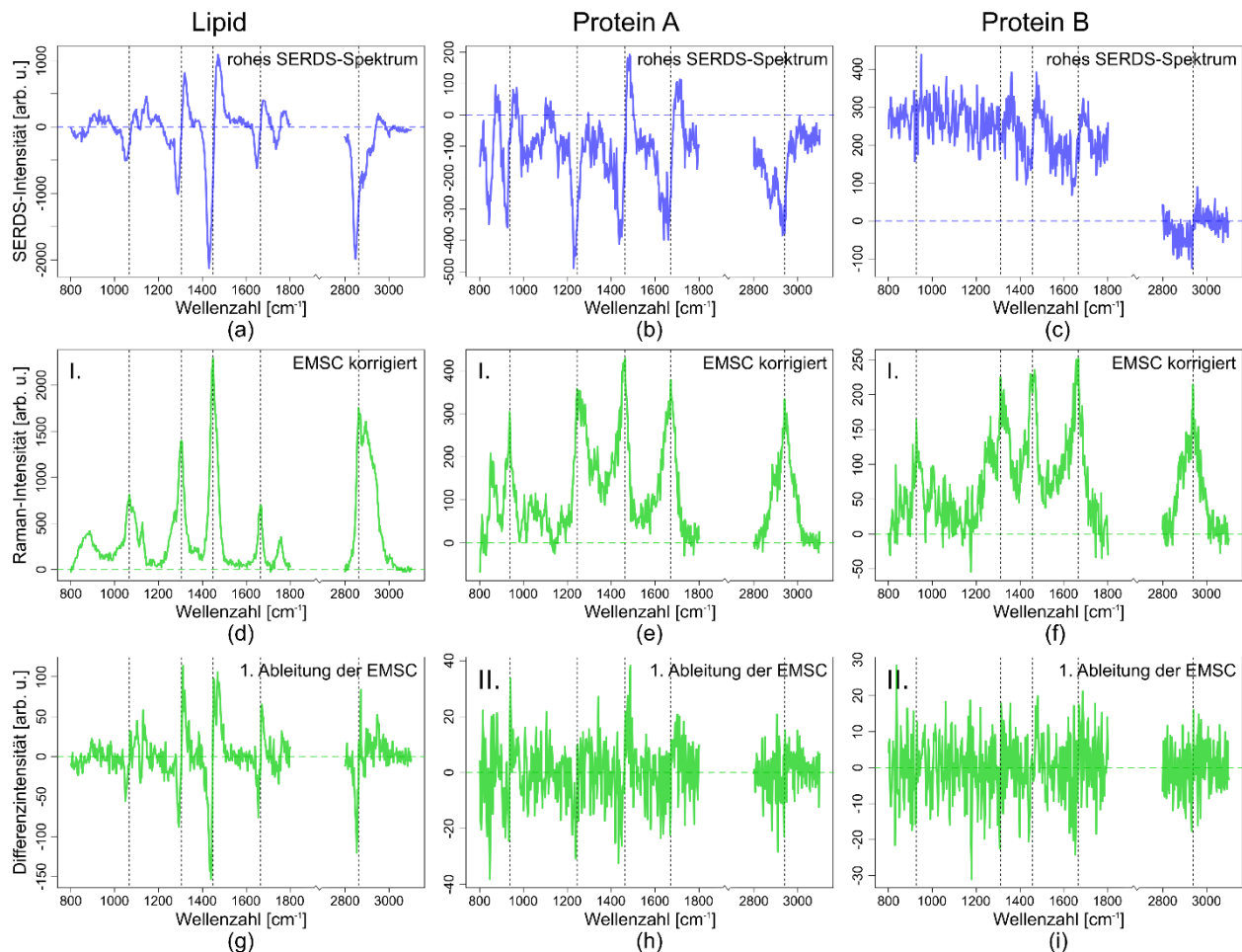


Abbildung 6: Vergleich zwischen gemessenen Lipid-Spektren (a,d,g) und den Spektren von Protein A (b,e,h) und Protein B (c,f,i); SERDS-Spektren (2 nm Anregungswellenlängenverschiebung, (a–c), blau); EMSC korrigierte Spektren (785 nm Anregungswellenlängenverschiebung, (d–f), grün); erste Ableitung der EMSC korrigierten Spektren (785 nm Anregungswellenlängenverschiebung, (g–i), grün).

*wellenlängenverschiebung, (g-i), grün); durch die vertikalen, schwarzen Linien markieren die Positionen der Raman-Banden. (entspricht Abbildung 5 [FK1])*

Dabei fällt auf, dass die Lipid-Spektren über die höchste spektrale Intensität verfügen, weshalb sie ein hohes Signal-Rausch-Verhältnis besitzen und die Untergrundkorrektur gut funktioniert. Dies liegt an dem größeren Raman-Streuquerschnitt der Lipide, aufgrund ihrer langen Alkylketten, im Vergleich zu den Proteinen. Die Proteinspektren sind deutlich schwächer, haben ein niedrigeres Signal-Rausch-Verhältnis und weisen nach der Untergrundkorrektur mittels SERDS noch immer einen Restuntergrund auf. Dies ist auf das Ausbleichen der Proben während der Messung zurückzuführen, was sich aufgrund der niedrigeren Intensität im Vergleich zum Untergrund und des höheren Fluoreszenzuntergrundes bei den Proteinen sehr viel stärker bemerkbar macht als bei Lipiden. Die Korrektur der Spektren mit Hilfe der EMSC führt zu einer guten Basislinienkorrektur und, bei genauerer Betrachtung der Skalierung der Spektren, zu einem besseren Signal-Rausch-Verhältnis als in den SERDS-Spektren. Vergleicht man die Bandenposition der mit Hilfe der EMSC-korrigierten Spektren mit den Wendepunkten der ersten Ableitung und der SERDS-Spektren, kann für die Lipidspektren eine sehr gute Übereinstimmung festgestellt werden. Für die Proteinspektren ist dies ebenfalls gegeben, aber das sehr niedrige Signal-Rausch-Verhältnis, besonders in der ersten Ableitung der Proteincluster, macht eine Unterscheidung von Banden und Rauschen sehr schwer. Da die Halbwertsbreite der Raman-Banden oft nicht der Verschiebung der Anregungswellenlänge entspricht, weichen die SERDS-Spektren in der Form der Differenzbanden von den Spektren der ersten Ableitung der EMSC korrigierten Spektren ab, wie beispielsweise im hohen Wellenzahlbereich des Lipidclusters. Die sehr breite Enveloppe der  $CH_n$  Banden im Bereich von  $2800\text{ cm}^{-1}$  bis  $3100\text{ cm}^{-1}$  führt zu einem verzerrten Bandenprofil der Differenzbanden, da die Halbwertsbreite der Enveloppe sehr viel größer als die Anregungsverschiebung von  $2\text{ nm}$  ( $\cong 32,46\text{ cm}^{-1}$ ) ist, wodurch es zu einer starken Bandenauslöschung kommt.

Wie oben demonstriert, reicht eine einfache Subtraktion der Rohspektren nicht aus, um den Untergrund vollständig zu entfernen. Ein Normierungsschritt vor der Differenzbildung der Spektren kann dabei helfen, Unterschiede in der Laserintensität oder Intensitätsunterschiede im Fluoreszenzuntergrund zwischen den Spektren-Paaren zur SERDS-Berechnung auszugleichen und eine bessere Überlappung des Untergrundes der voneinander zu subtrahierenden Spektren zu erreichen. Um den Einfluss dieses Normierungsschrittes auf die Differenzspektren zu untersuchen und die bestmögliche Normierungsmethode zu finden, wurden die

Flächennormierung, die z-score Normierung und eine Differenzoptimierungsmethode auf die Spektren des Lipid- und Proteinclusters angewandt und in Abbildung 6 [FK1] verglichen.

Hierbei ist zu beobachten, dass durch einen Normierungsschritt vor der Differenzbildung die Standardabweichung innerhalb der Cluster der Differenzspektren erheblich sinkt. Durch die Flächennormierung kann der spektrale Untergrund in den SERDS-Spektren verringert, aber nicht vollständig beseitigt werden, wie am schiefen Verlauf und einer Abweichung der Spektren von der Nulllinie zu erkennen ist. Durch die z-score Normierung besitzen die Spektren eine sehr geringe Standardabweichung und die Mittelwertspektren liegen fast auf der Nulllinie, allerdings ist die Korrektur für den hohen Wellenzahlbereich schlechter. Die Differenzoptimierung, bei der die Fläche unter den absoluten Differenzspektren minimiert wird, führt ebenfalls zu einem geringen Untergrund in den Differenzspektren, wobei insbesondere in den Proteinspektren ein verbliebener Untergrund sichtbar ist. Im Vergleich mit den anderen Methoden sind die Intensitätsunterschiede der Raman-Banden in den Differenzspektren aber größer und der Untergrund im hohen Wellenzahlbereich der Differenzspektren ist am geringsten.

Insgesamt kann festgestellt werden, dass die Untergrundkorrektur mittels EMSC sehr gute Resultate erzielt. Allerdings müssen für eine erfolgreiche Anwendung der EMSC bereits Informationen über den zu erwartenden Untergrund in der Probe vorliegen. Insbesondere wenn unterschiedliche Fluoreszenzprofile in die Raman-Spektren innerhalb eines Raman-Bildes einfließen, kann eine Berücksichtigung dieser unterschiedlichen Untergrundprofile in der EMSC nötig werden. Die Untergrundkorrektur mittels SERDS bedarf eines weiteren Normierungsschrittes vor der Differenzbildung, um Intensitätsunterschiede zwischen den Spektren-Paaren aufgrund von Ausbleichen und Unterschieden in der Anregungslaserintensität abzuschwächen. Dafür wird für diese Untergrundkorrektur keine Information über die Probe selbst benötigt und unterschiedliche Fluoreszenzprofile in einem Raman-Bild stellen für diese Korrekturmethode keine zusätzliche Schwierigkeit dar. Wird eine genaue Bandenzuordnung benötigt, muss jedoch ein Rekonstruktionsschritt durchgeführt werden, da reine SERDS-Spektren schwierig zu interpretieren sind.



## 2.2. Klassifizierung von SERDS-Daten ohne vorherige Rekonstruktion

([FK2] Korinth *et al.* (2020) *Scientific Reports* **10**: 11215, 1–12)

Wie bereits zu Beginn erwähnt, werden SERDS-Daten sehr aufwendig prozessiert [36,41,42,86,149]. Wie in Kapitel 2.1 gezeigt, können Intensitätsunterschiede zwischen den mit verschiedenen Anregungswellenlängen gemessenen Spektren des gleichen Messpunktes auftreten. Dies kann an Unterschieden in der Intensität des Anregungslaserlichtes, an unterschiedlicher Fluoreszenzintensität des Fluorophors bei den verschiedenen Anregungswellenlängen oder am Ausbleichen der Probe, was zu einer Verringerung des Fluoreszenzuntergrundes führt, liegen. Wie ebenfalls in Kapitel 2.1 demonstriert, können durch eine Normierung oder Optimierung der Spektren vor der Differenzbildung diese Intensitätsunterschiede ausgeglichen und dadurch der Restuntergrund in den SERDS-Spektren verringert werden. SERDS-Spektren können in erster Näherung als die erste Ableitung des ursprünglichen Raman-Spektrums betrachtet werden, was ihre Interpretation ungewohnt und schwierig macht. Aus diesem Grund wird vor der eigentlichen spektralen Analyse oder Klassifizierung von SERDS-Daten zuerst ein Raman-Spektrum aus dem Differenzspektrum rekonstruiert. Hierfür wurden bereits viele verschiedene Algorithmen vorgeschlagen [32–37,149]. Allen Rekonstruktionsalgorithmen ist gemein, dass sie zu Artefakten im rekonstruierten Raman-Spektrum führen können, insbesondere wenn durch die Anregungswellenlängenverschiebung eine Bande in eine benachbarte Bande geschoben wird.

Für komplexe Klassifizierungsmodelle ist es jedoch nicht notwendig, eine genaue Bandeninterpretation durchzuführen. Die notwendigen Informationen, die das Modell benötigt, um subtile Unterschiede in Klassen zu finden, sind bereits in den Differenzspektren enthalten. Ohne vorherige Rekonstruktion ist die Verarbeitung von SERDS-Daten vereinfacht und das Risiko einer Verfälschung des Raman-Bandenprofils durch eine Rekonstruktion eliminiert. Daher wurde ein Protokoll zur direkten Klassifikation von SERDS-Daten erarbeitet und das Resultat dieser direkten Klassifikation mit einer Klassifikation basislinienkorrigierter, rekonstruierter SERDS-Spektren und den basislinienkorrigierten, gemessenen Raman-Spektren verglichen.

Als Fallstudie wurden hierfür Pollen verschiedener Pflanzengenera verwendet. Pollen eignen sich besonders für diese Untersuchung, da sie häufig Autofluoreszenz zeigen [107–109] und, aufgrund der großen Vielfalt an Pflanzengenera, eine komplexe Klassifizierung in mehrere Klassen ermöglichen. Da außerdem der Goldstandard zur Pollenbestimmung noch immer das

Bestimmen und Auszählen von Pollen unter dem Mikroskop durch einen Experten darstellt, wäre das verwendete, automatisierte Hochdurchsatz-Raman-Spektrometer (engl. *high throughput Raman spectrometer* – HTRS) [124,150] in Kombination mit der SERDS-Technik ein großer Schritt hin zu einer vollautomatisierten Klassifikation von Pollen. Diese würde nicht auf deren Morphologie, sondern auf der biochemischen Zusammensetzung der Pollen basieren.

Für den Versuch wurden Raman-Spektren von 6028 einzelnen Pollen acht verschiedener Pflanzengenera (siehe Tabelle S3 in den *Supplementary Information* [FK2]) mittels eines für die SERDS-Technik angepassten HTRS-Aufbaus gemessen. Hierbei wurden die einzelnen Pollen in 10 mL *aqua dest.* suspendiert und auf ein vollständig mit *aqua dest.* bedecktes CaF<sub>2</sub>-Deckglas pipettiert. Nach der Sedimentation der Pollen wurden diese automatisch detektiert, fokussiert und bei drei verschiedenen Anregungswellenlängen ( $\lambda_{ex1} = 784,0 \text{ nm}$ ;  $\lambda_{ex2} = 785,0 \text{ nm}$ ;  $\lambda_{ex3} = 786,0 \text{ nm}$ ) für jeweils 0,5 s gemessen. Die gemessenen Pollen konnten grob in Pollen von Bäumen und von nicht-Bäumen unterteilt werden. Die Separation der Baumpollen und der Nicht-Baumpollen in ihre vier Pflanzengenera gewährte zwei weitere, Unterteilungen, um zu prüfen, ob eine Klassifizierung der Pollen mittels SERDS-Spektren basierend auf ihrem Genus möglich ist.

Abbildung 2 [FK2] zeigt eine Übersicht über die differenzoptimierten SERDS-Spektren, die basislinienkorrigierten, rekonstruierten SERDS-Spektren und die gemessenen Raman-Spektren nach Basislinienkorrektur, wobei jeweils die Mittelwertspektren (dunkel) und die Standardabweichung (schattiert) aller gemessener Pollen von Bäumen (obere Reihe) und Nicht-Bäumen (untere Reihe) dargestellt sind. Gemäß den Ergebnissen aus Kapitel 2.1 wurde die mit diesem Aufbau größtmögliche Anregungswellenlängenverschiebung von  $\Delta\lambda_{ex} = 2 \text{ nm}$  ( $\lambda_{ex1} - \lambda_{ex3} = 784,0 \text{ nm} - 786,0 \text{ nm}$ ) verwendet, um SERDS-Spektren zu errechnen. Vergleicht man die Rekonstruktion der Raman-Spektren aus den Differenzspektren mit den basislinienkorrigierten Raman-Spektren, so ist eine Verringerung der spektralen Auflösung, aber auch eine Verbesserung des Signal-Rausch-Verhältnisses durch den Integrationsschritt zu erkennen. Innerhalb der Baumpollen zeigen die Spektren der Lärchenpollen große spektrale Unterschiede zu den übrigen drei Baumgenera auf, die alle drei aus der Pflanzenfamilie der Birkengewächse (lat. *Betulaceae*) stammen. Besonders im Bereich zwischen  $1600 \text{ cm}^{-1}$  und  $1750 \text{ cm}^{-1}$  und im hohen Wellenzahlbereich sind die Unterschiede auffällig und auf den höheren Lipidgehalt aufgrund der in den Lärchenpollen enthaltenen ätherischen Öle zurückzuführen. Vergleicht man die Spektren der Nicht-Baumpollen, sind die größten Unterschiede zwischen den Pollen der verschiedenen Pflanzengenera im spektralen Bereich von

1600  $\text{cm}^{-1}$  bis 1750  $\text{cm}^{-1}$  und im niedrigen Wellenzahlbereich unterhalb von 1250  $\text{cm}^{-1}$  zu beobachten. Diese Unterschiede sind ausgeprägter als zwischen den Spektren der Baumpollen, was an der Heterogenität der Gruppe der Nicht-Baumpollen liegt. Alle Nicht-Baumpollen gehören unterschiedlichen Pflanzenfamilien an. Die Bande bei 1600  $\text{cm}^{-1}$  fehlt in den Pollenspektren des Pfeifengrases. Aber auch die Pollenspektren anderer Pflanzengenera, wie Birke, Lärche, Hasel, Erle und Ampfer weisen in dieser Bande eine besonders hohe Varianz in ihrer Intensität auf.

Für die erste Klassifizierung wurde nach der Datenvorbehandlung der gesamte Datensatz in einen Trainings- und einen Testdatensatz geteilt, wobei die Einteilung der Daten zufällig geschah. Es wurde aber darauf geachtet, dass für jedes Pflanzengenus die gleiche Anzahl an Spektren im Trainingsdatensatz vorhanden ist, um ein Bias im Klassifizierungsmodell zu verhindern. Für die beiden Klassifizierungen in die Pflanzengenera, wurden nur der entsprechende Teil des Trainings- und Testdatensatzes verwendet, der den Baumpollen oder Nicht-Baumpollen zugeordnet war. Als Klassifizierungsmethode wurde die Hauptkomponentenanalyse mit anschließender linearer Diskriminanzanalyse (PCA-LDA) gewählt. Die PCA reduziert hierbei die Dimensionalität des Datensatzes, wodurch auch das Rauschen in den SERDS-Spektren verringert wird. Die LDA ist als Klassifizierungsmethode gut geeignet für kleine Datensätze und birgt dadurch eine geringere Gefahr der Überanpassung des Modells. Mit Hilfe der Trainingsdaten sollte durch eine interne 10-fach Kreuzvalidierung die optimale Anzahl an Hauptkomponenten für jeden Klassifikationsschritt bestimmt werden. Die 10-fach Kreuzvalidierung wurde jeweils 10-mal durchgeführt und der Mittelwert der Sensitivität, Selektivität, Relevanz und Vertrauenswahrscheinlichkeit zusammen mit deren Standardabweichung über die Anzahl der verwendeten Hauptkomponenten aufgetragen. Dadurch ließ sich schließlich die optimale Anzahl der Hauptkomponenten für jede Klassifizierung bestimmen. Mit der jeweils ermittelten Anzahl an Hauptkomponenten und den vollständigen Trainingsdatensätzen wurden dann die Klassifizierungsmodelle für die jeweiligen Klassifikationen berechnet und die jeweiligen Testdaten mittels dieser Modelle klassifiziert. Eine externe Kreuzvalidierung wurde aufgrund der zu geringen Anzahl an Spektren pro Pflanzengenus nicht durchgeführt.

Für die Klassifikation in Pollen von Bäumen und Nicht-Bäumen wurden 10 Hauptkomponenten, für die Pflanzengenera-Klassifizierung der Baumpollen wurden 13 Hauptkomponenten und der Nicht-Baumpollen 11 Hauptkomponenten verwendet. Die Score-Plots der drei Klassifikationen

sind in Abbildung 7 dargestellt und zeigen graphisch das Ergebnis der drei Klassifikationen. Für ein ausführlicheres Ergebnis der Klassifikationen siehe [FK2].

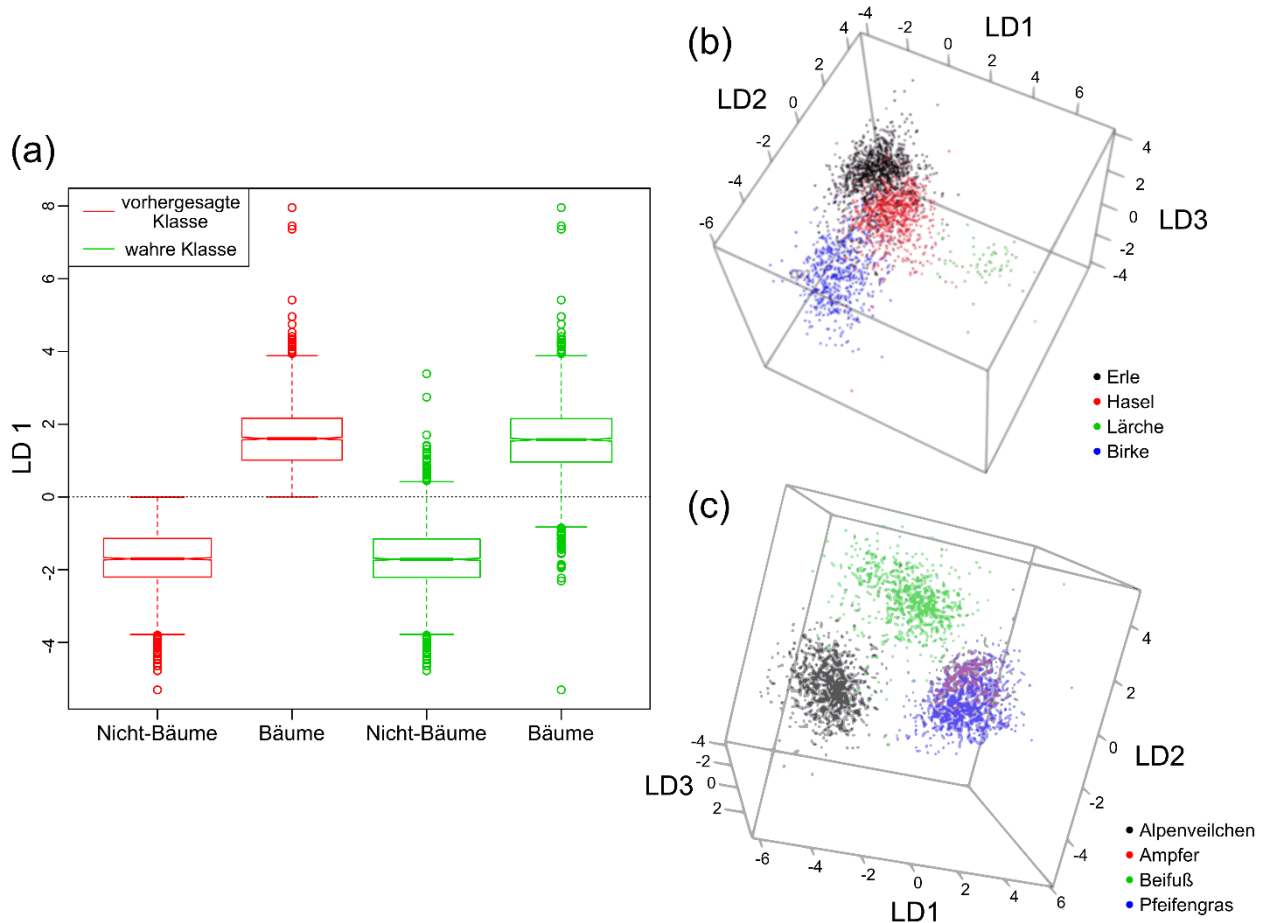


Abbildung 7: Score-Plots der drei PCA-LDA Klassifikationen, basierend auf den differenz-optimierten SERDS-Spektren der Testdatensätze; **(a)** Score-Box-Whiskers-Plot für die Klassifikation in Pollen von Bäumen und Nicht-Bäumen; rot: vorhergesagte Klassenzuordnung; grün: wahre Klassenzuordnung; **(b)** 3D-Streudiagramm der Klassifikation in die verschiedenen Baumgenera; **(c)** 3D-Streudiagramm der Klassifikation in die verschiedenen Nicht-Baumgenera.

Wie aus Abbildung 7 (a) ersichtlich, kann die Mehrheit der Testdaten durch das verwendete Klassifikationsmodell erfolgreich in Bäume und Nicht-Bäume auf Basis der einzelnen optimierten SERDS-Spektren unterschieden werden. Die Wahrscheinlichkeit einer Fehlklassifikation liegt nur bei 4,3 %. Betrachtet man Sensitivität, Spezifität, Relevanz und Vertrauenswahrscheinlichkeit kann man zusammenfassend sagen, dass für diese Klassifikation alle Werte über 94 % waren. Die Mittelwerte der Klassifikatoren lagen bei 95,8 % für Sensitivität und Selektivität und 95,9 % für Relevanz und Vertrauenswahrscheinlichkeit.

Die Klassifikation von Baumpollen in seine vier Pflanzengenera sind im 3D-Streudiagramm in Abbildung 7 (b) dargestellt. Die SERDS-Daten der Baumpollen lassen sich gut durch das Modell

den entsprechenden Genera zuweisen. Hierbei trennt LD1 die SERDS-Spektren von Lärchenpollen von den übrigen Pollenspektren, LD2 die SERDS-Spektren von Birkenpollen von den restlichen Pollenspektren und LD3 grob die SERDS-Spektren von Hasel- und Erlenpollen. Die häufigsten Missklassifikationen traten bei Hasel- und Erlenpollen auf. Die Pollen der Lärchen, die zu der Pflanzenfamilie Pinaceae gehören, grenzen sich deutlich von den anderen drei Baumpollen im Streudiagramm ab, was auf den bereits erwähnten, höheren Lipidanteil zurückzuführen ist. Die Mittelwerte für Sensitivität (91,3 %), Selektivität (95,9 %), Relevanz (90,0 %) und Vertrauenswahrscheinlichkeit (94,6 %) dieser Klassifikation sind sehr hoch.

In Abbildung 7 (c) ist das 3D-Streudiagramm der Klassifikation von SERDS-Spektren der Nicht-Baumpollen in seine Pflanzengenera dargestellt. Mit Hilfe der LD1 können Alpenveilchenpollen von Pfeifengras und Ampferpollen getrennt werden. Die LD2 ermöglicht eine Trennung zwischen Beifußpollen und allen anderen Nicht-Baumpollen. Mittels LD3 können Ampferpollen von anderen Nicht-Baumpollen unterschieden werden. Hierbei ist insbesondere die Unterscheidung zwischen Pfeifengraspollen und Ampferpollen mittels LD3 nicht sonderlich gut, da beide Punktwolken auch in dieser Ebene eine große Schnittmenge aufweisen. Dies lässt sich auch bei der Betrachtung der Missklassifikationen erkennen und ist darauf zurückzuführen, dass sich diese spektral sehr ähnlich sind. Die Mittelwerte der Klassifikatoren, die für Sensitivität bei 86,1 %, für Selektivität bei 96,3 %, für Relevanz bei 85,1 % und für die Vertrauenswahrscheinlichkeit bei 94,2 % liegen, sind etwas geringer als bei der Klassifikation der Baumpollen. Trotzdem kann von einer erfolgreichen Klassifizierung gesprochen werden.

Insgesamt waren alle Klassifikationen basierend auf optimierten Differenzspektren erfolgreich. Vergleicht man die Ergebnisse dieser Klassifikationen mit den Ergebnissen von Klassifikationen auf der Basis von rekonstruierten Raman-Spektren (siehe *Supplementary Information* [FK2]), wird deutlich, dass eine direkte Klassifikation mittels SERDS-Spektren von Vorteil ist. Lediglich die Klassifikation von Nicht-Baumpollen in ihre jeweiligen Pflanzengenera funktioniert mit Hilfe rekonstruierter Raman-Spektren ein wenig besser. Insgesamt sind die Abweichungen zwischen den Klassifikationen basierend auf SERDS-Spektren und auf rekonstruierten Raman-Spektren mit maximal +/- 2,1 % sehr gering. Ebenfalls vergleichbare Ergebnisse liefern die auf den SERDS-Spektren basierenden und die auf den gemessenen, basislinienkorrigierten Raman-Spektren basierenden Klassifikationen. Für die Klassifizierung in die verschiedenen Pflanzengenera ist jeweils die Klassifikation basierend auf den gemessenen, basislinienkorrigierten Spektren stärker, wobei die Baumpollen über die SERDS-Spektren besser

klassifiziert wurden. Auch die Unterschiede zwischen den Klassifikationen basierend auf SERDS-Spektren und auf den gemessenen und basislinienkorrigierten Raman-Spektren sind mit maximal +/- 2,75 % gering.

Zusammenfassend kann festgestellt werden, dass die direkte Klassifikation der SERDS-Daten gute bis sehr gute Ergebnisse erzielt. Durch die PCA, die vor der Klassifikation angewandt wird, wird ein großer Nachteil von SERDS, das verringerte Signal-zu-Rausch-Verhältnis aufgrund der Differenzbildung, kompensiert. Wie gezeigt werden konnte, stellt eine Rekonstruktion keinen Mehrwert für eine Klassifikation dar, sondern ist im Gegenteil der direkten Klassifikation der SERDS-Daten unterlegen. Das Risiko der Einführung von Artefakten in den Datensatz und der erhöhte Rechenaufwand durch einen Rekonstruktionsschritt kann somit umgangen werden. Ferner kann durch die direkte Klassifikation der SERDS-Daten die Vorverarbeitung vereinfacht und so optimiert werden.

### 2.3. Weitfeld-SERDS-Bildgebung mit Hilfe der „nod and shuffle“ Technologie

([FK3] Korinth *et al.* (2020) *Sensors* **20**: 6723, 1 – 19)

Bei Raman-Untersuchungen von biologischen Proben kann die gleichzeitig angeregte Autofluoreszenz eine große Herausforderung darstellen [12–15,148]. Insbesondere in der Raman-Bildgebung, bei der größere Unterschiede im Fluoreszenzuntergrund innerhalb eines hyperspektralen Raman-Bildes auftreten können, kann für die Korrektur des Untergrundes mittels mathematischer Methoden eine Herausforderung sein. SERDS stellt hier, wie bereits in Kapitel 2.1 und 2.2 gezeigt, eine Methode dar, um ohne große Kenntnis des Untergrundes selbigen zu korrigieren. Bisher wurde die SERDS-Technik bei biologischen Proben vor allem für die Korrektur von Einzelspektren oder Mittelwertspektren mehrerer Messungen an einem Punkt verwendet [39–42,81,83–87].

SERDS-Bildgebung mittels eines Rasterscans, bei dem jeder Messpunkt einzeln angefahren und zwei aufeinanderfolgende Spektren mit unterschiedlicher Anregungswellenlänge gemessen wird, findet nur sehr selten Anwendung [FK1], da es viel zeitaufwendiger als gewöhnliche Raman-Bildgebung ist. Durch die langen Messzeiten steigt die Gefahr der Probenaustrocknung und -beschädigung, nicht zuletzt aufgrund der verdoppelten Belichtungszeit. Vor Austrocknung kann die Benutzung einer Feuchteammer oder die Verringerung der Aufnahmezeit schützen [151]. Um die Aufnahmezeit eines hyperspektralen Bildes zu reduzieren, kann die Integralfeld-Spektroskopie (IFS) [48,49] verwendet werden. Sie wird in der Astrophysik dazu verwendet, um vollständige spektrale Weitfeld-Bilder von kosmischen Objekten mit nur einer Belichtung und ohne einen Punkt-für-Punkt Rasterscan zu erhalten. Hierbei wird das spektrale Bild mit Hilfe der Integralfeldeinheit (IFU) optisch zerlegt und vor dem großen Eintrittsspalt des IFS-Spektrographen aneinandergereiht. Dies kann beispielsweise mittels eines Faserbündels realisiert werden, welches probenseitig in einem zweidimensionalen Bildfeld angeordnet und auf der Seite des IFS-Spektrographen in einer Linie aufgereiht ist. Das vom Spektrographen spektral aufgespaltete, eingehende Signal wird von einem großflächigen Detektor registriert und nach der Prozessierung als hyperspektraler Datenkubus ausgegeben, der sowohl die vollständige räumliche als auch spektrale Information enthält. Die Integralfeld-Spektroskopie wurde bereits für die Weitfeld-Raman- und Weitfeld-SERDS-Bildgebung verwendet [38,50,51]. Hierfür wurde ein Spektrograph, der vom Aufbau ähnlich einer Spektrographeneinheit des MUSE (engl. *multi unit spectroscopic explorer*) [152] war, mit einem 4096 x 4096 Pixel großen, Stickstoff gekühlten

CCD-Chip als Detektionssystem verwendet und mit einem speziellen Probenkopf verbunden [153,154]. Dieser ermöglichte die Aufnahme eines Raman-Bildes mit 20 x 20 Spektren, also 400 Bildpunkten, so genannte spektrale Pixel oder „Spaxel“, mit nur einer Aufnahme. Durch Änderung der Anregungswellenlänge entstanden so nacheinander zwei Raman-Bilder, die zusammen ein SERDS-Bild ergaben. Mit diesem Aufbau wurden SERDS-Bilder von unterschiedlichen Proben wie einem Schweineohrquerschnitt, menschliche Haut und das Auflösen eines braunen Zuckerwürfels von Schmäzlin *et al.* [38] aufgenommen. Der Nachteil der IFS besteht darin, dass große CCD-Chips für ein großes Bildfeld nötig sind, welche eine lange Auslesezeit besitzen. Dadurch sind schnelle Messfolgen nicht möglich und kurze Aufnahmezeiten, bei denen das Auslesen des CCD-Chips deutlich länger dauert als die Aufnahmezeit, widersinnig. Durch die Implementierung einer weiteren, in der Astrophysik etablierte Technik, das „*nod and shuffle*“ [88], können Veränderungen des spektralen Untergrundes während der IFS-Bildgebung kompensiert werden. Diese Technik wurde am Leibniz-Institut für Astrophysik im Rahmen des HYPERAM-Projektes in den Weitfeld-SERDS-Bildgebungsaufbau in Form des „*interlaced nod and shuffle*“ [89,90] integriert, was die Verwendung und Akkumulation kurzer Aufnahmezeiten in der Weitfeld-SERDS-Bildgebung ermöglichte [FK3]. Hierbei entspricht der „*nod*“ dem Wechsel der Anregungswellenlänge, während der „*shuffle*“ weiterhin die Verschiebung der Landungen der Raman-Signale auf dem CCD-Chip bezeichnet.

Im Folgenden werden Ergebnisse vorgestellt, die mit der Weitfeld-SERDS-Bildgebung unter Verwendung der „*interlaced nod and shuffle*“ Technik am Aufbau in Potsdam gemessen wurden. Dadurch war es möglich, zwei Weitfeld-Raman-Bilder mit 20 x 20 Spaxeln und kurzer Aufnahmezeit bei unterschiedlichen Anregungswellenlängen viele Male zu akkumulieren, bevor der CCD-Chip einmal ausgelesen wurde. Die verwendeten Laserquellen ermöglichten Aufnahmezeiten von 200 ms (784,43 / 785,48 nm) und 50 ms (457,74 / 458,90 nm). Nach Subtraktion der beiden Raman-Bilder wurde ein SERDS-Bild erhalten. Für den genauen Aufbau des Probenkopfes und Messaufbaus siehe [FK3].

Durch SERDS-Bildgebung können nicht nur fluoreszenzuntergrundfreie Bilder generiert werden. Insbesondere Bandenprofile, die von Raumlicht oder der Systemfunktion des Spektrometers stammen, können mittels SERDS herausgefiltert werden, was bereits für Einzelspektren demonstriert wurde [82,155,156]. Anhand einer Paracetamol- und einer halbierten Aspirin-



Tablette konnte dies ebenfalls für die Weitfeld-SERDS-Bildgebung gezeigt werden (Abbildung 8 (a)). Hierfür wurden die beiden Tabletten auf einem Probenkopf mit einem  $1 \text{ cm}^2$  Bildfeld und 400 Bildpunkten arrangiert und zwei Raman-Bilder mit zwei verschiedenen Anregungswellenlängen im NIR-Bereich (784,43 nm / 785,48 nm) und der „*interlaced nod and shuffle*“ Technik aufgenommen. Die Gesamtaufnahmezeit betrug 40 s je Anregungswellenlänge, wobei jeweils 200 x 200 ms Messungen akkumuliert wurden. 1 s nach Beginn der Aufnahme wurde das Raumlicht für 3 s eingeschaltet. Um die Anordnung der Signalspuren, die durch die Weitfeld-SERDS-Bildgebung mittels „*interlaced nod and shuffle*“ auf dem CCD-Chip entstehen, zu veranschaulichen, wurde in Abbildung 4 (a) [FK3] ein Teil des CCD-Chips dargestellt. Darauf sind deutlich die einzelnen Raman-Spektren als Lichtspuren zu erkennen, deren Signale sich mit der Wellenlänge des Anregungslasers (helle Punkte ganz links) verschieben. Davon heben sich deutlich die intensiven Banden des Raumlichtes ab, die ihre Position nicht verändern. Die jeweils im blauen und orangenen Rechteck hervorgehobenen Datenspuren sind als Rohspektren in Abbildung 4 (b) [FK3] dargestellt. Die Raman-Spektren im orangenen Rechteck zeigen die Superposition von Raumlichtbanden und Paracetamol-Banden, die von der Paracetamol-Tablette stammen. In den Raman-Spektren im blauen Rechteck finden sich nur Raumlichtbanden. Es muss sich folglich um einen Teil auf dem Probenkopf handeln, der nicht von einer Probe bedeckt wird. Die Raumlichtbanden, deren Positionen durch die vertikalen Linien angezeigt werden und deren Position oberhalb der Abbildung in nm angegeben ist, entsprechen den Banden einer Krypton-Leuchtstoffröhre.

Durch Subtraktion der beiden Raman-Bilder voneinander, wird ein SERDS-Bild erhalten, welches mittels einer Clusteranalyse in drei Cluster unterteilt wurde. In Abbildung 8 (b) ist das Clusterbild dargestellt, das die Einteilung des SERDS-Bildes in die drei Cluster zeigt und welches eine gute Übereinstimmung mit dem Hellfeldbild der Probenanordnung aufweist (Abbildung 8 (a)).

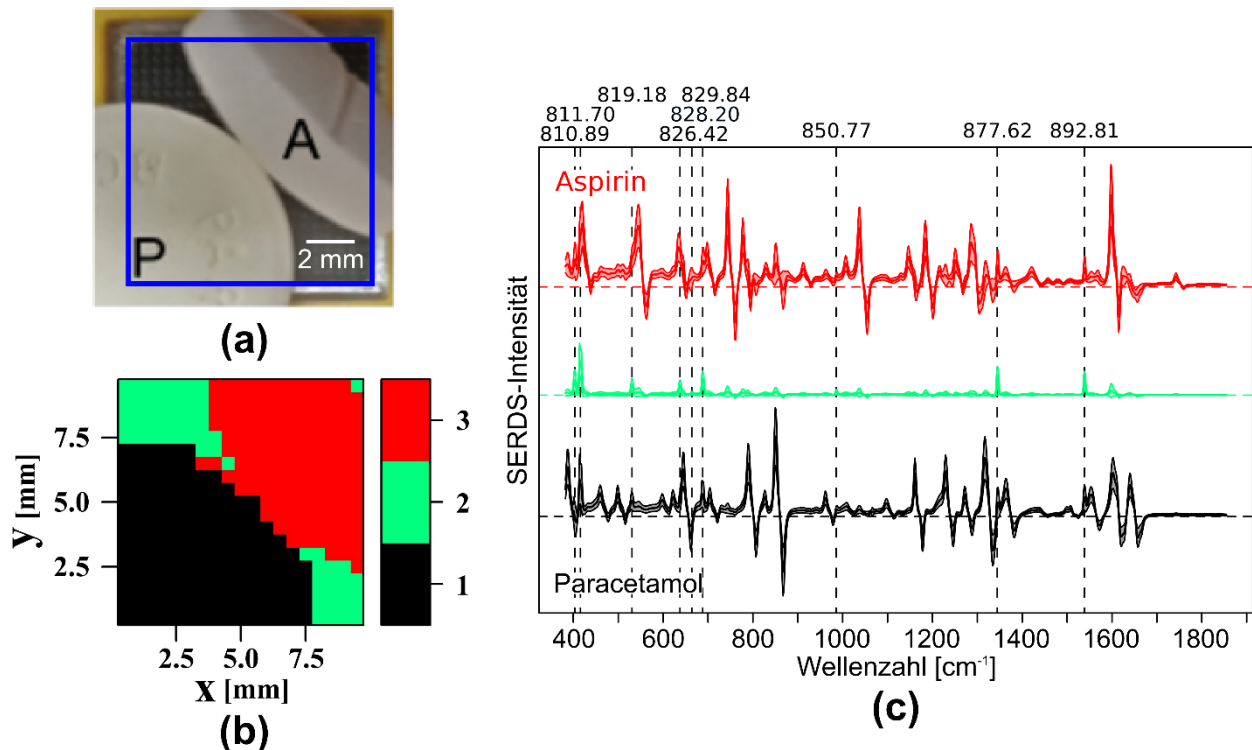


Abbildung 8: Filtern von Raumlichtbanden mittels Weitfeld-SERDS-Bildgebung in Kombination mit der „interlaced nod and shuffle“ Technik einer Paracetamol (P) und Aspirin (A) Tablette (Aufnahmezeit: 200 x 200 ms); (a) Hellfeldbild der Proben auf dem Probenkopf (blau: Bildfeld des Probenkopfes); (b) Clusterbild des SERDS-Bildes; (c) SERDS-Mittelwertspektren mit entsprechender Standardabweichung, Cluster 1 = Paracetamol (schwarz), Cluster 2 = ohne Probe / Rest von Raumlichtbanden (grün), Cluster 3 = Aspirin (rot); die gestichelten, schwarzen, senkrechten Linien zeigen die Position der Raumlichtbanden (Krypton, Bandenpositionen in [nm] darüber).

Diese Zuordnung der Cluster nach dem Hellfeldbild wird durch die Betrachtung der SERDS-Spektren bestätigt (Abbildung 8 (c)), wobei Cluster 1 Paracetamol, Cluster 2 der freien Fläche auf dem Probenkopf und Cluster 3 der Aspirin-Tablette entspricht. Die dominanten Raumlichtbanden, die in den Rohdaten deutlich zu sehen waren, konnten durch die Differenzbildung der beiden Raman-Bilder fast vollständig ausgelöscht werden, so dass die Cluster der beiden Proben fast vollständig frei von Raumlichtbanden sind.

Da der verwendete NIR Laser aufgrund der Ansteuerung keine kürzeren Messintervalle als 200 ms zuließ, wurde ein eigens für den Messaufbau und im Zuge des HYPERAM-Projektes vom Ferdinand-Braun-Institut hergestellter, blauer Zwillingsdiodenlaser ( $\lambda_{ex1} = 457,74 \text{ nm}$  /  $\lambda_{ex2} = 458,90 \text{ nm}$ ) [157] für die weiteren Messungen mit der „interlaced nod and shuffle“ Technik und einer sehr kurzen Aufnahmezeit von 50 ms pro Anregungswellenlänge verwendet.

Durch Akkumulation kurzer Aufnahmezeiten für zwei mittels der Weitfeld-SERDS-Bildgebung in Kombination mit der „*interlaced nod and shuffle*“ Technik gemessene Raman-Bilder, konnte der Effekt des Photobleichens kompensiert werden. Für diese und die weiteren Messungen wurde der Probenkopf leicht modifiziert und ein kleineres Bildfeld von  $0,02 \text{ cm}^2$  verwendet. Als Probe diente der Lipidbereich eines Schweinekoteletts, welcher über einen spektralen, vermutlich auf Autofluoreszenz basierenden, Untergrund verfügt: Dies liegt in der Anregung mit blauem Laserlicht begründet, welches in biologischen Proben häufig Autofluoreszenz anregt. Bei der ersten Messung wurde eine kurze Integrationszeit von 50 ms und 40 Wiederholungen verwendet. Bei einer zweiten Messung wurde die gleiche Stelle der Probe mit 2000 ms Aufnahmezeit ohne weitere Akkumulationen gemessen, um die typischen Messbedingungen einer Raman-Messung nachzustellen. Vergleicht man die Spektren der beiden SERDS-Bilder, die beide mit der gleichen Gesamtintegrationszeit gemessen wurden, stellt man fest, dass der spektrale Restuntergrund in den SERDS-Spektren der ersten Messung sehr viel geringer ist, als der spektrale Restuntergrund der SERDS-Spektren des zweiten SERDS-Bildes (siehe Abbildung 9 (a)). Dies ist darauf zurückzuführen, dass sich durch die kurze Belichtungszeit der einzelnen Messungen das Ausbleichen der Probe auf Aufnahmen der beiden Anregungswellenlängen gleichermaßen verteilt und durch Subtraktion abgezogen werden kann. Bei der langen Aufnahmezeit kann das Laserlicht der ersten Anregungswellenlänge die Probe über einen langen Zeitraum ausbleichen. Wird dann die zweite Anregungswellenlänge gemessen, ist der Fluoreszenzuntergrund bereits stark ausgebleicht und deutlich niedriger, was zu einem höheren Restuntergrund im Differenzspektrum führt. Es ist anzunehmen, dass die erste Messung einen stärkeren Fluoreszenzuntergrund als die zweite Messung besaß, da dieser bei der zweiten Messung bereits durch Ausbleichen während der ersten Messung reduziert wurde.

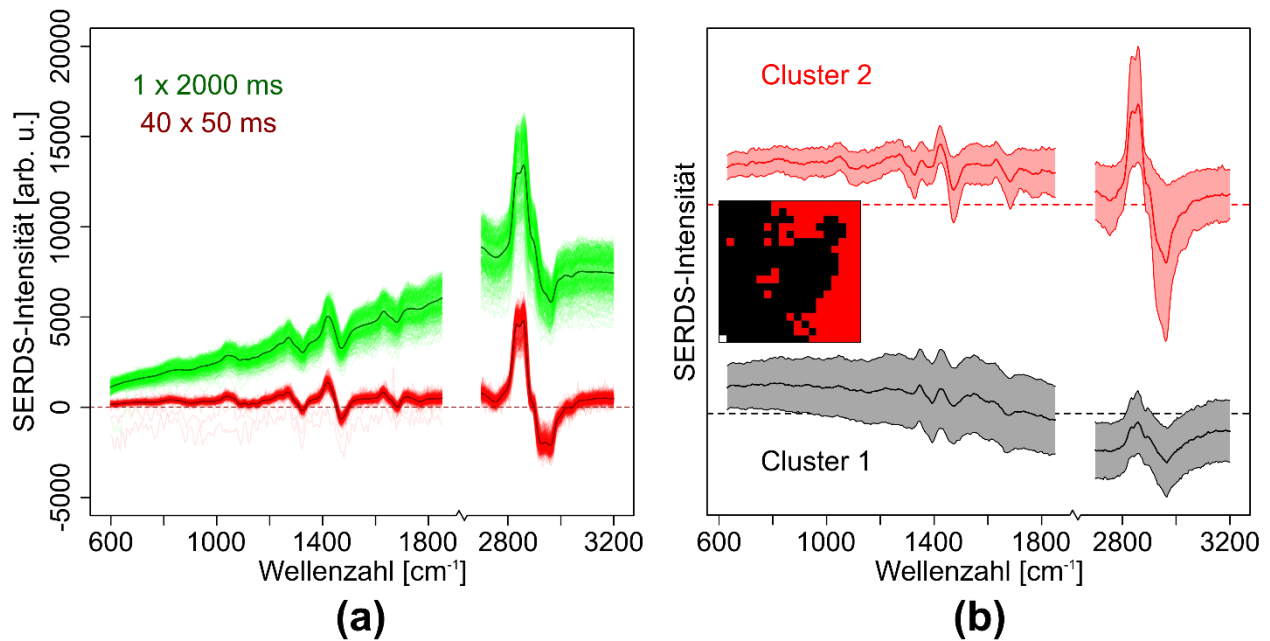


Abbildung 9: Beispiele für die Weitfeld-SERDS-Bildgebung in Kombination mit der „interlaced nod and shuffle“ Technik an biologischen Proben; **(a)** Demonstration der Kompensation von Photobleichen; Probe 1: Fettgewebe einer Schweinefleischprobe; dargestellte SERDS-Spektren (Mittelwertspektren in dunklerer Farbe) zweier SERDS-Bilder gemessen mit kurzer (rot, Aufnahmezeit: 40 x 50 ms) und langer Belichtungszeit (grün, Aufnahmezeit: 1 x 2000 ms), wobei die Gesamtaufnahmezeit für beide SERDS-Bilder 4 s beträgt; **(b)** Probe 2: inhomogenes Gewebeprobe vom Schwein (Aufnahmezeit: 40 x 50 ms); normierte SERDS-Mittelwertspektren mit entsprechender Standardabweichung gruppiert in zwei Cluster mittels hierarchischer Clusteranalyse; Cluster 1 = Protein (schwarz) und Cluster 2 = Lipid (rot); in der Mitte ist die Clusterkarte der beiden Clustern dargestellt.

Um die Auflösung des kleineren Bildfeldes zu prüfen, wurden Polystyrol (PS) ( $\varnothing = 50 \mu\text{m}$ ) und Polymethylmethacrylat (PMMA) Kügelchen ( $\varnothing = 120 \mu\text{m}$ ) auf dem Probenkopf aufgebracht und mit einer Aufnahmezeit von 100 ms und 40 Iterationen, also mit einer Integrationszeit von insgesamt 4 s pro Wellenlänge ( $\lambda_{ex1} = 457,74 \text{ nm}$ ;  $\lambda_{ex2} = 458,90 \text{ nm}$ ), gemessen. Die beiden erhaltenen Raman-Bilder wurden voneinander subtrahiert und die SERDS-Spektren des erhaltenen SERDS-Bildes mittels einer Aufsummierung aller Intensitäten zu rekonstruierten Raman-Spektren integriert. Die rekonstruierten Raman-Spektren wurden mit SNIP basislinienkorrigiert und für die Erstellung von Intensitätsbildern der einzelnen Polymere verwendet. Mit Hilfe des Intensitätsmittelwertes der für PS und PMMA charakteristischen Raman-Banden wurden zwei Intensitätsbilder erzeugt, eines für jede Polymerart. Die charakteristischen Raman-Banden waren für PS die aromatische Ringatmungsschwingung

(999  $\text{cm}^{-1}$ ), die Ringstrettschwingung (1590  $\text{cm}^{-1}$ ) und die CH Strettschwingung des Aromaten (3047  $\text{cm}^{-1}$ ). Bei der  $\text{CH}_3$  Deformationsschwingung (1444  $\text{cm}^{-1}$ ), der C=O Strettschwingung (1718  $\text{cm}^{-1}$ ) und der CH Strettschwingung der  $\text{CH}_2$  und  $\text{CH}_3$  Gruppen (2935  $\text{cm}^{-1}$ ) handelt es sich um die verwendeten, charakteristischen Raman-Banden des PMMA. Die so erstellten Intensitätsbilder wurden mit der Position der Polymerkügelchen, die auf dem Mikroskop-Bild anhand ihrer Größe unterschieden werden können, verglichen (siehe Abbildung 5 [FK3]). Hierbei konnte eine sehr gute Übereinstimmung zwischen den Positionen der Kügelchen auf dem Mikroskop-Bild und der Position der jeweiligen Polymere auf den SERDS-Intensitätsbildern festgestellt werden, wobei das rote Rechteck eine Gruppe der größeren PMMA-Perlen markiert. In Abbildung 5 [FK3] sind die SERDS-Mittelwertspektren mit ihrer Standardabweichung der neun Bildpunkte dargestellt, die von den beiden Rechtecken (grün und violett) in den Intensitätsbildern markiert werden. Die SERDS-Spektren in grün können dem Phenyl-enthaltenden Polystyrol, die violetten SERDS-Spektren dem Ester-enthaltenden Polymethylmethacrylat zugeordnet werden. Dies bestätigt sich auch nach einem Blick auf die rekonstruierten Mittelwertspektren mit ihrer Standardabweichung der gleichen Bildpunkte in Abbildung 5 [FK3].

Um die Weitfeld-SERDS-Bildgebung in Kombination mit der „*interlaced nod and shuffle*“ Technik an einer heterogenen, biologischen Probe zu demonstrieren, wurde eine Schweinefleischprobe am Übergang zwischen Fett- und Muskelgewebe auf dem Probenkopf mit dem kleinen Bildfeld platziert und für 50 ms mit 40 Wiederholungen, also mit einer Gesamtintegrationszeit von 2 s pro Wellenlänge ( $\lambda_{ex1} = 457,74 \text{ nm}$ ;  $\lambda_{ex2} = 458,90 \text{ nm}$ ), gemessen. Das mittels Subtraktion generierte SERDS-Bild wurde mit einer hierarchischen Clusteranalyse in zwei Cluster eingeteilt (Abbildung 9 (b)). Bei Betrachtung der SERDS-Spektren der beiden Cluster in Abbildung 9 (b) erkennt man, dass Cluster 2 eine deutlich größere Raman-Intensität besitzt als Cluster 1. Außerdem kann der Untergrund nicht vollständig korrigiert werden, was im Moment noch nicht erklärt werden kann und noch weiter untersucht werden muss. Ferner ist bereits im Bandenprofil der SERDS-Spektren zu erkennen, dass es sich bei den beiden Clustern um einen Protein- (Cluster 1) und einen Lipidcluster (Cluster 2) handelt. Um dies zu bestätigen, wurden die SERDS-Spektren durch Addition integriert und mittels SNIP basislinienkorrigiert. Diese rekonstruierten Spektren wurden dann für eine Zuordnung der Raman-Banden verwendet (Abbildung 6 (d) [FK3]). Das Auftreten der typischen Protein-Banden (Amid I: 1638  $\text{cm}^{-1}$ ; Amid III: 1282  $\text{cm}^{-1}$ ; Myoglobin: 1363  $\text{cm}^{-1}$ ; Tyrosin: 858  $\text{cm}^{-1}$ ; Tryptophan:

754  $\text{cm}^{-1}$ , 894  $\text{cm}^{-1}$ , 1587  $\text{cm}^{-1}$ ; CN: 1075  $\text{cm}^{-1}$ , 1099  $\text{cm}^{-1}$ , 1128  $\text{cm}^{-1}$ ) bestätigen die Zuordnung von Cluster 1 als Proteincluster. Dass es sich bei Cluster 2 um einen Lipidcluster handelt, kann ebenfalls anhand typischer Lipidbanden (Carbonyl: 1750  $\text{cm}^{-1}$ , C=C: 1649  $\text{cm}^{-1}$ ,  $\text{CH}_2 / \text{CH}_3$ : 1060  $\text{cm}^{-1}$ , 1300  $\text{cm}^{-1}$ , 1450  $\text{cm}^{-1}$ ) verifiziert werden. Da Lipide aufgrund ihrer langen Alkylketten einen größeren Raman-Streuquerschnitt besitzen als Proteine, erklärt diese Clusterzuordnung auch die unterschiedlich hohe Intensität der Raman-Signale der beiden Cluster. Eine Bildgebung mittels des neu-entwickelten Aufbaus wurde somit erfolgreich demonstriert.

In diesem Kapitel konnte gezeigt werden, dass die „*interlaced nod and shuffle*“ Technik aus der Astrophysik in der Weitfeld-SERDS-Bildgebung erfolgreich eingesetzt werden kann. Der Aufbau ermöglichte die Akkumulierung zweier Raman-Bilder mit unterschiedlicher Anregungswellenlänge und sehr kurzen Belichtungszeiten (50 ms pro Aufnahme) vor dem einmaligen Auslesen des CCD-Chips. Durch diese kurzen Aufnahmezeiten konnte das Photobleichen kompensiert und ein SERDS-Bild mit sehr geringem Untergrund, auch ohne einen Normierungs- oder Optimierungsschritt, erhalten werden. Ferner konnte zum ersten Mal die Elimination von Raumlichtbanden für die SERDS-Bildgebung demonstriert werden. Die Anwendung der Weitfeld-SERDS-Bildgebung in Kombination mit der „*interlaced nod and shuffle*“ Technik konnte sowohl für große als auch sehr kleine Proben mit großem Raman-Streuquerschnitt (Pharmazeutika und Polymere) erfolgreich angewandt werden, wobei eine Bestimmung der Probenposition mittels der SERDS-Spektren eine gute Übereinstimmung mit den jeweiligen Hellfeldbildern zeigte. Auch die Untersuchung einer heterogenen, biologischen Probe war erfolgreich, wobei die in relativen Wellenzahlen große Anregungswellenlängenverschiebung des blauen Lasers für die breitbandigeren biologischen Proben wie erwartet bessere Resultate nach der Rekonstruktion zeigte als für die schmalbandigen Polymerkugeln.

### 3. Zusammenfassung

Mit Hilfe der Raman-Spektroskopie ist es möglich, Informationen über die chemische Zusammensetzung einer Probe zu erhalten, ohne diese zu beschädigen oder im Vorfeld zu markieren. Daher findet die Raman-Spektroskopie immer häufiger Anwendung für die Untersuchung komplexer biologischer Proben wie Zellen, Bakterien und Gewebe. Dabei kann es zur Anregung von Autofluoreszenz in niedrig konzentrierten Substanzen und Chromophoren wie Hämabbauprodukten kommen, welche einen hohen spektralen Untergrund im Raman-Spektrum erzeugt und so zu einer Maskierung der Raman-Banden führen kann.

Der Schwerpunkt dieser Dissertation ist die Verwendung der instrumentellen Basislinienkorrekturmethode SERDS (engl. *shifted excitation Raman difference spectroscopy*) für die Untersuchung von biologischen Proben. Bei dieser Methode werden am gleichen Messpunkt zwei Raman-Spektren mit zwei verschiedenen Anregungswellenlängen gemessen und diese voneinander subtrahiert. Das daraus resultierende SERDS-Spektrum ist idealerweise ein untergrundfreies Differenzspektrum, das der ersten Ableitung eines Raman-Spektrums sehr ähnlich ist. Ziel dieser Dissertation war die Evaluierung und Optimierung der SERDS-Methode und der SERDS-Bildgebung an biologischen Proben. Um die Aufnahme eines SERDS-Bildes zu beschleunigen und den Untergrund zu minimieren, wurde erstmalig die Weitfeld-SERDS-Bildgebung mittels der „*interlaced nod and shuffle*“ Technik unter Verwendung sehr schnell wechselnder Laserwellenlängen verwendet.

Zuerst wurden Untersuchungen an einer Gewebeprobe vom Schwein durchgeführt, um wichtige Parameter wie die optimale Verschiebung der Anregungswellenlänge oder einen möglichen Normierungsschritt zur Kompensation von Photobleichen für die Anwendung von SERDS zu untersuchen. Ferner wurde ein Vergleich zwischen SERDS und der mathematischen Untergrundkorrekturmethode EMSC gezogen. Basierend auf diesen Ergebnissen wurde ein Arbeitsablauf für die Prozessierung und Klassifizierung von SERDS-Daten entwickelt und dieser anhand der Klassifizierung von Pollendaten verschiedener Pflanzengenera erprobt. Der entwickelte Arbeitsablauf weicht dabei von der üblichen Herangehensweise an SERDS-Daten dahingehend ab, dass normalerweise ein Raman-Spektrum aus dem SERDS-Spektrum rekonstruiert wird. Außerdem werden SERDS-Daten häufig gemittelt, um ein besseres Signal-Rausch-Verhältnis zu erhalten. Auf beide Schritte wurde in dem entwickelten Arbeitsablauf verzichtet. Dieser war wie folgt: Entfernen von kosmischen Spitzen, Intensitäts- und Wellenlängenkalibrierung, Differenzoptimierung und Bildung der SERDS-Spektren, Pearson-Korrelation mit den Mittelwertdifferenzspektren einer jeden

Pollenart und die Klassifizierung mittels PCA-LDA. Mit Hilfe der Weitfeld-SERDS-Spektroskopie in Kombination mit der „*interlaced nod and shuffle*“ Technik wurden im letzten Teil dieser Dissertation sowohl Proben mit einem guten Raman-Streuquerschnitt wie Paracetamol, Aspirin, Polystyrol und Polymethylmethacrylat als auch biologische Proben in Form von Schweinefleischproben gemessen und SERDS-Bilder von ihnen erstellt. Hierbei wurden auch zum ersten Mal die Vorteile eines schnellen Wechsels der Anregungswellenlänge und die generelle Stärke des SERDS-Ansatzes in Bezug auf externe Lichtquellen für die SERDS-Bildgebung demonstriert.

Für die im ersten Teil durchgeführten Untersuchungen zur Bestimmung der optimalen Verschiebung der Anregungswellenlänge wurden vier unterschiedliche Verschiebungen (0,5 nm; 1,0 nm; 1,5 nm; 2,0 nm) an einer Schweinefleischprobe getestet. Daraus resultierte, dass die mit der größtmöglichen, betrachteten Wellenlängenverschiebung gemessenen SERDS-Spektren über die größte erhaltene Gesamtintensität verfügten. Da für die SERDS-Technik das Signal-Rausch-Verhältnis der limitierende Faktor ist, ist folglich der Erhalt der größtmöglichen Intensität im Differenzspektrum vorteilhaft und erstrebenswert. Unter dieser Prämisse ist die betrachtete, größtmögliche Anregungswellenlängenverschiebung die für diesen Aufbau optimale Verschiebung. Dies bestätigten die von E. Cordero [FK1] durchgeführten Simulationen zur optimalen Wellenlängenverschiebung. Hierbei wurde festgestellt, dass eine Anregungswellenlängenverschiebung von  $110\text{ cm}^{-1}$  für Lipide und  $160\text{ cm}^{-1}$  für Proteine optimal ist. Die größtmögliche Verschiebung hängt dabei stark vom jeweiligen Aufbau und den darin integrierten Filtern ab. Für den in Kapitel 2.1 und 2.2 verwendeten Aufbau betrug die größtmögliche Verschiebung 2 nm (entspricht  $32,46\text{ cm}^{-1}$ ). In Kapitel 2.3 kamen zwei unterschiedliche Laser mit zwei fixen Wellenlängen zum Einsatz, wobei der kommerzielle NIR-Laser eine Anregungswellenlängenverschiebung von 1,05 nm (entspricht  $17,04\text{ cm}^{-1}$ ) aufwies. Der im Zuge des HYPERAM-Projektes entwickelte Laser verfügte über zwei Laserdioden, die eine Anregungswellenlängenverschiebung von 1,16 nm (entspricht  $55,22\text{ cm}^{-1}$ ) aufwiesen und somit am nächsten an die optimale Verschiebung für biologische Komponenten herankamen.

Der Vergleich der instrumentellen Untergrundkorrekturmethode SERDS mit der mathematischen Untergrundkorrekturmethode EMSC ergab folgendes: Die Untergrundkorrektur der Spektren bei Verwendung der EMSC ist sehr gut. Allerdings benötigt diese Methode entsprechendes Vorwissen über den Untergrund und die Komponenten, die zum Untergrund beitragen. Insbesondere für



die Korrektur eines Raman-Bildes, das an verschiedenen räumlichen Punkten unterschiedlich stark ausgeprägte spektrale Untergründe aufweist, kann die Korrektur mittels EMSC sehr aufwendig sein und die Vorgabe verschiedener Untergrundkomponenten erfordern. Die SERDS-Methode dagegen benötigt kein Vorwissen über den spektralen Untergrund einer Probe. Da Differenzspektren im Allgemeinen schwierig und ungewohnt zu interpretieren sind, erfolgt häufig eine Rekonstruktion. Allerdings können die Bandenpositionen bei rekonstruierten SERDS-Spektren, deren Rekonstruktion auf der Annahme beruht, dass ein SERDS-Spektrum der ersten Ableitung entspricht, nicht immer genau bestimmt werden, da es aufgrund der unterschiedlichen Halbwertsbreiten der Raman-Banden zu leichten Verschiebungen im rekonstruierten Spektrum kommen kann. Erschwert wird die Interpretation zusätzlich durch das Ineinanderschieben von benachbarten Banden, was zu einer starken Verzerrung des Bandenprofils führen kann. Die größte Herausforderung für SERDS stellt die Addition des spektralen Rauschens bei Bildung der Differenzspektren dar, wodurch sich das Signal-Rausch-Verhältnis im Differenzspektrum verschlechtert. Durch Unterschiede in der Laserintensität, Unterschiede in der Fluoreszenzemissionsintensität basierend auf der unterschiedlichen Absorption der jeweiligen Anregungswellenlänge oder durch Photobleichen kann es zu Intensitätsänderungen im spektralen Untergrund der beiden Raman-Spektren kommen. Diese lassen sich nicht durch simple Subtraktion korrigieren. Erkennbar ist dies an einem Restuntergrund in den Differenzspektren. Für die Kompensation dieses Restuntergrunds wurden verschiedene Normierungsmethoden probiert. Hierbei stellte sich heraus, dass die Flächennormierung am schlechtesten dafür geeignet ist, den Restuntergrund in den SERDS-Spektren zu entfernen. Die in [FK1] vorgestellte Differenzoptimierung konnte den Untergrund besser korrigieren und die Standardabweichung reduzieren.

Basierend auf diesen Erkenntnissen wurde für den zweiten Teil dieser Arbeit ein Arbeitsablauf entwickelt. Dieser wurde dazu verwendet, um zu überprüfen, in wie fern eine direkte Klassifikation mit Hilfe von SERDS-Daten eine erfolgreiche Vorhersage liefert. Diese wurden mit der Klassifikation basierend auf rekonstruierten, basislinienkorrigierten und gemessenen, basislinienkorrigierten Raman-Spektren verglichen. Durch die direkte Nutzung der Differenzspektren sollte die Bildung von Artefakten in den rekonstruierten Raman-Spektren vermieden werden. Der Arbeitsablauf enthielt die Verwendung der größtmöglichen Verschiebung der Anregungswellenlänge (2 nm) für den Erhalt der größtmöglichen Intensität in den SERDS-Spektren und die Differenzoptimierung der gemessenen SERDS-Daten, um das Ausbleichen der Probe während der

Messung und Unterschiede in der Laserintensität zu kompensieren. Um das Signal-Rausch-Verhältnis zu verbessern und die Dimensionalität des Datensatzes zu reduzieren, wurde eine Hauptkomponentenanalyse der Differenzspektren durchgeführt. Dazu wurde mit einem für SERDS-Messungen angepasstes Hochdurchsatz-Raman-System Pollen verschiedener Pflanzengenera als Fallstudie gemessen. Hierbei stellte sich heraus, dass die Schwankungen der Ergebnisse zwischen den Klassifikationen auf Basis unterschiedlich behandelte Spektren recht gering sind. Eine Rekonstruktion mit anschließender Basislinienkorrektur bedeutet einen größeren rechnerischen sowie zeitlichen Aufwand, und erhöht das Risiko von Artefakten in den rekonstruierten Spektren. Da das Ergebnis durch eine Rekonstruktion aber, wenn überhaupt, nur bei komplexeren Klassifikationen marginal verbessert wird, ist eine direkte Klassifikation basierend auf den SERDS-Spektren vorzuziehen und die bessere Wahl.

Der dritte Teil dieser Dissertation basiert auf der Weitfeld-SERDS-Bildgebung in Kombination mit der „*interlaced nod and shuffle*“ Technik, welche erprobt und evaluiert wurden. Die Verknüpfung dieser beiden Technologien erlaubte die Aufnahme eines SERDS-Bildes mit  $20 \times 20$  Spaxeln pro Belichtung, wobei durch die „*interlaced nod and shuffle*“ Technik die Akkumulation beider für SERDS notwendigen Wellenlängen mit sehr kurzen Einzelaufnahmezeiten auf dem CCD-Chip möglich war. Der Vorteil der Akkumulation kurzer Aufnahmezeiten in der SERDS-Technik besteht darin, dass die Änderungen im Fluoreszenzuntergrund gleichmäßiger auf die Signale beider Anregungswellenlängen verteilt werden. Dadurch kann der Effekt des Photobleichens kompensiert werden. Dies zeigte sich Vergleich der SERDS-Spektren, die in kurzen Intervallen von  $40 \times 50$  ms gemessen wurden, und der SERDS-Spektren, die mit einer einmaligen, langen Exposition von  $1 \times 2000$  ms gemessen wurden. Die andere Stärke der SERDS-Methode, das Filtern von Raumlichtbanden, konnte bereits für Einzelspektren demonstriert werden. In dieser Arbeit wurde diese Fähigkeit mit Hilfe der Weitfeld-SERDS-Bildgebung in Kombination mit „*interlaced nod and shuffle*“ erstmalig für die SERDS-Bildgebung anhand des SERDS-Bildes einer Paracetamol- und einer Aspirin-Tablette gezeigt.

Um den Weitfeld-SERDS Aufbau an einer heterogenen biologischen Probe zu testen, wurde stellvertretend das Muskel- und Fettgewebe einer Gewebeprobe vom Schwein gemessen. Hierbei konnte mittels der Differenzspektren eines SERDS-Bildes eine Region mit hohem Lipidanteil von einer Region mit hohem Proteinanteil durch eine Clusteranalyse der Differenzspektren unterschieden und somit erfolgreich die Weitfeld-SERDS-Bildgebung demonstriert werden.

Mit der vorliegenden wissenschaftlichen Arbeit konnten diese Ergebnisse festgestellt werden: SERDS kommt als instrumentelle Methode mit wenigen Prozessierungsschritten aus, sofern kurze Messintervalle und gleiche Intensitäten für die Anregungswellenlängen gewährleistet sind. Ist dies nicht der Fall, muss ein Normierungsschritt vor der Differenzbildung erfolgen, um Intensitätsunterschiede zwischen den beiden voneinander zu subtrahierenden Spektren auszugleichen. Um die Signalintensität SERDS-Spektrum zu maximieren, sollte die optimale Verschiebung verwendet werden, wobei die in den Simulationen von E. Cordero optimalen Anregungswellenlängenverschiebungen für Lipide und Proteine so groß sind, dass diese noch nicht experimentell erprobt wurden. Da eine Rekonstruktion eines Raman-Spektrums aus einem SERDS-Spektrum keinen signifikanten Mehrwert für eine Klassifikation mittels PCA-LDA besitzt, kann diese für eine Verschönerung der Datenprozessierung weggelassen werden. Der Weitfeld-SERDS-Aufbau in Kombination mit der „*interlaced nod and shuffle*“ Technik eignet sich sehr gut für die schnelle Aufnahme von SERDS-Bildern ohne langsames Punkt-für-Punkt-Messen einer Probe mit sehr kurzen Aufnahmezeiten, was das Ausbleichen der Probe kompensieren kann. Die Stärke von SERDS, anregungswellenlängenunabhängige Bandenprofile wie Raumlicht auszuschalten, konnte zum ersten Mal für die SERDS-Bildgebung demonstriert werden. Die größte Schwäche der SERDS-Methode stellt die Fehlerfortpflanzung in einer Messung dar: Die Subtraktion zweier Spektren voneinander führt immer zu einer Erhöhung des Rauschens im SERDS-Spektrum. Dies kann durch Glätten der Spektren oder durch Mittelung kompensiert werden. Insbesondere für hohe Fluoreszenzuntergründe, wechselnde spektrale Untergründe innerhalb eines Raman-Bildes und/oder wellenlängenunabhängige Bandenprofile (z.B. Raumlicht, Systemfunktion des Messsystems) stellt die Basislinienkorrektur mittels der SERDS-Technik eine sehr gute Alternative zu hoch entwickelten, anspruchsvollen mathematischen Korrekturmethode dar, ohne dass Kenntnisse über die Struktur des spektralen Hintergrundes notwendig wäre.

Insbesondere die Weitfeld-SERDS-Bildgebung mit integrierter „*interlaced nod and shuffle*“ Technik ist im hohen Maße dazu geeignet, in einem klinischen Umfeld angewendet zu werden. Durch die SERDS-Technik könnte das Raumlicht während der Messung angeschaltet bleiben, sofern es nicht direkt auf den Probenkopf fällt und so keine Detektorsättigung zu befürchten ist. Die Akkumulation kurzer Messintervalle würde eine Normierung vor Bildung der SERDS-Spektren obsolet machen und Photobleichen effektiv unterbinden. Durch eine direkte Klassifikation der SERDS-Daten könnte so eine schnelle Zuordnung der Messdaten erfolgen, was eine schnelle Diagnostik während der Operation unterstützen würde.

## 4. Summary

With the help of Raman spectroscopy, it is possible to obtain information about the chemical composition of a sample without damaging or labeling it in advance. Therefore, Raman spectroscopy is more and more often used for the investigation of complex biological samples like cells, bacteria and tissues. This can result in the excitation of autofluorescence in low-concentration substances and chromophores such as hemolytic products, which creates a high spectral background in the Raman spectrum and can lead to the masking of Raman bands.

The focus of this dissertation is the use of the instrumental baseline correction method SERDS (shifted excitation Raman difference spectroscopy) for the investigation of biological samples. In this method, two Raman spectra with two different excitation wavelengths are measured at the same measuring point and subtracted from each other. The resulting SERDS spectrum is ideally a background free difference spectrum which is very similar to the first derivative of a Raman spectrum. The aim of this thesis was to evaluate and optimize the SERDS method and SERDS imaging on biological samples. In order to accelerate the acquisition of a SERDS image and to minimize the background, the wide field SERDS imaging using the "interlaced nod and shuffle" technique with very fast changing laser wavelengths was employed for the first time.

First, investigations were performed on a porcine tissue sample to investigate important parameters such as the optimal shift of the excitation wavelength or a possible normalization step to compensate for photobleaching for the application of SERDS. Furthermore, a comparison between SERDS and the mathematical background correction method EMSC was made. Based on these results, a workflow for processing and classifying SERDS data was developed and tested by classifying pollen data of different plant genera. The developed workflow differs from the usual approach to SERDS data in that a Raman spectrum is usually reconstructed from the SERDS spectrum. In addition, SERDS data are often averaged to obtain a better signal-to-noise ratio. Both steps have been omitted in the developed workflow, which was as follows: Removal of cosmic peaks, intensity and wavelength calibration, difference optimization and formation of SERDS spectra, Pearson correlation with the mean difference spectra of each pollen species and classification by PCA-LDA. Using wide-field SERDS spectroscopy in combination with the "interlaced nod and shuffle" technique, the last part of this thesis measured samples with a good Raman scattering cross section such as paracetamol, aspirin, polystyrene and polymethyl methacrylate as well as biological samples in the form of pork samples and generated SERDS images of them. This was also the first time that the advantages of a fast change in excitation

wavelength and the general strength of the SERDS approach with respect to external light sources for SERDS imaging were demonstrated.

For the investigations carried out in the first part to determine the optimum shift of the excitation wavelength, four different shifts (0.5 nm; 1.0 nm; 1.5 nm; 2.0 nm) were tested on a pork sample. As a result, the SERDS spectra measured with the largest possible wavelength shift obtained the highest total intensity. As the signal-to-noise ratio is the limiting factor for the SERDS technique, it is therefore advantageous and desirable to obtain the highest possible intensity in the difference spectrum. Under this premise, the largest possible excitation wavelength shift is the optimal shift for this setup. This was confirmed by the simulations carried out by E. Cordero [FK1] for the optimal wavelength shift. It was found that an excitation wavelength shift of 110  $\text{cm}^{-1}$  for lipids and 160  $\text{cm}^{-1}$  for proteins is optimal. The maximum possible shift depends strongly on the structure and the integrated filters. For the set-up used in chapters 2.1 and 2.2, the largest possible shift was 2 nm (corresponds to 32.46  $\text{cm}^{-1}$ ). In chapter 2.3, two different lasers with two fixed wavelengths were used. The commercial NIR laser had an excitation wavelength shift of 1.05 nm (corresponding to 17.04  $\text{cm}^{-1}$ ). The laser developed in the course of the HYPERAM project had two laser diodes which had an excitation wavelength shift of 1.16 nm (corresponding to 55.22  $\text{cm}^{-1}$ ) and thus came closest to the optimal shift for biological components.

The comparison of the instrumental background correction method SERDS with the mathematical background correction method EMSC showed the following: The background correction of the spectra when using the EMSC is very good. However, this method requires appropriate knowledge of the background and the components that contribute to the background. Especially for the correction of a Raman image with spectral backgrounds of varying intensity at different spatial points, the correction with EMSC can be very complex and require the specification of different background components. The SERDS method, on the other hand, requires no prior knowledge of the spectral background of a sample. Since difference spectra are generally difficult and unusual to interpret, reconstruction is often necessary. However, the band positions of reconstructed SERDS spectra, whose reconstruction is based on the assumption that a SERDS spectrum corresponds to the first derivative, cannot always be determined exactly, since slight shifts in the reconstructed spectrum may occur due to the different FWHM of the Raman bands. The interpretation is further complicated by the fact that adjacent bands are shifted into each other, which can lead to a strong distortion of the band profile. The greatest challenge

for SERDS is the addition of spectral noise when forming the difference spectra, which leads to a deterioration of the signal-to-noise ratio in the difference spectrum. Differences in laser intensity, differences in fluorescence emission intensity based on the different absorption of the respective excitation wavelength, or photobleaching may cause intensity changes in the spectral background of the two Raman spectra. These changes cannot be corrected by simple subtraction. This can be recognized by a residual background in the difference spectra. Various normalization methods were tried to compensate for this residual background. It turned out that the area normalization is the least suitable for removing the residual background in the SERDS spectra. The difference optimization presented in [FK1] was better able to correct the background and reduce the standard deviation.

Based on these findings, a workflow was developed for the second part of this work. This was used to check how far a direct classification using SERDS data can deliver a successful prediction. These data were compared with the classification based on reconstructed, baseline corrected and measured, baseline corrected Raman spectra. By using the difference spectra directly, the formation of artifacts in the reconstructed Raman spectra should be avoided. The workflow included using the maximum excitation wavelength shift (2 nm) to obtain the highest possible intensity in the SERDS spectra and the difference optimization of the measured SERDS data to compensate for photobleaching during measurement and differences in laser intensity. A principal component analysis of the difference spectra was performed to improve the signal-to-noise ratio and reduce the dimensionality of the data set. A high-throughput Raman system adapted for SERDS measurements was used to measure pollen of different plant genera as a case study. It was found that the variation of results between classifications based on differently treated spectra is quite small. A reconstruction with subsequent baseline correction requires more time and effort and increases the risk of artifacts in the reconstructed spectra. However, since the result is marginally improved by reconstruction, if at all, only for more complex classifications, a direct classification based on the SERDS spectra is preferable and the better choice.

The third part of this dissertation is based on wide-field SERDS imaging in combination with the "interlaced nod and shuffle" technique, which has been tested and evaluated. The combination of these two technologies allowed the acquisition of a SERDS image with  $20 \times 20$  spaxels per exposure. The interlaced nod and shuffle technique allowed the accumulation of both wavelengths necessary for SERDS with very short single acquisition times on the CCD chip. The

advantage of the accumulation of short acquisition times in the SERDS technique is that the changes in the fluorescence background are distributed more evenly over the signals of both excitation wavelengths. Thus, the effect of the Photobleaching can be compensated. This was shown by comparing the SERDS spectra measured at short intervals of  $40 \times 50$  ms and the SERDS spectra measured with a single long exposure of  $1 \times 2000$  ms. The other strength of the SERDS method, the filtering of room light bands, has already been demonstrated for single spectra. In this work, this ability was demonstrated for the first time for SERDS imaging using wide-field SERDS imaging in combination with interlaced nod and shuffle by recording a SERDS image of a paracetamol and an aspirin pill.

In order to test the wide field SERDS setup on a heterogeneous biological sample, muscle and fat tissue of a porcine tissue sample was measured. Using the difference spectra of a SERDS image, a region with a high lipid content could be distinguished from a region with a high protein content by cluster analysis of the difference spectra, thus successfully demonstrating wide field SERDS imaging.

With the present scientific work these results could be established: SERDS as an instrumental method requires only a few processing steps, provided that short measuring intervals and equal intensities for the excitation wavelengths are guaranteed. If this is not the case, a normalization step must be performed before the difference is formed to compensate for differences in intensity between the two spectra, which are subtracted from each other. To maximize the signal intensity of the SERDS spectrum, the optimal shift should be used. The optimal excitation wavelength shifts for lipids and proteins in E. Cordero's simulations are so large that they have not yet been experimentally tested. Since a reconstruction of a Raman spectrum from a SERDS spectrum has no significant added value for a classification using a PCA-LDA, it can be omitted to streamline the data processing. The wide field SERDS setup in combination with the "interlaced nod and shuffle" technique is very well suited for the fast acquisition of SERDS images using very short acquisition times, which can compensate for photobleaching, without slow point-by-point measurements of a sample. The strength of SERDS to erase excitation wavelength independent band profiles such as ambient light could be demonstrated for the first time for SERDS imaging. The greatest weakness of the SERDS method is the error propagation in a measurement: Subtracting two spectra from each other always leads to an increase in noise in the SERDS spectrum. This can be compensated by smoothing the spectra or by averaging. Especially for high fluorescence backgrounds, changing spectral backgrounds within a Raman image and/or

wavelength-independent band profiles (e.g. room light, system function of the measurement system), baseline correction using the SERDS technique is a very good alternative to sophisticated mathematical correction methods without the need for knowledge of the structure of the spectral background.

Especially the wide field SERDS imaging with integrated "interlaced nod and shuffle" technique is highly suitable for clinical applications. With the SERDS technique, the room light could remain switched on during the measurement, as long as it does not directly shine onto the sample head and no detector saturation has to be feared. The accumulation of short measurement intervals would make normalization before the SERDS spectra are formed obsolete and effectively prevent photobleaching. Direct classification of the SERDS data would allow for a fast assignment of the measured data, which would support fast diagnostics during surgery.



## 5. Literaturverzeichnis

1. Butler, H.J.; Ashton, L.; Bird, B.; Cinque, G.; Curtis, K.; Dorney, J.; Esmonde-White, K.; Fullwood, N.J.; Gardner, B.; Martin-Hirsch, P.L.; et al. Using Raman spectroscopy to characterize biological materials. *Nat. Protoc.* **2016**, *11*, 664–687, doi:10.1038/nprot.2016.036.
2. Eberhardt, K.; Stiebing, C.; Matthäus, C.; Schmitt, M.; Popp, J. Advantages and limitations of Raman spectroscopy for molecular diagnostics: an update. *Expert Rev. Mol. Diagn.* **2015**, *15*, 773–787, doi:10.1586/14737159.2015.1036744.
3. Germond, A.; Kumar, V.; Ichimura, T.; Moreau, J.; Furusawa, C.; Fujita, H.; Watanabe, T.M. Raman spectroscopy as a tool for ecology and evolution. *J. R. Soc. Interface* **2017**, *14*, 1–7, doi:10.1098/rsif.2017.0174.
4. Krafft, C.; Schie, I.W.; Meyer, T.; Schmitt, M.; Popp, J. Developments in spontaneous and coherent Raman scattering microscopic imaging for biomedical applications. *Chem. Soc. Rev.* **2016**, *45*, 1819–1849, doi:10.1039/c5cs00564g.
5. Hubbard, T.J.E.; Shore, A.; Stone, N. Raman spectroscopy for rapid intra-operative margin analysis of surgically excised tumour specimens. *Analyst* **2019**, *144*, 6479–6496, doi:10.1039/c9an01163c.
6. Krafft, C.; Schmitt, M.; Schie, I.W.; Cialla-May, D.; Matthaes, C.; Bocklitz, T.; Matthäus, C.; Bocklitz, T.; Popp, J. Label-free molecular imaging of biological cells and tissues by linear and non-linear Raman spectroscopic approaches. *Angew. Chemie Int. Ed.* **2016**, 4392–4430, doi:10.1002/anie.201607604.
7. Cheng, J.X.; Xie, X.S. Vibrational spectroscopic imaging of living systems: An emerging platform for biology and medicine. *Science (80- )*. **2015**, *350*, 1–9, doi:10.1126/science.aaa8870.
8. Monici, M. Cell and tissue autofluorescence research and diagnostic applications. *Biotechnol. Annu. Rev.* **2005**, *11*, 227–256, doi:10.1016/S1387-2656(05)11007-2.
9. McCreery, R.L. *Raman Spectroscopy for Chemical Analysis*; Winefordner, J.D., Ed.; John Wiley & Sons, Inc.: Hoboken, NJ, USA, 2000; ISBN 9780471721642.
10. Sinjab, F.; Kong, K.; Gibson, G.; Varma, S.; Williams, H.; Padgett, M.; Notingher, I. Tissue diagnosis using power-sharing multifocal Raman micro-spectroscopy and auto-fluorescence imaging. *Biomed. Opt. Express* **2016**, *7*, 1–14, doi:10.1364/BOE.7.002993.
11. Kong, K.; Zaabar, F.; Rakha, E.; Ellis, I.; Koloydenko, A.; Notingher, I. Towards intra-operative diagnosis of tumours during breast conserving surgery by selective-sampling Raman micro-spectroscopy. *Phys. Med. Biol.* **2014**, *59*, 6141–6152, doi:10.1088/0031-9155/59/20/6141.
12. Galli, R.; Meinhardt, M.; Koch, E.; Schackert, G.; Steiner, G.; Kirsch, M.; Uckermann, O. Rapid Label-Free Analysis of Brain Tumor Biopsies by Near Infrared Raman and Fluorescence Spectroscopy — A Study of 209 Patients. *Front. Oncol.* **2019**, *9*, 1–13, doi:10.3389/fonc.2019.01165.
13. Desroches, J.; Jermyn, M.; Pinto, M.; Picot, F.; Tremblay, M.A.; Obaid, S.; Marple, E.; Urmey, K.; Trudel, D.; Soulez, G.; et al. A new method using Raman spectroscopy for in vivo targeted brain cancer tissue biopsy. *Sci. Rep.* **2018**, *8*, 1–10, doi:10.1038/s41598-018-20233-3.
14. Cordero, E.; Rüger, J.; Marti, D.; Mondol, A.S.; Hasselager, T.; Mogensen, K.; Hermann, G.G.; Popp, J.; Schie, I.W. Bladder tissue characterization using probe-based Raman spectroscopy: Evaluation of tissue heterogeneity and influence on the model prediction. *J. Biophotonics* **2020**, *13*, 1–15, doi:10.1002/jbio.201960025.
15. Bergholt, M.S.; Zheng, W.; Lin, K.; Wang, J.; Xu, H.; Ren, J.L.; Ho, K.Y.; Teh, M.; Yeoh, K.G.; Huang, Z. Characterizing variability of in vivo Raman spectroscopic properties of different anatomical sites of normal colorectal tissue towards cancer diagnosis at colonoscopy. *Anal. Chem.* **2015**, *87*, 960–966, doi:10.1021/ac503287u.
16. Becker, W. Fluorescence lifetime imaging - techniques and applications. *J. Microsc.* **2012**, *247*, 119–136, doi:10.1111/j.1365-2818.2012.03618.x.
17. Wei, D.; Chen, S.; Liu, Q. Review of Fluorescence Suppression Techniques in Raman Spectroscopy. *Appl. Spectrosc. Rev.* **2015**, *50*, 387–406, doi:10.1080/05704928.2014.999936.

18. Lieber, C.A.; Mahadevan-Jansen, A.; Lieber, C.A. Automated Method for Subtraction of Fluorescence from Biological Raman Spectra. *Appl. Spectrosc.* **2003**, *57*, 1363–1367, doi:10.1366/000370203322554518.
19. Pirzer, M.; Sawatzki, J. US Patent Application Publication Pub. No. : US 2006 / 0211562 A1, Pub. Date: Sep. 21, 2006, 2006, 1–11.
20. Kneen, M.A.; Annegarn, H.J. Algorithm for fitting XRF, SEM and PIXE X-ray spectra backgrounds. *Nucl. Instruments Methods Phys. Res. Sect. B Beam Interact. with Mater. Atoms* **1996**, *109/110*, 209–213, doi:10.1016/0168-583X(95)00908-6.
21. Afseth, N.K.; Kohler, A. Extended multiplicative signal correction in vibrational spectroscopy, a tutorial. *Chemom. Intell. Lab. Syst.* **2012**, *117*, 92–99, doi:10.1016/j.chemolab.2012.03.004.
22. Martens, H.; Stark, E. Extended multiplicative signal correction and spectral interference subtraction: New preprocessing methods for near infrared spectroscopy. *J. Pharm. Biomed. Anal.* **1991**, *9*, 625–635, doi:10.1016/0731-7085(91)80188-F.
23. Morhác, M. An algorithm for determination of peak regions and baseline elimination in spectroscopic data. *Nucl. Instruments Methods Phys. Res. Sect. A Accel. Spectrometers, Detect. Assoc. Equip.* **2009**, *600*, 478–487, doi:10.1016/j.nima.2008.11.132.
24. Morhác, M.; Matousek, V. Peak clipping algorithms for background estimation in spectroscopic data. *Appl. Spectrosc.* **2008**, *62*, 91–106, doi:10.1366/000370208783412762.
25. Kasha, M. Characterization of electronic transitions in complex molecules. *Discuss. Faraday Soc.* **1950**, *1*.
26. Ariese, F.; Meuzelaar, H.; Kerssens, M.M.; Buijs, J.B.; Gooijer, C. Picosecond Raman spectroscopy with a fast intensified CCD camera for depth analysis of diffusely scattering media. *Analyst* **2009**, *134*, 1192–1197, doi:10.1039/b821437a.
27. Kögler, M.; Heilala, B. Time-gated Raman spectroscopy – a review. *Meas. Sci. Technol.* **2020**, *32*, 1–17, doi:10.1088/1361-6501/abb044.
28. De Luca, A.; Dholakia, K.; Mazilu, M. Modulated Raman Spectroscopy for Enhanced Cancer Diagnosis at the Cellular Level. *Sensors* **2015**, *15*, 13680–13704, doi:10.3390/s150613680.
29. Dochow, S.; Bergner, N.; Krafft, C.; Clement, J.; Mazilu, M.; Praveen, B.B.; Ashok, P.C.; Marchington, R.; Dholakia, K.; Popp, J. Classification of Raman spectra of single cells with autofluorescence suppression by wavelength modulated excitation. *Anal. Methods* **2013**, *5*, 4608–4614, doi:10.1039/c3ay40193f.
30. Craig, D.; Mazilu, M.; Dholakia, K. Quantitative detection of pharmaceuticals using a combination of paper microfluidics and wavelength modulated Raman spectroscopy. *PLoS One* **2015**, *10*, 1–10, doi:10.1371/journal.pone.0123334.
31. Wirth, M.J.; Chou, S.H. Comparison of Time and Frequency Domain Methods for Rejecting Fluorescence from Raman Spectra. *Anal. Chem.* **1988**, *60*, 1882–1886, doi:10.1021/ac00169a009.
32. Shreve, A.P.; Cherepy, N.J.; Mathies, R.A. Effective Rejection of Fluorescence Interference in Raman Spectroscopy Using a Shifted Excitation Difference Technique. *Appl. Spectrosc.* **1992**, *46*, 707–711, doi:10.1366/0003702924125122.
33. Schmidt, H.; Kaiser, D.P.; Maiwald, M. METHOD FOR GENERATING AND FOR DETECTING A RAMAN SPECTRUM, Pat. No. WO 2011/033017 AI 2010, 13.
34. Matousek, P.; Towrie, M.; Parker, A.W. Simple Reconstruction Algorithm for Shifted Excitation Raman Difference Spectroscopy. *Appl. Spectrosc.* **2005**, *59*, 848–851, doi:10.1366/0003702054280757.
35. Zhao, J.; Carrabba, M.M.; Allen, F.S. Automated Fluorescence Rejection Using Shifted Excitation Raman Difference Spectroscopy. *Appl. Spectrosc.* **2002**, *56*, 834–845, doi:10.1366/000370202760171491.
36. Guo, S.; Chernavskaya, O.; Popp, J.; Bocklitz, T. Spectral reconstruction for shifted-excitation Raman difference spectroscopy (SERDS). *Talanta* **2018**, *186*, 372–380, doi:10.1016/j.talanta.2018.04.050.
37. Willett, R. Multiscale Reconstruction for Photon-Limited Shifted Excitation Raman Spectroscopy. In Proceedings of the 2007 IEEE International Conference on Acoustics, Speech and Signal

- Processing - ICASSP '07; IEEE, 2007; pp. 833–836.
38. Schmäzlin, E.; Moralejo, B.; Bodenmüller, D.; Darvin, M.E.; Thiede, G.; Roth, M.M. Ultrafast imaging Raman spectroscopy of large-area samples without stepwise scanning. *J. Sensors Sens. Syst.* **2016**, *5*, 261–271, doi:10.5194/jsss-5-261-2016.
  39. Sowoidnich, K.; Kronfeldt, H.-D. Fluorescence Rejection by Shifted Excitation Raman Difference Spectroscopy at Multiple Wavelengths for the Investigation of Biological Samples. *ISRN Spectrosc.* **2012**, *2012*, 1–11, doi:10.5402/2012/256326.
  40. Noack, K.; Eskofier, B.; Kiefer, J.; Dilk, C.; Bilow, G.; Schirmer, M.; Buchholz, R.; Leipertz, A. Combined shifted-excitation Raman difference spectroscopy and support vector regression for monitoring the algal production of complex polysaccharides. *Analyst* **2013**, *138*, 5639–5646, doi:10.1039/c3an01158e.
  41. Knipfer, C.; Motz, J.; Adler, W.; Brunner, K.; Gebrekidan, M.T.; Hankel, R.; Agaimy, A.; Will, S.; Braeuer, A.; Neukam, F.W.; et al. Raman difference spectroscopy: a non-invasive method for identification of oral squamous cell carcinoma. *Biomed. Opt. Express* **2014**, *5*, 3252, doi:10.1364/BOE.5.003252.
  42. Gebrekidan, M.T.; Knipfer, C.; Stelzle, F.; Popp, J.; Will, S.; Braeuer, A. A shifted-excitation Raman difference spectroscopy (SERDS) evaluation strategy for the efficient isolation of Raman spectra from extreme fluorescence interference. *J. Raman Spectrosc.* **2016**, *47*, 198–209, doi:10.1002/jrs.4775.
  43. Jürgens, M.; Mayerhöfer, T.; Popp, J.; Lee, G.; Matthews, D.L.; Wilson, B.C. Introduction to Biophotonics. In *Handbook of Biophotonics*; Wiley-VCH Verlag GmbH & Co. KGaA: Weinheim, Germany, 2013.
  44. Long, D.A. *The Raman Effect*; John Wiley & Sons, Ltd: Chichester, UK, 2002; ISBN 0471490288.
  45. Raman, C. V. A new radiation. *Indian J. Phys.* **1928**, *2*, 387–398, doi:10.1007/BF03052651.
  46. Vandenabeele, P. *Practical Raman Spectroscopy - An Introduction*; John Wiley & Sons, Ltd: Chichester, UK, 2013; ISBN 9781119961284.
  47. Stewart, S.; Priore, R.J.; Nelson, M.P.; Treado, P.J. Raman Imaging. *Annu. Rev. Anal. Chem.* **2012**, *5*, 337–360, doi:10.1146/annurev-anchem-062011-143152.
  48. Duxbury, G. 3D Spectroscopy in Astronomy, edited by E. Mediavilla, S. Arribas, M. M. Roth, J. Cepa-Nogué and F. Cepa-Nogué. *Contemp. Phys.* **2012**, *53*, 267–268, doi:10.1080/00107514.2012.661466.
  49. Allington-Smith, J. Basic principles of integral field spectroscopy. *New Astron. Rev.* **2006**, *50*, 244–251, doi:10.1016/j.newar.2006.02.024.
  50. Schmäzlin, E.; Moralejo, B.; Rutowska, M.; Monreal-Ibero, A.; Sandin, C.; Tarcea, N.; Popp, J.; Roth, M.M. Raman imaging with a fiber-coupled multichannel spectrograph. *Sensors (Switzerland)* **2014**, *14*, 21968–21980, doi:10.3390/s141121968.
  51. Schmäzlin, E.; Moralejo, B.; Gersonde, I.; Schleusener, J.; Darvin, M.E.; Thiede, G.; Roth, M.M. Nonscanning large-area Raman imaging for ex vivo/in vivo skin cancer discrimination. *J. Biomed. Opt.* **2018**, *23*, 1–11, doi:10.1117/1.JBO.23.10.105001.
  52. Dörfer, T.; Bocklitz, T.; Tarcea, N.; Schmitt, M.; Popp, J. Checking and improving calibration of raman spectra using chemometric approaches. *Zeitschrift für Phys. Chemie* **2011**, *225*, 753–764, doi:10.1524/zpch.2011.0077.
  53. Stark, E.W.; Martens, H. Multiplicative signal correction method and apparatus, Pat. No. US005568400A 1990, 1–19.
  54. Pearson, K. Note on Regression and Inheritance in Case of Two Parents. *Proc. R. Soc. London* **1895**, *58*, 240–242.
  55. Barnes, R.J.; Dhanoa, M.S.; Lister, S.J. Correction to the Description of Standard Normal Variate (SNV) and De-Trend (DT) Transformations in Practical Spectroscopy with Applications in Food and Beverage Analysis—2 nd Edition. *J. Near Infrared Spectrosc.* **1993**, *1*, 185–186, doi:10.1255/nirn.248.
  56. Barnes, R.J.; Dhanoa, M.S.; Lister, S.J. Standard normal variate transformation and de-trending of near-infrared diffuse reflectance spectra. *Appl. Spectrosc.* **1989**, *43*, 772–777,

- doi:10.1366/0003702894202201.
57. Bonnier, F.; Byrne, H.J. Understanding the molecular information contained in principal component analysis of vibrational spectra of biological systems. *Analyst* **2012**, *137*, 322–332, doi:10.1039/c1an15821j.
  58. Abdi, H.; Williams, L.J. Principal component analysis. *Wiley Interdiscip. Rev. Comput. Stat.* **2010**, *2*, 433–459, doi:10.1002/wics.101.
  59. Jolliffe, I.T. *Principal Component Analysis*; Springer Series in Statistics; 2nd ed.; Springer-Verlag: New York, 2002; ISBN 0-387-95442-2.
  60. Revelle, W. Hierarchical cluster analysis and the internal structure of tests. *Multivariate Behav. Res.* **1979**, *14*, 57–74, doi:10.1207/s15327906mbr1401\_4.
  61. Bonifacio, A.; Beleites, C.; Sergo, V. Application of R-mode analysis to Raman maps: a different way of looking at vibrational hyperspectral data. *Anal. Bioanal. Chem.* **2015**, *407*, 1089–1095, doi:10.1007/s00216-014-8321-7.
  62. MacQueen, J. SOME METHODS FOR CLASSIFICATION AND ANALYSIS OF MULTIVARIATE OBSERVATIONS. In Proceedings of the 5th Berkeley Symposium on Mathematical Statistics and Probability; 1. University of California Press, 1967; pp. 281–297.
  63. Guo, S.; Bocklitz, T.; Neugebauer, U.; Popp, J. Common mistakes in cross-validating classification models. *Anal. Methods* **2017**, *9*, 4410–4417, doi:10.1039/c7ay01363a.
  64. McLachlan, G.J. *Discriminant Analysis and Statistical Pattern Recognition*; Wiley Series in Probability and Statistics; John Wiley & Sons, Inc.: Hoboken, NJ, USA, 1992; ISBN 9780471725299.
  65. Fisher, R.A. THE USE OF MULTIPLE MEASUREMENTS IN TAXONOMIC PROBLEMS. *Ann. Eugen.* **1936**, *7*, 179–188, doi:10.1111/j.1469-1809.1936.tb02137.x.
  66. Cortes, C.; Vapnik, V. Support-vector networks. *Mach. Learn.* **1995**, *20*, 273–297, doi:10.1007/BF00994018.
  67. Wold, S.; Sjöström, M. SIMCA: A Method for Analyzing Chemical Data in Terms of Similarity and Analogy. In; 1977; pp. 243–282.
  68. Bottiroli, G.; Croce, A.C.; Locatelli, D.; Marchesini, R.; Pignoli, E.; Tomatis, S.; Cuzzoni, C.; Di Palma, S.; Dalfante, M.; Spinelli, P. Natural fluorescence of normal and neoplastic human colon: A comprehensive “ex vivo” study. *Lasers Surg. Med.* **1995**, *16*, 48–60, doi:10.1002/lsm.1900160107.
  69. Zięba-Palus, J.; Michalska, A. Photobleaching as a useful technique in reducing of fluorescence in Raman spectra of blue automobile paint samples. *Vib. Spectrosc.* **2014**, *74*, 6–12, doi:10.1016/j.vibspec.2014.06.007.
  70. Yakubovskaya, E.; Zaliznyak, T.; Martínez Martínez, J.; Taylor, G.T. Tear Down the Fluorescent Curtain: A New Fluorescence Suppression Method for Raman Microspectroscopic Analyses. *Sci. Rep.* **2019**, *9*, 1–9, doi:10.1038/s41598-019-52321-3.
  71. Shreve, A.P.; Cherepy, N.J.; Franzen, S.; Boxer, S.G.; Mathies, R.A. Rapid-flow resonance Raman spectroscopy of bacterial photosynthetic reaction centers. *Proc. Natl. Acad. Sci. U. S. A.* **1991**, *88*, 11207–11211, doi:10.1073/pnas.88.24.11207.
  72. Cherepy, N.J.; Shreve, A.P.; Moore, L.J.; Franzen, S.; Boxer, S.G.; Mathies, R.A. Near-infrared resonance Raman spectroscopy of the special pair and the accessory bacteriochlorophylls in photosynthetic reaction centers. *J. Phys. Chem.* **1994**, *98*, 6023–6029, doi:10.1021/j100074a032.
  73. Cherepy, N.J.; Holzwarth, A.R.; Mathies, R.A. Near-Infrared Resonance Raman Spectra of Chloroflexus Aurantiacus Photosynthetic Reaction Centers. *Biochemistry* **1995**, *34*, 5288–5293, doi:10.1021/bi00015a044.
  74. Cherepy, N.J.; Du, M.; Holzwarth, A.R.; Mathies, R.A. Near-infrared resonance Raman spectra of chlorosomes: Probing nuclear coupling in electronic energy transfer. *J. Phys. Chem.* **1996**, *100*, 4662–4671, doi:10.1021/jp952992e.
  75. Cherepy, N.J.; Shreve, A.P.; Moore, L.J.; Boxer, S.G.; Mathies, R.A. Electronic and nuclear dynamics of the accessory bacteriochlorophylls in bacterial photosynthetic reaction centers from resonance Raman intensities. *J. Phys. Chem. B* **1997**, *101*, 3250–3260, doi:10.1021/jp963051k.
  76. Bell, S.E.J.J.; Bourguignon, E.S.O.O.; Dennis, A. Analysis of luminescent samples using

- subtracted shifted Raman spectroscopy. *Analyst* **1998**, *123*, 1729–1734, doi:10.1039/a802802h.
77. Mosier-Boss, P.A.; Lieberman, S.H.; Newbery, R. Fluorescence Rejection in Raman Spectroscopy by Shifted-Spectra, Edge Detection, and FFT Filtering Techniques. *Appl. Spectrosc.* **1995**, *49*, 630–638, doi:10.1366/0003702953964039.
78. Kiefer, J. Instantaneous shifted-excitation Raman difference spectroscopy (iSERDS). *J. Raman Spectrosc.* **2014**, *45*, 980–983, doi:10.1002/jrs.4566.
79. Maiwald, M.; Schmidt, H.; Sumpf, B.; Güther, R.; Erbert, G.; Kronfeldt, H.-D.; Tränkle, G. Microsystem Light Source at 488 nm for Shifted Excitation Resonance Raman Difference Spectroscopy. *Appl. Spectrosc.* **2009**, *63*, 1283–1287, doi:10.1366/000370209789806803.
80. Maiwald, M.; Schmidt, H.; Sumpf, B.; Erbert, G.; Kronfeldt, H.-D.; Tränkle, G. Microsystem 671 nm light source for shifted excitation Raman difference spectroscopy. *Appl. Opt.* **2009**, *48*, 2789–2792, doi:10.1364/ao.48.002789.
81. Martins, M.A. da S.; Ribeiro, D.G.; Pereira dos Santos, E.A.; Martin, A.A.; Fontes, A.; Martinho, H. da S. Shifted-excitation Raman difference spectroscopy for in vitro and in vivo biological samples analysis. *Biomed. Opt. Express* **2010**, *1*, 617–626, doi:10.1364/BOE.1.000617.
82. Maiwald, M.; Müller, A.; Sumpf, B.; Tränkle, G. A portable shifted excitation Raman difference spectroscopy system: device and field demonstration. *J. Raman Spectrosc.* **2016**, *47*, 1180–1184, doi:10.1002/jrs.4953.
83. Sowoidnich, K.; Kronfeldt, H.-D. In-situ species authentication of frozen-thawed meat and meat juice using shifted excitation Raman difference spectroscopy. In Proceedings of the Biophotonics: Photonic Solutions for Better Health Care VI; Popp, J., Tuchin, V. V., Pavone, F.S., Eds.; SPIE, 2018; pp. 1–12.
84. Han, Z.; Strycker, B.D.; Commer, B.; Wang, K.; Shaw, B.D.; Scully, M.O.; Sokolov, A. V. Molecular origin of the Raman signal from *Aspergillus nidulans* conidia and observation of fluorescence vibrational structure at room temperature. *Sci. Rep.* **2020**, *10*, 5428: 1–8, doi:10.1038/s41598-020-62112-w.
85. Baraga, J.J.; Feld, M.S.; Rava, R.P. Rapid Near-Infrared Raman Spectroscopy of Human Tissue with a Spectrograph and CCD Detector. *Appl. Spectrosc.* **1992**, *46*, 187–190, doi:10.1366/0003702924125555.
86. Gebrekidan, M.T.; Erber, R.; Hartmann, A.; Fasching, P.A.; Emons, J.; Beckmann, M.W.; Braeuer, A. Breast Tumor Analysis Using Shifted-Excitation Raman Difference Spectroscopy (SERDS). *Technol. Cancer Res. Treat.* **2018**, *17*, 153303381878253, doi:10.1177/1533033818782532.
87. Strobbia, P.; Odion, R.A.; Maiwald, M.; Sumpf, B.; Vo-Dinh, T. Direct SERDS sensing of molecular biomarkers in plants under field conditions. *Anal. Bioanal. Chem.* **2020**, *412*, 3457–3466, doi:10.1007/s00216-020-02544-5.
88. Glazebrook, K.; Bland-Hawthorn, J. Microslit Nod-Shuffle Spectroscopy: A Technique for Achieving Very High Densities of Spectra. *Publ. Astron. Soc. Pacific* **2002**, *113*, 197–214, doi:10.1086/318625.
89. Roth, M.M.; Cardiel, N.; Cenarro, J.; Schönberner, D.; Steffen, M. Nod & Shuffle 3D Spectroscopy. In *Scientific detectors for astronomy 2005*; BELETIC, J.E., BELETIC, J.W., AMICO, P., Eds.; Springer Netherlands, 2005; pp. 99–108.
90. Roth, M.M.; Fechner, T.; Wolter, D.; Kelz, A.; Becker, T. Ultra-Deep Optical Spectroscopy with PMAS. Using the Nod-and-Shuffle Technique. *Exp. Astron.* **2002**, *14*, 99–105, doi:10.1023/B:EXPA.0000004352.56068.a8.
91. Stillman, E.C.; Flenley, J.R. The needs and prospects for automation in palynology. *Quat. Sci. Rev.* **1996**, *15*, 1–5, doi:10.1016/0277-3791(95)00076-3.
92. Zimmermann, B.; Kohler, A. Infrared spectroscopy of pollen identifies plant species and genus as well as environmental conditions. *PLoS One* **2014**, *9*, 1–12, doi:10.1371/journal.pone.0095417.
93. *Pollen and Pollination*; Dafni, A., Hesse, M., Pacini, E., Eds.; Springer Vienna: Vienna, 2000; ISBN 978-3-7091-7248-3.
94. Bjerg, A.; Ekerljung, L.; Eriksson, J.; Näslund, J.; Sjölander, S.; Rönmark, E.; Dahl, Holmberg, K.; Wennergren, G.; Torén, K.; et al. Increase in pollen sensitization in Swedish adults and protective

- effect of keeping animals in childhood. *Clin. Exp. Allergy* **2016**, *46*, 1328–1336, doi:10.1111/cea.12757.
95. Bergmann, K.-C.; Heinrich, J.; Niemann, H. Current status of allergy prevalence in Germany. *Allergo J. Int.* **2016**, *25*, 6–10, doi:10.1007/s40629-016-0092-6.
96. Ivleva, N.P.; Niessner, R.; Panne, U. Characterization and discrimination of pollen by Raman microscopy. *Anal. Bioanal. Chem.* **2005**, *381*, 261–267, doi:10.1007/s00216-004-2942-1.
97. Werchan, M.; Werchan, B.; Bergmann, K.-C. German pollen calendar 4.0: update of the regional pollen calendars 4.0 with measurement data for the period 2011–2016. *Allergo J. Int.* **2019**, *28*, 160–162, doi:10.1007/s40629-019-0095-1.
98. Bağcıoğlu, M.; Zimmermann, B.; Kohler, A. A multiscale vibrational spectroscopic approach for identification and biochemical characterization of pollen. *PLoS One* **2015**, *10*, 1–19, doi:10.1371/journal.pone.0137899.
99. Holt, K.A.; Bennett, K.D. Principles and methods for automated palynology. *New Phytol.* **2014**, *203*, 735–742, doi:10.1111/nph.12848.
100. Holt, K.; Allen, G.; Hodgson, R.; Marsland, S.; Flenley, J. Progress towards an automated trainable pollen location and classifier system for use in the palynology laboratory. *Rev. Palaeobot. Palynol.* **2011**, *167*, 175–183, doi:10.1016/j.revpalbo.2011.08.006.
101. LI, P.; Treloar, W.J.; Flenley, J.R.; Empson, L. Towards automation of palynology 2: the use of texture measures and neural network analysis for automated identification of optical images of pollen grains. *J. Quat. Sci.* **2004**, *19*, 755–762, doi:10.1002/jqs.874.
102. Ticay-Rivas, J.R.; del Pozo-Baños, M.; Travieso, C.M.; Arroyo-Hernández, J.; Pérez, S.T.; Alonso, J.B.; Mora-Mora, F. Pollen Classification Based on Geometrical, Descriptors and Colour Features Using Decorrelation Stretching Method. In Proceedings of the IFIP Advances in Information and Communication Technology; Springer Berlin Heidelberg: Berlin / Heidelberg, Germany, 2011; pp. 342–349.
103. Koutsoukos, I. Automated Classification of Pollen Grains from Microscope Images using Computer Vision and Semantic Web Technologies, Technical University of Crete, 2013.
104. Kleiber, A.; Ramoji, A.; Mayer, G.; Neugebauer, U.; Popp, J.; Henkel, T. 3-Step flow focusing enables multidirectional imaging of bioparticles for imaging flow cytometry. *Lab Chip* **2020**, *20*, 1676–1686, doi:10.1039/D0LC00244E.
105. Vega, G.L.; Benezeth, Y.; Uhler, M.; Boochs, F.; Marzani, F. Sketch of an automatic image based pollen detection system. In Proceedings of the 32. Wissenschaftlich-Technische Jahrestagung der DGPF; DGPF Tagungsband 21; Potsdam, Germany, 2012; pp. 202–209.
106. Haas, N.Q. Automated Pollen Image Classification, University of Tennessee, Knoxville, 2011.
107. Mularczyk-Oliwa, M.; Bombalska, A.; Kaliszewski, M.; Włodarski, M.; Koczyński, K.; Kwaśny, M.; Szpakowska, M.; Trafny, E.A. Comparison of fluorescence spectroscopy and FTIR in differentiation of plant pollens. *Spectrochim. Acta - Part A Mol. Biomol. Spectrosc.* **2012**, *97*, 246–254, doi:10.1016/j.saa.2012.05.063.
108. Yeloff, D.; Hunt, C. Fluorescence microscopy of pollen and spores: a tool for investigating environmental change. *Rev. Palaeobot. Palynol.* **2005**, *133*, 203–219, doi:10.1016/j.revpalbo.2004.10.002.
109. Urbanczyk, J.; Fernandez Casado, M.A.; Díaz, T.E.; Heras, P.; Infante, M.; Borrego, A.G. Spectral fluorescence variation of pollen and spores from recent peat-forming plants. *Int. J. Coal Geol.* **2015**, *139*, 206–216, doi:10.1016/j.coal.2014.10.011.
110. Pappas, C.S.; Tarantilis, P.A.; Harizanis, P.C.; Polissiou, M.G. New method for pollen identification by FT-IR spectroscopy. *Appl. Spectrosc.* **2003**, *57*, 23–27, doi:10.1366/000370203321165160.
111. Dell’Anna, R.; Lazzeri, P.; Frisanco, M.; Monti, F.; Malvezzi Campeggi, F.; Gottardini, E.; Bersani, M. Pollen discrimination and classification by Fourier transform infrared (FT-IR) microspectroscopy and machine learning. *Anal. Bioanal. Chem.* **2009**, *394*, 1443–1452, doi:10.1007/s00216-009-2794-9.
112. Gottardini, E.; Rossi, S.; Cristofolini, F.; Benedetti, L. Use of Fourier transform infrared (FT-IR)

- spectroscopy as a tool for pollen identification. *Aerobiologia (Bologna)*. **2007**, *23*, 211–219, doi:10.1007/s10453-007-9065-z.
113. Zimmermann, B. Characterization of pollen by vibrational spectroscopy. *Appl. Spectrosc.* **2010**, *64*, 1364–1373, doi:10.1366/000370210793561664.
114. Pummer, B.G.; Bauer, H.; Bernardi, J.; Chazallon, B.; Facq, S.; Lendl, B.; Whitmore, K.; Grothe, H. Chemistry and morphology of dried-up pollen suspension residues. *J. Raman Spectrosc.* **2013**, *44*, 1654–1658, doi:10.1002/jrs.4395.
115. Guedes, A.; Ribeiro, H.; Fernández-González, M.; Aira, M.J.; Abreu, I. Pollen Raman spectra database: Application to the identification of airborne pollen. *Talanta* **2014**, *119*, 473–478, doi:10.1016/j.talanta.2013.11.046.
116. Schulte, F.; Mäder, J.; Kroh, L.W.; Panne, U.; Kneipp, J. Characterization of pollen carotenoids with in situ and high-performance thin-layer chromatography supported resonant Raman spectroscopy. *Anal. Chem.* **2009**, *81*, 8426–8433, doi:10.1021/ac901389p.
117. Schulte, F.; Lingott, J.; Panne, U.; Kneipp, J. Chemical characterization and classification of pollen. *Anal. Chem.* **2008**, *80*, 9551–9556, doi:10.1021/ac801791a.
118. Schulz, H.; Baranska, M.; Baranski, R. Potential of NIR-FT-Raman spectroscopy in natural carotenoid analysis. *Biopolymers* **2005**, *77*, 212–221, doi:10.1002/bip.20215.
119. Schulte, F.; Panne, U.; Kneipp, J. Molecular changes during pollen germination can be monitored by Raman microspectroscopy. *J. Biophotonics* **2010**, *3*, 542–547, doi:10.1002/jbio.201000031.
120. Seifert, S.; Merk, V.; Kneipp, J. Identification of aqueous pollen extracts using surface enhanced Raman scattering (SERS) and pattern recognition methods. *J. Biophotonics* **2016**, *9*, 181–189, doi:10.1002/jbio.201500176.
121. Laucks, M.L.; Roll, G.; Schweiger, G.; Davis, E.J. Physical and chemical (RAMAN) characterization of bioaerosols-pollen. *J. Aerosol Sci.* **2000**, *31*, 307–319, doi:10.1016/S0021-8502(99)00058-0.
122. Sengupta, A.; Laucks, M.L.; James Davis, E. Surface-enhanced Raman spectroscopy of bacteria and pollen. *Appl. Spectrosc.* **2005**, *59*, 1016–1023, doi:10.1366/0003702054615124.
123. Boyain-Goitia, A.R.; Beddows, D.C.S.; Griffiths, B.C.; Telle, H.H. Single-pollen analysis by laser-induced breakdown spectroscopy and Raman microscopy. *Appl. Opt.* **2003**, *42*, 6119–6132, doi:10.1364/AO.42.006119.
124. Mondol; Patel; Rüger; Stiebing; Kleiber; Henkel; Popp; Schie Application of High-Throughput Screening Raman Spectroscopy (HTS-RS) for Label-Free Identification and Molecular Characterization of Pollen. *Sensors* **2019**, *19*, 4428: 1–16, doi:10.3390/s19204428.
125. Samuels, A.C.; DeLucia, F.C.; McNesby, K.L.; Miziolek, A.W. Laser-induced breakdown spectroscopy of bacterial spores, molds, pollens, and protein: initial studies of discrimination potential. *Appl. Opt.* **2003**, *42*, 6205, doi:10.1364/ao.42.006205.
126. Dössel, O. *Bildgebende Verfahren in der Medizin - Von der Technik zur medizinischen Anwendung*; 2nd ed.; Springer Berlin Heidelberg: Berlin / Heidelberg, Germany, 2016; ISBN 978-3-642-54406-4.
127. *Bildgebende Systeme für die medizinische Diagnostik*; Morneburg, H., Ed.; 3rd ed.; Publicis-MCD-Verlag: München, Germany, 1995;
128. Krafft, C. Modern trends in biophotonics for clinical diagnosis and therapy to solve unmet clinical needs. *J. Biophotonics* **2016**, *9*, 1362–1375, doi:10.1002/jbio.201600290.
129. Krafft, C.; von Eggeling, F.; Guntinas-Lichius, O.; Hartmann, A.; Waldner, M.J.; Neurath, M.F.; Popp, J. Perspectives, potentials and trends of ex vivo and in vivo optical molecular pathology. *J. Biophotonics* **2018**, *11*, e201700236: 1–6, doi:10.1002/jbio.201700236.
130. Krafft, C.; Sergo, V. Biomedical applications of Raman and infrared spectroscopy to diagnose tissues. *Spectroscopy* **2006**, *20*, 195–218, doi:10.1155/2006/738186.
131. Manoharan, R.; Wang, Y.; Feld, M.S. Histochemical analysis of biological tissues using Raman spectroscopy. *Spectrochim. Acta Part A Mol. Biomol. Spectrosc.* **1996**, *52*, 215–249, doi:10.1016/0584-8539(95)01573-6.
132. Talari, A.C.S.; Movasaghi, Z.; Rehman, S.; Rehman, I. ur Raman Spectroscopy of Biological

- Tissues. *Appl. Spectrosc. Rev.* **2015**, *50*, 46–111, doi:10.1080/05704928.2014.923902.
133. Lasch, P.; Chiriboga, L.; Yee, H.; Diem, M. Infrared Spectroscopy of Human Cells and Tissue: Detection of Disease. *Technol. Cancer Res. Treat.* **2002**, *1*, 1–7, doi:10.1177/153303460200100101.
134. Jermyn, M.; Mercier, J.; Aubertin, K.; Desroches, J.; Urme, K.; Karamchandiani, J.; Marple, E.; Guiot, M.C.; Leblond, F.; Petrecca, K. Highly accurate detection of cancer in situ with intraoperative, label-free, multimodal optical spectroscopy. *Cancer Res.* **2017**, *77*, 3942–3950, doi:10.1158/0008-5472.CAN-17-0668.
135. Kong, K.; Kendall, C.; Stone, N.; Notingher, I. Raman spectroscopy for medical diagnostics — From in-vitro biofluid assays to in-vivo cancer detection. *Adv. Drug Deliv. Rev.* **2015**, *89*, 121–134, doi:10.1016/j.addr.2015.03.009.
136. Caspers, P.J.; Lucassen, G.W.; Puppels, G.J. Combined In Vivo Confocal Raman Spectroscopy and Confocal Microscopy of Human Skin. *Biophys. J.* **2003**, *85*, 572–580, doi:10.1016/S0006-3495(03)74501-9.
137. Krafft, C.; Dochow, S.; Latka, I.; Dietzek, B.; Popp, J. Diagnosis and screening of cancer tissues by fiber-optic probe Raman spectroscopy. *Biomed. Spectrosc. Imaging* **2012**, *1*, 39–55, doi:10.3233/BSI-2012-0004.
138. Rygula, A.; Majzner, K.; Marzec, K.M.; Kaczor, A.; Pilarczyk, M.; Baranska, M. Raman spectroscopy of proteins: A review. *J. Raman Spectrosc.* **2013**, *44*, 1061–1076, doi:10.1002/jrs.4335.
139. Czamara, K.; Majzner, K.; Pacia, M.Z.; Kochan, K.; Kaczor, A.; Baranska, M. Raman spectroscopy of lipids: A review. *J. Raman Spectrosc.* **2015**, *46*, 4–20, doi:10.1002/jrs.4607.
140. Koltzenburg, S.; Maskos, M.; Nuyken, O. *Polymere: Synthese, Eigenschaften und Anwendungen*; Springer Berlin Heidelberg: Berlin / Heidelberg, Germany, 2014; ISBN 978-3-642-34772-6.
141. Britannica, E. of E. Polymethyl methacrylate Available online: <https://www.britannica.com/science/polymethyl-methacrylate> (accessed on Oct 9, 2020).
142. Ali, U.; Karim, K.J.B.A.; Buang, N.A. A Review of the Properties and Applications of Poly (Methyl Methacrylate) (PMMA). *Polym. Rev.* **2015**, *55*, 678–705, doi:10.1080/15583724.2015.1031377.
143. Gray, J.E. *Polystyrene: Properties, performance and applications*; Nova Science Publishers, 2011;
144. Wünsch, J.R. *Polystyrene - Synthesis, Production and Applications*; Dolbey, R., Ed.; Rapra Technology Ltd., 2000;
145. Britannica, E. of E. Polystyrene Available online: <https://www.britannica.com/science/polystyrene> (accessed on Oct 9, 2020).
146. Palm, A. Raman spectrum of polystyrene. *J. Phys. Colloid Chem.* **1951**, *55*, 1320–1324, doi:10.1021/j150491a005.
147. Willis, H.A.; Zichy, V.J.I.; Hendra, P.J. The laser-Raman and infra-red spectra of poly(methyl methacrylate). *Polymer (Guildf)*. **1969**, *10*, 737–746, doi:10.1016/0032-3861(69)90101-3.
148. Jermyn, M.; Mok, K.; Mercier, J.; Desroches, J.; Pichette, J.; Saint-Arnaud, K.; Bernstein, L.; Guiot, M.-C.; Petrecca, K.; Leblond, F. Intraoperative brain cancer detection with Raman spectroscopy in humans. *Sci. Transl. Med.* **2015**, *7*, 274ra19: 1–9, doi:10.1126/scitranslmed.aaa2384.
149. McCain, S.T.; Willett, R.M.; Brady, D.J. Multi-excitation Raman spectroscopy technique for fluorescence rejection. *Opt. Express* **2008**, *16*, 10975–10991, doi:10.1364/OE.16.010975.
150. Schie, I.W.; Rüger, J.; Mondol, A.S.; Ramoji, A.; Neugebauer, U.; Krafft, C.; Popp, J. High-Throughput Screening Raman Spectroscopy Platform for Label-Free Cellomics. *Anal. Chem.* **2018**, *90*, 2023–2030, doi:10.1021/acs.analchem.7b04127.
151. Beleites, C. Raman-spektroskopische Diagnostik von primären Hirntumoren mit Hilfe weicher chemometrischer Klassifikationsmethoden, Friedrich-Schiller-Universität, 2014.
152. Bacon, R.; Monnet, G. Recent Trends in Integral Field Spectroscopy. In *Optical 3D-Spectroscopy for Astronomy*; Wiley-VCH Verlag GmbH & Co. KGaA: Weinheim, Germany, 2017; pp. 115–128.



153. Moralejo, B.; Roth, M.M.; Godefroy, P.; Fechner, T.; Bauer, S.M.; Schmäzlin, E.; Kelz, A.; Haynes, R. The Potsdam MRS spectrograph: heritage of MUSE and the impact of cross-innovation in the process of technology transfer. In Proceedings of the Advances in Optical and Mechanical Technologies for Telescopes and Instrumentation II; Navarro, R., Burge, J.H., Eds.; 2016; Vol. 9912, pp. 991222: 1–13.
154. Moralejo, B.; Schmäzlin, E.; Bodenmüller, D.; Fechner, T.; Roth, M.M. Improving the frame rates of Raman image sequences recorded with integral field spectroscopy using windowing and binning methods. *J. Raman Spectrosc.* **2018**, *49*, 372–375, doi:10.1002/jrs.5268.
155. Sowoidnich, K.; Towrie, M.; Maiwald, M.; Sumpf, B.; Matousek, P. Shifted Excitation Raman Difference Spectroscopy with Charge-Shifting Charge-Coupled Device (CCD) Lock-In Detection. *Appl. Spectrosc.* **2019**, *73*, 1265–1276, doi:10.1177/0003702819859352.
156. Dochow, S.; Bergner, N.; Matthäus, C.; Praveen, B.B.; Ashok, P.C.; Mazilu, M.; Krafft, C.; Dholakia, K.; Popp, J. Etaloning, fluorescence and ambient light suppression by modulated wavelength Raman spectroscopy. *Biomed. Spectrosc. Imaging* **2012**, *1*, 383–389, doi:10.3233/BSI-120031.
157. Sumpf, B.; Müller, A.; Maiwald, M. Tailored diode lasers: enabling Raman spectroscopy in the presence of disturbing fluorescence and background light. In Proceedings of the Plasmonics in Biology and Medicine XVI; Vo-Dinh, T., Ho, H.-P.A., Ray, K., Eds.; SPIE, 2019; Vol. 1089411, pp. 1089411: 1–8.

## 6. Publikationen

Die folgenden Publikationsnachdrucke wurden für die vorliegende Dissertation berücksichtigt.

[FK1] Evaluation of Shifted Excitation Raman Difference Spectroscopy and Comparison to Computational Background Correction Methods Applied to Biochemical Raman Spectra

Eliana Cordero\*, Florian Korinth\*, Clara Stiebing, Christoph Krafft, Iwan W. Schie, Jürgen Popp (2017)  
*Sensors*, **17**: 1724, 1 – 17.

[FK2] New methodology to process shifted excitation Raman difference spectroscopy data: a case study of pollen classification

Florian Korinth, Abdullah S. Mondol, Clara Stiebing, Iwan W. Schie, Christoph Krafft, Jürgen Popp (2020)  
*Scientific Reports*, **10**(1): 11215, 1 – 12.

[FK3] Wide Field Spectral Imaging with Shifted Excitation Raman Difference Spectroscopy Using the Nod and Shuffle Technique

Florian Korinth, Elmar Schmälzlin, Clara Stiebing, Tanya Urrutia, Genoveva Micheva, Christer Sandin, André Müller, Martin Maiwald, Bernd Sumpf, Christoph Krafft, Martin M. Roth, Jürgen Popp (2020)  
*Sensors*, **20**: 6723, 1 – 19.

\* geteilte Erstautorenschaft

## [Sensors] Manuscript ID: sensors-974262 - Accepted for Publication

aleksic@mdpi.com im Auftrag von Sensors Editorial Office <sensors@mdpi.com>

Do 19.11.2020 13:55

An: Krafft, Christoph // Leibniz-IPHT <christoph.krafft@leibniz-ipht.de>;

Cc: Korinth, Florian // Leibniz-IPHT <florian.korinth@leibniz-ipht.de>; Elmar Schmäzlin <eschmaezlin@aip.de>; Stiebing, Clara // Leibniz-IPHT <clara.stiebing@leibniz-ipht.de>; Tanya Urrutia <turrutia@aip.de>; Genoveva Micheva <gmicheva@aip.de>; Christer Sandin <chistersandin@yahoo.se>; André Müller <andre.mueller@fbh-berlin.de>; Martin Maiwald <martin.maiwald@fbh-Berlin.de>; Bernd Sumpf <bernd.sumpf@fbh-berlin.de>; Günther Tränkle <guenther.traenkle@fbh-berlin.de>; Martin M. Roth <mmroth@aip.de>; Juergen, Popp // Leibniz-IPHT <juergen.popp@ipht-jena.de>; Sensors Editorial Office <sensors@mdpi.com>;

Dear Dr. Krafft,

We are writing to you concerning the below referenced manuscript which you submitted to the Sensors. Based on the completed set of reviews, the manuscript has been accepted in its present format.

Manuscript ID: sensors-974262

Type of manuscript: Article

Title: Wide Field Spectral Imaging with Shifted Excitation Raman Difference Spectroscopy Using the Nod and Shuffle Technique

Authors: Florian Korinth, Elmar Schmäzlin, Clara Stiebing, Tanya Urrutia, Genoveva Micheva, Christer Sandin, André Müller, Martin Maiwald, Bernd Sumpf, Christoph Krafft \*, Günther Tränkle, Martin M. Roth, Jürgen Popp

Received: 6 October 2020

E-mails: florian.korinth@leibniz-ipht.de, eschmaezlin@aip.de, clara.stiebing@leibniz-ipht.de, turrutia@aip.de, gmicheva@aip.de, chistersandin@yahoo.se, andre.mueller@fbh-berlin.de, martin.maiwald@fbh-Berlin.de, bernd.sumpf@fbh-berlin.de, christoph.krafft@leibniz-ipht.de, guenther.traenkle@fbh-berlin.de, mmroth@aip.de, juergen.popp@leibniz-ipht.de

Submitted to section: Sensing and Imaging,

[https://www.mdpi.com/journal/sensors/sections/sensing\\_imaging](https://www.mdpi.com/journal/sensors/sections/sensing_imaging)

Advances in Spectroscopy and Spectral Imaging

[https://www.mdpi.com/journal/sensors/special\\_issues/Spectroscopy\\_Spectral\\_Imaging](https://www.mdpi.com/journal/sensors/special_issues/Spectroscopy_Spectral_Imaging)

[https://susy.mdpi.com/user/manuscripts/review\\_info/527d5b32548446d471f51e8a1612d51e](https://susy.mdpi.com/user/manuscripts/review_info/527d5b32548446d471f51e8a1612d51e)

We will now edit and finalize your paper which will then be returned to you for your approval. In order to shorten the processing time, it is important for the authors to respond to the Production Staff in proofing stage within 48 hours of receiving the proof.

Congratulations on the acceptance of your manuscript, and thanks again for your interest in submitting your work to Sensors.

We encourage you to set up your profile at SciProfiles.com, MDPI's researcher network platform. Articles you publish with MDPI will be linked to your SciProfiles page, where colleagues and peers will be able to see all of your publications, citations, as well as your other academic contributions

We also invite you to contribute to Encyclopedia (<https://encyclopedia.pub>), a scholarly platform providing accurate information about the latest research results. You can adapt parts of your paper to provide valuable reference information for others in the field.

## Publikationen

---

If you have any questions, please contact MDPI Sensors Publication Office at [sensors@mdpi.com](mailto:sensors@mdpi.com).

Mr. Vladimir Aleksic  
Assistant Editor  
MDPI  
[sensors@mdpi.com](mailto:sensors@mdpi.com) Editorial Office

MDPI Belgrade Office  
Veljka Dugoševića 54  
11060 Belgrade  
Serbia  
Tel. +381 11 414 75 49

Sensors Editorial Office  
[sensors@mdpi.com](mailto:sensors@mdpi.com)  
<https://www.mdpi.com/journal/sensors>  
Sensors Impact Factor 2019: 3.275

20th Anniversary of Sensors: A series of special content and events at  
<https://www.mdpi.com/journal/sensors/anniversary>.

7th International Electronic Conference on Sensors and Applications (ECSA-7)  
Abstract Submission Deadline: 10 September 2020  
No fees for participation  
<https://ecsa-7.sciforum.net/>

Sensors 2021 Academic Conference Grants (2,500 CHF)  
Open for Application: [www.mdpi.com/journal/sensors/awards/1059](http://www.mdpi.com/journal/sensors/awards/1059)

Open Access Week 2020! Join our webinar on Preprints and other MDPI initiatives on Thursday, 22nd October 2020. Register here:  
<https://oaweek.sciforum.net/>

Disclaimer: The information and files contained in this message are confidential and intended solely for the use of the individual or entity to whom they are addressed. If you have received this message in error, please notify me and delete this message from your system. You may not copy this message in its entirety or in part, or disclose its contents to anyone.

**6.1. Evaluation of Shifted Excitation Raman Difference Spectroscopy and Comparison to Computational Background Correction Methods Applied to Biochemical Raman Spectra [FK1]**

Eliana Cordero\*, Florian Korinth\*, Clara Stiebing, Christoph Krafft, Iwan W. Schie, Jürgen Popp (2017)

*Sensors*, **17**: 1724, 1 – 17.

\* geteilte Erstautorenschaft

Der Nachdruck der folgenden Publikation, welche unter einer internationalen Creative Commons Attribution 4.0-Lizenz steht (<http://creativecommons.org/licenses/by/4.0/>), erscheint mit freundlicher Genehmigung von MDPI.

**Erklärung zu den Eigenanteilen des Promovenden sowie der weiteren Doktoranden/ Doktorandinnen als Koautoren an den Publikationen und Zweitpublikationsrechten bei einer kumulativen Dissertation.**

Doktoranden	Florian Korinth	Eliana Cordero
Konzeption des Forschungsansatzes	x	x
Planung der Untersuchungen	x	x
Datenerhebung	x	x
Datenanalyse und –interpretation	x	x
Theoretischer Teil		x
Experimenteller Teil	x	
Schreiben des Manuskripts	x	x
Vorschlag Anrechnung Publikationsäquivalente	1,0	

Article

# Evaluation of Shifted Excitation Raman Difference Spectroscopy and Comparison to Computational Background Correction Methods Applied to Biochemical Raman Spectra

Eliana Cordero <sup>1,†</sup>, Florian Korinth <sup>1,†</sup>, Clara Stiebing <sup>1</sup>, Christoph Krafft <sup>1</sup>, Iwan W. Schie <sup>1,\*</sup> and Jürgen Popp <sup>1,2</sup>

<sup>1</sup> Leibniz Institute of Photonic Technology (IPHT), Albert-Einstein-Straße 9, Jena 07743, Germany; eliana.cordero@leibniz-ipht.de (E.C.); florian.korinth@leibniz-ipht.de (F.K.); clara.stiebing@leibniz-ipht.de (C.S.); christoph.krafft@ipht-jena.de (C.K.); juergen.popp@leibniz-ipht.de (J.P.)

<sup>2</sup> Institute of Physical Chemistry and Abbe Center of Photonics, Friedrich Schiller University Jena, Helmholtzweg 4, Jena 07743, Germany

\* Correspondence: iwan.schie@leibniz-ipht.de

† These authors contributed equally to this work.

Received: 26 June 2017; Accepted: 20 July 2017; Published: 27 July 2017

**Abstract:** Raman spectroscopy provides label-free biochemical information from tissue samples without complicated sample preparation. The clinical capability of Raman spectroscopy has been demonstrated in a wide range of in vitro and in vivo applications. However, a challenge for in vivo applications is the simultaneous excitation of auto-fluorescence in the majority of tissues of interest, such as liver, bladder, brain, and others. Raman bands are then superimposed on a fluorescence background, which can be several orders of magnitude larger than the Raman signal. To eliminate the disturbing fluorescence background, several approaches are available. Among instrumental methods shifted excitation Raman difference spectroscopy (SERDS) has been widely applied and studied. Similarly, computational techniques, for instance extended multiplicative scatter correction (EMSC), have also been employed to remove undesired background contributions. Here, we present a theoretical and experimental evaluation and comparison of fluorescence background removal approaches for Raman spectra based on SERDS and EMSC.

**Keywords:** Raman spectroscopy; SERDS; EMSC; background correction; signal to noise ratio

## 1. Introduction

There is a significant requirement for rapid and minimally to non-invasive tools for cancer diagnosis. The ability to obtain specific biochemical information from biological samples without the need for labeling makes Raman spectroscopy attractive for many diagnostic applications in medicine [1,2]. For instance, Raman spectroscopy has been used to accurately identify and grade transitional cell carcinoma (TCC) in vitro and has shown promising results as an auxiliary method for pathological identification of bladder tissue [3–6]. The development of optical fiber Raman probes with high efficiency and throughput provided the opportunity to perform in vivo measurements of skin, brain, esophagus, and bladder, demonstrating that data acquisition, analysis and diagnostics can be performed at the patient in real time [7–10].

Human tissue is mainly composed of proteins, lipids, nucleic acids, and carbohydrates [11]. One of the main challenges for the implementation of Raman spectroscopy in the clinic is the excitation of auto-fluorescence in tissue. Biological tissues can show significant auto-fluorescence [12], which depends on the excited fluorophores, the excitation wavelength, and is several magnitudes stronger

than the Raman signal, leading to high shot noise. A considerable number of instrumental [13–16] and computational methods have been proposed to reduce or subtract the fluorescence background contribution in Raman spectra [17–20].

Computational methods include, for example, polynomial fitting [21], different least squares methods [22] and extended multiplicative scatter correction (EMSC) [23]. Polynomial fitting approximates the broad fluorescence background as an  $n$ -order polynomial function, fitting the polynomial function to spectral areas without Raman bands. Next to manually deciding which areas should be used, automatic methods for curve fitting in chromatographic analysis have been proposed under high noise circumstances, which is a limiting factor for this method [24]. Least squares methods rely on fitting of linear combinations of reference data to the measured spectra, where the sum of the squared differences between the observed values and the fitted values is minimized [25]. Different least squares approaches have previously been implemented, such as for instance iterative least squares or weighted least squares [26,27]. One very promising framework for model-based background correction in Raman spectroscopy is EMSC [28]. It is also based on a least squares fitting of pre-defined background spectra, but also including the fitting of pure components spectra [23]. Further computational techniques used to separate the fluorescence background from Raman spectra are principal component analysis [29], and wavelets analysis [30]. Wavelets analysis decomposes the spectrum into different frequency components and the background is suppressed by setting the very low frequency components to zero. Furthermore, by setting the high frequency components to zero as well, noise contributions can be removed. However, the transformation of the signal into frequency bands may result in distortion in some spectral areas [19,31].

As a methodical approach photobleaching has been suggested to remove fluorescence. By irradiating the sample with an excitation laser for a long period of time, a photolytic decomposition of the fluorescent interfering molecules is induced [14,15,32]. Another technique that addresses the reduction of the fluorescence background, as well as low signal to noise ratio (SNR) problems, is time-gating Raman spectroscopy. It employs ultra-short laser pulses that drive an all-optical Kerr shutter to gate early-arriving Raman photons, while blocking the later-arriving fluorescence photons. However, the systems are highly complex, costly, and challenging to modify [33]. Modulated excitation wavelength shifting is an instrumental method, where Raman measurements are performed at two closely spaced excitation wavelengths to obtain two shifted Raman spectra. By introducing a low-frequency modulator, a Raman spectrum is reconstructed. The main limitation is the need of lock-in detection [34]. Modulated Raman spectroscopy was introduced with a frequency-modulated excitation laser, continuous acquisition of Raman spectra, and without lock-in detection [35]. A popular instrumental method that has been widely applied is shifted excitation Raman difference spectroscopy (SERDS) [16,36–39]. SERDS is based on the principle that small changes in the excitation wavelength result in a spectral shift of the Raman spectrum, while the fluorescence contribution does not change spectrally. By calculating the difference between closely shifted Raman spectra all wavelength-independent contributions are removed. It was shown that not only fluorescence can be effectively removed by this method, but also ambient light, etaloning, and any other non-varying source [40–42]. Since the positions of the Raman bands are used for the interpretation of Raman spectra, it was previously suggested that the optimal shift in excitation wavelength should correspond to the full width at half maximum of a relevant Raman band [43,44]. Applying this shift results in a difference spectrum where the band position corresponds to the inflection point between the minimum and maximum of the respective band. This assumption is valid for samples, which have spectral bands with similar spectral widths, such as powders or crystalline proteins, and are acquired at very high spectral resolution. Since the Raman bandwidth of specific biological components vary within one spectrum, this theoretical optimal shift for the reconstruction of band positions cannot be applied for complex biological Raman spectra. Moreover, for biomedical applications there is not just one single Raman band, which is important for the differentiation between, e.g., tumor and non-tumor tissues.

Previous studies have evaluated the capability of SERDS to subtract strong fluorescence background exceeding the Raman signal up to a ratio of 200:1 [36,44–48]. A main topic in these studies is the necessary processing of SERDS spectra, using computational methods in order to acquire typical Raman spectra [37,49–51]. However, there are no studies where SERDS is evaluated and compared directly to computational background correction methods.

In this study, theoretical and experimental results for SERDS spectra of biological components, such as lipids and proteins, are evaluated. SNRs are determined based on different fluorescent background estimations. Additionally the concept of an optimal shift for SERDS is discussed theoretically and experimentally. Different algorithms for optimizing the spectral quality of the difference spectra are tested and compared to EMSC as a conventional computational background correction method.

## 2. Materials and Methods

### 2.1. Theoretical Approach

Raman spectra of lipid and protein components of chicken meat with a low fluorescence background were recorded, using a commercial Raman microscope setup (Holoprobe, Kaiser Optical System, Ann Arbor, MI, USA) with an excitation wavelength of 785 nm and an integration time of 1 s, see Figure 1a,b. These spectra were used as a basis for the theoretical analysis on the influence of fluorescent background contributions and noise levels on the recovery of informational content.

Data analysis of the Raman spectra and spectral simulations were performed in R [52], using the packages *hyperSpec*, *Ramancal*, *baseline*, and *pracma* [53–56]. The recorded Raman spectra were wavelength calibrated, during which all spectra were corrected to the same wavenumber axis relative to 785 nm. Furthermore, the spectra were background corrected by using support points determined from a convex hull of the spectrum and smoothed by applying a local polynomial regression fitting. The processed spectra were shifted by multiple wavelength steps between 1 nm and 4 nm to simulate Raman spectra recorded at different excitation wavelengths. The optimal shift was evaluated using the autocorrelation function from the *forecast* package [57,58]. The computational background correction was performed on the measured Raman spectra at 785 nm excitation, using the *emsc* function available in the *cbmodels* package [59]. For the simulations of different auto-fluorescence contributions, fluorescence spectra were measured on the commercial Raman setup and fitted by a polynomial function. The different fluorescence intensity levels were simulated by the multiplication of a constant factor and added to the Raman spectra of lipids and proteins. The noise contribution was estimated by applying a Poisson distribution function on the square root of the intensity, see Figure 1c,d.

SNRs were determined under the shot noise-limited definition [60], where the noise is calculated as the square root of the signal intensity. The SNR was calculated for each pixel of the spectrum, leading to a wavenumber-dependent SNR spectrum. Regions without relevant bands were removed. To determine a single SNR value for each spectrum, the second derivative of the spectrum without noise was calculated and the maxima including surrounding points of a certain wavenumber window were detected. A threshold was used to determine spectral locations to calculate the SNRs of importance, see Figure 1e,f. Those selected SNRs were averaged to obtain a mean SNR for the entire spectrum. The second derivative and smoothing of the preprocessed spectrum were performed by using the polynomial filtering method of Savitzky and Golay [55].

### 2.2. Experimental Approach

Raman measurements were performed using a tunable diode laser DL Pro (Toptica Photonics AG, Gräfelfing, Germany) enabling a tuning range from 765 to 805 nm. To achieve a higher output power the laser was coupled, using a single mode fiber, into a laser amplifier (BoosTA, Toptica Photonics AG). The output laser power at 785 nm after the amplifier was adjusted to 200 mW. The laser power at 785 nm after the objective was 95 mW. No damage to the tissue was observed.



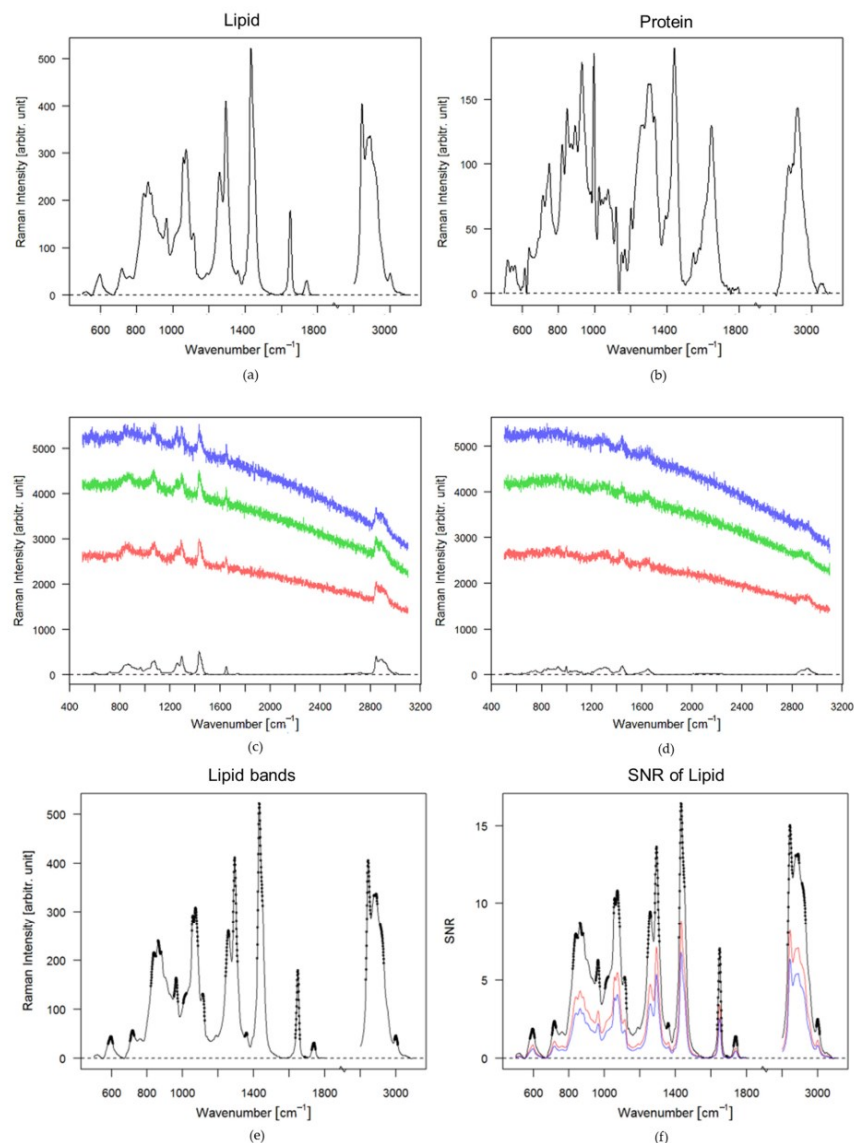


**Figure 1.** Baseline corrected spectra and spectra with simulated fluorescence backgrounds and shot noise levels: (a) Baseline corrected spectrum of lipids; (b) Baseline corrected spectrum of proteins; (c) Lipid spectra with added fluorescence intensities, i.e., 10 (blue), 8 (green) and 5 (red) times the maximal band of the lipid signal, including corresponding noise levels. The black spectrum is the lipid spectrum without fluorescence; (d) Protein spectra with added fluorescence intensities, i.e., 10 (blue), 8 (green) and 5 (red) times the maximal band of the lipid signal, including corresponding noise levels. The black spectrum is the protein spectrum without fluorescence; (e) Spectral bands and windows of the measured lipid spectrum, the black points are the maxima and the windows estimated by the Savitzky and Golay function; (f) SNR of the lipid spectra with fluorescence, the black spectrum is the SNR of the lipid spectrum, the red spectrum correspond to the SNR of the lipid spectrum with fluorescence 5 times the maximal band of the lipid signal, the blue spectrum is the SNR of the lipid spectrum with fluorescence factor 10 of the lipid signal.

Excitation wavelengths between 784 and 786 nm were chosen. Wavelengths below and higher than this range experienced high losses due to filter parameters, resulting in reduced excitation power and lower Raman signals. The laser was guided into a home-built microscope setup with a 40×

magnification, NA = 0.55 objective lens. The setup has been previously described [61]. The sample was placed on a holder, which is mounted on two motorized x-y translational stages (CONEX MFA-Series; Newport, Irvine, CA, USA). To allow a sample translation in z-direction the motorized x-y translational stages were mounted on an automated z-positioning stage (MTS25-Z8, Thorlabs, Newton, NJ, USA). The generated Raman signal was collected by the same objective lens and separated from the excitation light by a dichroic notch filter (785 nm, bandwidth 89 nm; Semrock, Rochester, NY, USA). An additional notch filter (785 nm  $\pm$  19 nm; Laser Components, Olching, Germany) was used for a reliable suppression of the excitation light. An achromatic doublet (100 mm; Thorlabs) focuses the Raman signal onto a multimode fiber (105  $\mu$ m core, Thorlabs). The signal was then fiber-coupled into a spectrometer (IsoPlane160, Princeton Instruments, Acton, MA, USA) that is equipped with a grating with 400 grooves/mm, blazed at 750 nm, and allows a spectral resolution of 9  $\text{cm}^{-1}$ . The signal is dispersed onto a charge-coupled device (CCD) (PIXIS-400BR-eXcelon; Princeton Instruments) with a nominal quantum efficiency of up to 98% at 800 nm. The setup is controlled by in-house written data-acquisition software in LabView (National Instruments, Austin, TX, USA). The data acquisition was designed such that at each spatial location in the sample five Raman spectra at different excitation wavelengths, ranging between 784 nm to 786 nm with an interval of 0.5 nm, were measured consecutively. After all measurements for one spatial location were performed, the next location was measured.

Raman images were acquired of meat samples, providing typical biological spectra of fibrous protein from muscle tissue and tendons, non-fibrous proteins, lipids, and bone. Images were acquired of 10 mm by 10 mm areas with a step size of 0.5 mm, and an integration time of 1 s. Data analyses were performed in R [52]. All spectra were cleared from cosmic spikes [62,63]. To generate background corrected Raman spectra, the spectra measured at 785.0 nm were baseline corrected by EMSC. Seven components, i.e., constant offset, a linear function, and multiple fluorescence functions were used as background estimates; and Raman spectra of collagen, protein, lipid spectrum and bone were used for pure component spectra. The components were fitted to the measured Raman spectra. The determined coefficients multiplied with the background component spectra were subtracted from the raw spectra. The corrected spectra were area normalized and grouped into four clusters by hierarchical cluster analysis (HCA).

Difference spectra were obtained by subtracting the Raman spectra acquired at different excitation wavelengths from the Raman spectrum measured at the excitation wavelength of 786 nm of the same spatial location in the tissue sample. Thereby, four SERDS spectra per image point with different wavelength shifts, i.e., 0.5 nm, 1.0 nm, 1.5 nm, 2.0 nm, were obtained, which can be represented in four SERDS images containing 400 Raman difference spectra. Before calculating the differences spectra, the cosmic spike-corrected spectra were normalized or optimized. Three different types of processing methods were tested:

$$\text{area normalization : } S_{an}(\tilde{\nu}_i) = \frac{S(\tilde{\nu}_i)}{\sum_{i=1}^n S(\tilde{\nu}_i)} \quad (1)$$

z-score normalization/standard normal variate [64]:

$$S_{zn}(\tilde{\nu}_i) = \frac{S(\tilde{\nu}_i) - \text{mean}(S)}{SD(S)} \quad (2)$$

$$\text{subtraction optimization : } \text{minimization of } AUC (|S_1 - (x \cdot S_2)|) \quad (3)$$

with  $S$ —signal;  $\tilde{\nu}$ —relative wavenumber;  $SD$ —standard deviation;  $AUC$ —area under the curve.

For the subtraction optimization a random value  $x$  is multiplied to the spectrum, which is being subtracted, and the area under the curve ( $AUC$ ) of the absolute values of the difference spectrum is calculated. The value  $x$  is then iteratively adjusted, so that the  $AUC$  is minimized.

### 3. Results

#### 3.1. Theoretical Approach

Ideally, Raman spectra show defined bands, as seen in Figure 1a for lipids and Figure 1b for proteins. However, due to the high auto-fluorescence background in biological tissue, Raman bands are superimposed with an auto-fluorescence background and as well as accompanying shot noise, shown in Figure 1c,d.

Even small amounts of fluorescent molecules in a sample can cause high background intensities. The fluorescence scattering cross-section is usually several orders of magnitude higher than the Raman scattering cross-section [65,66].

After adding the simulated fluorescence background and shot noise to the Raman signal, as shown in Figure 1, the Raman bands can barely be distinguished, because the noise level is increasing with the intensity of the fluorescence signal, following the square root of the total signal intensity. Therefore, at higher fluorescence contributions the SNR is lower for a constant Raman signal intensity, as shown in Figure 1f. An estimated average SNR value of the main bands for each spectrum was calculated based on the described algorithm in the materials and method Section 2.1. The average SNR for the lipid spectrum without fluorescence is approximately 6.8 (Figure 1f, black spectrum). If the lipid spectrum has a fluorescence intensity five times higher than the maximal band intensity of the lipid spectrum the average SNR decreases to 3.4 (Figure 1f, red spectrum). For a fluorescence intensity 10 times higher than the maximal band intensity of the lipid spectrum the average SNR is only 2.5.

In order to evaluate different methods to correct auto-fluorescence background contributions a set of fluorescence intensities was created to simulate fluorescence contributions at different intensities and hence, different SNRs for a Raman signal with constant signal intensity. SERDS simulations were then performed on the set of created noise and background affected spectra. Before the evaluation of SERDS for background correction, an optimal laser wavelength shift had to be determined. The optimal shift distance has often been defined as the wavelength difference, which corresponds to the half-width of a Raman band [43]. However, this is only valid when bands with similar bandwidth are present within a spectrum, which is not the case in Raman spectra of most biological samples as discussed in the introduction. Therefore, the optimal wavelength shift was defined as the shift, which retains most of the signal information in the difference spectrum. Autocorrelation of pure Raman spectra were performed to determine the optimal shift. The autocorrelation function of lipid (black) and protein (red) is shown in Figure 2a.

A complete overlap between the spectrum and itself results in a perfect autocorrelation ( $acf = 1$ ), seen in Figure 2a. Meaning, if two signals are fully overlapped the difference spectrum of those signals will have zero informational content. A very low autocorrelation coefficient indicates a low self-similarity of the signal and will result in high signal intensities in the difference spectra. Hence, high 1- $acf$  values will result in higher signal of difference spectra. This approach was used as an indicator for the optimal shift for pure spectra of lipid and protein. Shifts were analyzed in a region between 0 to 12.6 nm because a higher shift might result in effects on the fluorescence spectrum and are technically very challenging to implement. The highest intensities retained in the difference spectra were for a shift of 7 nm for lipid, and 10 nm for protein, corresponding to 110 and 160  $\text{cm}^{-1}$ , respectively (see Figure 2b). These values are much higher than commonly reported [37,67,68]. It is also visible in Figure 2b that when the shift in wavelength for lipid is higher than 7 nm the 1- $acf$  decreases, resulting in a reduction of signal. The influence of the shift on the retained signal intensity can be best visualized by plotting the corresponding difference Raman spectra for lipids with and without noise, as seen in Figure 2c,d. For a shift of 1 nm (green) there is 47% of the signal retained, for a shift of 2 nm (black) 54% of the signal is retained and by shifting 4 nm (blue) a considerable part of the signal is retained (68%).

To compare SERDS and EMSC the simulated Raman spectra with fluorescence and noise from Figure 1c,d, with a fluorescence intensity level of five times the maximal band of the lipid signal,

were chosen. A Raman shift of 4 nm was used and after applying SERDS the absolute values of the difference lipid and protein spectra were calculated (see Figure 3a,b, blue spectra).

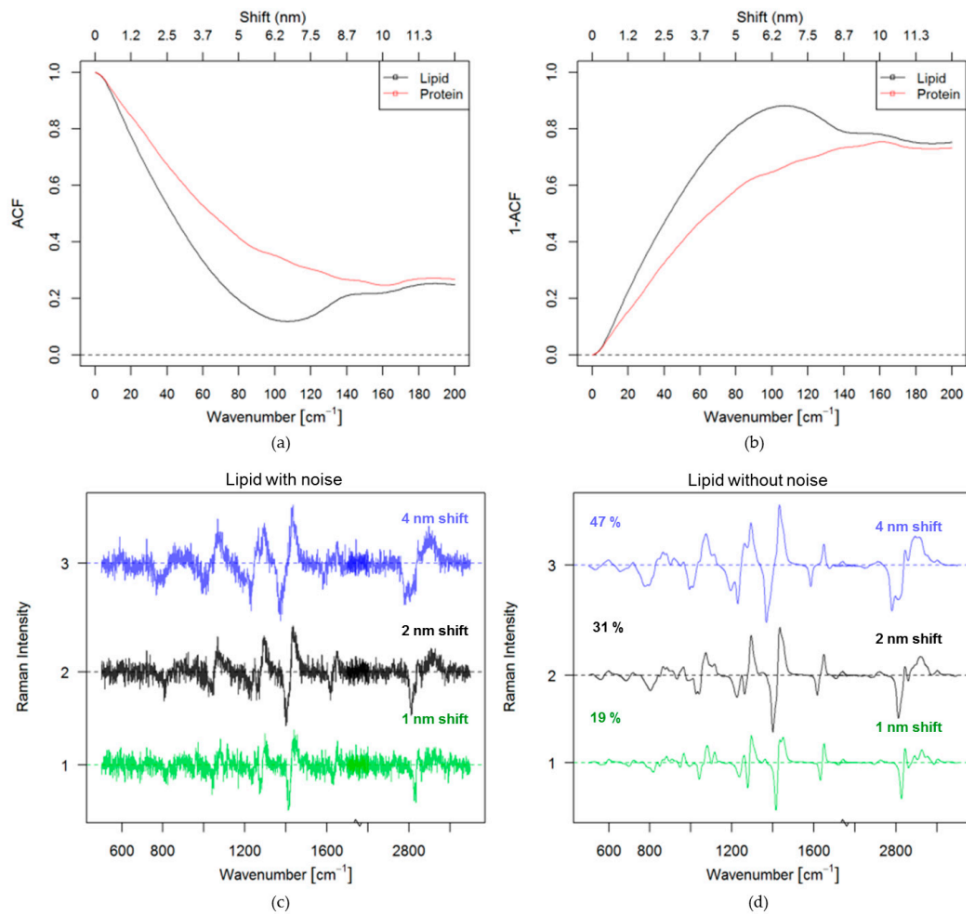


**Figure 2.** Optimal shift: (a) Estimation by using the autocorrelation function of lipid and protein spectra (b) Estimation by using the 1-autocorrelation function of lipid and protein spectra; (c) Simulation of the difference spectra of lipid at 1 nm shift (green), 2 nm shift (black) and 4 nm shift (blue) with noise, the values are the percentage values of the retained signal; (d) Simulation of the difference spectra of lipid at 1 nm shift (green), 2 nm shift (black) and 4 nm shift (blue) without noise.

The absolute values of the difference spectra are illustrated in order to indicate how much signal is retained in the difference spectra. The same plot also shows the EMSC corrected spectra (green), and the original Raman spectra with and without noise, colored red and black, respectively. The processed SERDS signal (blue) has lower intensity than the EMSC corrected spectra (green). When comparing the EMSC corrected spectra (green) with the original spectra with noise (red) in Figure 3, one can see that it resembles the original spectra with noise quite well. The intensity of the signal is not reduced as in the case of the difference spectrum based on SERDS (blue). The reader should keep in mind that the acquisition time for SERDS is twice as long, as for a normal spectrum, because two spectra are acquired. Hence, the intensity of the Raman signal for the background corrected case should actually be twice as high.

In a shot noise limited measurement the SNR of a Raman signal is inversely proportional to the square root of the sum of the Raman signal and the fluorescence (Equation (4)). Consequently, the SNR will be very low at very high fluorescence intensities. For SERDS a further problem occurs, which is

that while the signal intensity is subtractive, the noise contribution is additive, Equation (5). Hence, one disadvantage in SERDS is the reduction of the overall SNR in the difference spectra. It is possible to express the SNR of SERDS measurements in terms of the SNR of Raman measurements for identical acquisition conditions, i.e., the acquisition time of a Raman spectrum has to match the acquisition time of two SERDS spectra.

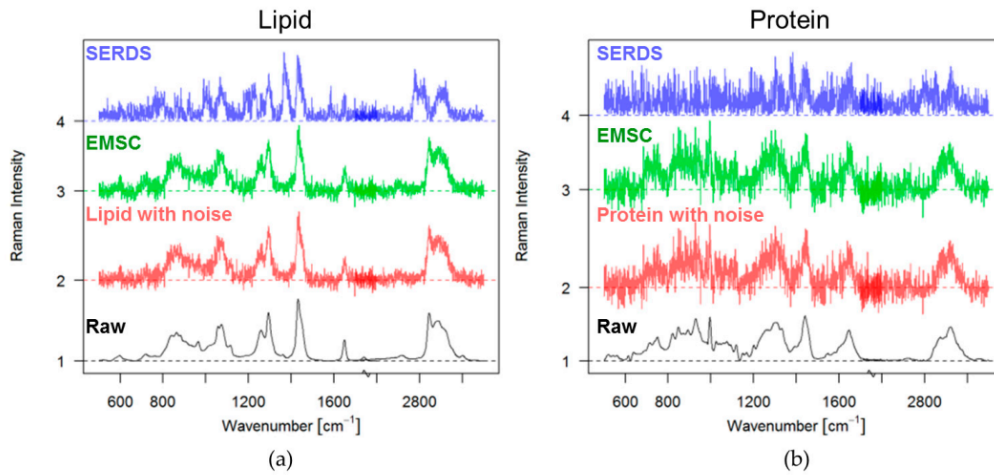


**Figure 3.** EMSC and SERDS spectra for lipid and protein: (a) Lipid spectrum without background (black); lipid spectrum with noise added (red, noise corresponds to the poison distribution of original spectrum and the added fluorescence five times the maximal band of the lipid signal); EMSC corrected lipid spectrum after adding a fluorescence background five times the maximal band of the lipid signal (green); absolute values of SERDS difference spectrum of lipid after shifting 4 nm (blue); (b) Protein spectrum without background (black); protein spectrum with noise added (red, this noise corresponds to the poison distribution of original spectrum and the added fluorescence five times the maximal band of the protein signal); EMSC corrected protein spectrum after having fluorescence background five times the maximal band of the protein signal (green); absolute values of SERDS difference spectrum of protein after shifting 4 nm (blue).

Equation (9) shows that for  $S_2$  smaller than  $S_1$  the  $SNR_{SERDS}$  will be smaller or equal to half of the  $SNR_{RAMAN}$ ; for  $S_2 = S_1$   $SNR_{SERDS}$  is 0; and for  $S_2 \geq 2S_1$   $SNR_{SERDS} \geq SNR_{RAMAN}/2$ . The last term indicates that the SERDS difference spectrum can locally have a higher SNR as a Raman spectrum. However, in general the total spectral SNR is of importance and the local SNR is not always meaningful. The summation in Equation (10) allows assessing the SNR over the entire measurable spectral region or a region of interest. Because the autocorrelation function for any reasonable shift is non-zero (see also Figure 2a), the total SNR of SERDS is always smaller than the SNR of Raman.

$$SNR_{RAMAN}(\lambda_i) = \frac{S_1(\lambda_i)}{\sqrt{S_1(\lambda_i) + F_1(\lambda_i)}} \quad (4)$$

$$SNR_{SERDS}(\lambda_i) = \left| \frac{S_1(\lambda_i) - S_2(\lambda_i)}{\sqrt{S_1(\lambda_i) + F_1(\lambda_i) + S_2(\lambda_i) + F_2(\lambda_i)}} \right| \quad (5)$$

for  $S \ll F$  and  $F_1(\lambda_i) \approx F_2(\lambda_i)$

$$SNR_{SERDS}(\lambda_i) = \frac{1}{\sqrt{2}} \left| \frac{S_1(\lambda_i) - S_2(\lambda_i)}{\sqrt{S_1(\lambda_i) + F_1(\lambda_i)}} \right| \quad (6)$$

for identical acquisition parameters for Raman and SERDS  $t_{SERDS} = 2 \cdot t_{RAMAN}$

$$SNR_{RAMAN}(\lambda_i) = \frac{2 \cdot S_1(\lambda_i)}{\sqrt{2} \cdot \sqrt{S_1(\lambda_i) + F_1(\lambda_i)}} \quad (7)$$

$$\frac{SNR_{SERDS}(\lambda_i)}{SNR_{RAMAN}(\lambda_i)} = \frac{1}{2} \cdot \left| \frac{S_1(\lambda_i) - S_2(\lambda_i)}{S_1(\lambda_i)} \right| \quad (8)$$

$$SNR_{SERDS}(\lambda_i) = \frac{SNR_{RAMAN}(\lambda_i)}{2} \cdot \left( \left| 1 - \frac{S_2(\lambda_i)}{S_1(\lambda_i)} \right| \right) \quad (9)$$

$$SNR_{SERDS} = \frac{1}{2} \cdot \sum_{i=1}^n SNR_{RAMAN}(\lambda_i) \cdot \left( \left| 1 - \frac{S_2(\lambda_i)}{S_1(\lambda_i)} \right| \right) \text{ for } S_1 \geq 1 \quad (10)$$

with  $S$ —Raman signal;  $F$ —fluorescence signal;  $\lambda_i$ —wavelength;  $t$ —acquisition time.

### 3.2. Experimental Approach

Since the simulations showed the influence of the shift in excitation wavelength on the SERDS spectra, SERDS measurements of tissue samples were performed with different wavelength shifts. Because the largest shift that could be realized in our experimental setup was 2 nm (ca.  $32 \text{ cm}^{-1}$ ), four different shifts in excitation wavelength were measured in a 0.5 nm interval. In Figure 4 these different mean SERDS spectra of raw data for the lipid cluster of a tissue sample are shown. They show the same tendencies that could be seen in the simulations: the largest shift (blue) has the highest intensity, while the lowest can be observed for the smallest shift (black). This 0.5 nm shift is so small that the retained background is significant to the retained signal and cannot correct the spectra efficiently. It is also evident that the subtraction of raw spectra does not remove the background completely.

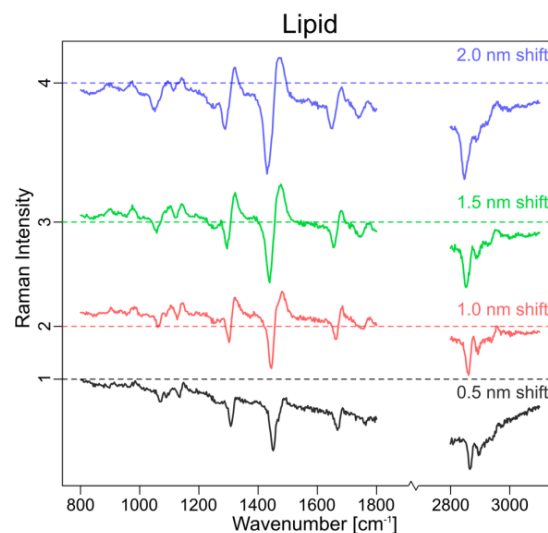


**Figure 4.** Measured difference mean raw spectra of a lipid cluster at different excitation wavelength shifts (shift: 0.5 nm (black), 1.0 nm (red), 1.5 nm (green), 2.0 nm (blue)).

For the comparison of SERDS and EMSC, the largest possible shift was applied for the experimental measurements. Raw spectra ( $\lambda_1 = 786 \text{ nm}$ ,  $\lambda_2 = 784 \text{ nm}$ ,  $\lambda_{SERDS} = \lambda_1 - \lambda_2$ ) were used to generate the SERDS spectra. The EMSC correction was performed on the spectra measured at 785.0 nm.

The correction of real data with the computational background correction method EMSC can be demanding, if there are no pure component spectra available for the measuring system. For a

system where all contributing spectral components are known this method works very well even for spectra with a high fluorescence background. The fluorescence background can be approximated by a higher polynomial and used as a background component. For a Raman image of a complex tissue with multiple spectra of different components, background estimation for fluorescence can be challenging since the contribution might vary locally. Even if multiple fluorescence background estimates are used for the EMSC algorithm, unknown varying backgrounds can cause performance problems for the EMSC background correction. On the other hand, SERDS difference spectra are hard to interpret since the band position cannot be reconstructed easily. Since difference spectra can be compared to the 1st derivative of a Raman spectrum, the 1st derivative of the EMSC corrected Raman spectra were calculated (Figure 5g–i). The black vertical lines show the band position in the EMSC corrected spectra (Figure 5d–f). For the lipid spectrum the band positions of the EMSC corrected spectrum overlaps quite nicely with the inflection points of the 1st derivative and the SERDS spectrum as seen in Figure 5a,d,g. For protein spectra, the band position of the EMSC corrected spectra also overlap with the inflection points of the 1st derivative of the EMSC and the SERDS spectra (Figure 5b,e,h and Figure 5c,f,i). However, the difference spectra are noisy and the bands are not easily located. It is even worse for the 1st derivative EMSC corrected spectra of proteins, which has a very high noise level. In the weaker protein spectrum in Figure 5c,f,i, bands are very hard to discern because of the high noise in the 1st derivative spectrum.

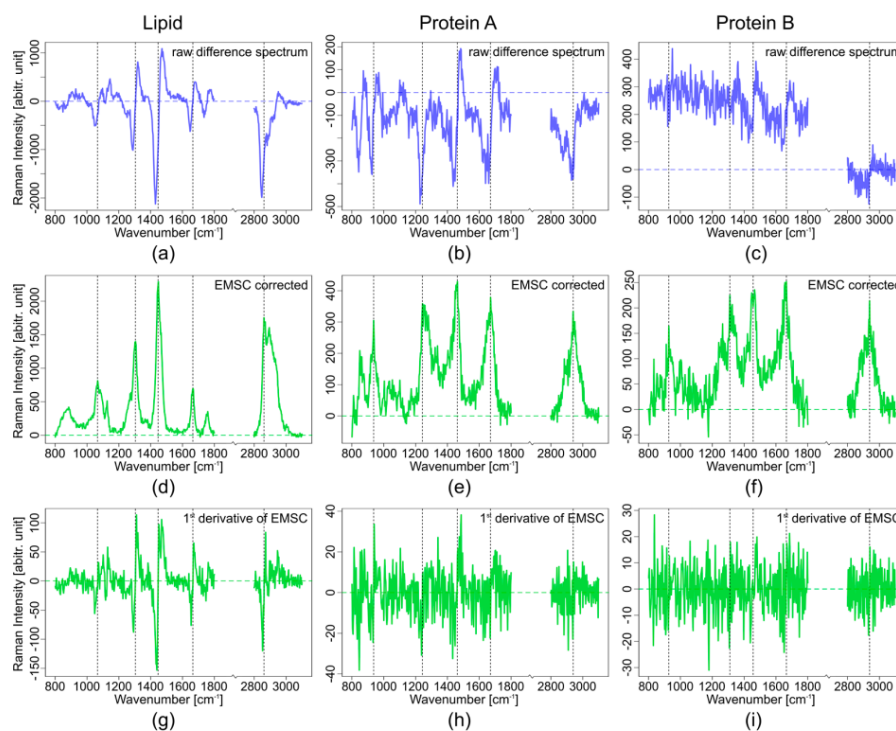


**Figure 5.** Comparison of measured lipid spectrum (a,d,g) and two protein spectra (b,e,h) and (c,f,i). Raw SERDS difference spectra (2 nm shift, (a–c), blue); EMSC corrected spectra at 785 nm ((d–f), green); 1st derivative of the EMSC corrected spectra at 785 nm ((g–i), green); the vertical black lines mark band positions.

The intensity loss due to the subtraction of two raw spectra to generate the SERDS spectrum is clearly evident. The SERDS intensity is approximately half of the intensity of the EMSC spectra as seen in Figure 5. The SNR for the SERDS spectra is also lower than for the EMSC corrected spectra.

Unlike in the simulated data the measured Raman spectra cannot be corrected by subtraction of one Raman spectrum from another. As shown in Figure 5 (blue spectra) and Figure 6a,b (black spectra), a simple subtraction of the raw spectra does not result in background-free difference spectra. For example, the mean spectrum of lipids is below zero intensity and has a bent in the spectral profile (Figure 6, black spectra). Photobleaching and variation in the laser power at the different excitation wavelengths cause changes in the background and total intensity, making the simple correction approach not suitable for most biological samples. A better overlap of the SERDS pair has to be accomplished, which requires further data processing before calculating the difference spectra.

Spectral normalization is one possible approach to obtain same relative intensities for all excitation wavelengths. Two different normalization procedures, as well as a subtraction optimization, were applied to the raw spectra as explained in the methods section. In Figure 4 the effect of the different spectral processing methods on lipid and protein spectra with fluorescence contributions are shown.

Lipids have a high Raman scattering cross-section and frequently occur at high local concentrations and therefore have a high Raman intensity as in comparison to protein for identical acquisition conditions, leading to strong difference bands. Due to the high intensity in comparison to the noise contribution, the noise-related standard deviation of the lipid difference spectra is low in comparison to protein spectra. Proteins have a smaller Raman scattering cross-section in comparison to lipids and have a lower local concentration, and a higher noise-related standard deviation in the protein difference spectra.

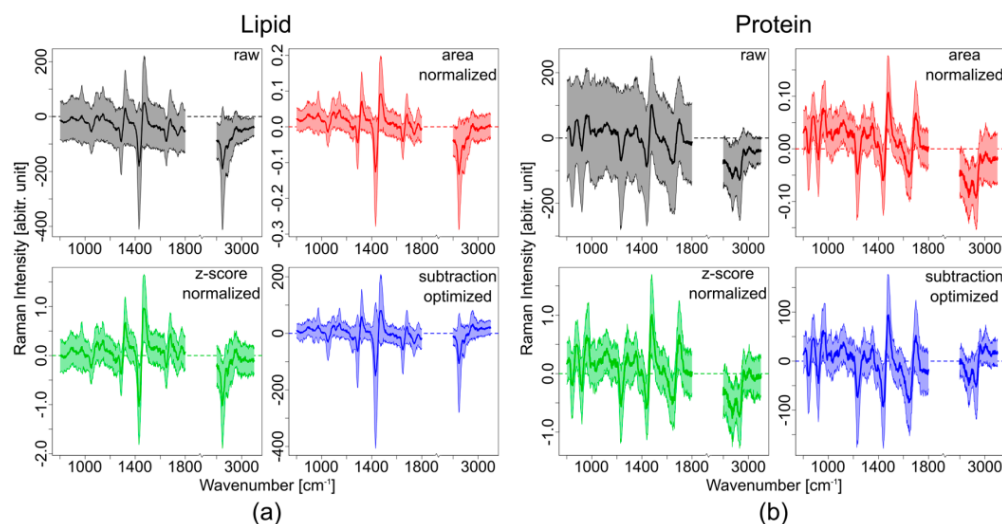


**Figure 6.** Comparison of different SERDS data processing methods with a 2 nm shift for (a) measured lipid spectra and (b) measured protein spectra. For every method the mean spectrum (darker shade) along with its standard deviation is shown. Black: difference spectra obtained by subtraction of raw data; red: difference spectra after area normalization; green: difference spectra after z-score normalization; blue: difference spectra after subtraction optimization.

By applying area normalization to the SERDS spectra before subtraction, an improvement of the background correction can be observed. This improvement is a result of the better overlap between the spectra (Figure 6a,b, red spectra). There are still background contributions left in the difference spectra, which are clearly visible in the bending and the offset of the protein spectra (Figure 6b, red spectrum).

The z-score normalization results in an even better overlap between the spectra (Figure 6a,b, green spectra). The background in the difference spectra is minimized and the mean spectra are close to zero intensity for areas with no signal. Especially for the lipid spectra the z-score normalized difference



spectrum has almost no background and no bending. For the high wavenumber region, however, this normalization also does not work well.

A further approach, which was tested, is based on subtraction optimization. Due to minimization of the area under the difference spectra, artifacts based on different laser intensities at the different excitation wavelength, and filter throughput of the different wavelength can be corrected. Still, after the subtraction optimization small background contributions are left (Figure 6a,b, blue spectra). Although the difference spectra are closer to zero where there is no signal, there is still a deviation visible especially in the protein difference spectrum. The intensity differences of the Raman bands in the difference spectrum are more pronounced than in the other methods and the standard deviation is minimized. The high wavenumber region is better corrected than for the other methods.

The results show that a simple subtraction of the raw spectra is not suitable to remove background contributions in a Raman spectrum with high auto-fluorescence contributions. With preprocessing of the spectra based on normalization or subtraction optimization a better overlap of the SERDS pair can be achieved. Nevertheless, some background artifacts still remain. Especially the difference spectra of the broad envelope of  $\text{CH}_n$  bands between 2800 and 3100  $\text{cm}^{-1}$  result in not very pronounced difference bands. This shows that the small wavelength shift of 2 nm is not sufficient to have a clear separation of the broad  $\text{CH}_n$  bands. Hence, the  $\text{CH}_n$  bands are canceled out by subtracting the two spectra. Z-score normalization and the subtraction optimization both result in a better spectral overlap of the background and provide a better correction than the area normalization. The remaining background of the difference spectra can be corrected, using a polynomial fitting approach.

#### 4. Discussion

The goal of this research was to compare an instrumental with a computational background correction method for Raman spectroscopy of biological samples. One of the most common instrumentation-based methods for background correction of Raman spectra is SERDS, which was compared to the computational method EMSC. The evaluation between the methods was first performed on simulated fluorescence and noise levels, and then on measured spectra.

The simulation of the effect of fluorescence and shot noise showed that Raman bands can be barely distinguished even if the fluorescence intensity is just five times higher than the maximal Raman band of the lipid signal, because of the shot noise resulting from fluorescence background. The SNR at each wavenumber of the simulated spectra was calculated and an estimated value was used to evaluate the overall SNR for different fluorescence signal intensities and difference spectra. This demonstrated that the SNR of the difference spectrum is lower than for a normal Raman spectrum, because the signal is subtractive while the noise is additive. It was also shown that the SNR is reduced inversely proportional to the square root of the fluorescence background for a Raman spectrum with fixed signal intensity. In contrary to previous suggestions to use very small shifts, which correspond to the full width at half maximum of a Raman band, a new criterion was proposed: i.e., the optimal shift is defined as the wavelength shift that retains the most information in the spectrum. By using the autocorrelation function, an optimal shift for lipids and proteins, using the proposed criterion was estimated. It was found that there is a region between 5 and 7.5 nm (for lipid) that retains the highest information and results in the highest SNR. This corresponds to a wavenumber shift of 80 to 120  $\text{cm}^{-1}$ . If the spectra are shifted by more than 7.5 nm, the correlation between the spectra will result in reduced signal after the subtraction. The reduction is due to an increase in an overlap between bands, which do not correspond to the same vibrations, being shifted into each other, resulting in misleading Raman difference information.

For EMSC it was shown that broad polynomial backgrounds could be removed without distorting the Raman bands and compromising the signal intensity nor adding additional noise to the spectra. Furthermore, EMSC can be superior to SERDS, since the spectral acquisition of SERDS requires the acquisition of two spectra, and hence, twice the acquisition time.

For the experimental implementation of SERDS a shift of 5 to 7.5 nm, as required for lipid spectra, can currently not be implemented in our setup, due to limits imposed by the used filters and the intensity stability of the excitation source. A wavelength shift of 2.0 nm was the largest implementable shift without a loss in excitation power. Still, the experimental data supported the simulated results, i.e., the larger the shift, the higher the retained intensities in SERDS spectra, which was shown experimentally for shifts of 0.5 nm, 1.0 nm, 1.5 nm and 2.0 nm for lipids, and the better the SNR. The experiments have shown that for protein and lipid spectra a simple subtraction of the shifted raw spectra, as is usually done for SERDS, does not suffice to obtain background-free SERDS spectra, and more complex computational methods, such as normalization or optimization, have to be used. From the three tested methods, z-score normalization and the subtraction optimization gave the best results. After performing EMSC on single Raman spectra, it was shown theoretically and experimentally that the EMSC corrected spectra can recover the main Raman bands for lipids and proteins. The simulation of the EMSC corrected spectra provided the same information as the original spectra, even when shot noise was added. In contrast to the SERDS difference spectra, the spectral interpretation of the Raman bands is not affected. To have a better comparison between difference spectra and EMSC corrected spectra, the 1st derivatives of the EMSC corrected spectra were calculated based on the experimental data set. It is clearly visible that SERDS experiences a high loss of intensity information due to the subtraction. Since for SERDS two Raman spectra have to be acquired, the measurement time is doubled compared to conventional Raman spectroscopy, leading to long acquisition times for Raman imaging of tissue samples. However, a drawback of the EMSC method is the estimation of very complex unknown backgrounds or multiple different fluorescence backgrounds, which can occur in a single Raman images, due to photobleaching or presence of different fluorophores in the sample.

## 5. Conclusions

For SERDS a reasonably good SNR is necessary to achieve a good background correction. The spectra have to be normalized or optimized before calculation of the SERDS spectra to compensate for fluctuations in signal intensity of the fluorescence background. Even then a further background correction is needed to obtain background-free difference spectra. The larger the shift of the excitation wavelength, the more signal intensity in a spectrum can be retained after the subtraction. For lipids the optimal shift is at  $110\text{ cm}^{-1}$  (7 nm for 785 nm excitation) and for protein at  $160\text{ cm}^{-1}$  (10 nm for 785 nm excitation). The proposed wavelength shifts are rather large, and can lead to changes in fluorescence intensity or, in the worst case, can excite different fluorophores and result in completely different fluorescence profiles. The interpretation of the difference spectra can be challenging, since it is hard to determine the exact band positions. On the other hand, SERDS is advantageous because no previous knowledge of the background is necessary for a correction.

Background correction with EMSC gives promising results for the simulated and the experimental data. It can, however, be challenging when dealing with complex samples and complex backgrounds. Pure spectra have to be generated and fluorescence background components have to be approximated. For Raman images with different fluorescence backgrounds, this can be tedious since more than one fluorescence component will be necessary.

In summary, SERDS and EMSC are both powerful tools for fluorescence background correction, with distinct advantages and disadvantages. When background spectra can be estimated, EMSC outperforms SERDS, because it keeps the fidelity of the Raman spectrum, does not require additional equipment, and guarantees a higher SNR. When, however, backgrounds are too complex to be estimated, SERDS could be a good choice as a background correction method.

**Acknowledgments:** We thank Claudia Beleites for the helpful discussion about the optimization of the experimental dataset. This work is supported by the EU-funded project MIB (No 667933) and by the Leibniz Association through the project HYPERAM (SAW-2016-IPHT-2). The publication of this article was funded by the Open Access Fund of the Leibniz Association.

**Author Contributions:** I.W.S. and C.S. designed the experiments; E.C. and I.W.S. performed the simulations and the theoretical evaluation of the methods; I.W.S. developed the program for device controlling of SERDS imaging; F.K. and C.S. performed the experiments and analyzed the experimental data; E.C., F.K., I.W.S., C.S., C.K., and J.P. wrote the paper.

**Conflicts of Interest:** The authors declare no conflict of interest.

## References and Notes

1. Krafft, C.; Schie, I.; Meyer, T.; Schmitt, M.; Popp, J. Development in spontaneous and coherent Raman scattering microscopic imaging for biomedical applications. *Chem. Soc. Rev.* **2016**, *45*, 1819–1849. [CrossRef] [PubMed]
2. Krafft, C.; Schmitt, M.; Schie, I.; Cialla-May, D.; Matthäus, C.; Bocklitz, T.; Popp, J. Label-free molecular imaging of biological cells and tissues by linear and non-linear Raman spectroscopic approaches. *Angew. Chem.* **2017**, *56*, 4392–4430. [CrossRef] [PubMed]
3. Stone, N. The use of Raman spectroscopy to provide an estimation of the gross biochemistry associated with urological pathologies. *Anal. Bioanal. Chem.* **2007**, *387*, 1657–1668. [CrossRef] [PubMed]
4. Crow, P.; Uff, J.A.; Farmer, J.A.; Wright, M.P.; Stone, N. The use of Raman spectroscopy to identify and characterize transitional cell carcinoma in vitro. *BJU Int.* **2004**, *93*, 1232–1236. [CrossRef] [PubMed]
5. Kerr, L.T.; Domikan, K.; Cullen, I.; Hennelly, B.M. Applications of Raman spectroscopy to the urinary bladder for cancer diagnostics. *Photonics Lasers Med.* **2014**, *3*, 193–224. [CrossRef]
6. Crow, P.; Molckovsky, A.; Stone, N.; Uff, J.; Wilson, B.; Wongkeesong, L.-M. Assessment of fiberoptic Near-infrared Raman spectroscopy for diagnostics of bladder and prostate cancer. *J. Urol.* **2005**, *65*, 1126–1130. [CrossRef] [PubMed]
7. Bergholt, M.S.; Zheng, W.; Ho, K.Y.; Teh, M.; Yeoh, K.G.; So, J.B.Y.; Shabbir, A.; Huang, Z. Fiberoptic confocal Raman spectroscopy for real-time in vivo diagnosis of dysplasia in Barrett's esophagus. *Gastroenterology* **2014**, *146*, 27–32. [CrossRef] [PubMed]
8. Eberhardt, K.; Stiebing, C.; Matthäus, C.; Schmitt, M.; Popp, J. Advantages and limitations of Raman spectroscopy for molecular diagnostics: An update. *Expert Rev. Mol. Diagn.* **2015**, *15*, 773–787. [CrossRef] [PubMed]
9. Motz, J.T.; Gandhi, S.J.; Scepanovic, O.R.; Feld, M.S. Real-time Raman system for in vivo disease diagnosis. *J. Biomed. Opt.* **2005**, *10*, 031113. [CrossRef] [PubMed]
10. Draga, R.O.P.; Grimbergen, M.C.M.; Vijverberg, P.L.M.; Bosch, J.L.H.R. In Vivo Bladder Cancer Diagnosis by High-Volume Raman Spectroscopy. *Anal. Chem.* **2010**, *82*, 5993–5999. [CrossRef] [PubMed]
11. De Jong, B.W.D.; Schut, T.C.B.; Wolffenbuttel, K.P.; Nijman, J.M.; Kok, D.J.; Puppels, G.J. Identification of bladder wall layers by Raman spectroscopy. *J. Urol.* **2002**, *168*, 1771–1778. [CrossRef]
12. Monici, M. Cell and tissue autofluorescence research and diagnostic applications. *Biotechnol. Annu. Rev.* **2005**, *11*, 227–256. [PubMed]
13. McCain, S.T.; Willett, R.M.; Brady, D.J. Multi-excitation Raman Spectroscopy Technique for Fluorescence Rejection. *Opt. Express* **2008**, *16*, 10975–10991. [CrossRef] [PubMed]
14. Macdonald, A.M.; Wyeth, P. On the use of photobleaching to reduce fluorescence background in Raman spectroscopy to improve the reliability of pigment identification on painted textiles. *J. Raman Spectrosc.* **2006**, *37*, 830–835. [CrossRef]
15. Zięba-Palus, J.; Michalska, A. Photobleaching as a useful technique in reducing of fluorescence in Raman spectra of blue automobile paint samples. *Vib. Spectrosc.* **2014**, *74*, 6–12. [CrossRef]
16. Da Silva, M.A.; Riveiro, D.G.; Pereira, E.A.; Martin, A.A.; Fontes, A.; da Silva Martinho, H. Shifted-excitation difference spectroscopy for in vitro and in vivo biological samples analysis. *Biomed. Opt. Express* **2017**, *1*, 617–626.
17. Zhang, Z.-M.; Chen, S.; Liang, Y.-Z.; Liu, Z.-X.; Zhang, Q.-M.; Ding, L.-X.; Yec, F.; Zhou, H. An intelligent background-correction algorithm for highly fluorescent samples in Raman spectroscopy. *J. Raman Spectrosc.* **2009**, *41*, 659–669. [CrossRef]
18. Venables, B.; Hornik, K.; Maechler, M. Polynom: A Collection of Functions to Implement a Class for Univariate Polynomial Manipulations. R Package v 1.3-8. 2014. Available online: <https://rdr.io/github/eestileib/ComplexPoly/> (accessed on 26 July 2017).

19. Kourkoumelis, N.; Polymeros, A.; Tzaphlidou, M. Background estimation of biomedical Raman spectra using a geometric approach. *Spectrosc. Int. J.* **2012**, *27*, 441–447. [CrossRef]
20. Gautam, R.; Vanga, S.; Ariese, F.; Umapathy, S. Review of multidimensional data processing approaches for Raman and infrared spectroscopy. *EPJ Tech. Instrum.* **2015**, *2*, 8. [CrossRef]
21. Lieber, C.A.; Mahadevan-Jansen, A. Automated Method for Subtraction of Fluorescence from Biological Raman Spectra. *Appl. Spectrosc.* **2003**, *57*, 1363–1367. [CrossRef] [PubMed]
22. Cadusch, P.J.; Hlaing, M.M.; Wade, S.A.; MxArthur, S.L.; Stoddart, P.R. Improved methods for fluorescence background subtraction from Raman spectra. *Mater. Sci.* **2013**, *44*, 1587–1595.
23. Martens, H.; Nielsen, J.P.; Engelsen, S.B. Light scattering and light absorbance separated by extended multiplicative signal correction. Application to near-infrared transmission analysis of powder mixtures. *Anal. Chem.* **2003**, *75*, 593–604. [CrossRef]
24. Mecozzi, M. A Polynomial Curve Fitting Method for Baseline Drift Correction in the Chromatographic Analysis of Hydrocarbons in Environmental Samples. *APCBEE Procedia* **2014**, *10*, 2–6. [CrossRef]
25. Massart, D.L.; Vandeginste, B.G.M.; Buydens, L.C.M.; Jong, S.D.; Lewi, P.J.; Smeyers-Verbeke, J. *Data Handling in Science and Technology, Handbook of Chemometrics and Qualimetrics, Vols. 20A and 20B*; Elsevier: Amsterdam, The Netherlands, 1997.
26. Vinzi, V.E.; Chin, W.W.; Henseler, J.; Wang, H. *Handbook of Partial Least Squares: Concepts, Methods and Applications*; Springer Science & Business Media: Berlin, Germany, 2010.
27. Baek, S.J.; Park, A.; Ahn, Y.J.; Choo, J. Baseline correction using asymmetrically reweighted penalized least squares smoothing. *Analyst* **2014**, *140*, 17–38. [CrossRef] [PubMed]
28. Liland, K.H.; Kohler, A.; Afseth, N.K. Model-based pre-processing in Raman spectroscopy of biological samples. *J. Raman Spectrosc.* **2015**, *47*, 643–650. [CrossRef]
29. Hasegawaa, T.; Nishijoa, J.; Umemurab, J. Separation of Raman spectra from fluorescence emission background by principal component analysis. *Chem. Phys. Lett.* **2000**, *317*, 642–646. [CrossRef]
30. Asfour, H.; Swift, L.M.; Sarvazyan, N.; Doroslovacki, M.; Kay, M.W. Signal Decomposition of Transmembrane Voltage-Sensitive Dye Fluorescence Using a Multiresolution Wavelet Analysis. *IEEE Trans. Biomed. Eng.* **2011**, *58*, 2083–2093. [CrossRef] [PubMed]
31. Qu, H.-B.; Ou, D.-L.; Cheng, Y.-Y. Background correction in near-infrared spectra of plant extracts by orthogonal signal correction. *J. Zhejiang Univ. Sci. B* **2015**, *6*, 838–843. [CrossRef] [PubMed]
32. Dennis, A. *Photo-Bleaching and Automatic Baseline Correction for Raman Spectroscopy*; R Package v 1.2-1; PerkinElmer: Waltham, MA, USA, 2007.
33. Knorr, F.; Smith, Z.J.; Wachsmann-Hogiu, S. Development of a time-gated system for Raman spectroscopy of biological samples. *J. Opt. Soc. Am.* **2010**, *18*, 20049–20058. [CrossRef] [PubMed]
34. Shreve, A.P.; Cherepy, N.J.; Mathies, R.A. Effective Rejection of Fluorescence Interference in Raman Spectroscopy Using a Shifted Excitation Difference Technique. *Spectrosc. Tech.* **1992**, *46*, 707. [CrossRef]
35. De Luca, A.C.; Mazilu, M.; Riches, A.; Herrington, C.S.; Dholakia, K. Online Fluorescence Suppression in Modulated Raman Spectroscopy. *Anal. Chem.* **2010**, *82*, 738–745. [CrossRef] [PubMed]
36. Dongy, S.; Melnik, E.D.; Ban, V.S.; Volodin, B.L. A novel Method for practical implementation of shifted-excitation Raman difference spectroscopy (SERDS). *Spectroscopy* **2012**, *47*, 198–209.
37. Gebrekidan, M.T.; Knipfer, C.; Stelzle, F.; Popp, J.; Will, S.; Braeuer, A. A shifted-excitation Raman difference spectroscopy (SERDS) evaluation strategy for the efficient isolation of Raman spectra from extreme fluorescence interference. *J. Raman Spectrosc.* **2015**, *47*, 198–209. [CrossRef]
38. Osticioli, I.; Zoppi, A.; Castellucci, E.M. Shift-Excitation Raman difference spectroscopy-difference deconvolution methods for the luminescence background rejection from Raman spectra of solid samples. *Appl. Spectrosc.* **2007**, *61*, 839–844. [CrossRef] [PubMed]
39. Oshima, Y.; Komachi, Y.; Furihata, C.; Tashiro, H.; Sato, H. Fluorescence-suppressed Raman technique for quantitative analysis of protein solution using a micro-Raman probe, the shifted excitation method, and partial least squares regression analysis. *Appl Spectrosc.* **2006**, *60*, 964–970. [CrossRef] [PubMed]
40. Dochow, S.; Ma, D.; Latka, I.; Bocklitz, T.; Hartl, B.; Bec, J.; Fatakdawala, H.; Marple, E.; Urmey, K.; Wachsmann-Hogiu, S.; et al. Combined fiber probe for fluorescence lifetime and Raman spectroscopy. *Anal. Bioanal. Chem.* **2015**, *407*, 8291–8301. [CrossRef] [PubMed]
41. Zhao, J.; Short, M.; Braun, T.; Lui, H.; McLean, D.; Zeng, H. Clinical Raman measurements under special ambient lighting illumination. *J. Biomed. Opt.* **2014**, *19*, 111609. [CrossRef] [PubMed]

42. Maiwald, M.; Müller, A.; Sumpf, B.; Erbert, G.; Tränkle, G. Capability of shifted excitation Raman difference spectroscopy under ambient daylight. *Appl. Opt.* **2015**, *54*, 5520–5524. [CrossRef] [PubMed]
43. Zhao, J.; Carrabba, M.M.; Allen, F.S. Automated Fluorescence Rejection Using Shifted Excitation Raman Difference Spectroscopy. *Appl. Spectrosc.* **2002**, *56*, 834–845. [CrossRef]
44. Dochow, S.; Bergner, N.; Krafft, C.; Clement, J.; Mazilu, M.; Praveen, B.B.; Ashok, P.C.; Marchington, R.; Dholakia, K.; Popp, J. Classification of Raman spectra of single cells with autofluorescence suppression by wavelength modulated excitation. *Anal. Methods* **2013**, *5*, 4608–4614. [CrossRef]
45. Mazilu, M.; Luca, A.C.D.; Riches, A.; Herrington, C.S.; Dholakia, K. Optimal algorithm for fluorescence suppression of modulated Raman spectroscopy. *Opt. Express* **2010**, *18*, 11382–11395. [CrossRef] [PubMed]
46. Krafft, C.; Dochow, S.; Bergner, N.; Clement, J.H.; Praveen, B.B.; Mazilu, M.; Marchington, R.; Dholakia, K.; Popp, J. Raman spectra of single cells with autofluorescence suppression by modulated wavelength excitation. In Proceedings of the Biomedical Vibrational Spectroscopy V: Advances in Research and Industry, San Francisco, CA, USA, 9 February 2012.
47. Schmidt, H.; Sowoidnich, K.; Kronfeldt, H.-D. A Prototype Hand-Held Raman Sensor for the in situ Characterization of Meat Quality. *Appl. Spectrosc.* **2010**, *64*, 888–894. [CrossRef] [PubMed]
48. Bell, S.E.J.; Bourguignon, E.S.O.; Dennis, A. Analysis of luminescent samples using subtracted shifted Raman spectroscopy. *Analyst* **1998**, *123*, 1729–1734. [CrossRef]
49. Matousek, P.; Towrie, M.; Parker, A.W. Simple reconstruction algorithm for shifted excitation Raman difference spectroscopy. *Appl. Spectrosc.* **2005**, *59*, 848–851. [CrossRef] [PubMed]
50. Willett, R. Multiscale reconstruction for photon-limited shifted excitation Raman spectroscopy. In Proceedings of the IEEE International Conference on Acoustics, Speech and Signal Processing—ICASSP, Honolulu, HI, USA, 16–20 April 2007.
51. Schmidt, H.; Kaiser, D.P.; Maiwald, M. Method for Generating and for Detecting a Raman Spectrum. U.S. Patent 8,310, 672, 28 June 2012.
52. Team, R.C. *R: A Language and Environment for Statistical Computing*; R Foundation for Statistical Computing: Vienna, Austria, 2016.
53. Beleites, C.; Sergo, V. HyperSpec: A Package to Handle Hyperspectral Data Sets in R. R package v 0.98-20150805. 2015.
54. Liland, K.H.; Mevik, B.-H. Baseline: Baseline Correction of Spectra. R Package v 1.2-1. 2015. Available online: <https://cran.r-project.org/web/packages/baseline/index.html> (accessed on 26 July 2017).
55. Borchers, H.W. Pracma: Practical Numerical Math Functions. R Package v 1.9.9. 2017. Available online: <https://www.rdocumentation.org/packages/pracma/versions/1.9.9> (accessed on 26 July 2017).
56. Beleites, C. Ramancal: Calibration Routines for Raman Spectrometers. R Package v 0.1. 2013.
57. Hyndman, R. (Partial) Autocorrelation and Cross Correlation Function Estimation. From Forecast v7.3. 2016. Available online: <https://www.rdocumentation.org/packages/forecast/versions/7.3> (accessed on 26 July 2017).
58. Hyndman, R.J. Forecast: Forecasting Functions for Time Series and Linear Models. 2017. Available online: <https://rdrr.io/cran/forecast/> (accessed on 26 July 2017).
59. Beleites, C. Cbmodels: Collection of “Combined” Models: PCA-LDA, PLS-LDA, PLS-LR as Well as EMSC. R Package v 0.5-20160412. 2016.
60. McCreery, R.L. *Raman Spectroscopy for Chemical Analysis*; Wiley-interscience: Hoboken, NJ, USA, 2000.
61. Kiselev, R.; Schie, I.W.; Askrabic, S.; Krafft, C.; Popp, J. Design and first applications of a flexible Raman micro-spectroscopic system for biological imaging. *Biomed. Spectrosc. Imaging* **2016**, *5*, 115–127. [CrossRef]
62. Ryabchykov, O. Spikes: Spike Correction of Raman Spectral Data. R Package v 1.0. 2016.
63. Ryabchykov, O.; Bocklitz, T.; Ramoji, A.; Neugebauer, U.; Foerster, M.; Kroegel, C.; Bauer, M.; Kiehnopf, M.; Popp, J. Automatization of spike correction in Raman spectra of biological samples. *Chemom. Intell. Lab. Syst.* **2016**, *155*, 1–6. [CrossRef]
64. Dhanoa, M.S.; Barnes, R.J.; Lister, S.J. Standard normal variate transformation and de-trending of near-infrared diffuse reflectance spectra. *Appl. Spectrosc.* **1989**, *43*, 772–777.
65. Slobodan, S. *Pharmaceutical Applications of Raman Spectroscopy*; John Wiley & Sons, Inc.: Sandwich, UK, 2008.
66. Long, D.A. *The Raman Effect: A Unified Treatment of the Theory of Raman Scattering by Molecules*; John Wiley & Sons Ltd.: Bradford, UK, 2002.

67. Maiwald, M.; Müller, A.; Sumpf, B.; Tränkle, G. A portable shifted excitation Raman difference spectroscopy system: Device and field demonstration. *J. Raman Spectrosc.* **2016**, *47*, 1180–1184. [CrossRef]
68. De Luca, A.C.; Dholakia, K.; Mazilu, M. Modulated Raman Spectroscopy for Enhanced Cancer Diagnosis at the Cellular Level. *Sensors* **2015**, *15*, 13680–13704. [CrossRef] [PubMed]



© 2017 by the authors. Licensee MDPI, Basel, Switzerland. This article is an open access article distributed under the terms and conditions of the Creative Commons Attribution (CC BY) license (<http://creativecommons.org/licenses/by/4.0/>).

**6.2. New methodology to process shifted excitation Raman difference spectroscopy data: a case study of pollen classification [FK2]**

Florian Korinth, Abdullah S. Mondol, Clara Stiebing, Iwan W. Schie, Christoph Krafft, Jürgen Popp (2020)

*Scientific Reports*, **10**(1): 11215, 1 – 12.

Der Nachdruck der folgenden Publikation, welche unter einer internationalen Creative Commons Attribution 4.0-Lizenz steht (<http://creativecommons.org/licenses/by/4.0/>), erscheint mit freundlicher Genehmigung von Springer Nature.

**Erklärung zu den Eigenanteilen des Promovenden sowie der weiteren Doktoranden/ Doktorandinnen als Koautoren an den Publikationen und Zweitpublikationsrechten bei einer kumulativen Dissertation.**

Doktoranden	Florian Korinth	Abdullah S. Mondol
Konzeption des Forschungsansatzes	x	x
Aufbau und Programmierung des Messaufbaus		x
Planung der Untersuchungen	x	x
Datenerhebung	x	
Datenanalyse und –interpretation	x	
Schreiben des Manuskripts	x	x
Vorschlag Anrechnung Publikationsäquivalente	1,0	



# OPEN New methodology to process shifted excitation Raman difference spectroscopy data: a case study of pollen classification

F. Korinth<sup>1</sup>, A. S. Mondol<sup>1</sup>, C. Stiebing<sup>1</sup>, I. W. Schie<sup>1,2</sup>, C. Krafft<sup>1,3</sup> & J. Popp<sup>1,3</sup>

Shifted excitation Raman difference spectroscopy (SERDS) is a background correction method for Raman spectroscopy. Here, the difference spectra were directly used as input for SERDS-based classification after an optimization procedure to correct for photobleaching of the autofluorescence. Further processing included a principal component analysis to compensate for the reduced signal to noise ratio of the difference spectra and subsequent classification by linear discriminant analysis. As a case study 6,028 Raman spectra of single pollen originating from plants of eight different genera and four different growth habits were automatically recorded at excitation wavelengths 784 and 786 nm using a high-throughput screening Raman system. Different pollen were distinguished according to their growth habit, i.e. tree versus non-tree with an accuracy of 95.9%. Furthermore, all pollen were separated according to their genus, providing also insight into similarities based on their families. Classification results were compared using spectra reconstructed from the differences and raw spectra after state-of-art baseline correction as input. Similar sensitivities, specificities, accuracies and precisions were found for all spectra with moderately background. Advantages of SERDS are expected in scenarios where Raman spectra are affected by variations due to detector etaloning, ambient light, and high background.

Raman spectroscopy is a vibrational spectroscopy technique that is used for the assessment of the chemical composition of samples. Even complex biological samples can be analyzed in a non-destructive and label-free manner and classified using their specific molecular fingerprints assessed by this method<sup>1–4</sup>. However, intense and strongly varying backgrounds, e.g. due to autofluorescence (with or without photobleaching), detector etaloning effects and ambient light, are an often occurring challenge in Raman spectroscopy. If the Raman intensity is too low relative to the background intensity, Raman bands are hard to discern or are masked completely. Although it cannot be excluded that an autofluorescence background contains useful information, background correction procedures are state-of-art in Raman spectroscopy of biological material. Autofluorescence contributions in Raman spectra seem to be sensitive, but specificity might be problematic due to bleaching and quenching effects, which are prone to variations and lack proper reproducibility.

Therefore, different approaches were suggested to tackle the challenge of intense and varying backgrounds. One option for autofluorescence is the destruction of the fluorophores by photobleaching<sup>5–7</sup>, which is rather time-consuming and might cause side effects, such as sample contamination with chemiphotobleaching agents or thermal stress due to extended laser exposure of the sample. A review divided other techniques roughly into two groups: computational and instrumental background correction methods<sup>8</sup>. Examples of typically used computational background correction algorithms are extended multiplicative signal correction<sup>9,10</sup> (EMSC), multiplicative signal correction<sup>11</sup> (MSC), rubberband<sup>12,13</sup>, sensitive nonlinear iterative peak<sup>14</sup> (SNIP), and polynomial fittings<sup>15</sup>. These approaches often require high computational effort and need experienced personal for the data analysis. Cordero et al. corrected a high fluorescence background in Raman spectra of bladder biopsies using EMSC<sup>16</sup>. For in vivo Raman spectra of colorectal tissue Bergholt et al. corrected autofluorescence background by a high-order

<sup>1</sup>Leibniz Institute of Photonic Technology, Albert-Einstein-Straße 9, 07745 Jena, Germany. <sup>2</sup>Department of Medical Engineering and Biotechnology, University of Applied Sciences, Carl-Zeiss-Promenade 2, 07745 Jena, Germany. <sup>3</sup>Institute of Physical Chemistry and Abbe Center of Photonics, Friedrich Schiller University Jena, Helmholtzweg 4, 07743 Jena, Germany. ✉email: Christoph.krafft@leibniz-ipht.de



polynomial fitting<sup>17</sup>. The *in vivo* acquired Raman spectra of brain cancer by Desroches et al. were also background corrected using a polynomial<sup>18</sup>. Galli et al. found a high fluorescence background in Raman spectra of brain biopsies, where 88.4–96.5% of the collected intensities were attributed to fluorescence. For separating the background-free Raman signal and the fluorescence profile a baseline estimation toolkit was used. The authors concluded that the classification was best, when both information were used<sup>19</sup>.

Instrumental background correction methods for fluorescence rejection are time-gating approaches, where the fast Raman scattering is detected before the slower fluorescence emission, and phase or wavelength modulated techniques, where the Raman scattering changes according to the wavelength or phase modulation whereas the fluorescence emission does not<sup>8</sup>. Another promising method is shifted excitation Raman difference spectroscopy (SERDS)<sup>20</sup>.

SERDS belongs to the instrumental background correction methods, which uses two slightly shifted excitation wavelengths to acquire two Raman spectra consecutively at the same lateral position. The shift in excitation wavelength is chosen to be only a few nanometers, leading to two slightly shifted Raman spectra with the same fluorescence background profile, since the same fluorophores are excited. After subtraction of the shifted Raman spectra from each other, the resulting difference spectrum is ideally free of background contributions and only contains Raman information. Furthermore, other constant spectral contributions such as ambient light or the system transfer function (e.g. detector etaloning effects) can be suppressed<sup>21</sup>. Proof of principle studies demonstrated SERDS using several combinations of solvents and dyes as model analytes, especially for the introduction of new lasers with two or more excitation wavelengths<sup>20,22–25</sup>. Sowoidnich and Kronfeldt analyzed different laser wavelengths for SERDS experiments on parts of beef and pork tissues like fat, connective tissue, bone and meat<sup>26</sup>. Noack et al. conducted SERDS measurements to measure algae cultivation samples and monitor sulfated exopolysaccharides (EPS) concentrations in the reactors. For this, 10 raw spectra were averaged, smoothed and baseline corrected before the subtraction. A principle component analysis (PCA) and different regression models were then applied to the smoothed difference spectra to determine the EPS concentration, which worked poorly for the partial least squares regression (PLSR) model, but very well for the support vector regression (SVR) model<sup>27</sup>. Martins et al. studied molar teeth *ex vivo* and human skin *in vivo* using SERDS with an excitation wavelength of 830 nm/830.5 nm and regular Raman spectroscopy at 1,064 nm as a control. For data analysis the difference spectra were integrated to reconstruct the Raman spectrum<sup>28</sup>. Gebrekidan et al. measured difference spectra of pig tissue (bone, fat, gland and mucosal). After a sophisticated data processing including normalization, first baseline correction, reconstruction and second baseline correction to receive fluorescence-free pure Raman spectra, a classification by PCA was performed<sup>29</sup>. By measuring a plate of clear polystyrene, Maiwald et al. showed that SERDS was able to filter out ambient light passing through polystyrene. They also conducted SERDS in an orchard measuring the wax on the skin of an apple and the chlorophyll in a leaf using a handheld device with a high numerical aperture<sup>30,31</sup>. Schmäzlin et al. obtained SERDS images from different samples, e.g. cross-section of a pig ear, skin and a dissolving brown sugar cube using a custom-built multi-focus probe head and an integral field spectrograph. This system was able to simultaneously detect 400 spectra delivered by the probe head of  $20 \times 20$  pixels<sup>32</sup>.

Since photobleaching and intensity variations due to e.g. laser power and filter characteristics often result in varying background intensities, most difference spectra are not completely background-free. This makes additional background correction steps necessary. Also reconstruction steps are usually implemented to transform the difficult to interpret difference spectra into accustomed Raman spectra. There are several reconstruction approaches, such as deconvolution, linear data manipulation, integration, kernel function, or non-negative least squares fitting<sup>33–34</sup>. These reconstruction methods always harbor the risk of introducing artefacts into the reconstructed Raman spectrum, due to the correlation between the fixed wavelength shift and varying Raman band widths<sup>35</sup>.

As a case study pollen samples of eight different plant genera were investigated. Pollen are a valuable case study, since their Raman spectra experience intensity differences in the fluorescence backgrounds (see supplementary information in Ref.<sup>36</sup>). In palynology, pollen are taxonomically evaluated under a microscope considering their morphology. This is time-consuming and requires a highly trained expert to differentiate several hundreds of different pollen. There are several ideas for automatization and technical improvement of this gold standard<sup>37–39</sup>. Other spectroscopic approaches like infrared absorption<sup>40–42</sup>, laser-induced breakdown<sup>43</sup> or Raman scattering have been applied<sup>45,43–55</sup>. Raman spectroscopy was implemented to build a spectral database of pollen including a chemometrical classification by their growth habit<sup>36</sup>.

The approach in this work to differentiate several pollen genera uses difference spectra, that were obtained by novel processing of SERDS data, and lends itself as a case study to classify biological samples. The new streamlined method to handle and classify SERDS data of biological samples is based on their single difference spectra without a reconstruction step to retrieve the familiar profile of Raman spectra or baseline correction procedures. Furthermore, spectra were reconstructed from the differences and Raman spectra were processed by state-of-art baseline correction. For classification using difference spectra, reconstructed spectra and baseline corrected spectra as input, a PCA followed by a linear discriminant analysis (PCA-LDA) was chosen. The classification results were compared with respect to sensitivities, specificities, accuracies and precisions.

## Results and discussion

**Data acquisition and processing.** Representative raw spectra of a single birch and hazel pollen grain at three consecutively measured excitation wavelengths of  $\lambda_1 = 784$  nm (130 mW),  $\lambda_2 = 785$  nm (180 mW) and  $\lambda_3 = 786$  nm (200 mW) are shown in Fig. 1a. The series of consecutive measurements started with 784 nm followed by 785 nm and 786 nm. The spectra show similarities in e.g. amide bands ( $1,310$  and  $1,650$   $\text{cm}^{-1}$ ) and the sporopollenin bands ( $1,007$ ,  $1,454$  and  $1,614$   $\text{cm}^{-1}$ ) but vary in intensity. When separately evaluating the two sets

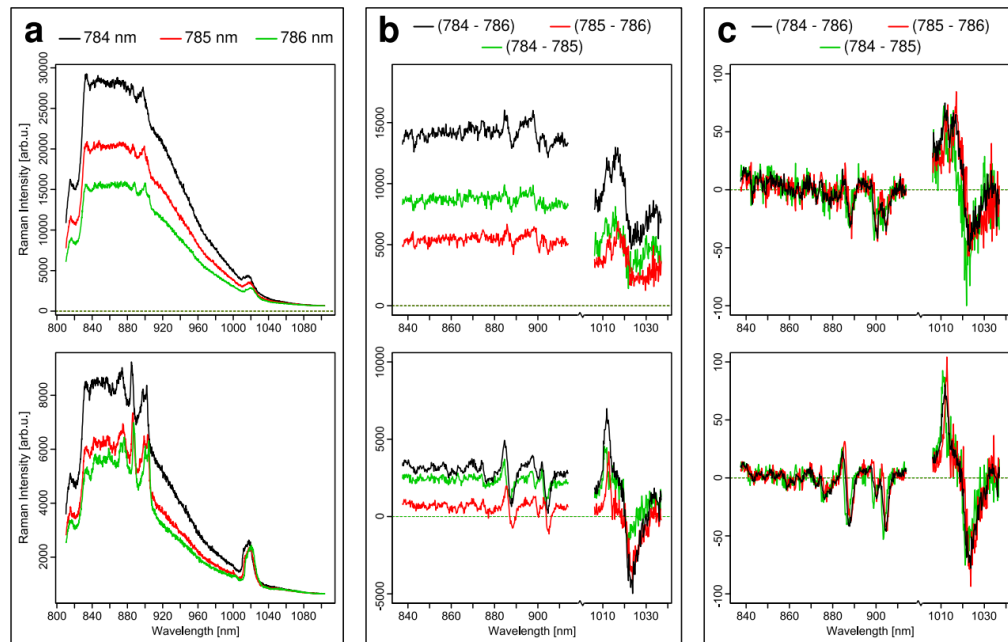


**Figure 1.** Overview of the data processing steps. top row, spectra of one birch pollen grain; bottom row, spectra of one hazel pollen grain; (a) raw spectra at the three different excitation wavelengths; (b) raw difference spectra; (c) normalized and optimized difference spectra; the color codes of excitation wavelengths are indicated on top.

of Raman spectra, the Raman signals shift by approx.  $16 \text{ cm}^{-1}$  per 1 nm wavelength shift. Although the laser intensities increased from 130 to 180 mW and 200 mW for 784 nm, 785 nm, and 786 nm, the signal intensities decrease in the same order. This is due to photobleaching of the autofluorescence background. Therefore, the decrease of spectral background during the onset of the measurements is stronger than the increase of the Raman bands due to elevated laser intensities. Figure 1b shows the three resulting difference spectra. For the red and green difference spectra a 1 nm shift (green: 784–785 nm; red: 785–786 nm) was realized, whereas the black difference spectrum resulted from a 2 nm shift. A significant, variable offset remained between the difference spectra, clearly originating from the varying fluorescence profile, which is maximum for the 2 nm shift. Figure 1c shows the normalized and optimized difference spectra (see data preprocessing in the methods section) of aforementioned difference spectra. The background is successfully corrected. Closer inspection reveals that a 1 nm shift results in difference spectra with higher noise than the 2 nm shift due to smaller amplitudes in the raw differences (see Fig. 1b). The shift in excitation wavelength should be near the full width at half maximum (FWHM) of the Raman band for the proper interpretation and reconstruction of a Raman spectrum. But since Raman bands have different FWHM as can be seen in Fig. 1a, there is not one wavelength shift that fits all FWHM of the Raman bands. Furthermore, technical parameters such as the transmission range of the laser line filter limit the wavelength shift to 2 nm.

Therefore, further data analysis was performed on the wavelength pair 784–786 nm. A trend is evident that negative difference bands are more intense than positive difference bands, which is a consequence of optimization step and the higher laser intensity at 786 nm. In the optimization step the subtrahend is multiplied by a factor to compensate for differences in background intensity. Since the subtracted spectra with the excitation wavelength of 786 nm always have a lower background due to photobleaching, all spectra are multiplied by an optimization factor larger than 1 resulting also in higher peak intensity and therefore more intense negative difference peaks.

Figure 2 gives an overview of the mean spectra (dark) and their respective standard deviation (shaded). Figure 2a shows the four tree pollen difference spectra and Fig. 2b the four non-tree pollen difference spectra for the 2 nm shift, that constitute the basis for the following classification. Figure 2c, d show the reconstructed Raman spectra after baseline correction, and Fig. 2e, f the raw Raman spectra ( $\lambda_{\text{ex}} = 784 \text{ nm}$ ) after baseline correction for comparison. Spectral differences in the tree pollen occur between  $1,600$  and  $1,750 \text{ cm}^{-1}$ , and in the high wavenumber region for larch, most likely due to higher lipid contributions of the conifer typical essential oils. Differences in non-tree pollen are also observed between  $1,600$  and  $1,750 \text{ cm}^{-1}$  and additionally in the low wavenumber region below  $1,200 \text{ cm}^{-1}$ , which can be explained by their different families and growth habits (i.e. herb, grass, and shrub). One exception is rumex and cyclamen, which show a distinct difference in band structure although they stem from the same growth habit. In moor grass, the band near  $1,600 \text{ cm}^{-1}$  is weak. The

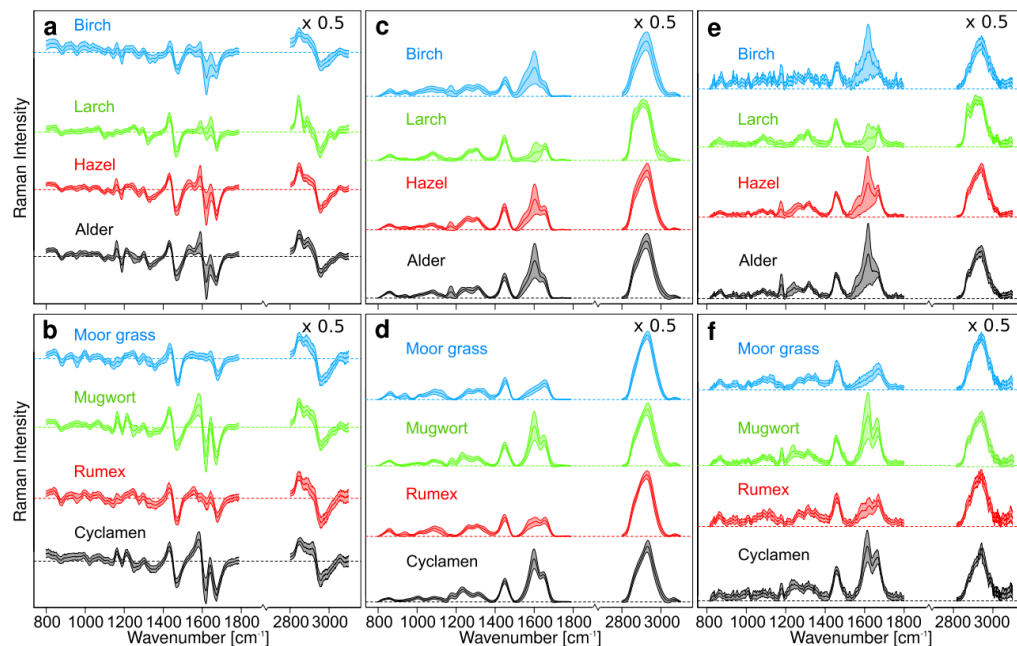


**Figure 2.** Mean and standard deviation of difference spectra (784–786 nm) after normalization and optimization for tree pollen (a) and non-tree pollen (b), spectra reconstructed from differences after SNIP baseline correction of tree pollen (c) and non-tree pollen (d) and Raman spectra ( $\lambda_{ex} = 784$  nm) after SNIP baseline correction for tree pollen (e) and non-tree pollen (f). High wavenumber regions were multiplied by 0.5.

standard variations of the  $1,600\text{ cm}^{-1}$  band is high for all pollen. In particular, some Raman spectra of birch, larch, hazel, alder and rumex pollen also have weak intensities near  $1,600\text{ cm}^{-1}$ . The reconstruction results in spectra that properly mimic the raw Raman spectra after both data were baseline corrected using the SNIP algorithm. The main difference between reconstructed and raw spectra is that the reconstruction algorithm reduces the spectral resolution. It is important to note that the subtraction algorithm does not alter the spectral resolution of the difference spectra.

**Classification of tree vs non-tree pollen data.** In the first classification step the whole data set was divided into a training data set and a test data set. A PCA was performed on the whole training data set of all pollen samples to separate major variations in the lower principal components (PCs) from noise in the higher PCs. Supplementary Fig. S1 shows the loadings of the first 15 PCs and the loading of the LDA model. Only the first 10 PCs accounting for ca. 68.6% of the variance were used for training the LDA model (for the explained variance curve see Supplementary Fig. S2). Intense variations in the loadings of the first 10 PCs can easily be seen. Almost no information is anymore provided in PC 14 and higher, whereas the high wavenumber region is dominated by noise starting from PC 11 due the lower quantum efficiency of the detector and hence lower signal intensities. A band assignment is not straightforward in the case of PC loadings based on difference spectra, since their variations are related to positive and negative Raman difference bands. This is also the case for the LD loading presented in Supplementary Fig. S1d. In the high wavenumber region the  $\text{CH}_3$  stretching (symmetric and asymmetric) bands, the  $\text{CH}_2$  stretching (symmetric and asymmetric) bands and the  $\text{CH}$  stretching bands overlap to a very broad convoluted band structure. Due to the 2 nm shift in excitation wavelength a lot of signal intensity is lost in the difference spectrum as the bands are shifted into each other. This, combined with the lower quantum efficiency of the detector, leads to a LD1 spectrum with more noise in the high wavenumber region.

The LD scores of the separation between tree pollen and non-tree pollen are shown in the box and whiskers plots in Fig. 3. In the prediction of the test data, all scores with a negative LD1 score belong to the non-tree class, all scores with a positive LD1 score belong to the tree class. Some misclassifications can be seen for the real classes. However, the medians and 0.25/0.75 quantiles are well separated and away from the class boundary at 0.

The confusion matrix is provided in Table 1. High sensitivity, specificity, accuracy and precision of over 95% are achieved with the constructed PCA-LDA model on average for all classifiers. The two classes can be very well separated using the normalized and optimized difference spectra and the constructed PCA-LDA model. Of the 133 misclassified tree pollen 22% were alder, 28% hazel and 50% birch pollen. Larch pollen contain a lot

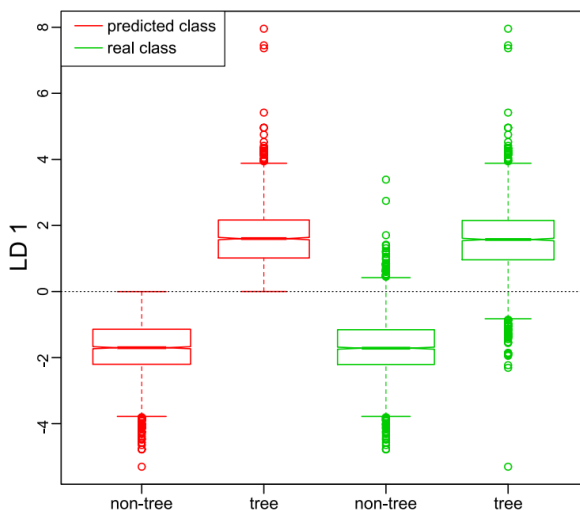


**Figure 3.** Box and whiskers LDA score plot for classification of tree vs. non-tree. Red, predicted classes of the scores of the test data set; green, real classes of the scores of the test data set.

Tree vs. non-tree	Real classes	
	Non-tree	Tree
Non-tree, predicted	2,700	133
Tree, predicted	86	2,371
Sensitivity	96.9	94.7
Specificity	94.7	96.9
Accuracy	95.9	95.9
Precision	95.3	96.5

**Table 1.** Confusion matrix of non-tree versus tree classification: real classes vs. predicted classes of the classified test spectra; sensitivity, specificity, accuracy and precision in %.

of lipids due to the conifer-typical essential oils, as also indicated in the difference spectra in Fig. 2, which leads to a clear separation without any misclassification.

**Classification of the different pollen genera.** To further analyze the feasibility of classification schemes based on SERDS difference spectra, the data set was separated into their simplified growth habits, i.e. tree and non-tree data, to classify each group into their genera. Again, the data sets were split into training and test, and a PCA-LDA model including internal cross validation was implemented for each group. The LD loadings for the discrimination of the different tree pollen types are shown in the Supplementary Fig. S3a and for the different non-tree pollen types in the Supplementary Fig. S3b. As before, the loadings and their interpretation are very complex. Nevertheless, LD3 for the non-tree separation shows a less intense spectrum. Consequently the noise has a much higher impact on the spectrum, which can be seen especially for the high wavenumber region.

For LDA modelling of the different tree pollen types, the first 13 PCs were used explaining a cumulative variance of 78.6% (for the explained variance curve see Supplementary Fig. S4). The LD scores for the different tree pollen types were successfully separated, which is shown in the LD score plot (Fig. 4). LD1 separates larch from the other trees, LD2 separates birch from the other trees and LD3 grossly separates alder from hazel. The 3D score plot shows the separation of the scores of each type.

The classification results of the different tree pollen genera are summarized in Table 2. Especially the rates for the larch pollen samples show the best values: a specificity of 99.8% and an accuracy of 99.7% are the highest values for all pollen sample classifications. This is not surprising since larch is from a different family (Pinaceae) than the other three tree types (Betulaceae). Due to the high lipid content, larch pollen did not sediment very well onto the substrate causing an overall low number of automatically detected larch pollen samples for Raman

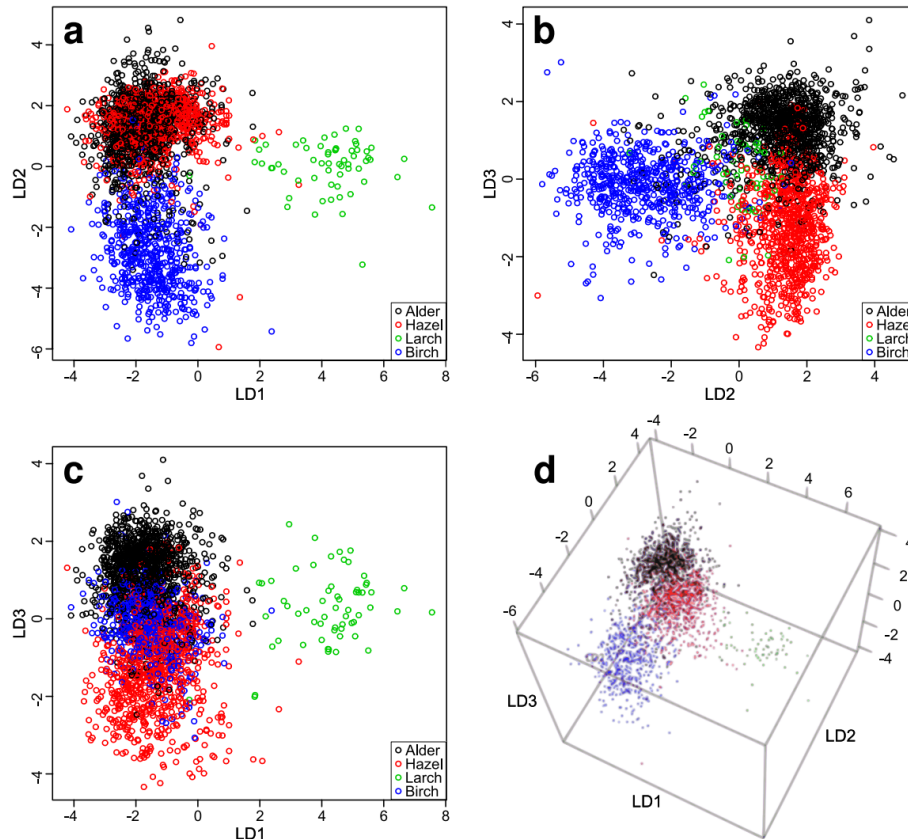


**Figure 4.** LDA score plots for classification and separation of different tree pollen genera. (a) LD1–LD2 plane of the score plot; (b) LD2–LD3 plane of the score plot; (c) LD1–LD3 plane of the score plot; (d) 3D score plot.

	Real classes			
	Alder	Hazel	Larch	Birch
Alder, predicted	947	107	0	19
Hazel, predicted	54	696	2	16
Larch, predicted	3	2	59	0
Birch, predicted	52	14	0	533
Sensitivity	89.7	85.0	96.7	93.8
Specificity	91.3	95.7	99.8	96.6
Accuracy	90.6	92.2	99.7	96.0
Precision	88.3	90.6	92.2	89.0

**Table 2.** Confusion matrix for classification and separation of tree pollen types. Upper part: real classes vs. predicted classes of the classified test spectra; lower part: sensitivity, specificity, accuracy and precision in %.

spectra acquisition (in total 61 spectra). For the separation of the tree pollen types, approx. 90% of alder pollen, 85% of hazel pollen, 97% of larch pollen and 94% of birch pollen were correctly classified.

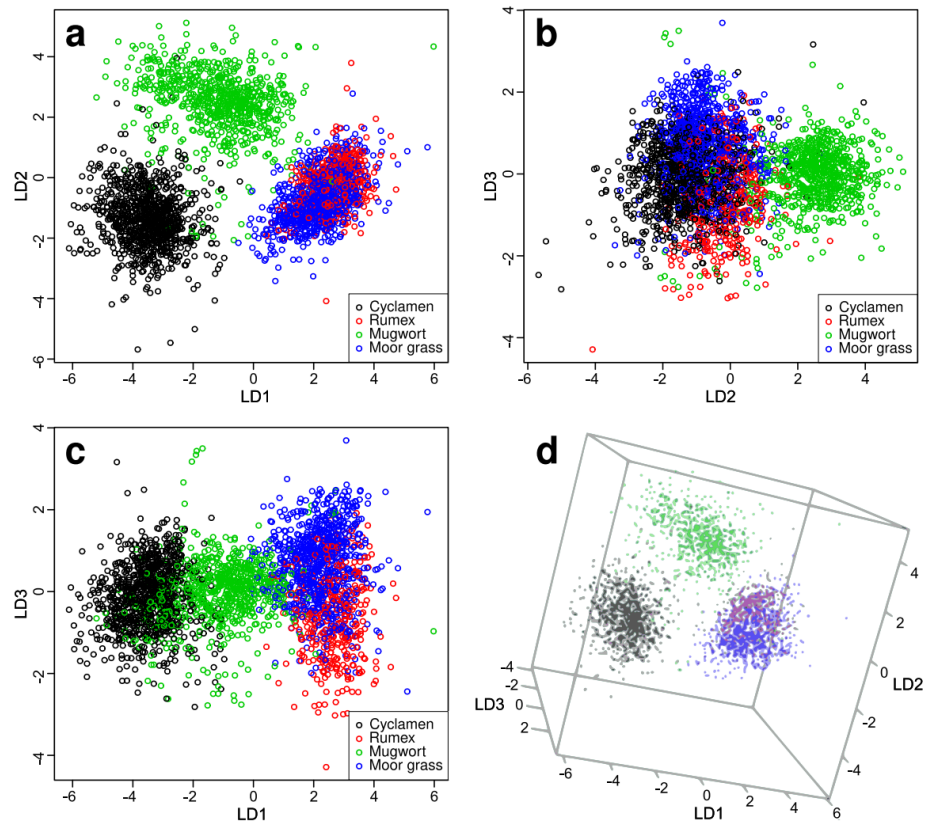


**Figure 5.** LDA score plot for classification and separation of different non-tree pollen types. (a) LD1–LD2 plane of the score plot; (b) LD2–LD3 plane of the score plot; (c) LD1–LD3 plane of the score plot; (d) 3D score plot.

For the discrimination of the non-tree data set 11 PCs were included after an internal cross validation of the training data set, explaining 61.8% of the cumulative variance (the explained variance curve see Supplementary Fig. S5). The PCA-LDA model was then used for the classification of the test data set into the four different non-tree types: mugwort, cyclamen, moor grass and rumex. The score plots of the test data classification are shown in Fig. 5. The cyclamen scores are separated from moor grass by LD1, and mugwort from all other non-tree pollen by LD2. The rumex scores can be best separated by LD3, but still exhibit a significant overlap with moor grass. In the 3D plot the scores of cyclamen and mugwort are very well separated from the other two classes, whereas rumex and moor grass have a larger overlap, thus making it hard to separate the two pollen types from one another. Table 3 shows the results of the classification of the non-tree pollen types and the corresponding classifiers in form of a confusion matrix.

In the separation between the different non-tree pollen, 98% of the cyclamen pollen, 74% of the rumex pollen, 94% of the mugwort pollen and 79% of the moor grass pollen were correctly classified. Rumex and cyclamen are herbs, mugwort a shrub type plant and moor grass a grass. The SERDS spectra of rumex and moor grass pollen are quite similar resulting in the most misclassifications. The classification of grass pollen genera by Raman spectroscopy was challenging which was also found by Mondol et al.<sup>36</sup>

**Comparison with classification of reconstructed and raw Raman spectra.** Reconstructed and raw Raman spectra after baseline correction as shown in Fig. 2 for tree and non-tree pollen were subjected to the analogous PCA-LDA classification. Confusion matrixes are presented in Supplementary Table S2. To simplify the comparison, average values for sensitivity, specificity, accuracy and precision were calculated and displayed in Supplementary Table S1. The classification rates of tree versus non-tree pollen agreed well for difference spectra and spectra at 784 and 786 nm excitation, but are 2–3% lower for the reconstructed spectra. The classification rates of tree types varied between 88 and 98%, and the reconstructed spectra tended to give lower values than

	Real classes			
	Cyclamen	Rumex	Mugwort	Moor grass
Cyclamen, predicted	897	0	18	0
Rumex, predicted	0	267	16	168
Mugwort, predicted	16	0	676	0
Moor grass, predicted	0	96	10	622
Sensitivity	98.2	73.6	93.9	78.7
Specificity	99.0	92.4	99.2	94.7
Accuracy	98.8	89.9	97.8	90.2
Precision	98.0	59.2	97.7	85.4

**Table 3.** Confusion matrix for classification and separation of non-tree pollen types. Upper part: real classes vs. predicted classes of the classified test spectra; lower part: sensitivity, specificity, accuracy and precision in %.

difference, 784 nm and 786 nm data. The classification rates of non-tree types show even stronger variations between 85 and 98%. Here, the 784 and 786 nm data gave slightly better results. Overall, the classification results differed only little. Another comparison of baseline corrected Raman spectra with difference spectra collected by wavelength modulation was presented for leukocytes and tumor cells and confirmed only small difference in classification rates<sup>57</sup>. Similar to this pollen study, the spectral background was moderate in the previous cell study. A true benefit of SERDS is expected for high spectral background and contributions from ambient light and etaloning which cannot be suppressed by state-of-art baseline correction and goes well beyond.

### Conclusions

In this contribution, the methodology was described to use difference spectra based on SERDS for classification of pollen data. Its main advantage is the analysis of single difference spectra by PCA and subsequent LDA with few PCs as input without complex data pre-processing. An optimization procedure compensated the photobleaching effects and minimized the remaining background in the difference spectra, whereas the normalization was necessary to obtain the same intensity range for all measured pollen difference spectra. This resulted in a classification based on the spectral features of the difference spectra and not based on the overall intensity of the Raman spectrum of a pollen sample. A further improvement would be rapid, serial acquisitions of Raman spectra at both wavelengths, which suppresses photobleaching effects and avoids the optimization procedure<sup>58</sup>. Since no reconstruction of the familiar profiles of Raman spectra is necessary, possible artefacts are not introduced into the spectra. The down side of this direct classification using SERDS spectra is the difficult spectral analysis of difference spectra and especially the resulting PC and LD loadings. The increase in noise level due to the subtraction of two spectra compared to a single Raman spectrum is compensated by PCA, which separated the spectral variations in the first PCs from the noise in the higher PCs. The possibility to classify different pollen samples using normalized and optimized difference spectra by a linear PCA-LDA model was successfully demonstrated. In Supplementary Table S1 the average values for sensitivity, specificity, accuracy and precision for all classifications are shown that achieved good to very good results using difference spectra as input. Since birch, hazel and alder all belong to the same family, in case of birch and alder even to the same subfamily, the pollen could even be separated on a genus level. For comparison, the reconstructed spectra and the raw spectra at 784 and 786 nm excitation after baseline correction were subjected to PCA-LDA classification. The classification rates only show small variations with a tendency of worse results for reconstructed spectra. This demonstrates the validity of our new approach based on difference spectra. The full potential of SERDS will become evident for Raman spectra that are affected by high autofluorescence background, ambient light or etaloning effects. Since the pollen detection, the laser focusing, the wavelength shifting and the data recording was fully automated, this streamlined method could be a robust and versatile system for the automated differentiation of different pollen into their genera.

### Methods

**Sample specifications.** Pollen samples used in this study were collected by the Department of Indoor Climatology (University Hospital Jena, Germany) over the last two decades and transferred to the Leibniz Institute of Photonic Technology (Jena, Germany) for storage and research purposes. Eight different pollen genera were analyzed, which can be grouped into two classes based on their growth habit: tree and non-tree (see Supplementary Table S3).

**Set-up description and specification.** The previously developed high throughput screening Raman spectroscopy platform (HTS-RS)<sup>59</sup> was modified for the implementation of SERDS and the investigation of pollen grains. A tunable laser source (DLC DL pro 780, Toptica Photonics, Germany) with a tuning range from 765 to 805 nm in combination with an amplifier (BoosTA Pro, Toptica Photonics, Germany) was fiber-coupled into a microscope set-up by a multimode fiber with a 60  $\mu\text{m}$  core diameter and 0.22 NA (Thorlabs, Germany).

The booster enhanced the laser power of the three operating wavelengths ( $\lambda = 784 \text{ nm}/785 \text{ nm}/786 \text{ nm}$ ) to the system. The incoming laser beam passed through a clean-up filter ( $785 \pm 1.5 \text{ nm}$ ; Semrock, USA) and was collimated using a 30 mm focal length lens (Thorlabs, Germany). The collimated beam was guided to the back aperture of the microscope objective ( $60\times$ , NA = 1, water immersion, Nikon, Japan) via a dichroic notch filter ( $785 \text{ nm}$ , bandwidth 89 nm; Semrock, USA) and a  $45^\circ$  tilted mirror (Thorlabs, Germany). At the end of the objective, the pollen grains were excited with an approximate focus spot diameter of  $10 \mu\text{m}$  on the sample plane. The back reflected Raman signals from the samples were collected and projected to a 100 mm focal length lens (Thorlabs, Germany) while passing through the same objective lens and the notch filter, which blocked most of the Rayleigh signal. An extra notch filter operating at  $785 \text{ nm} \pm 19 \text{ nm}$  (Laser Components, Germany) was placed before the 100 mm collection lens ensuring maximal rejection of Rayleigh signal propagation. The 100 mm collection lens focused the Raman signal to a  $100 \mu\text{m}$ , 0.22 NA multimode fiber (Thorlabs, Germany) coupling it to a spectrograph (IsoPlane160, Princeton Instruments, USA) with a 400 grooves/mm grating blazed at 750 nm. The Raman signals were projected to a charge-coupled device (CCD) (PIXIS-400BR-eXcelon; Princeton Instruments, USA) with an operating temperature of  $-60^\circ\text{C}$ . A bright field channel was integrated into the set-up for the automation of particle detection, of various calibrations and for visualization purposes. A white LED source (Thorlabs, Germany) was employed to illuminate the sample from below and the light was guided to a CCD camera (DCC1645C, Thorlabs, Germany) via a long pass filter (Semrock, USA) and a 70 mm focal length lens (Thorlabs, Germany). The bright field microscopic image was used in an in-house developed pollen detection algorithm for the automated detection of single pollen grain. All the required translations were realized using two CONEX MFA-Series motor (Newport, USA) for xy plane and a MTS25-Z8 motor (Thorlabs, Germany) for z direction<sup>36,59</sup>.

**Sample preparation and data acquisition.** Each pollen sample was suspended in 10 mL deionized water and pipetted onto a  $\text{CaF}_2$  cover slip fully immersed in deionized water. After sedimentation of the pollen, single pollen samples were automatically detected, the signal focused and measured at three different excitation wavelengths ( $\lambda_1 = 784 \text{ nm}/130 \text{ mW}$ ;  $\lambda_2 = 785 \text{ nm}/180 \text{ mW}$ ;  $\lambda_3 = 786 \text{ nm}/200 \text{ mW}$ ) before moving to the next pollen. The acquisition time for each spectrum was 0.5 s with a short dwell time of 0.5 s after each measurement to allow for wavelength shifting.

**Data preprocessing.** The collected data was analyzed in R<sup>60</sup> using the following packages: hyperSpec<sup>61</sup>, cbmodels<sup>62</sup>, Ramancal<sup>63</sup>, rgl<sup>64</sup>, pracma<sup>65</sup>, gtools<sup>66</sup> and ROCR<sup>67</sup>. The raw spectra were first corrected for cosmic spikes<sup>68</sup>, wavelength calibrated in relation to  $\lambda_{\text{ex}} = 785 \text{ nm}$  using 4-Acetaminophenole and then intensity calibrated using a white-light source calibration lamp (Raman Calibration Accessory—HCA, Kaiser Optical Systems, Inc., USA). Since the background between the different excitation wavelengths varies due to photobleaching and differences in laser intensity, the spectra of different excitation wavelengths were difference-optimized before subtraction as described previously<sup>35</sup>. For comparison, Raman spectra were reconstructed from the SERDS spectra by summation of the signal intensities ( $S(n) = \sum_{x=1}^n S(x)$ , where  $S(n)$  corresponds to the signal intensity at pixel  $n$ ) and subsequent baseline correction using the SNIP algorithm<sup>14,69</sup>. Furthermore, Raman spectra ( $\lambda_{\text{ex}} = 784 \text{ nm}$  and  $\lambda_{\text{ex}} = 786 \text{ nm}$ ) were also baseline corrected (SNIP) after cosmic spike correction, wavelength and intensity calibration.

For each pollen type a Pearson correlation of the optimized difference spectra to the respective pollen type's mean optimized difference spectrum was performed as a spectral quality control to detect outliers. To make sure that also pollen debris spectra, out-of-focus pollen spectra and pure water spectra are excluded from the data set, all spectra with a Pearson correlation coefficient below 0.52 were discarded, leading to 4–24% of spectra being discarded. However, for the larch pollen the highest percentage of 52% was discarded because of poor sedimentation and therefore a lot of out-of-focus measurements due to the high lipid content of the pollen.

The overall intensity of the Raman signal varies between pollen types. To make sure the classification occurs due to spectral features and not overall intensity differences, the difference spectra were normalized. The performed normalization was a Euclidean-distance-like area normalization.

**Data classification.** The preprocessed, optimized and normalized data was separated into a test and training data set. The training data set was chosen in a way that every pollen type was represented by the same number of spectra (ca. 60% of the smallest data set resulting in 90 spectra). The remaining spectra were used for testing. As a classification scheme the training data was first dimensionally reduced using a Principal Component Analysis (PCA) and then used to construct a Linear Discriminant Analysis (LDA) classification model. The models were internally validated using a tenfold cross validation to determine the optimal number of principal components (PCs) for building robust PCA-LDA models. In a first step 10 PCs of all eight pollen genera were classified into the two growth habits: tree and non-tree. In a second step 13 PCs of all measured tree pollen were classified based on their genera: alder, birch, hazel and larch. In the final step 11 PCs of all measured non-tree pollen were classified into their different genera: mugwort, cyclamen, moor grass and rumex. Herein, we present the  $\Delta\lambda_{\text{ex}} = 2 \text{ nm}$  shift in excitation wavelength ( $\lambda_1 = 784 \text{ nm}$ ;  $\lambda_2 = 786 \text{ nm}$ ;  $\Delta\lambda_{\text{ex}} = \lambda_1 - \lambda_2 = 2 \text{ nm}$ ). For comparison, the same classification schemes were used on the reconstructed Raman spectra and the baseline corrected Raman spectra.

Received: 2 March 2020; Accepted: 15 June 2020

Published online: 08 July 2020



## References

1. Germond, A. *et al.* Raman spectroscopy as a tool for ecology and evolution. *J. R. Soc. Interface* **14**, 20170174 (2017).
2. Butler, H. J. *et al.* Using Raman spectroscopy to characterize biological materials. *Nat. Protoc.* **11**, 664–687 (2016).
3. Cheng, J. X. & Xie, X. S. Vibrational spectroscopic imaging of living systems: An emerging platform for biology and medicine. *Science* **350**, aaa8870 (2015).
4. Hubbard, T. J. E., Shore, A. & Stone, N. Raman spectroscopy for rapid intra-operative margin analysis of surgically excised tumour specimens. *Analyst* **144**, 6479–6496 (2019).
5. Monici, M. Cell and tissue autofluorescence research and diagnostic applications. *Biotechnol. Annu. Rev.* **11**, 227–256 (2005).
6. Zięba-Palus, J. & Michalska, A. Photobleaching as a useful technique in reducing of fluorescence in Raman spectra of blue automobile paint samples. *Vib. Spectrosc.* **74**, 6–12 (2014).
7. Yakubovskaya, E., Zaliznyak, T., Martinez, J. & Taylor, G. T. Tear down the fluorescent curtain: A new fluorescence suppression method for raman microspectroscopic analyses. *Sci. Rep.* **9**, 1–9 (2019).
8. Wei, D., Chen, S. & Liu, Q. Review of fluorescence suppression techniques in Raman spectroscopy. *Appl. Spectrosc. Rev.* **50**, 387–406 (2015).
9. Afseth, N. K. & Kohler, A. Extended multiplicative signal correction in vibrational spectroscopy, a tutorial. *Chemom. Intell. Lab. Syst.* **117**, 92–99 (2012).
10. Martens, H. & Stark, E. Extended multiplicative signal correction and spectral interference subtraction: New preprocessing methods for near infrared spectroscopy. *J. Pharm. Biomed. Anal.* **9**, 625–635 (1991).
11. Stark, E. W. & Martens, H. Multiplicative signal correction method and apparatus. US Patent US005568400A, 1–19 (1990).
12. Pirzer, M. & Sawatzki, J. Patent Application Publication Pub. No.: US 2006/0211562 A1. 1–11 (2006).
13. Kneen, M. A. & Annegarn, H. J. Algorithm for fitting XRF, SEM and PIXE X-ray spectra backgrounds. *Nucl. Instrum. Methods Phys. Res. Sect. B Beam Interact. Mater. At.* **109–110**, 209–213 (1996).
14. Morhac, M. Software Package for R—Peaks: Background estimation, Markov smoothing, deconvolution and peaks search functions. (2012). <https://rdrr.io/cran/Peaks/>.
15. Mahadevan-jansen, A. & Lieber, C. A. Automated method for subtraction of fluorescence from biological Raman spectra. *Appl. Spectrosc.* **57**, 1363–1367 (2003).
16. Cordero, E. *et al.* Bladder tissue characterization using probe-based Raman spectroscopy: Evaluation of tissue heterogeneity and influence on the model prediction. *J. Biophotonics* **13**, e201960025 (2020).
17. Bergholt, M. S. *et al.* Characterizing variability of in vivo Raman spectroscopic properties of different anatomical sites of normal colorectal tissue towards cancer diagnosis at colonoscopy. *Anal. Chem.* **87**, 960–966 (2015).
18. Desroches, J. *et al.* A new method using Raman spectroscopy for in vivo targeted brain cancer tissue biopsy. *Sci. Rep.* **8**, 1–10 (2018).
19. Galli, R. *et al.* Rapid label-free analysis of brain tumor biopsies by near infrared Raman and fluorescence spectroscopy—A study of 209 patients. *Front. Oncol.* **9**, 1–13 (2019).
20. Shreve, A. P., Cherepy, N. J. & Mathies, R. A. Effective rejection of fluorescence interference in Raman spectroscopy using a shifted excitation difference technique. *Appl. Spectrosc.* **46**, 707–711 (1992).
21. Dochow, S. *et al.* Etaloning, fluorescence and ambient light suppression by modulated wavelength Raman spectroscopy. *Biomed. Spectrosc. Imaging* **1**, 383–389 (2012).
22. Maiwald, M. *et al.* Microsystem 671 nm light source for shifted excitation Raman difference spectroscopy. *Appl. Opt.* **48**, 2789 (2009).
23. Bell, S. E. J. J., Bourguignon, E. S. O. O. & Dennis, A. Analysis of luminescent samples using subtracted shifted Raman spectroscopy. *Analyst* **123**, 1729–1734 (1998).
24. Maiwald, M. *et al.* Microsystem light source at 488 nm for shifted excitation resonance Raman difference spectroscopy. *Appl. Spectrosc.* **63**, 1283–1287 (2009).
25. Kiefer, J. Instantaneous shifted-excitation Raman difference spectroscopy (iSERDS). *J. Raman Spectrosc.* **45**, 980–983 (2014).
26. Sowidnich, K. & Kronfeldt, H.-D. Fluorescence rejection by shifted excitation Raman difference spectroscopy at multiple wavelengths for the investigation of biological samples. *ISRN Spectrosc.* **2012**, 1–11 (2012).
27. Noack, K. *et al.* Combined shifted-excitation Raman difference spectroscopy and support vector regression for monitoring the algal production of complex polysaccharides. *Analyst* **138**, 5639–5646 (2013).
28. Martins, M. A. *et al.* Shifted-excitation Raman difference spectroscopy for in vitro and in vivo biological samples analysis. *Biomed. Opt. Express* **1**, 617 (2010).
29. Gebrekidan, M. T. *et al.* A shifted-excitation Raman difference spectroscopy (SERDS) evaluation strategy for the efficient isolation of Raman spectra from extreme fluorescence interference. *J. Raman Spectrosc.* **47**, 198–209 (2016).
30. Maiwald, M., Müller, A., Sumpf, B., Erbert, G. & Tränkle, G. Capability of shifted excitation Raman difference spectroscopy under ambient daylight. *Appl. Opt.* **54**, 5520 (2015).
31. Maiwald, M., Müller, A., Sumpf, B. & Tränkle, G. A portable shifted excitation Raman difference spectroscopy system: Device and field demonstration. *J. Raman Spectrosc.* **47**, 1180–1184 (2016).
32. Schmälzlin, E. *et al.* Ultrafast imaging Raman spectroscopy of large-area samples without stepwise scanning. *J. Sens. Sens. Syst.* **5**, 261–271 (2016).
33. Zhao, J., Carrabba, M. M. & Allen, F. S. Automated fluorescence rejection using shifted excitation Raman difference spectroscopy. *Appl. Spectrosc.* **56**, 834–845 (2002).
34. Guo, S., Chernavskaia, O., Popp, J. & Bocklitz, T. Spectral reconstruction for shifted-excitation Raman difference spectroscopy (SERDS). *Talanta* **186**, 372–380 (2018).
35. Cordero, E. *et al.* Evaluation of shifted excitation raman difference spectroscopy and comparison to computational background correction methods applied to biochemical Raman spectra. *Sensors (Switzerland)* **17**, 1724 (2017).
36. Mondol, *et al.* Application of high-throughput screening Raman spectroscopy (HTS-RS) for label-free identification and molecular characterization of pollen. *Sensors* **19**, 4428 (2019).
37. Holt, K., Allen, G., Hodgson, R., Marsland, S. & Flenley, J. Progress towards an automated trainable pollen location and classifier system for use in the palynology laboratory. *Rev. Palaeobot. Palynol.* **167**, 175–183 (2011).
38. Haas, N. Q. *Automated Pollen Image Classification*. Master thesis, University of Tennessee (2011).
39. Koutsoukos, I. *Automated Classification of Pollen Grains from Microscope Images using Computer Vision and Semantic Web Technologies*. Diploma thesis, Technical University of Crete (2013).
40. Dell'Anna, R. *et al.* Pollen discrimination and classification by Fourier transform infrared (FT-IR) microspectroscopy and machine learning. *Anal. Bioanal. Chem.* **394**, 1443–1452 (2009).
41. Gottardini, E., Rossi, S., Cristofolini, F. & Benedetti, L. Use of Fourier transform infrared (FT-IR) spectroscopy as a tool for pollen identification. *Aerobiologia (Bologna)* **23**, 211–219 (2007).
42. Pappas, C. S., Tarantilis, P. A., Harizanis, P. C. & Polissiou, M. G. New method for pollen identification by FT-IR spectroscopy. *Appl. Spectrosc.* **57**, 23–27 (2003).
43. Samuels, A. C., DeLucia, F. C., McNesby, K. L. & Miziolek, A. W. Laser-induced breakdown spectroscopy of bacterial spores, molds, pollens, and protein: Initial studies of discrimination potential. *Appl. Opt.* **42**, 6205 (2003).

44. Schulte, F., Panne, U. & Kneipp, J. Molecular changes during pollen germination can be monitored by Raman microspectroscopy. *J. Biophotonics* **3**, 542–547 (2010).
45. Laucks, M. L., Roll, G., Schweiger, G. & Davis, E. J. Physical and chemical (RAMAN) characterization of bioaerosols-pollen. *J. Aerosol. Sci.* **31**, 307–319 (2000).
46. Bağcıoğlu, M., Zimmermann, B. & Kohler, A. A multiscale vibrational spectroscopic approach for identification and biochemical characterization of pollen. *PLoS ONE* **10**, 1–19 (2015).
47. Merlin, J. C. Resonance Raman spectroscopy of carotenoids and carotenoid-containing systems. *Pure Appl. Chem.* **57**, 785–792 (2007).
48. Wang, C., Pan, Y. L., Hill, S. C. & Redding, B. Photophoretic trapping-Raman spectroscopy for single pollens and fungal spores trapped in air. *J. Quant. Spectrosc. Radiat. Transf.* **153**, 4–12 (2015).
49. Pummer, B. G. *et al.* Chemistry and morphology of dried-up pollen suspension residues. *J. Raman Spectrosc.* **44**, 1654–1658 (2013).
50. Seifert, S., Merk, V. & Kneipp, J. Identification of aqueous pollen extracts using surface enhanced Raman scattering (SERS) and pattern recognition methods. *J. Biophotonics* **9**, 181–189 (2016).
51. Schulte, F., Mäder, J., Kroh, L. W., Panne, U. & Kneipp, J. Characterization of pollen carotenoids with in situ and high-performance thin-layer chromatography supported resonant Raman spectroscopy. *Anal. Chem.* **81**, 8426–8433 (2009).
52. Zimmermann, B. Characterization of pollen by vibrational spectroscopy. *Appl. Spectrosc.* **64**, 1364–1373 (2010).
53. Schulz, H., Baranska, M. & Baranski, R. Potential of NIR-FT-Raman spectroscopy in natural carotenoid analysis. *Biopolymers* **77**, 212–221 (2005).
54. Sengupta, A., Laucks, M. L. & James Davis, E. Surface-enhanced Raman spectroscopy of bacteria and pollen. *Appl. Spectrosc.* **59**, 1016–1023 (2005).
55. Schulte, F., Lingott, J., Panne, U. & Kneipp, J. Chemical characterization and classification of pollen. *Anal. Chem.* **80**, 9551–9556 (2008).
56. Ivleva, N. P., Niessner, R. & Panne, U. Characterization and discrimination of pollen by Raman microscopy. *Anal. Bioanal. Chem.* **381**, 261–267 (2005).
57. Dochow, S. *et al.* Classification of Raman spectra of single cells with autofluorescence suppression by wavelength modulated excitation. *Anal. Methods* **5**, 4608–4614 (2013).
58. Sowoidnich, K., Towrie, M., Maiwald, M., Sumpf, B. & Matousek, P. Shifted excitation Raman difference spectroscopy with charge-shifting CCD lock-in detection. *Appl. Spectrosc.* **73**, 1265–1276 (2019).
59. Schie, I. W. *et al.* High-throughput screening Raman spectroscopy platform for label-free celloomics. *Anal. Chem.* **90**, 2023–2030 (2018).
60. R Core Team. R: A Language and Environment for Statistical Computing. (2018).
61. Beleites, C. & Sergio, V. Software Package for R-hyperSpec: A package to handle hyperspectral data sets in R. (2018).
62. Beleites, C. Software Package for R-cbmodels: Collection of ‘combined’ models: PCA-LDA, PLS-LDA, PLS-LR as well as EMSC. (2015).
63. Beleites, C. Software Package for R-Ramancal: Calibration routines for Raman spectrometers. (2013).
64. Adler, D., Murdoch, D. & others. Software Package for R-rgl: 3D Visualization Using OpenGL. (2018).
65. Borchers, H. W. Software Package for R-pracma: Practical Numerical Math Functions. (2018).
66. Warnes, G. R., Bolker, B. & Lumley, T. Software Package for R-gtools: Various R Programming Tools. (2018).
67. Sing, T., Sander, O., Beerenwinkel, N. & Lengauer, T. Software Package for R-ROCR: Visualizing classifier performance in R. *Bioinformatics* **21**, 7881 (2005).
68. Ryabchikov, O. Software Package for R-Spikes: Spike Correction of Raman Spectral Data. (2016).
69. Gibb, S. & Strimmer, K. MALDIquant: A versatile R package for the analysis of mass spectrometry data. *Bioinformatics* **28**, 2270–2271 (2012).

### Acknowledgements

We thank Thomas Bocklitz and Jan Rüger for the fruitful discussions about the statistical analysis. For providing us the pollen samples, we thank Thomas Henkel und Andreas Kleiber. This work was funded by the Leibniz Association through the project HYPERAM (SAW-2016-IPHT-2). The publication fee of this article was funded by the Open Access Fund of the Leibniz Association.

### Author contributions

The initial conceptualization and methodology was done by F.K., C.S., C.K. and J.P. A.S.M. and I.W.S. built the set-up and programmed the automated pollen detection, automated focus and automated shifting of the laser source. F.K. performed the measurements and the data analysis. C.K., I.W.S. and J.P. provided materials, equipment and laboratory. All authors discussed and agreed the results. F.K. and A.S.M. wrote the original draft of the manuscript. All authors reviewed and edited the manuscript. Supervision of the work was done by C.S., C.K. and J.P.

### Competing interests

The authors declare no competing interests.

### Additional information

**Supplementary information** is available for this paper at <https://doi.org/10.1038/s41598-020-67897-4>.

**Correspondence** and requests for materials should be addressed to C.K.

**Reprints and permissions information** is available at [www.nature.com/reprints](http://www.nature.com/reprints).

**Publisher’s note** Springer Nature remains neutral with regard to jurisdictional claims in published maps and institutional affiliations.

www.nature.com/scientificreports/



**Open Access** This article is licensed under a Creative Commons Attribution 4.0 International License, which permits use, sharing, adaptation, distribution and reproduction in any medium or format, as long as you give appropriate credit to the original author(s) and the source, provide a link to the Creative Commons license, and indicate if changes were made. The images or other third party material in this article are included in the article's Creative Commons license, unless indicated otherwise in a credit line to the material. If material is not included in the article's Creative Commons license and your intended use is not permitted by statutory regulation or exceeds the permitted use, you will need to obtain permission directly from the copyright holder. To view a copy of this license, visit <http://creativecommons.org/licenses/by/4.0/>.

© The Author(s) 2020

# New Methodology to Process Shifted Excitation Raman Difference Spectroscopy Data: A Case Study of Pollen Classification

F. Korinth<sup>1</sup>, A.S. Mondol<sup>1</sup>, C. Stiebing<sup>1</sup>, I.W. Schie<sup>1,2</sup>, C. Krafft<sup>1\*</sup>, J. Popp<sup>1,3</sup>

<sup>1</sup> Leibniz Institute of Photonic Technology, Jena, Albert-Einstein-Straße 9, 07745 Jena, Germany

<sup>2</sup> Department of Medical Engineering and Biotechnology, University of Applied Sciences, Jena, Carl-Zeiss-Promenade 2, 07745 Jena, Germany

<sup>3</sup> Institute of Physical Chemistry and Abbe Center of Photonics, Friedrich Schiller University Jena, Jena, Helmholtzweg 4, 07743 Jena, Germany

\* christoph.krafft@leibniz-ipht.de

## Supplementary Information: Tables

**Supplementary Tables S1. Average sensitivity, specificity, accuracy and precision in % using difference, reconstructed, 784 nm and 786 nm excited Raman spectra as input.**

### A: tree versus non-tree classification

Classifiers	Difference	Reconstructed	784 nm	786 nm
Sensitivity	95.8	92.8	95.7	95.2
Specificity	95.8	92.8	95.7	95.2
Accuracy	95.9	92.7	95.7	95.1
Precision	95.9	92.7	95.6	95.1

### B: tree types

Classifiers	Difference	Reconstructed	784 nm	786 nm
Sensitivity	91.3	89.9	93.8	95.6
Specificity	95.9	95.2	96.8	98.2
Accuracy	94.6	93.7	95.9	97.5
Precision	90.0	88.3	91.5	93.6

### C: non-tree types

Classifiers	Difference	Reconstructed	784 nm	786 nm
Sensitivity	86.1	89.8	91.5	90.3
Specificity	96.3	97.3	97.7	97.3
Accuracy	94.2	95.8	96.4	95.7
Precision	85.1	89.3	90.6	88.8

## Supplementary Tables S2A: tree versus non-tree classification

<i>Reconstructed</i>		<b>REAL CLASSES</b>	
		<i>Non-tree</i>	<i>Tree</i>
<b>PREDICTED CLASSES</b>	<i>Non-tree</i>	2579	179
	<i>Tree</i>	207	2325
Sensitivity		92.6	92.9
Specificity		92.9	92.6
Accuracy		92.7	92.7
Precision		93.5	91.8

<i>784 nm</i>		<b>REAL CLASSES</b>	
		<i>Non-tree</i>	<i>Tree</i>
<b>PREDICTED CLASSES</b>	<i>Non-tree</i>	2649	93
	<i>Tree</i>	137	2411
Sensitivity		95.1	96.3
Specificity		96.3	95.1
Accuracy		95.7	95.7
Precision		96.6	94.6

<i>786 nm</i>		<b>REAL CLASSES</b>	
		<i>Non-tree</i>	<i>Tree</i>
<b>PREDICTED CLASSES</b>	<i>Non-tree</i>	2607	79
	<i>Tree</i>	179	2425
Sensitivity		93.6	96.8
Specificity		96.8	93.6
Accuracy		95.1	95.1
Precision		97.1	93.1

**Supplementary Tables S2B: classification of tree types**

<i>Reconstructed</i>		<b>REAL CLASSES</b>			
		<i>Alder</i>	<i>Hazel</i>	<i>Larch</i>	<i>Birch</i>
<b>PREDICTED CLASSES</b>	<i>Alder</i>	903	93	0	38
	<i>Hazel</i>	83	703	2	8
	<i>Larch</i>	0	4	59	1
	<i>Birch</i>	70	19	0	521
Sensitivity		85.5	85.8	96.7	91.7
Specificity		91.0	94.5	99.8	95.4
Accuracy		88.7	91.7	99.7	94.6
Precision		87.3	88.3	92.2	85.4

<i>784 nm</i>		<b>REAL CLASSES</b>			
		<i>Alder</i>	<i>Hazel</i>	<i>Larch</i>	<i>Birch</i>
<b>PREDICTED CLASSES</b>	<i>Alder</i>	954	54	0	47
	<i>Hazel</i>	57	764	0	0
	<i>Larch</i>	5	2	61	1
	<i>Birch</i>	40	0	0	520
Sensitivity		90.3	93.3	100.0	91.5
Specificity		93.0	96.6	99.7	97.9
Accuracy		91.9	95.5	99.7	96.5
Precision		90.4	93.1	89.7	92.9

<i>786 nm</i>		<b>REAL CLASSES</b>			
		<i>Alder</i>	<i>Hazel</i>	<i>Larch</i>	<i>Birch</i>
<b>PREDICTED CLASSES</b>	<i>Alder</i>	987	29	0	17
	<i>Hazel</i>	29	788	2	5
	<i>Larch</i>	5	2	59	0
	<i>Birch</i>	35	0	0	546
Sensitivity		93.5	96.2	96.7	96.1
Specificity		96.8	97.9	99.7	98.2
Accuracy		95.4	97.3	99.6	97.7
Precision		95.5	95.6	89.4	94.0

## Supplementary Tables S2C: classification of non-tree types

<i>Reconstructed</i>		REAL CLASSES			
		<i>Cyclamen</i>	<i>Rumex</i>	<i>Mugwort</i>	<i>Moor grass</i>
PREDICTED CLASSES	<i>Cyclamen</i>	896	0	24	0
	<i>Rumex</i>	1	289	10	93
	<i>Mugwort</i>	15	0	671	0
	<i>Moor grass</i>	1	74	15	697
Sensitivity		98.1	79.6	93.2	88.2
Specificity		98.7	95.7	99.3	95.5
Accuracy		98.5	93.6	97.7	93.4
Precision		97.4	73.5	97.8	88.6

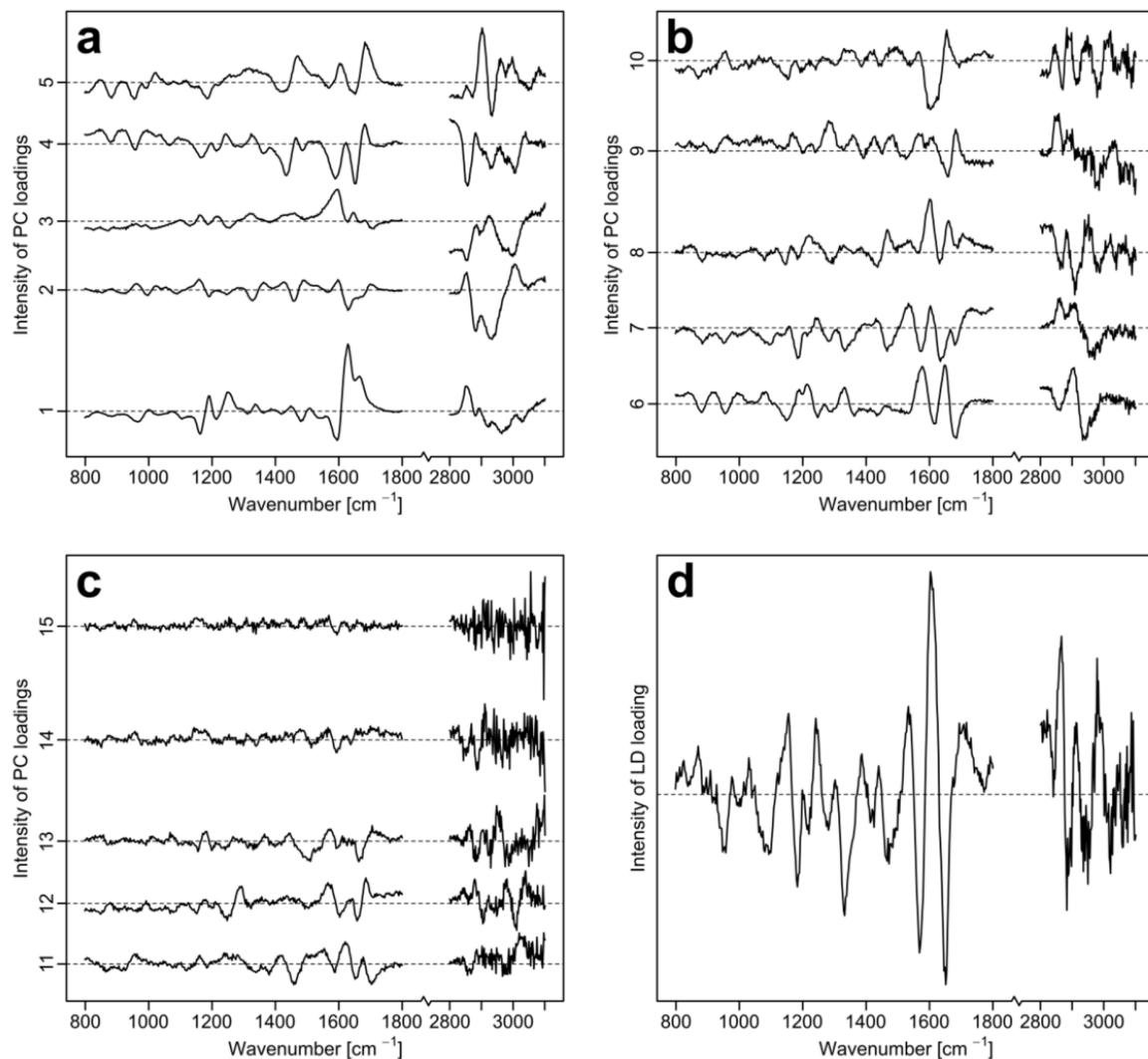
<i>784 nm</i>		REAL CLASSES			
		<i>Cyclamen</i>	<i>Rumex</i>	<i>Mugwort</i>	<i>Moor grass</i>
PREDICTED CLASSES	<i>Cyclamen</i>	899	0	18	1
	<i>Rumex</i>	2	309	6	93
	<i>Mugwort</i>	10	0	679	0
	<i>Moor grass</i>	2	54	17	696
Sensitivity		98.5	85.1	94.3	88.1
Specificity		99.0	95.8	99.5	96.3
Accuracy		98.8	94.4	98.2	94.0
Precision		97.9	75.4	98.5	90.5

<i>786 nm</i>		REAL CLASSES			
		<i>Cyclamen</i>	<i>Rumex</i>	<i>Mugwort</i>	<i>Moor grass</i>
PREDICTED CLASSES	<i>Cyclamen</i>	901	0	7	0
	<i>Rumex</i>	3	307	12	135
	<i>Mugwort</i>	9	0	684	0
	<i>Moor grass</i>	0	56	17	655
Sensitivity		98.7	84.6	95.0	82.9
Specificity		99.6	93.8	99.6	96.3
Accuracy		99.3	92.6	98.4	92.5
Precision		99.2	67.2	98.7	90.0

**Supplementary Table S3. Data Set Overview:** Name, growth habit, family, genus and number of spectra for the training and test data set of the analyzed pollen samples.

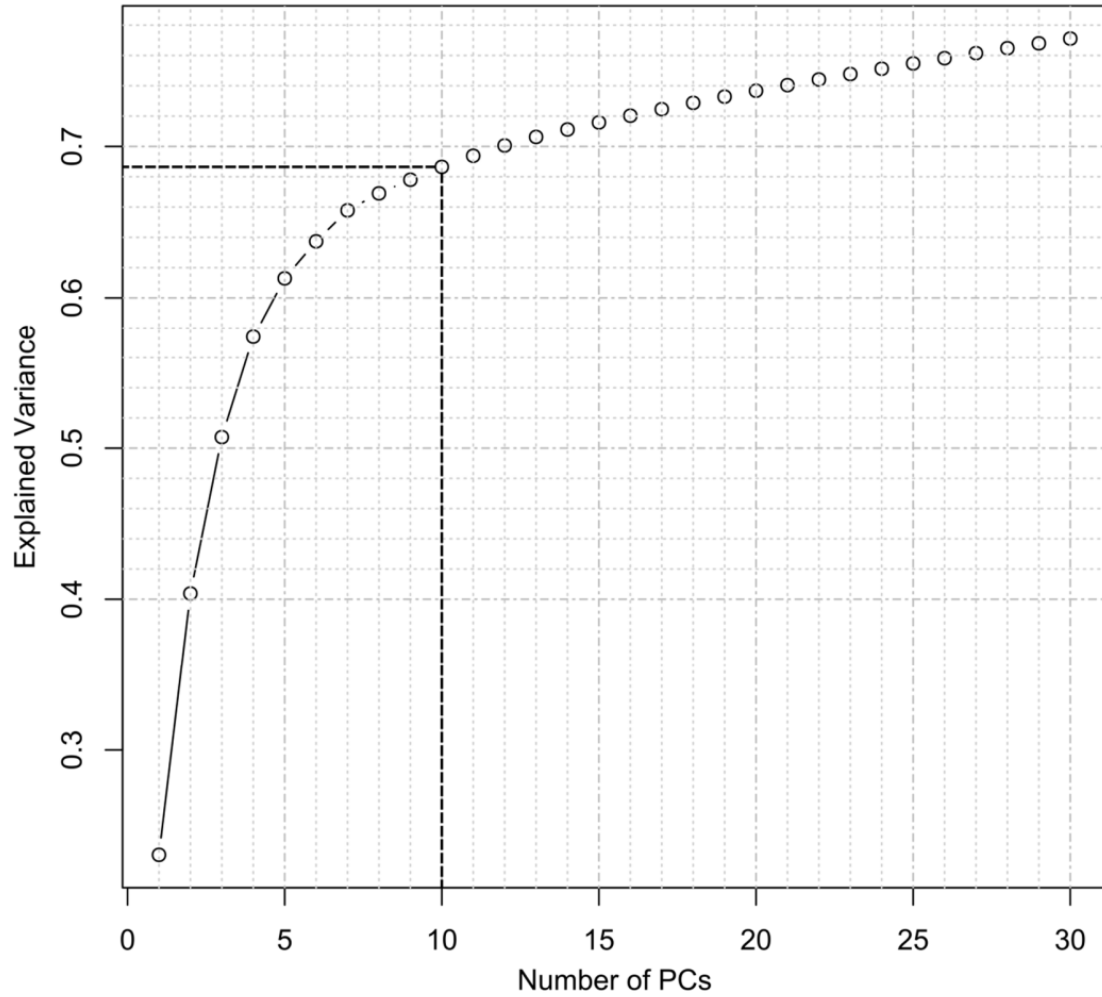
Name	Growth habit	Family	Genus	Training set Number of spectra	Test set Number of spectra
Alder	Tree	Betulaceae	Alnus	90	1056
Birch	Tree	Betulaceae	Betula	90	586
Hazel	Tree	Betulaceae	Corylus	90	819
Larch	Tree	Pinaceae	Larix	90	61
Cyclamen	Non-tree (herb)	Primulaceae	Cyclamen	90	913
Rumex	Non-tree (herb)	Polygonaceae	Rumex	90	363
Mugwort	Non-tree (shrub)	Asteraceae	Artemisia	90	720
Moor grass	Non-tree (grass)	Poaceae	Molinia	90	790

**Supplementary Information: Figures**

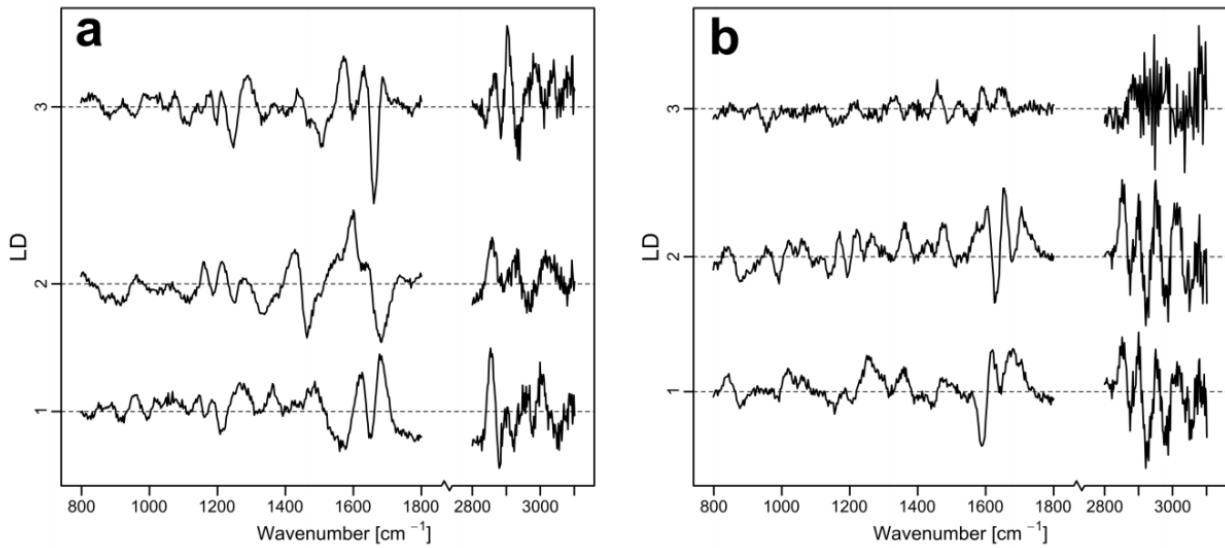


**Supplementary Figure S1. Loadings of the PCA and the LDA of the whole training data set (8 pollen types) – classification of tree vs. non-tree:** loadings 1 – 5 (a), loadings 6 – 10 (b), loadings 11 – 15 (c) of the PCA, d, loading of the LDA (d).

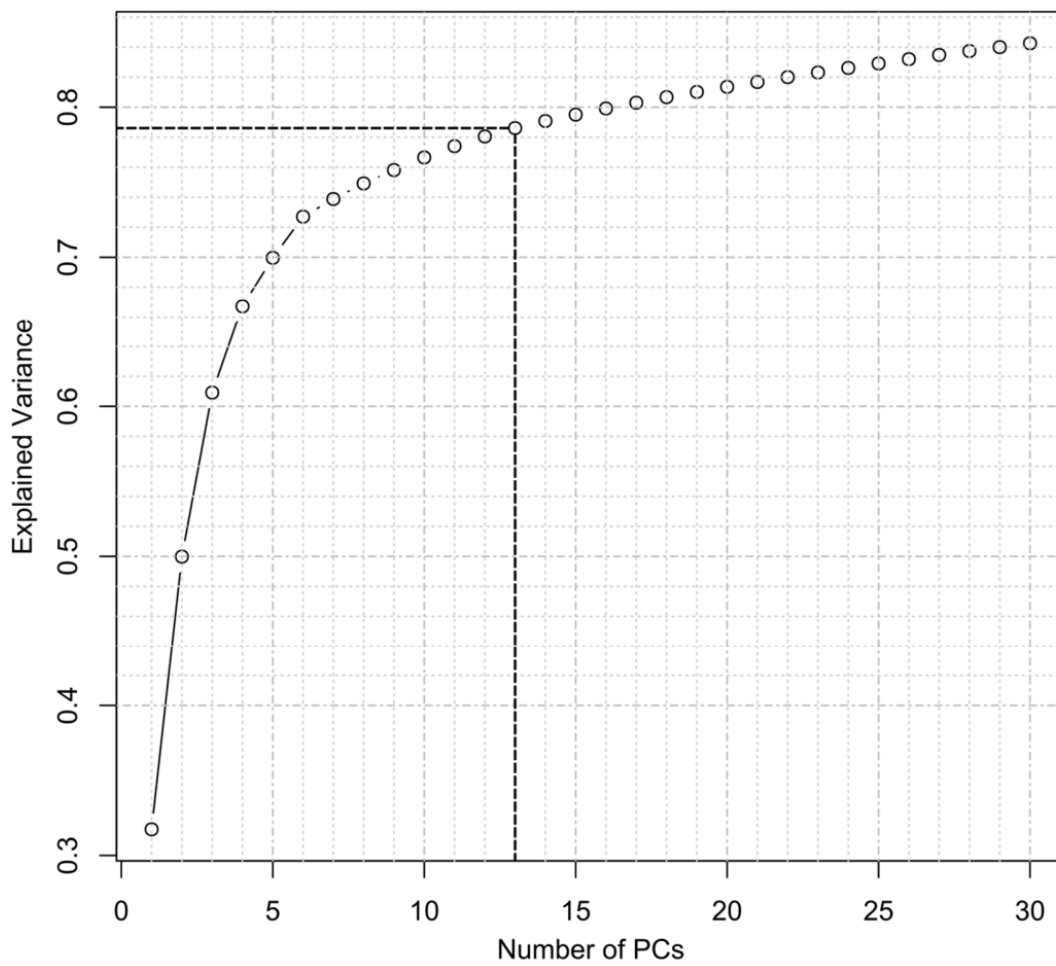




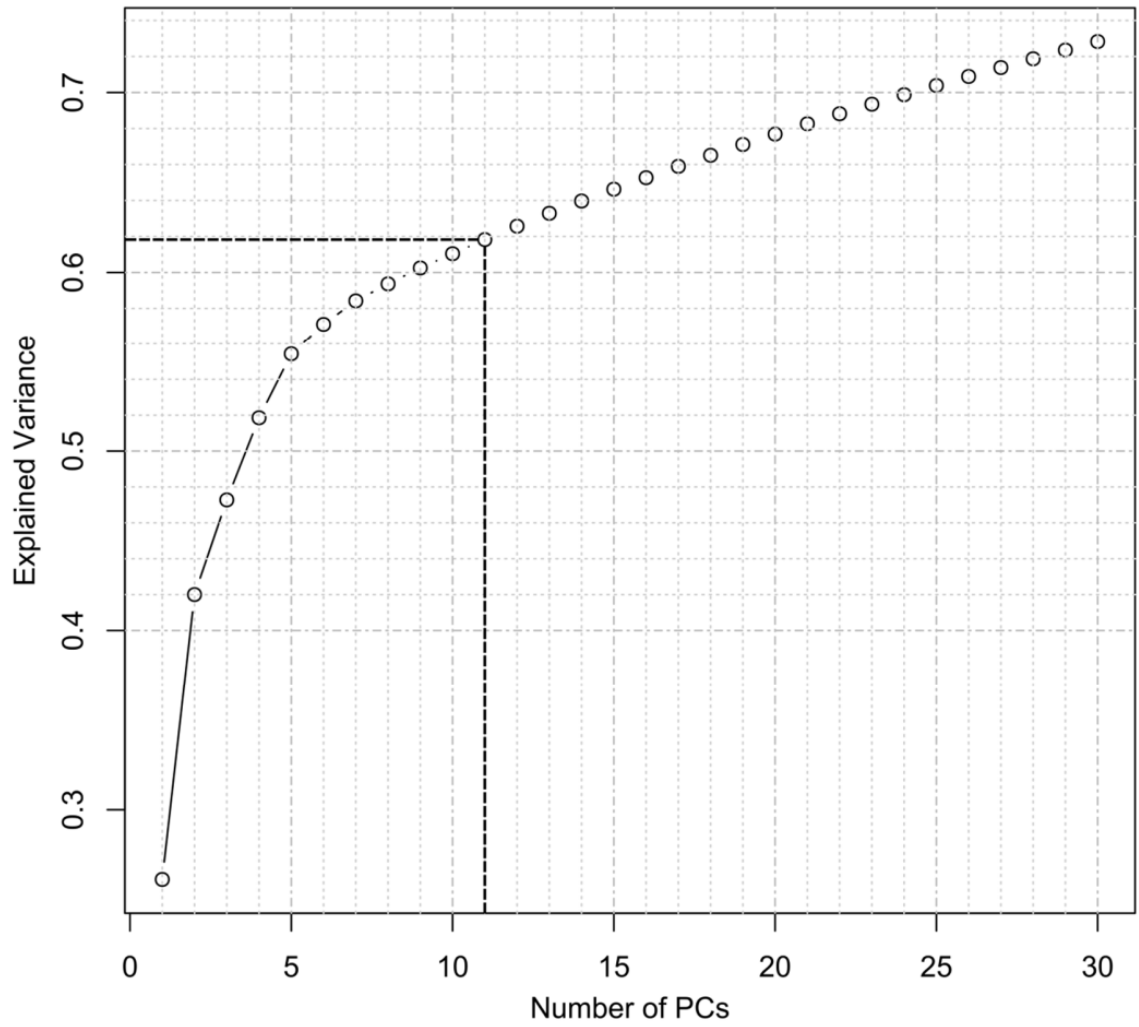
**Supplementary Figure S2. Explained variance curve of the PCA of the whole training data set (8 different pollen types) – classification of tree vs. non-tree, and optimal number of PCs according to the 10-fold cross validation results (dashed line).**



**Supplementary Figure S3. LD loadings for classification and separation of pollen genera:** tree pollen types (A) and non-tree pollen types (B).



**Supplementary Figure S4. Explained variance curve of the PCA for the separation of tree genera:** optimal number of PCs according to the 10-fold cross validation results was 13 (dashed line).



**Supplementary Figure S5. Explained variance curve of the PCA for the separation of non-tree genera:** optimal number of PCs according to the 10-fold cross validation results was 11 (dashed line).

### **6.3. Wide Field Spectral Imaging with Shifted Excitation Raman Difference Spectroscopy Using the Nod and Shuffle Technique [FK3]**

Florian Korinth, Elmar Schmäzlin, Clara Stiebing, Tanya Urrutia, Genoveva Micheva, Christer Sandin, André Müller, Martin Maiwald, Bernd Sumpf, Christoph Krafft, Bernd Tränkle, Martin M. Roth, Jürgen Popp (2020)  
*Sensors*, **20**: 6723, 1 – 19.

Der Nachdruck der folgenden Publikation, welche unter einer internationalen Creative Commons Attribution 4.0-Lizenz steht (<http://creativecommons.org/licenses/by/4.0/>), erscheint mit freundlicher Genehmigung von MDPI.

**Erklärung zu den Eigenanteilen des Promovenden sowie der weiteren Doktoranden/ Doktorandinnen als Koautoren an den Publikationen und Zweitpublikationsrechten bei einer kumulativen Dissertation.**

Doktoranden	Florian Korinth
Konzeption des Forschungsansatzes	
Aufbau und Programmierung des Messaufbaus	
Planung der Untersuchungen	x
Datenerhebung	x
Datenanalyse und –interpretation	x
Schreiben des Manuskripts	x
Vorschlag Anrechnung Publikationsäquivalente	1,0



Article

# Wide Field Spectral Imaging with Shifted Excitation Raman Difference Spectroscopy Using the Nod and Shuffle Technique

Florian Korinth <sup>1</sup>, Elmar Schmälzlin <sup>2</sup>, Clara Stiebing <sup>1</sup>, Tanya Urrutia <sup>2</sup>, Genoveva Micheva <sup>2</sup>, Christer Sandin <sup>3</sup>, André Müller <sup>4</sup>, Martin Maiwald <sup>4</sup>, Bernd Sumpf <sup>4</sup>, Christoph Krafft <sup>1,\*</sup>, Günther Tränkle <sup>4</sup>, Martin M. Roth <sup>2</sup> and Jürgen Popp <sup>1,5</sup>

- <sup>1</sup> Leibniz Institute of Photonic Technology (Leibniz IPHT), Member of Research Alliance “Health Technologies”, Albert-Einstein-Straße 9, Jena 07743, Germany; florian.korinth@leibniz-ipht.de (F.K.); clara.stiebing@leibniz-ipht.de (C.S.); juergen.popp@leibniz-ipht.de (J.P.)
  - <sup>2</sup> Leibniz Institute for Astrophysics Potsdam (AIP), Associated Member of Research Alliance “Health Technologies”, An der Sternwarte 16, Potsdam 14482, Germany; eschmaelzlin@aip.de (E.S.); turrutia@aip.de (T.U.); gmicheva@aip.de (G.M.); mmroth@aip.de (M.M.R.)
  - <sup>3</sup> Sandin Advanced Visualization, Tylögränd 14, 12156 Johanneshov, Sweden; christersandin@yahoo.se (Ch.S.)
  - <sup>4</sup> Ferdinand-Braun-Institut, Leibniz-Institut für Höchstfrequenztechnik, Member of Research Alliance “Health Technologies”, Gustav-Kirchhoff-Str. 4, Berlin 12489, Germany; andre.mueller@fbh-berlin.de (A.M.); martin.maiwald@fbh-Berlin.de (M.M.); bernd.sumpf@fbh-berlin.de (B.S.); guenther.traenkle@fbh-berlin.de (G.T.)
  - <sup>5</sup> Institute of Physical Chemistry and Abbe Center of Photonics, Friedrich Schiller University Jena, Helmholtzweg 4, Jena 07743, Germany;
- \* Correspondence: christoph.krafft@leibniz-ipht.de

Received: 06 October 2020; Accepted: 20 November 2020; Published: date

**Abstract:** Wide field Raman imaging using the integral field spectroscopy approach was used as a fast, one shot imaging method for the simultaneous collection of all spectra composing a Raman image. For the suppression of autofluorescence and background signals such as room light, shifted excitation Raman difference spectroscopy (SERDS) was applied to remove background artifacts in Raman spectra. To reduce acquisition times in wide field SERDS imaging, we adapted the nod and shuffle technique from astrophysics and implemented it into a wide field SERDS imaging setup. In our adapted version, the nod corresponds to the change in excitation wavelength, whereas the shuffle corresponds to the shifting of charges up and down on a Charge-Coupled Device (CCD) chip synchronous to the change in excitation wavelength. We coupled this improved wide field SERDS imaging setup to diode lasers with 784.4/785.5 and 457.7/458.9 nm excitation and applied it to samples such as paracetamol and aspirin tablets, polystyrene and polymethyl methacrylate beads, as well as pork meat using multiple accumulations with acquisition times in the range of 50 to 200 ms. The results tackle two main challenges of SERDS imaging: gradual photobleaching changes the autofluorescence background, and multiple readouts of CCD detector prolong the acquisition time.

**Keywords:** Raman spectroscopy; SERDS; wide field imaging; nod and shuffle; photobleaching; autofluorescence; integral field spectroscopy; background suppression; diode lasers

## 1. Introduction

Raman spectroscopy provides a label-free, non-destructive insight into the biochemical composition of a sample. It can be used for the pathological assessment of biological samples such as cells and tissues [1–5]. Although the majority of biomolecules such as nucleic acids, proteins, lipids, and carbohydrates do not fluoresce at visible excitation, autofluorescence is often excited along with Raman scattering in biological samples [6]. Since the fluorescence absorption cross-section is much larger than the Raman scattering cross-section, even trace amounts of autofluorescent molecules often result in high-intensity spectral backgrounds. This high background can mask the Raman fingerprint information and increases the shot noise in spectra [7].

Approaches to solve this challenge can be divided into computational and instrumental methods [8]. Computational methods correct Raman spectra for their background using mathematical algorithms such as extended multiplicative scatter correction (EMSC) [9,10], rubberband [11,12], sensitive nonlinear iterative peak (SNIP) [13,14], and polynomial fittings [15]. Examples for the application of polynomial fitting are the correction during *in vivo* Raman studies of colorectal tissue [16] and brain cancer [17]. EMSC was used for the autofluorescence correction of Raman spectra of bladder biopsies [18]. Depending on the complexity of the algorithm, the computational data processing can be time consuming.

Instrumental methods for autofluorescence suppression enable less time consuming data processing, but they usually require more complex experimental setups. Examples for these methods are time-gated methods [19,20], phase or wavelength modulation techniques [21–24], and shifted excitation Raman difference spectroscopy (SERDS) [25]. For SERDS, two Raman spectra are measured at the same spatial position with two slightly shifted excitation wavelengths. Raman bands, which are a function of the exciting laser light, follow the shift in excitation wavelength. The background, a function of the instrument (filters, optics, and detection system), the sample's autofluorescence, room light, and other background components, does not shift. The two spectra are subtracted from each other, ideally resulting in a background-free difference spectrum with a first derivative-like appearance. For a proper reconstruction of the Raman spectrum from the difference spectrum, the shift in excitation wavelength, and therefore also the shift in relative wavenumbers, should be selected in accordance with the band widths of the expected Raman spectra. The target classification can be derived directly from the SERDS spectra, which was demonstrated for pollen [26], or from algorithm-based reconstructed Raman spectra, which was demonstrated for formalin fixed patient samples of breast tumors [27]. Further studies have already been published on biological samples using the SERDS technique. The investigated samples were molar tooth slices and *in vivo* human skin [28], algae produced complex polysaccharides [29], tissues from different animals [30–32], *ex vivo* oral squamous cell carcinoma biopsies [33], and spores of *Aspergillus nidulans* conidia [34].

There are only few examples of SERDS imaging so far, in which each point of the image corresponds to a difference spectrum. In the first implementation, such images were collected by performing a point-by-point raster scan of the sample, measuring each point twice with two different wavelengths. Cordero et al. [7] measured a beef steak in this fashion. After clustering the mean spectra of each cluster and assigning them to two different types of proteins and lipid, they compared the results of different wavelength shifts for SERDS with results based on EMSC and the 1<sup>st</sup> derivative of the EMSC corrected spectra. A second implementation applied a so-called integral field spectroscopy (IFS) approach [35,36], which belongs to the wide field imaging techniques. Whereas point scanning or line mapping approaches move the laser spot or line across the sample to sequentially collect a Raman image, wide field imaging instruments project the sample onto a multichannel detector such as a Charge-Coupled Device (CCD) chip and acquire the full Raman image simultaneously [37]. The spectral information can be obtained by fixed wavelength or tunable filters. In the context of light sheet Raman imaging, an interferometric detection scheme was developed [38]. More than 1000 Raman images were registered within minutes from which the Raman spectra were calculated via Fourier transformation. Another group of Raman imaging techniques generates several laser foci spots on the sample simultaneously by using fiber arrays, micro lens arrays, galvomirrors, or spatial modulators (such as liquid-crystal spatial modulators or

digital micromirror devices). Then, the spectra from all foci are imaged on a CCD either by the use of integral field spectrographs or by producing several pinholes using the spatial modulators [39].

In astronomical observatories, integral field spectroscopy (IFS) [40] is used to create a complete spectral image of cosmic objects in one shot without raster scanning the object, which saves valuable and rare observation time. For this one shot imaging, the image is optically dissected by a so-called integral field unit (IFU). The sections (e.g., slices, spots, squares, hexagons) are re-arranged in front of the rather large entrance slit of a wide field spectrograph or even several such spectrographs. One of the options to realize an IFU is using a fiber bundle that is arranged in a two-dimensional array on the side facing the sample and in a row-like fashion on the side facing the spectrograph. The row of fiber front surfaces acts as long pseudo-slit at the entrance side of the spectrograph. If the fibers of the bundle have round cores, the image will be dissected into round spots. At the spectrograph, the dispersed signals emerging from the fibers are collected by a large area detector. Each signal trace correlates to a specific image location. The spectrograph is designed in a way that signal traces originating from light at the ends of the entrance slit show nearly the same quality as light traces originating from the slit's center, meaning the spectrographs works over a "wide field" with regard to signal position at the entrance. The raw signal is processed into a data cube that contains the full spectral and lateral information. So far, the most powerful IFS spectrograph developed for astronomy is M.U.S.E. (Multi Unit Spectroscopic Explorer) [41] at the Very Large Telescope Observatory, Paranal, Chile. It consists of 24 IFUs, each with its own attached spectrograph, and it detects a total of 90,000 spectra (and therefore image pixels called "spaxels") with a spectral resolution of 0.25 nm in the range of 465 to 930 nm in one exposure simultaneously. An IFS spectrograph with 400 spaxels, built as a clone of a M.U.S.E. spectrograph module, was successfully used for Raman and SERDS imaging [35,36]. A custom-made probe head focuses the excitation laser in 400 measuring spots on the sample and guides the backscattered Raman signal into the IFS spectrograph. This setup was used by Schmälzlin et al. [36] for Raman and SERDS imaging of different samples, e.g., a cross-section of a pig ear, skin, and a dissolving brown sugar cube.

Another technique from astrophysics that could be translated to wide field SERDS imaging is the nod and shuffle concept [42–44]. This concept was originally developed to measure deep spectra of very faint galaxies whose surface brightness is usually a fraction of the night sky brightness, sometimes orders of magnitude fainter than the sky. In order to overcome the systematic errors introduced by atmospheric background intensity fluctuations, it is necessary to employ a technique called beam switching, which essentially means to measure pairs of (object + sky) and (sky) in rapid succession. While fast readout detectors such as infrared arrays have no problem to accomplish this in real time, Charge-Coupled Devices (CCD) in the optical wavelength domain incur substantial readout times per image. To accommodate beam switching with CCDs, the original nod and shuffle technique allows for a "nod" as a small offset of the telescope to switch its focus between the target and the neighboring background night sky. The "shuffle" stands for shifting charges on a frame transfer CCD from an active exposure area into one of two storage areas: one for (object + sky), another one for (sky). By synchronizing the nod process with the charge shuffle on the chip, it is possible to create the beam switching short exposure pairs that are necessary to eliminate the rapid sky brightness fluctuations without having to read out the CCD every time. After a sufficiently high total exposure time has been acquired by a series of many nod-shuffles (of order several tens), the exposure is stopped, and the entire CCD is read out. This technique works particularly well with fiber-coupled spectrographs, where the spacing of fibers on the entrance slit provides gaps between spectral traces on the detector and the gaps are wide enough to accommodate an extra trace between two adjacent spectral traces in an interlaced fashion. A virtue of this technique lies in the ability to subtract (object + sky) and (sky) on a pixel-by-pixel basis, thus avoiding further systematic errors that occur in the process of data reduction, specifically optimal extraction of the spectral traces: the illumination of each pair of pixels in the (object + sky) and (sky) storage areas has occurred under (almost) exactly the same circumstances.

In this work, the nod and shuffle technique from astrophysics is adapted and implemented into a wide field SERDS imaging setup. As a result, this concept addresses the two main challenges of

SERDS imaging. First, photobleaching between consecutive Raman spectra at two excitation wavelengths reduces the auto-fluorescent background and causes a residual background slope in the difference spectrum. Second, short exposure times in the millisecond range can be applied to minimize the photobleaching effect that results in low signal to noise ratios or long total acquisition times for hundreds of single spectra. Since the CCD chip has to be read out in a traditional setup after each acquisition and readout time can take up to a minute or more in particular for large CCDs, the strategy of very short acquisitions and multiple readouts would increase the overall measurement time tremendously. The nod and shuffle technique can be adapted to support SERDS imaging and overcome these challenges of SERDS imaging. The nod corresponds to the shift in excitation wavelength at the same spatial position, whereas the shuffle remains the shuffling of the charges on the CCD, saving, and accumulating both signals on the same CCD until numerous cycles revealed to sufficiently high signal to noise ratio. For a single channel setup with a rectangle CCD chip ( $1024 \times 256$  pixels), this was previously demonstrated by Sowoidnich et al. [45,46] as a Charge-Shifting Charge-Coupled Device, based on the previous works of Heming et al. [47].

In comparison to a previous conference proceeding paper [48], this publication provides more details of the nod and shuffle approach and the laser diode development, and it demonstrates wide field spectral imaging with nod and shuffle SERDS for a tissue specimen for the first time.

## 2. Materials and Methods

### 2.1. Wide Field SERDS Setup

In the experiments, an IFS spectrograph unit of the M.U.S.E. system (Winlight System, Pertuis, France) with a large area  $4096 \times 4096$  CCD chip (CCD231, Teledyne e2v, UK) was used. A detailed description of the spectrograph and detector system can be found in [49] and [50]. Two different laser sources were used during the presented experiments. They were selected for their shift in their emitted wavelength, which should correlate to the expected band widths of the Raman profiles of the samples (see below in Table 1).

1. A fiber-coupled near infrared (NIR) laser source LS 2-VBG, Ushio, Tokyo, Japan (formerly PD-LD, Pennington, USA) was used. The laser emits at 784.43 and 785.48 nm with a maximum laser power of 400 mW. This 1.05 nm shift ( $17 \text{ cm}^{-1}$ ) in excitation wavelength was the largest possible shift without a high loss of laser intensity due to the filters used in the setup. This small shift in wavenumbers was used for the investigation of two pharmaceutical pills, which show Raman spectra with narrow band profiles.
2. A custom-made laser source based on two external wavelength stabilized blue laser diodes with spatially overlapping laser emissions at 457.74 and 458.90 nm in a conduction cooled package mount with a  $25 \times 25 \text{ mm}^2$  footprint was designed and realized [51]. The diode lasers are wavelength stabilized at both target wavelengths with volume Bragg gratings with spectral bandwidths of  $< 0.2 \text{ nm}$  ( $< 10 \text{ cm}^{-1}$ ) and diffraction efficiencies of 15%. The spectral distance of 1.16 nm ( $55 \text{ cm}^{-1}$ ) is selected for SERDS with respect to the spectral resolution of the spectrometer with  $0.22 \text{ nm}$  ( $\approx 10.4 \text{ cm}^{-1}$ ) and for the investigation of biological tissue samples, since these samples have broader Raman band structures. For the spatial overlap of both laser emissions, using a high-reflection coated prism as well as a polarizing beam splitter, one laser is rotated by  $90^\circ$ . During the measurements, the laser was mounted on a heatsink (hsa-series, Ostech, Berlin, Germany), which was set to an operating temperature of  $40^\circ\text{C}$ . For the individual operation of both laser diodes, two laser drivers were used (ds-series, Ostech, Berlin, Germany). The optical output power at



both wavelengths was 0.4 W at 0.5 A. Figure 1 shows the corresponding emission spectra.

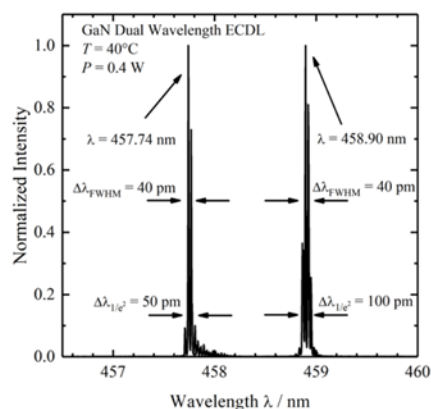


**Figure 1.** Emission spectra of the dual-wavelength GaN external cavity diode laser (ECDL) measured at an operating temperature of 40°C and an optical output power of 0.4 W.

The basic setup for Raman measurements was already reported in [36]. Briefly, 400 fibers of a bundle are arranged in a line at the spectrograph entrance to function as an IFU. On the sample side of the fiber bundle, the fibers form a 1 cm × 1 cm square, consisting of a 20 × 20 fiber matrix with a micro lens array (MLA) attached, so that the backscattered Raman signal can be efficiently coupled into the fibers. The laser light is guided via mirrors and filters on the sample. Two different probe head configurations were used: In the first configuration, another MLA focuses the laser light onto the sample by creating 400 foci (50 μm diameter; 0.5 mm center to center distance between focal spots) simultaneously while also collecting the Raman signal. This results in an imaging area of 1 cm<sup>2</sup>. The probe head in combination with the sample-side MLA was originally designed to measure thick skin samples with a low depth resolution. The low confocality is a consequence of 1 to 1 projection of 50 μm diameter foci onto 114 μm fiber cores to compensate alignment tolerances [52]. Due to the scattering, the achievable resolution was only 0.5 mm and, thus, a denser packing of the fibers was not useful. However, a far denser packing is possible and was already realized [53]. Figure 2 shows a schematic of the setup. The doublet lenses act as a telescope. They project the front surface of the sample onto the front surface of the fiber array. Furthermore, they project the exit pupil of the sample-side lens array to the entrance pupil of the fiber-side lens array. The second configuration with a field of view of approximately 0.02 cm<sup>2</sup> is used for smaller samples. Here, the MLA on the sample side is exchanged by an objective lens (Magnification = 10×, NA = 0.25). The two 50 mm doublet lenses are exchanged by a 200 mm tube lens. To implement the nod and shuffle technique, the wavelength axis has to be parallel to the readout register of the spectrograph, since the charge shuffle is only possible in the direction of the readout registers. Therefore the wavelength axis has to be orthogonal to the readout direction. In the original configuration of the spectrograph, this was not the case [36]; thus, the CCD chip had to be rotated by 90°. Unfortunately, a rotation of the existing CCD chip was not possible, since it had a graded index anti-reflection coating that was designed to maximize the throughput along the CCD chip's original wavelength axis. After the rotation, the profile of the anti-reflection coating would not match the wavelengths of the incident light anymore. Thus, a new CCD chip of the same type but with a uniform anti-reflection coating was purchased and built-in in the proper rotation. The loss of transmission caused by the simpler coating was insignificant. The camera control was changed to enable the shifting of the charges and the triggering of the lasers according to the settings in the user interface. For the generation of data cubes with single Raman spectra and difference spectra, the data reduction software also had to be adjusted to the new detector raw signal, which consisted of twice as many signal traces after the nod and shuffle changes.

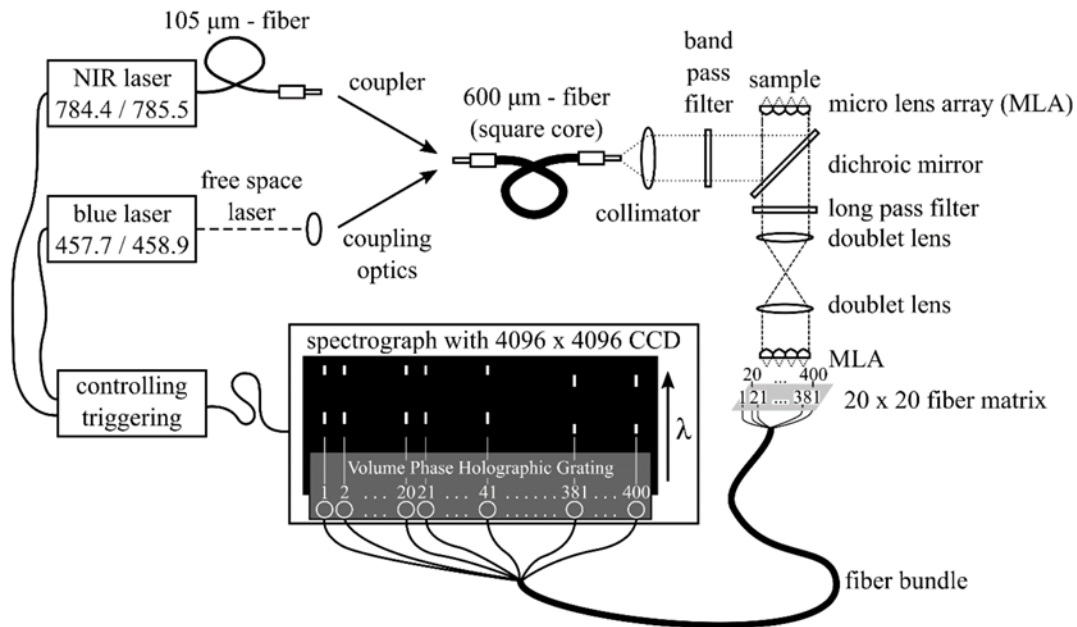


**Figure 2.** Wide field shifted excitation Raman difference spectroscopy (SERDS) imaging setup based on two micro lens arrays.

### 2.2. Nod and Shuffle

As briefly explained in the introduction the nod and shuffle technique for SERDS is a technique adapted from astrophysics. In SERDS, the nod corresponds to the change in excitation wavelength and the shuffle is, as in astronomy, the shift of charges on the CCD chip. In Figure 3, the interlaced nod and shuffle technique for SERDS is depicted.

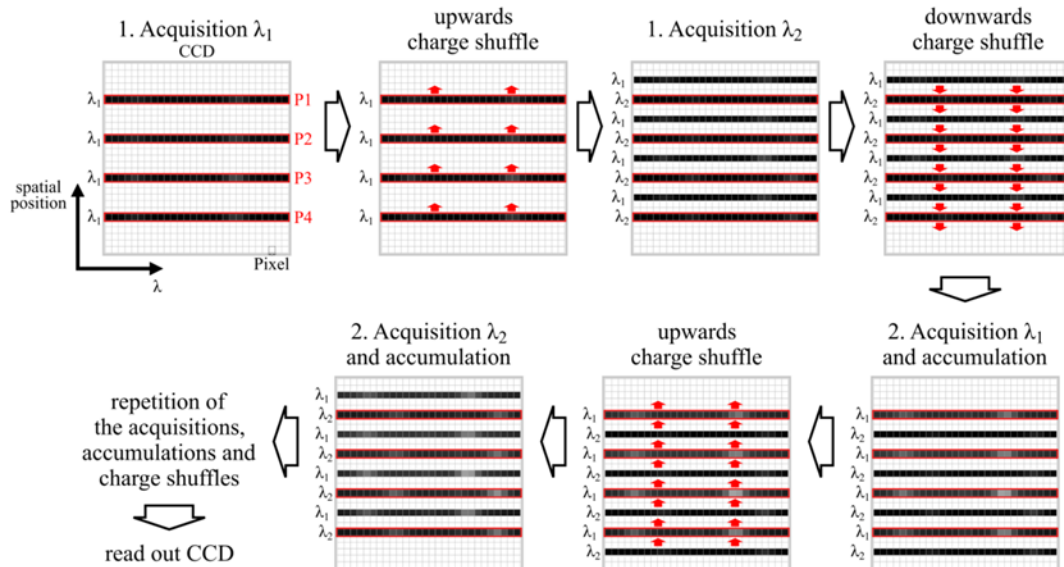


**Figure 3.** Illustration of the nod and shuffle technique by schematically showing the Charge-Coupled Device (CCD) chip (one square denotes one pixel on the CCD) and the shifting of charges (red arrows) after each acquisition and accumulation. The black lines symbolize the spectral signal traces with the corresponding excitation wavelengths to the left of them. The white spots inside the black lines display increasing signal strength, i.e., Raman bands that get more pronounced during the accumulation. The red boxes show the respective regions on the CCD, which are illuminated during

the acquisition, where each box corresponds to the same spaxel (spatial Position P1, P2, P3, and P4) of the Raman image. For simplicity, only four spaxels of the Raman image are shown.

At first, a wide field Raman image of the sample is measured with the first excitation wavelength ( $\lambda_1$ ). Each signal trace corresponds to a full spectrum at a distinct spatial position. Then, all charges are shifted up by 5 pixels on the CCD, the excitation wavelength is changed to  $\lambda_2$ , and a new wide field Raman image of the sample is taken. A CCD consists of a light-sensitive area organized in vertical columns of electrodes. Four electrodes in series form a pixel in our case. They are separated horizontally by potential wells. Applying high or low voltage to the electrodes in a special scheme allows collecting electrons (charge) underneath. Clocking the electrodes with a dedicated voltage pattern moves the charge from electrode to electrode. All electrodes are equivalent and therefore charge transfer vertically up and down is possible. A shift of 5 pixels transfers the signal traces into the centers of the spaces in between their recording positions. A transfer to the centers minimizes the risk of crosstalk to the respective new recorded upper and lower signal traces. Then, all charges are shifted down by 5 pixels on the CCD, and the excitation wavelength is shifted back to  $\lambda_1$ . This ends the first acquisition cycle. By repeating these steps, several acquisitions with two different wavelengths can be accumulated without reading out the CCD chip in between measurements. The challenge of this technique is the high instrumental complexity and, in case of very intense signals, the danger of crosstalk due to the lower pixel distance between the signal traces. However, there are several advantages to this method:

1. Readout noise is only applied once to the complete set of data.
2. Readout time only factors into the complete measurement time once. As for a large CCD chip, the readout time can take up to a minute or more, the total measurement time is significantly increased, when reading out the CCD chip after every single measurement. In our case, a sample was measured with 200 accumulations for each wavelength before reading out the CCD once. If the CCD was read out after each acquisition, readout times alone would have taken 400 min instead of 1 min with nod and shuffle.
3. The technique allows measurements with very short acquisition times, which were accumulated with multiple iterations over a long time period using a wide field imaging setup. The accumulation of single measurements with very short acquisition times is favorable in the presence of signal fluctuations, e.g., photobleaching and fluctuating high-intensity background light (see Section 3.2.1).
4. Spectra measured at the same spatial position with different wavelengths are recorded on the same pixels of the CCD chip. Therefore, Raman images of both excitation wavelengths have the same artifacts originating from the sensitivity and noise variations of the CCD pixels.

### 2.3. Samples and Experimental Parameters

The samples used for the experiments were:

- Sample 1: Paracetamol tablet and a piece of an aspirin tablet were arranged on the large field of view probe head. Both samples show intense Raman bands.
- Sample 2: Polystyrene (PS) beads (50  $\mu\text{m}$  diameter) and polymethyl methacrylate (PMMA) beads (120  $\mu\text{m}$  diameter) were mixed and applied on a  $\text{CaF}_2$  window. Both samples show intense Raman bands and have diameters to demonstrate the lateral resolution.
- Sample 3: The lipid-rich part of a pork chop fresh from a butcher was placed on a  $\text{CaF}_2$  window. Pork tissue served as model for biological material with less intense Raman bands and elevated background.

- Sample 4: The transition region from meat to fat of a pork chop fresh from a butcher was placed on a CaF<sub>2</sub> window.

The technical measurement conditions are shown in Table 1. The maximum acquisition time of 2 s for no. 3 and 4 gave the highest overall signal intensity on the CCD chip without crosstalk. This time was divided by the shortest achievable acquisition time of 50 ms for the laser system and resulted in 40 acquisitions. In the future, control of the lasers and the charge shift shuffling are improved to realize even shorter acquisitions and systematic studies are planned to obtain a good signal-to-noise ratio and zero baseline at the same time.

**Table 1.** Overview over the technical measurement conditions shown by samples.

No.	Sample	Laser ( $\lambda_1/\lambda_2$ ) in nm	Intensity in W/mm <sup>2</sup>	Imaging area in cm <sup>2</sup>	Acquisition times <sup>1</sup>
1	Aspirin/Paracetamol	NIR (784.43/785.48)	0.004 <sup>2</sup>	1	200 × 200 ms
2	PS/PMMA	blue (457.74/458.90)	0.1	0.02	40 × 100 ms
3	Lipid-rich pork tissue	blue (457.74/458.90)	0.2	0.02	40 × 50 ms and 1 × 2000 ms
4	Pork tissue	blue (457.74/458.90)	0.2	0.02	40 × 50 ms

<sup>1</sup> Number of acquisitions × acquisition time for each excitation wavelength. Example: 40 × 50 ms results in a total acquisition time of 4 s for each excitation wavelength. The one-time final readout of the CCD takes 1 min.

<sup>2</sup> The micro lens array (MLA) facing the sample generates 400 × 0.25 mm<sup>2</sup> laser foci with a power of approx. 1 mW each.

#### 2.4. Data Handling

The raw data were extracted, the wavelength was calibrated using a mercury (neon) lamp and an argon lamp (PenRay, Quantum Design Europe, Germany), and intensity was calibrated by a broad emission white light source. All of these preprocessing steps have been performed using the software p3d [54,55,56]. Afterwards, the data were further processed using the computer language R [57] and the following R packages: hyperSpec [58], FITSio [59], Ramancal [60], pracma [61], MALDIquant [62], and viridis [63].

In a first step, all spectra were cosmic spike corrected as well as corrected for pixel errors. As the MLAs were not exactly cut along the spaces in between the lenses, the MLAs were no more centrosymmetric. One outer horizontal and outer vertical lens row moved close to border of the holder aperture, which caused some shading of these rows. Consequently, the top spaxel row and/or the last spaxel row to the right were not usable and discarded for some images. Then, in order to obtain a SERDS image, the spatially corresponding spectra of the two Raman images were pairwise subtracted from one another, always subtracting the higher excitation wavelength spectra from the lower excitation wavelength spectra. A wavenumber calibration was performed on reconstructed spectra of paracetamol. For Sample 1 and Sample 4, a hierarchical cluster analysis (HCA) was performed using the SERDS spectra as input. For this analysis, the Pearson correlation distance between the SERDS spectra was first calculated and then clustered following Ward's minimum variance method [64]. The reconstruction of the Raman spectra was calculated by summation of the signal intensities over the wavenumber channels. Since this reconstruction method leads to an underlying background in the reconstructed Raman spectrum, the sensitive nonlinear iterative peak (SNIP) algorithm was implemented. The SERDS spectra of Sample 4 were normalized by a vector normalization before clustering. For better visualization purposes, the difference spectra of sample 1 were not normalized. The normalization would apparently amplify the residual room light and would give a poor signal-to-noise cluster.

### 3. Results and Discussion

#### 3.1. Wide-Field SERDS Imaging Using Nod and Shuffle and the Large Field of View (1 cm<sup>2</sup>) Probe Head

##### 3.1.1. Illustration of the Raw Wide-Field Raman Images on the CCD Chip Using Nod and Shuffle

To demonstrate the nod and shuffle technique, a Raman image of a paracetamol and an aspirin pill (sample 1) was measured with the large 1 cm<sup>2</sup> field of view probe head (Figure 4a) configuration for 200 ms with 200 acquisitions before reading out the CCD camera. Since the laser power per fiber was low for a NIR laser source, this long acquisition time was necessary to obtain strong Raman signals. The two pills did not cover the probe head completely (Figure 5a). This was done on purpose to show that even room light directly shining into the detection system for a short period can be filtered out with this setup. One second after the measurement had started, the fluorescent lamp of room light was turned on for 3 s. In Figure 4a, a zoomed image of the CCD chip, which is turned by 90° compared to the schematic CCD chip in Figure 2, is shown for a better visualization. Higher signal intensity corresponds to higher brightness, and the horizontally arranged traces correspond to complete Raman spectra of two intertwined Raman images taken at two different excitation wavelengths  $\lambda_1$  and  $\lambda_2$ . The traces are arranged in blocks, where each block consists of 20 spectra of each excitation wavelength corresponding to an image pixel row of 20 spaxels on the probe head. The black square bracket marks one of these blocks in Figure 4a.

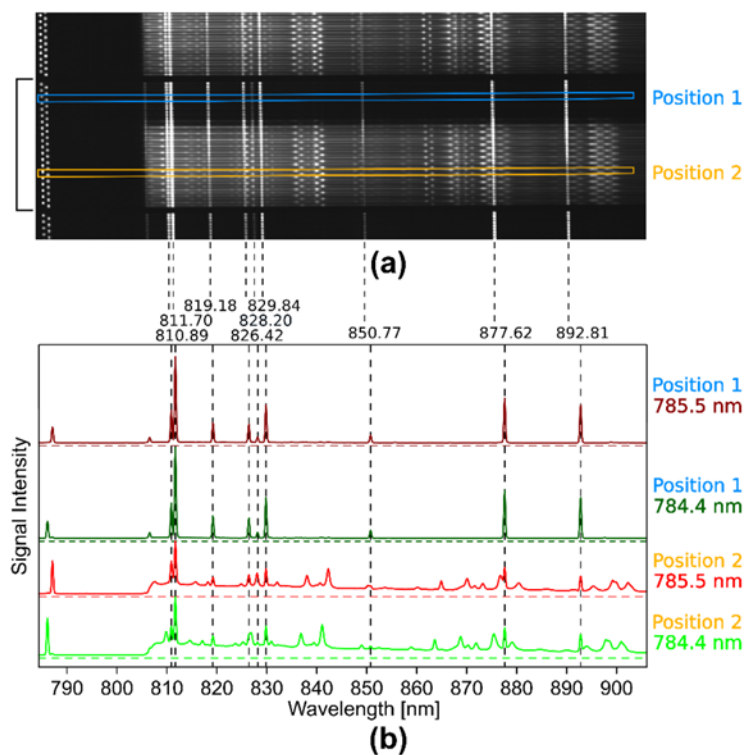


**Figure 4.** Illustration of the raw, wide field Raman data measured with two different excitation wavelengths ( $\lambda_1 = 784.4$  nm,  $\lambda_2 = 785.5$  nm) and the nod and shuffle technique: (a) zoomed view on a part of the CCD chip after acquisition for a closer look on the signal traces. Twenty spectra of each wavelength are always arranged in a block of traces (black square bracket), corresponding to one row of pixels in the Raman images. The upper blue box marks two intensity traces (Position 1) that correspond to a spaxel in the Raman image without a sample. The lower orange box marks two intensity traces (Position 2) that correspond to a spaxel on the Raman image with a paracetamol pill; (b) signal intensities of the two signal traces (in dark red and dark green) marked by the upper blue box in the CCD image showing only the room light spectra. In red ( $\lambda_1$ ) and green ( $\lambda_2$ ), the signal

intensities of the two signal traces marked by the lower orange box in the CCD image are shown, which correspond to the paracetamol Raman spectra superposed by room light spectra. The dotted, vertical black lines indicate the position of the fluorescent lamp bands and above their spectral position in nm.

The two Raman images are shifted on the CCD by 5 pixels in the vertical direction. Therefore, every second trace belongs to the same excitation wavelength and hence the Raman image and each neighboring wavelength pair belong to the same spatial position on the probe head. The oscillating dots on the left side of every trace correspond to the residual intensity of the excitation laser light that reached the detector in spite of the long-pass filter. The spots on the right of the laser signals correspond to Raman bands that shift with the excitation wavelength and to very intense, non-shifting signals of the fluorescent lamp. Figure 4b shows the profile plots of the four signal traces ( $\lambda_1$  in green and dark green;  $\lambda_2$  in red and dark red) inside the blue (Position 1) and orange (Position 2) boxes in Figure 4a. At the position of the blue box, there are fluorescent lamp bands only, whereas at the position of the orange box, the Raman signals are superposed with these bands that are shown by black vertical, dotted lines. Their positions were indicated on top in nm and coincide well with the emission bands of Krypton [65]. After comparison of the profiles, the Raman bands can be discriminated from the fluorescent lamp bands. Some Raman bands overlap with the fluorescent lamp bands after the shift of excitation wavelength (red spectrum), which would make it hard to correct for the fluorescent lamp contributions with computational methods. According to the position of the Raman bands and their profile, the selected Raman spectra belong to paracetamol. The image of the CCD chip also shows how close together all the signal traces are. If the signal intensities on the exposed pixels on the CCD are too high, the intensities cause crosstalk in the surrounding pixels and even in the neighboring shifted spectra. This is a limitation of the nod and shuffle approach, requiring careful monitoring of the overall intensity distribution between the spectra and the use of appropriately weighted extraction schemes such as optimal extraction [66].

### 3.1.2. Filtering Out Room Light by SERDS Imaging

A strength of SERDS is the capability to filter out room light or ambient light with a distinct band structure. This has been shown for single spectra before [67–69] but not for a complete Raman image or, in our case, a wide field Raman image. Since the room light bands do not shift with the change in excitation wavelength, the difference spectra of the SERDS image are ideally free of any room light bands. This advantage is demonstrated with help of the aforementioned samples (Section 3.1.1) of paracetamol and aspirin. The room light illumination time of a fluorescent tube was limited to 3 s to avoid overexposure of the CCD and the above-mentioned signal crosstalk. As shown before in Figure 4b, the room light bands are very dominant in the Raman spectra of the two Raman images. After subtraction, the room light bands vanish almost completely (Figure 5c). An HCA cluster analysis of the SERDS image using three clusters, one for paracetamol, one for aspirin, and one for empty space as the probe head, was not completely covered by the two pills. The resulting cluster map is depicted in Figure 5b and agrees well with the original bright field image (Figure 5a). In Figure 5c, the mean SERDS spectra and their respective standard deviation of the three clusters are shown. These clusters can be identified based on their SERDS spectra as paracetamol (cluster 1, black), empty space with residual room light (cluster 2, green), and aspirin (cluster 3, red). Residual traces of room light are still visible, which might be due to uneven exposure of one of the Raman images resulting in a higher room light intensity as the other, since the room light had to be turned off to avoid overexposure. Still, the strength of SERDS filtering out room light is obvious, which presents a huge advantage in operating theaters where room light needs to be switched on. Shorter acquisitions times will further reduce the interference of room light. However, the interface that was used to control a 784.43/785.48 nm laser source by polling the TTL (transistor-transistor-logic, square signal pulses that use +5 V for “1” or “high” and 0 V for “0” or “low”) trigger signals of the spectrograph with an USB digital input output device did not allow exposure times shorter than 200 ms.

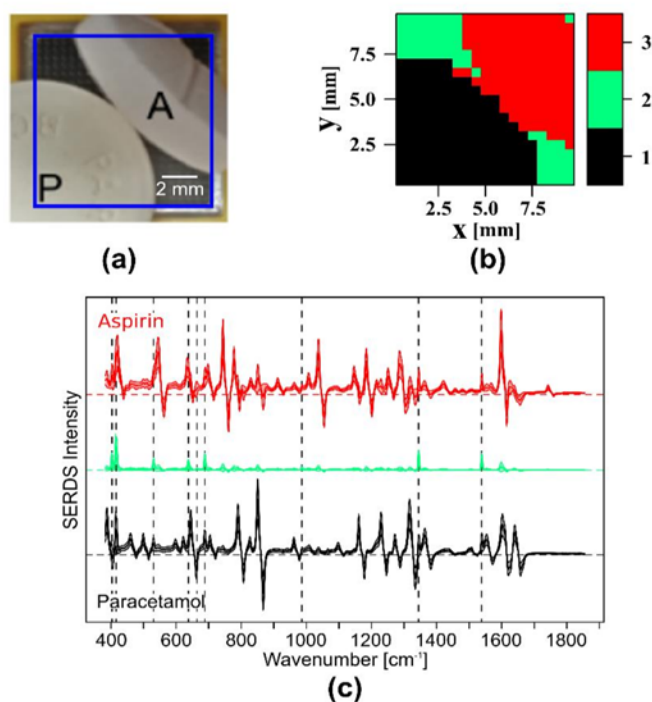


**Figure 5.** SERDS imaging using nod and shuffle of a paracetamol (P) and an aspirin (A) pill with an acquisition of 200 times 200 ms. (a) Picture of the sample on the probe head, the blue square corresponds to the field of view; (b) cluster map of the SERDS image; (c) clustered mean SERDS spectra and their standard deviation, cluster 1 = paracetamol (black), cluster 2 = no sample/residual room light (green), cluster 3 = aspirin (red); the dotted, vertical black lines indicate the position of the room light bands.

### 3.2. Wide-Field SERDS Imaging Using Nod and Shuffle, the Smaller Field of View Probe Head ( $0.02 \text{ cm}^2$ ), and the Rapidly Shifting Dual-Wavelength Blue Diode Laser Source

#### 3.2.1. Wide Field SERDS Imaging with Nod and Shuffle to Differentiate Different Polymer Beads

Since the spatial resolution of the larger field of view of  $1 \text{ cm}^2$  with 400 image points (1 spectrum per  $0.5 \text{ mm}$ ) is quite low for polymer beads, the setup was changed to a smaller field of view of  $0.02 \text{ cm}^2$ , resulting in approximately 1 spectrum per  $70 \text{ }\mu\text{m}$ . To demonstrate the imaging capability and the higher lateral resolution of this setup, polystyrene (PS) and polymethyl methacrylate (PMMA) beads were distributed on a  $\text{CaF}_2$  slide and placed on the probe head. The Raman spectra were collected with the nod and shuffle technique with an acquisition time of 100 ms and 40 accumulations using the dual-wavelength blue diode laser light source ( $\lambda_1 = 457.7 \text{ nm}$ ,  $\lambda_2 = 458.9 \text{ nm}$ ). In the bright field camera image (Figure 6a), groups of small PS beads ( $50 \text{ }\mu\text{m}$  diameter) and a region of bigger PMMA beads ( $120 \text{ }\mu\text{m}$  diameter, red box) can be seen. To generate Raman intensity maps for PS and PMMA, specific marker bands of the reconstructed and baseline corrected Raman spectra were used. The PS intensity map (Figure 6b) shows the mean value of the aromatic ring breathing vibration  $999 \text{ cm}^{-1}$ , the ring stretching vibration at  $1590 \text{ cm}^{-1}$ , and the aromatic CH stretching vibration at  $3047 \text{ cm}^{-1}$ . To create the PMMA intensity map (Figure 6c), the mean value of the  $\text{CH}_3$  deformation vibration at  $1444 \text{ cm}^{-1}$ , the  $\text{C}=\text{O}$  stretching vibration at  $1718 \text{ cm}^{-1}$ , and the CH stretching vibration in  $\text{CH}_2$  and  $\text{CH}_3$  at  $2935 \text{ cm}^{-1}$  was calculated and mapped. A comparison of the bright field image with the two Raman intensity maps of PS and PMMA shows that the position of the PMMA beads and the PS beads corresponds to the Raman intensity maps very well. The squares on the intensity maps show regions of high intensity in the respective bands (green box for PS, blue box for PMMA).

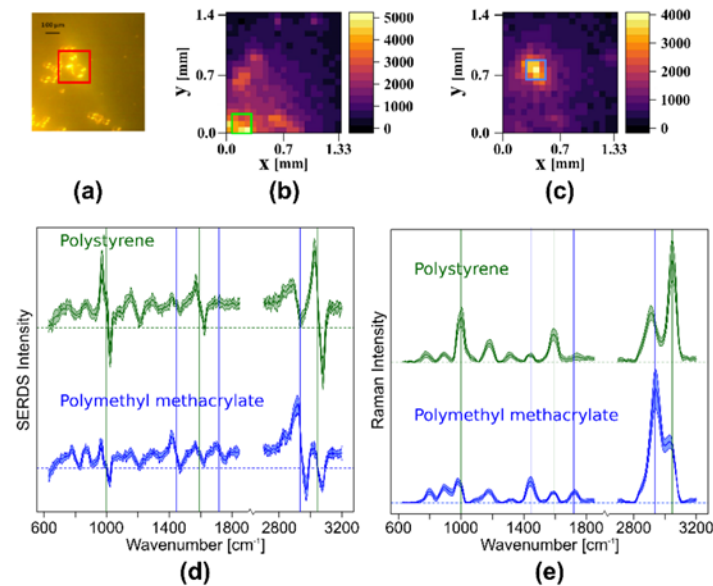


**Figure 6.** SERDS imaging of polystyrene and polymethyl methacrylate beads: (a) bright field image of the sample, red box shows a region of larger PMMA beads; (b) PS intensity map based on the intensity of three marker bands in the baseline corrected, reconstructed Raman spectra; (c) PMMA intensity map based on the intensity of three marker bands in the baseline corrected, reconstructed Raman spectra; (d) mean SERDS spectra and their standard deviation for nine spectra with the highest intensities for PMMA and PS marked by boxes (green for PS, blue for PMMA) in the corresponding intensity maps; (e) baseline corrected and reconstructed mean Raman spectra with standard deviation of the SERDS spectra shown in (d); The vertical lines in (d) and (e) indicate the marker bands (green for PS; blue for PMMA) that were used to create the intensity maps (b) and (c).

In Figure 6d, the mean SERDS spectra of these marked areas are shown in green (PS) and blue (PMMA). The vertical lines show the three marker bands for the intensity maps in the same colors. In Figure 6e, the mean and baseline corrected Raman spectra reconstructed from SERDS spectra of Figure 6d are plotted. The typical spectral profile of PS and PMMA are clearly visible, although the bands are rather broad. Since the laser was designed for the investigation of biological samples, the large spectral shift of approximately  $55\text{ cm}^{-1}$  is more appropriate for the SERDS investigation of tissue samples, which have a Raman profile with a larger band width. For the narrow-banded Raman profiles of polymers, this large shift results in the observed broadening during the integration in the reconstruction step and also yields a high risk of introducing artifacts into the reconstructed Raman spectra, since neighboring bands are shifted into one another.

### 3.2.2. Photobleaching Compensation in Wide Field SERDS Imaging by Very Fast Nod and Shuffle

A great challenge of SERDS is the variation in background intensities during the measurement, especially when the wavelength pair is affected differently. The main cause of changes in spectral background of biological samples is photobleaching of intrinsic fluorophores. Their generated autofluorescence gets bleached by the continuous laser radiation, which mainly causes a uniform decrease of the fluorescence. This leads to a SERDS spectrum with a background slope that needs further correction with some kind of computational solution such as normalization or optimization. Another possibility to deal with this challenge is to use very short acquisitions, thereby only allowing for minimal changes. Here, the nod and shuffle technique with fast switching between the wavelengths is promising, since the accumulation of multiple cycles allows for enough Raman signal collection, while equally distributing the photobleaching effect on the Raman measurements at both excitation wavelengths. In combining this with wide field imaging and hence simultaneous irradiation of all image pixels, differences within one SERDS image can be eliminated.



Since the change in excitation wavelength was limited to 200 ms with the commercially available red laser system, the custom-built dual-wavelength blue diode laser system with the possibility for fast wavelength switching was used for the following experiments. A change from a NIR to a blue excitation will usually lead to a huge increase of the amount of fluorescence especially for biological samples. However, this drawback should be eliminated by the SERDS technique.

To demonstrate the compensation of photobleaching in wide field SERDS imaging using nod and shuffle, a piece of pork meat (Figure 7 a) was imaged ( $\lambda_1 = 457.7$  nm,  $\lambda_2 = 458.9$  nm) with a total acquisition time of 2 s in two approaches:

1. Two Raman images were measured with a 50 ms acquisition time and 40 accumulations for each excitation wavelength before reading out the CCD chip once. Thus, the overall acquisition time was 2 s for each excitation wavelength.
2. Two Raman images were measured with a 2 s acquisition time and one accumulation for each excitation wavelength before reading out the CCD chip once. Thus, the total acquisition time was also 2 s for each excitation wavelength.

The two resulting Raman images of each measurement were subtracted. The SERDS spectra for the two SERDS images, with the mean difference spectra marked as dark colored lines (see Figure 7b), show the typical difference profile of lipid-rich tissue with bands at  $1446$   $\text{cm}^{-1}$ ,  $1650$   $\text{cm}^{-1}$ , and  $1740$   $\text{cm}^{-1}$ . While the SERDS bands have comparable absolute intensities, it is clearly visible that the difference spectra show a stronger residual background for the longer acquisition time (green spectra) due to the aforementioned photobleaching effect: At the beginning of the measurement at  $\lambda_1$ , the pork shows remarkable autofluorescence that significantly decreases during the 2 s measurement time. At the beginning of the measurement at  $\lambda_2$ , the autofluorescence is already decreased.

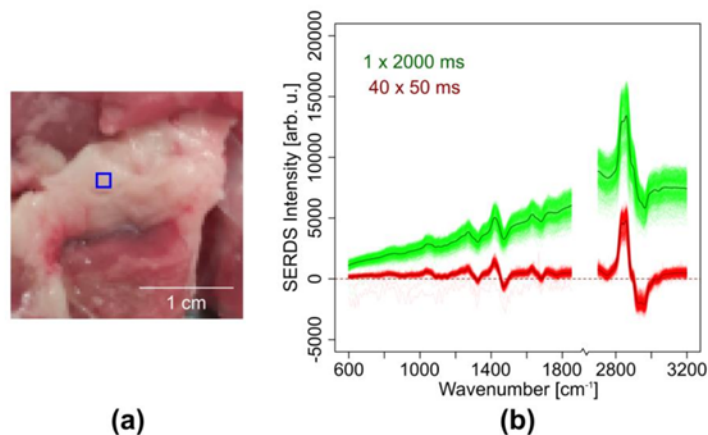


**Figure 7.** Compensation of photobleaching in SERDS imaging of the fat region of a pork chop using nod and shuffle: (a) image of the pork chop sample with measurement area marked by a blue square; (b) SERDS spectra of the SERDS image (red) with an acquisition time of 50 ms and 40 accumulations, SERDS spectra of the SERDS image (green) with an acquisition time of 2000 ms in a single accumulation. The darker lines (dark green and dark red, respectively) show the mean SERDS spectra of the respective SERDS image. The total exposure time is 4 s for each difference spectrum (2 s for each excitation wavelength).

Thus, the two measurement pairs show different backgrounds, leading to a non-zero baseline after the subtraction. For the short acquisition times, this residual background is not present, resulting in difference spectra almost on the zero line (red spectra). The reason for this effect is the equal distribution of the photobleaching on both measurements at  $\lambda_1$  and  $\lambda_2$ , when switching rapidly and repeatedly between the excitation wavelengths. Within a short 50 ms exposure time, the change of background signal is negligibly small. Each single measurement pair contains the same amount of

background. When subtracting their sums, the background vanishes, and a zero baseline is obtained. This clearly demonstrates the advantage of the nod and shuffle technique in combination with wide field SERDS imaging and rapid switchable laser diodes. Even though the photobleaching must have been higher in the image with the short acquisition times, since it was recorded first, this setup configuration successfully circumvents this challenge and distributes the photobleaching equally on both excitation wavelengths.

### 3.2.3. Wide Field SERDS Imaging of Different Tissues in Pork Meat Using Nod and Shuffle

To test the introduced wide field SERDS setup on a heterogeneous biological sample, another piece of pork meat was imaged. As before, the custom made dual-wavelength blue diode laser source ( $\lambda_1 = 457.7$  nm,  $\lambda_2 = 458.9$  nm) and the smaller field of view probe head with the nod and shuffle technique was used to image a section including proteins and lipids. Figure 8a shows an intensity map of the SERDS spectra based on the intensity at  $2900\text{ cm}^{-1}$ .

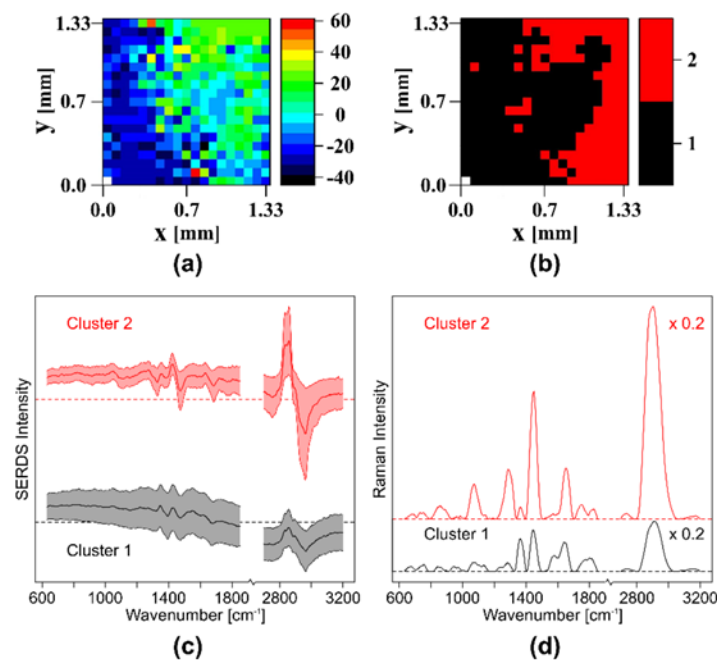


**Figure 8.** SERDS imaging of a piece of pork meat with protein and lipid-rich areas: (a) intensity map of the SERDS spectra at  $2900\text{ cm}^{-1}$ ; (b) cluster map of the SERDS spectra; (c) clustered normalized, mean SERDS spectra and their standard deviation; (d) reconstructed and baseline corrected mean Raman spectra of the two clusters shown in (c). The high wavenumber regions were multiplied by 0.2 for better visualization.

After hierarchical clustering, two clusters visualize the regions with protein and lipids in the cluster map (see Figure 8b). In Figure 8c, the normalized, mean difference spectra with standard deviation of the two clusters are shown. It is obvious that the intensity of cluster 2, the lipid cluster, is much higher than the intensity of cluster 1, the protein cluster. The larger standard deviation is a consequence of the lower intensity and the higher background in the protein cluster. For a better visualization of the band positions, the reconstructed and baseline corrected mean Raman spectra of the two clusters can be seen in Figure 8d. Typical protein bands such as amide I at  $1638\text{ cm}^{-1}$ , amide III at  $1282\text{ cm}^{-1}$ , myoglobin at  $1363\text{ cm}^{-1}$  [32], tyrosine at  $858\text{ cm}^{-1}$ , tryptophane ( $754, 894\text{ cm}^{-1}$  and  $1587\text{ cm}^{-1}$ ), and CN ( $1075\text{ cm}^{-1}$ ,  $1099\text{ cm}^{-1}$  and  $1128\text{ cm}^{-1}$ ) classify cluster 1 as proteins, while cluster 2 shows lipid typical bands (carbonyl at  $1750\text{ cm}^{-1}$ , C=C  $1649\text{ cm}^{-1}$ , CH<sub>2</sub> and CH<sub>3</sub> at  $1060\text{ cm}^{-1}$ ,  $1300\text{ cm}^{-1}$  and  $1450\text{ cm}^{-1}$ ) and can therefore be assigned to lipids. This also explains the already observed intensity differences between the two clusters, since lipids have a higher Raman scattering

cross-section than proteins. In conclusion, with the chosen setup configuration, SERDS images of a biological sample can be recorded in one shot with small photobleaching effects, and the lipid and protein-rich regions can be easily identified.

#### 4. Conclusions

Using wide field Raman imaging, several spectra of an area can be recorded in a relatively short time, since all spectra are collected simultaneously. Consequently, the total acquisition time of a Raman image, in our case consisting of 400 spectra of a 20 by 20 fiber array, is orders of magnitude faster than in point-by-point Raman imaging. The fibers were arranged in a square probe head to image an area of  $10 \times 10 \text{ mm}^2$  with  $0.5 \times 0.5 \text{ mm}^2$  per pixel in standard mode or  $1.4 \times 1.4 \text{ mm}^2$  with  $0.07 \times 0.07 \text{ mm}^2$  per pixel in higher magnification mode. As the readout times of the usually employed, very large CCD chips are quite long, measurements in quick successions cannot be realized in this configuration. This is especially problematic for wide field SERDS imaging, where the accumulation of short measurements at two slightly different excitation wavelengths is favorable.

The presented wide field SERDS imaging approach using the nod and shuffle technique allows accumulating very short acquisition times before reading out the CCD chip. The structure of the signal traces on the CCD chip was presented. Since the signal traces on the CCD chip are closer together in the interlaced nod and shuffle approach, the risk of crosstalk from very high intensities into the neighboring spectra belonging to the other excitation wavelength can be problematic. For this reason, the signal intensity has to be monitored closely during the experiments.

Using the nod and shuffle approach, the advantages of SERDS and fast acquisition times was demonstrated for wide field SERDS imaging for the first time. As expected from previous single spectra measurements, room light filtering was one of these advantages, where the measurement was interfered by an external light source during the acquisition. This was compensated due to the SERDS technique and the fast acquisition times, which made it possible to filter out the room light, even when it directly shone into the detection system for a short period. If the sample covers the probe head completely, only stray light can enter the detection system. This will allow much longer acquisition times. The other demonstrated advantage of the fast acquisition times is the compensation of photobleaching resulting in minimal background in the SERDS spectra of the SERDS images. This compensation makes the usual normalization or optimization steps before the calculation of the SERDS spectra unnecessary and the whole SERDS approach faster and less computational.

It was demonstrated that structural differences can be resolved based on almost background free wide field SERDS images. The resulting reconstructed Raman spectra had to be baseline corrected, since the used quasi integration introduced a background into the reconstructed spectra. Especially for the investigation of the narrow band Raman profiles of polymers, the 1.16 nm wavelength shift of the custom-made, dual-wavelength blue diode laser, which corresponds to a  $55 \text{ cm}^{-1}$  shift of the Raman spectra, as well as the spectral broadening due to the reconstruction was quite large. For the investigation of biological samples, which was the targeted application for the blue diode laser, this large spectral shift is more appropriate.

The nod and shuffle technique will enable a compensation of the photobleaching and by directly using the difference spectra for a classification of the measured samples, no reconstruction will be necessary. This combination will streamline the wide field SERDS imaging and reduce the computational effort for this instrumental background correction method.

#### 5. Patents

For results of the work, a patent application was filed at the German Patent and Trade Mark Office. Patent application no. DE 10 2018 130 582 A1.

**Author Contributions:** Conceptualization: M.M.R., E.S., C.K., J.P. Realizing of the setup: E.S. Performing the measurements: F.K., E.S. Upgrading of the data reduction software: Ch.S. Data analysis and visualization: F.K., T.U., G.M. Evaluation and validation: C.S., C.K. Design and realization of dual wavelength (457.74 nm / 458.90

nm) diode laser source: A.M., M.M., B.S, G.T. Supervision: C.S., C.K., J.P. Original draft preparation: F.K. Review and editing of the manuscript: all.

**Funding:** This research was funded by the Leibniz Association through the project HYPERAM (SAW-2016-IPHT-2). The publication of this article was funded by the Open Access Fund of the Leibniz Association.

**Acknowledgments:** This research has made use of the integral-field spectroscopy data-reduction software p3d, which is provided by the Leibniz-Institute for Astrophysics Potsdam (AIP) and maintained by Sandin Advanced Visualization (Stockholm). We thank Thomas Fechner from the AIP's electronics workshop for upgrading the spectrograph. Furthermore, we thank DECHEMA e.V. for the possibility to present results at the 14. Dresdner Sensor Symposium. Parts of the figures are adapted from the conference proceeding [48].

**Conflicts of Interest:** The authors declare no conflict of interest. The funders had no role in the design of the study; in the collection, analyses, or interpretation of data; in the writing of the manuscript, or in the decision to publish the results.

## References

1. Krafft, C.; Schie, I.W.; Meyer, T.; Schmitt, M.; Popp, J. Developments in spontaneous and coherent Raman scattering microscopic imaging for biomedical applications. *Chem. Soc. Rev.* **2016**, *45*, 1819–1849, doi:10.1039/c5cs00564g.
2. Hubbard, T.J.E.; Shore, A.; Stone, N. Raman spectroscopy for rapid intra-operative margin analysis of surgically excised tumour specimens. *Analyst* **2019**, *144*, 6479–6496, doi:10.1039/c9an01163c.
3. Cheng, J.X.; Xie, X.S. Vibrational spectroscopic imaging of living systems: An emerging platform for biology and medicine. *Science* **2015**, *350*, 1–9, doi:10.1126/science.aaa8870.
4. Krafft, C.; Schmitt, M.; Schie, I.W.; Cialla-May, D.; Matthaues, C.; Bocklitz, T.; Matthäus, C.; Bocklitz, T.; Popp, J. Label-free molecular imaging of biological cells and tissues by linear and non-linear Raman spectroscopic approaches. *Angew. Chemie Int. Ed.* **2017**, 4392–4430, doi:10.1002/anie.201607604.
5. Butler, H.J.; Ashton, L.; Bird, B.; Cinque, G.; Curtis, K.; Dorney, J.; Esmonde-White, K.; Fullwood, N.J.; Gardner, B.; Martin-Hirsch, P.L.; et al. Using Raman spectroscopy to characterize biological materials. *Nat. Protoc.* **2016**, *11*, 664–687, doi:10.1038/nprot.2016.036.
6. Monici, M. Cell and tissue autofluorescence research and diagnostic applications. *Biotechnol. Annu. Rev.* **2005**, *11*, 227–256, doi:10.1016/S1387-2656(05)11007-2.
7. Cordero, E.; Korinith, F.; Stiebing, C.; Krafft, C.; Schie, I.; Popp, J. Evaluation of Shifted Excitation Raman Difference Spectroscopy and Comparison to Computational Background Correction Methods Applied to Biochemical Raman Spectra. *Sensors* **2017**, *17*, 1724, doi:10.3390/s17081724.
8. Wei, D.; Chen, S.; Liu, Q. Review of Fluorescence Suppression Techniques in Raman Spectroscopy. *Appl. Spectrosc. Rev.* **2015**, *50*, 387–406, doi:10.1080/05704928.2014.999936.
9. Afseth, N.K.; Kohler, A. Extended multiplicative signal correction in vibrational spectroscopy, a tutorial. *Chemom. Intell. Lab. Syst.* **2012**, *117*, 92–99, doi:10.1016/j.chemolab.2012.03.004.
10. Martens, H.; Stark, E. Extended multiplicative signal correction and spectral interference subtraction: New preprocessing methods for near infrared spectroscopy. *J. Pharm. Biomed. Anal.* **1991**, *9*, 625–635, doi:10.1016/0731-7085(91)80188-F.
11. Pirzer, M.; Sawatzki, J. US Patent Application Publication, Pub. No.: US 2006/0211562 A1 2006, Pub. Date: Sep. 21, 2006, 1–11.
12. Kneen, M.A.; Annegam, H.J. Algorithm for fitting XRF, SEM and PIXE X-ray spectra backgrounds. *Nucl. Instrum. Methods Phys. Res. Sect. B Beam Interact. Mater. Atoms* **1996**, *109/110*, 209–213, doi:10.1016/0168-583X(95)00908-6.
13. Morháč, M. An algorithm for determination of peak regions and baseline elimination in spectroscopic data. *Nucl. Instrum. Methods Phys. Res. Sect. A Accel. Spectrometers Detect. Assoc. Equip.* **2009**, *600*, 478–487, doi:10.1016/j.nima.2008.11.132.
14. Morháč, M.; Matoušek, V. Peak clipping algorithms for background estimation in spectroscopic data. *Appl. Spectrosc.* **2008**, *62*, 91–106, doi:10.1366/000370208783412762.
15. Lieber, C.A.; Mahadevan-Jansen, A. Automated Method for Subtraction of Fluorescence from Biological Raman Spectra. *Appl. Spectrosc.* **2003**, *57*, 1363–1367, doi:10.1366/000370203322554518.
16. Bergholt, M.S.; Zheng, W.; Lin, K.; Wang, J.; Xu, H.; Ren, J.L.; Ho, K.Y.; Teh, M.; Yeoh, K.G.; Huang, Z.

- Characterizing variability of in vivo Raman spectroscopic properties of different anatomical sites of normal colorectal tissue towards cancer diagnosis at colonoscopy. *Anal. Chem.* **2015**, *87*, 960–966, doi:10.1021/ac503287u.
17. Desroches, J.; Jermyn, M.; Pinto, M.; Picot, F.; Tremblay, M.A.; Obaid, S.; Marple, E.; Urmev, K.; Trudel, D.; Soulez, G.; et al. A new method using Raman spectroscopy for in vivo targeted brain cancer tissue biopsy. *Sci. Rep.* **2018**, *8*, 1–10, doi:10.1038/s41598-018-20233-3.
  18. Cordero, E.; Rüger, J.; Marti, D.; Mondol, A.S.; Hasselager, T.; Mogensen, K.; Hermann, G.G.; Popp, J.; Schie, I.W. Bladder tissue characterization using probe-based Raman spectroscopy: Evaluation of tissue heterogeneity and influence on the model prediction. *J. Biophotonics* **2020**, *13*, 1–15, doi:10.1002/jbio.201960025.
  19. Ariese, F.; Meuzelaar, H.; Kerssens, M.M.; Buijs, J.B.; Gooijer, C. Picosecond Raman spectroscopy with a fast intensified CCD camera for depth analysis of diffusely scattering media. *Analyst* **2009**, *134*, 1192–1197, doi:10.1039/b821437a.
  20. Kögler, M.; Heilala, B. Time-gated Raman spectroscopy—A review. *Meas. Sci. Technol.* **2020**, *32*, 1–17, doi:10.1088/1361-6501/abb044.
  21. De Luca, A.; Dholakia, K.; Mazilu, M. Modulated Raman Spectroscopy for Enhanced Cancer Diagnosis at the Cellular Level. *Sensors* **2015**, *15*, 13680–13704, doi:10.3390/s150613680.
  22. Dochow, S.; Bergner, N.; Krafft, C.; Clement, J.; Mazilu, M.; Praveen, B.B.; Ashok, P.C.; Marchington, R.; Dholakia, K.; Popp, J. Classification of Raman spectra of single cells with autofluorescence suppression by wavelength modulated excitation. *Anal. Methods* **2013**, *5*, 4608–4614, doi:10.1039/c3ay40193f.
  23. Craig, D.; Mazilu, M.; Dholakia, K. Quantitative detection of pharmaceuticals using a combination of paper microfluidics and wavelength modulated Raman spectroscopy. *PLoS ONE* **2015**, *10*, e0123334, doi:10.1371/journal.pone.0123334.
  24. Wirth, M.J.; Chou, S.H. Comparison of Time and Frequency Domain Methods for Rejecting Fluorescence from Raman Spectra. *Anal. Chem.* **1988**, *60*, 1882–1886, doi:10.1021/ac00169a009.
  25. Shreve, A.P.; Cherepy, N.J.; Mathies, R.A. Effective Rejection of Fluorescence Interference in Raman Spectroscopy Using a Shifted Excitation Difference Technique. *Appl. Spectrosc.* **1992**, *46*, 707–711, doi:10.1366/0003702924125122.
  26. Korinth, F.; Mondol, A.S.; Stiebing, C.; Schie, I.W.; Krafft, C.; Popp, J. New methodology to process shifted excitation Raman difference spectroscopy data: A case study of pollen classification. *Sci. Rep.* **2020**, *10*, 11215, doi:10.1038/s41598-020-67897-4.
  27. Gebrekidan, M.T.; Erber, R.; Hartmann, A.; Fasching, P.A.; Emons, J.; Beckmann, M.W.; Braeuer, A. Breast Tumor Analysis Using Shifted-Excitation Raman Difference Spectroscopy (SERDS). *Technol. Cancer Res. Treat.* **2018**, *17*, 153303381878253, doi:10.1177/1533033818782532.
  28. Martins, M.A.d.S.; Ribeiro, D.G.; Pereira dos Santos, E.A.; Martin, A.A.; Fontes, A.; Martinho, H. da S. Shifted-excitation Raman difference spectroscopy for in vitro and in vivo biological samples analysis. *Biomed. Opt. Express* **2010**, *1*, 617–626, doi:10.1364/BOE.1.000617.
  29. Noack, K.; Eskofier, B.; Kiefer, J.; Dilk, C.; Bilow, G.; Schirmer, M.; Buchholz, R.; Leipertz, A. Combined shifted-excitation Raman difference spectroscopy and support vector regression for monitoring the algal production of complex polysaccharides. *Analyst* **2013**, *138*, 5639–5646, doi:10.1039/c3an01158e.
  30. Gebrekidan, M.T.; Knipfer, C.; Stelzle, F.; Popp, J.; Will, S.; Braeuer, A. A shifted-excitation Raman difference spectroscopy (SERDS) evaluation strategy for the efficient isolation of Raman spectra from extreme fluorescence interference. *J. Raman Spectrosc.* **2016**, *47*, 198–209, doi:10.1002/jrs.4775.
  31. Sowoidnich, K.; Kronfeldt, H.-D. In-situ species authentication of frozen-thawed meat and meat juice using shifted excitation Raman difference spectroscopy. In *Biophotonics: Photonic Solutions for Better Health Care VI, Proceedings of the SPIE Photonics Europe, Strasbourg, France, 22–26 April 2018*; Popp, J., Tuchin, V.V., Pavone, F.S., Eds.; 2018; 106850L: pp. 1–12.
  32. Sowoidnich, K.; Kronfeldt, H.-D. Fluorescence Rejection by Shifted Excitation Raman Difference Spectroscopy at Multiple Wavelengths for the Investigation of Biological Samples. *ISRN Spectrosc.* **2012**, *2012*, 1–11, doi:10.5402/2012/256326.
  33. Knipfer, C.; Motz, J.; Adler, W.; Brunner, K.; Gebrekidan, M.T.; Hankel, R.; Agaimy, A.; Will, S.; Braeuer, A.; Neukam, F.W.; et al. Raman difference spectroscopy: A non-invasive method for identification of oral squamous cell carcinoma. *Biomed. Opt. Express* **2014**, *5*, 3252–3265, doi:10.1364/BOE.5.003252.
  34. Han, Z.; Strycker, B.D.; Commer, B.; Wang, K.; Shaw, B.D.; Scully, M.O.; Sokolov, A.V. Molecular origin of

- the Raman signal from *Aspergillus nidulans* conidia and observation of fluorescence vibrational structure at room temperature. *Sci. Rep.* **2020**, *10*, 5428, doi:10.1038/s41598-020-62112-w.
35. Schmälzlin, E.; Moralejo, B.; Rutowska, M.; Monreal-Ibero, A.; Sandin, C.; Tarcea, N.; Popp, J.; Roth, M.M. Raman imaging with a fiber-coupled multichannel spectrograph. *Sensors* **2014**, *14*, 21968–21980, doi:10.3390/s141121968.
36. Schmälzlin, E.; Moralejo, B.; Bodenmüller, D.; Darvin, M.E.; Thiede, G.; Roth, M.M. Ultrafast imaging Raman spectroscopy of large-area samples without stepwise scanning. *J. Sensors Sens. Syst.* **2016**, *5*, 261–271, doi:10.5194/jsss-5-261-2016.
37. Stewart, S.; Priore, R.J.; Nelson, M.P.; Treado, P.J. Raman Imaging. *Annu. Rev. Anal. Chem.* **2012**, *5*, 337–360, doi:10.1146/annurev-anchem-062011-143152.
38. Müller, W.; Kielhorn, M.; Schmitt, M.; Popp, J.; Heintzmann, R. Light sheet Raman micro-spectroscopy. *Optica* **2016**, *3*, 452–457, doi:10.1364/OPTICA.3.000452.
39. Sinjab, F.; Liao, Z.; Notingher, I. Applications of Spatial Light Modulators in Raman Spectroscopy. *Appl. Spectrosc.* **2019**, *73*, 727–746, doi:10.1177/0003702819834575.
40. Allington-Smith, J. Basic principles of integral field spectroscopy. *New Astron. Rev.* **2006**, *50*, 244–251, doi:10.1016/j.newar.2006.02.024.
41. Bacon, R.; Monnet, G. Recent Trends in Integral Field Spectroscopy. In *Optical 3D-Spectroscopy for Astronomy*; Wiley-VCH: Weinheim, Germany, 2017; pp. 115–128.
42. Glazebrook, K.; Bland-Hawthorn, J. Microslit Nod-Shuffle Spectroscopy: A Technique for Achieving Very High Densities of Spectra. *Publ. Astron. Soc. Pac.* **2002**, *113*, 197–214, doi:10.1086/318625.
43. Roth, M.M.; Cardiel, N.; Cenarro, J.; Schönberner, D.; Steffen, M. Nod & Shuffle 3D Spectroscopy. In *Scientific Detectors for Astronomy 2005*; Beletic, J.E., Beletic, J.W., Amico, P., Eds.; Springer: Dordrecht, The Netherlands, 2005; pp. 99–108.
44. Roth, M.M.; Fechner, T.; Wolter, D.; Kelz, A.; Becker, T. Ultra-Deep Optical Spectroscopy with PMAS. Using the Nod-and-Shuffle Technique. *Exp. Astron.* **2002**, *14*, 99–105, doi:10.1023/B:EXPA.0000004352.56068.a8.
45. Sowoidnich, K.; Maiwald, M.; Sumpf, B.; Towrie, M.; Matousek, P. Charge-shifting optical lock-in detection with shifted excitation Raman difference spectroscopy for the analysis of fluorescent heterogeneous samples. In *Biomedical Vibrational Spectroscopy, Proceedings of the SPIE BiOS, San Francisco, CA, USA, 1–6 February 2020*; Petrich, W., Huang, Z., Eds.; 2020; 112360K; pp. 1–10.
46. Sowoidnich, K.; Towrie, M.; Maiwald, M.; Sumpf, B.; Matousek, P. Shifted Excitation Raman Difference Spectroscopy with Charge-Shifting Charge-Coupled Device (CCD) Lock-In Detection. *Appl. Spectrosc.* **2019**, *73*, 1265–1276, doi:10.1177/0003702819859352.
47. Heming, R.; Herzog, H.; Deckert, V. Optical CCD lock-in device for Raman difference spectroscopy. in *DGAO Proc.* **2008**, *109*, p. 33.
48. Schmälzlin, E.; Urrutia, T.; Korinth, F.; Stiebing, C.; Krafft, C.; Popp, J.; Roth, M.M. Bildgebende Differenz-Raman-Spektroskopie mit “Nod and Shuffle“-Technik. In Proceedings of the 14th Dresdner Sensor-Symposium, Dresden, Germany, 2–4 December 2019; pp. 96–101, doi:10.5162/14dss2019/6.4
49. Moralejo, B.; Roth, M.M.; Godefroy, P.; Fechner, T.; Bauer, S.M.; Schmälzlin, E.; Kelz, A.; Haynes, R. The Potsdam MRS spectrograph: Heritage of MUSE and the impact of cross-innovation in the process of technology transfer. In *Advances in Optical and Mechanical Technologies for Telescopes and Instrumentation II, Proceedings of the SPIE Astronomical Telescopes + Instrumentation, Edinburgh, UK, 26 June–1 July 2016*; Navarro, R., Burge, J.H., Eds.; 2016; 991222; pp. 1–13.
50. Moralejo, B.; Schmälzlin, E.; Bodenmüller, D.; Fechner, T.; Roth, M.M. Improving the frame rates of Raman image sequences recorded with integral field spectroscopy using windowing and binning methods. *J. Raman Spectrosc.* **2018**, *49*, 372–375, doi:10.1002/jrs.5268.
51. Sumpf, B.; Müller, A.; Maiwald, M. Tailored diode lasers: Enabling Raman spectroscopy in the presence of disturbing fluorescence and background light. In *Plasmonics in Biology and Medicine XVI, Proceedings of the SPIE BiOS, San Francisco, CA, USA, 2–7 February 2019*; Vo-Dinh, T., Ho, H.-P.A., Ray, K., Eds.; 2019; 1089411; pp. 1–8.
52. Schmälzlin, E.; Moralejo, B.; Gersonde, I.; Schleusener, J.; Darvin, M.E.; Thiede, G.; Roth, M.M. Nonscanning large-area Raman imaging for ex vivo/in vivo skin cancer discrimination. *J. Biomed. Opt.* **2018**, *23*, 1–11, doi:10.1117/1.JBO.23.10.105001.
53. Kelz, A.; Verheijen, M.A.W.; Roth, M.M.; Bauer, S.M.; Becker, T.; Paschke, J.; Popow, E.; Sánchez, S.F.;

- Laux, U. PMAS: The Potsdam Multi-Aperture Spectrophotometer. II. The Wide Integral Field Unit PPak. *Publ. Astron. Soc. Pac.* **2006**, *118*, 129–145, doi:10.1086/497455.
54. Sandin, C.; Becker, T.; Roth, M.M.; Gerssen, J.; Monreal-Ibero, A.; Böhm, P.; Weilbacher, P. P3D: A general data-reduction tool for fiber-fed integral-field spectrographs. *Astron. Astrophys.* **2010**, *515*, 1–18, doi:10.1051/0004-6361/201014022.
55. Sandin, C.; Becker, T.; Roth, M.M.; Gerssen, J.; Monreal-Ibero, A.; Böhm, P.; Weilbacher, P. p3d: General data-reduction tool for fiber-fed integral-field spectrographs 2012, ascl:1205.002.
56. p3d a general data-reduction tool for fiber-fed integral-field spectrographs. Available online: <https://p3d.sourceforge.io/> (accessed on 20. November 2020)
57. R Core Team. *R: A Language and Environment for Statistical Computing*; R Foundation for Statistical Computing: Vienna, Austria, 2018.
58. Beleites, C.; Sergio, V. *hyperSpec: A Package to Handle Hyperspectral Data Sets in R*; <https://CRAN.R-project.org/package=hyperSpec> (accessed on 23.11.2020) .
59. Harris, A. *FITSio: FITS (Flexible Image Transport System) Utilities*; <https://rdr.io/cran/FITSio/> (accessed on 23.11.2020)
60. Beleites, C. *RamanCal: Calibration Routines for Raman Spectrometers*; 2013.
61. Borchers, H.W. *pracma: Practical Numerical Math Functions*; <https://rdr.io/rforge/pracma/> (accessed on 23.11.2020)
62. Gibb, S.; Strimmer, K. MALDIquant: A versatile R package for the analysis of mass spectrometry data. *Bioinformatics* **2012**, *28*, 2270–2271, doi:10.1093/bioinformatics/bts447.
63. Garnier, S. *viridis: Default Color Maps from "matplotlib"*; <https://rdr.io/cran/viridis/> (accessed on 23.11.2020)
64. Bonifacio, A.; Beleites, C.; Sergio, V. Application of R-mode analysis to Raman maps: A different way of looking at vibrational hyperspectral data. *Anal. Bioanal. Chem.* **2015**, *407*, 1089–1095, doi:10.1007/s00216-014-8321-7.
65. Arc Line Lamps on the Website of W. M. Keck Observatory. Available online: [https://www2.keck.hawaii.edu/inst/Iris/arc\\_calibrations.html](https://www2.keck.hawaii.edu/inst/Iris/arc_calibrations.html) (accessed on 20. November 2020)
66. Horne, K. An optimal extraction algorithm for CCD spectroscopy. *Publ. Astron. Soc. Pac.* **1986**, *98*, 609, doi:10.1086/131801.
67. Dochow, S.; Bergner, N.; Matthäus, C.; Praveen, B.B.; Ashok, P.C.; Mazilu, M.; Krafft, C.; Dholakia, K.; Popp, J. Etaloning, fluorescence and ambient light suppression by modulated wavelength Raman spectroscopy. *Biomed. Spectrosc. Imaging* **2012**, *1*, 383–389, doi:10.3233/BSI-120031.
68. Maiwald, M.; Müller, A.; Sumpf, B.; Tränkle, G. A portable shifted excitation Raman difference spectroscopy system: Device and field demonstration. *J. Raman Spectrosc.* **2016**, *47*, 1180–1184, doi:10.1002/jrs.4953.
69. Sowoidnich, K.; Towrie, M.; Matousek, P. Lock-in detection in Raman spectroscopy with charge-shifting CCD for suppression of fast varying backgrounds. *J. Raman Spectrosc.* **2019**, *50*, 983–995, doi:10.1002/jrs.5597.

**Publisher's Note:** MDPI stays neutral with regard to jurisdictional claims in published maps and institutional affiliations.



© 2020 by the authors. Licensee MDPI, Basel, Switzerland. This article is an open access article distributed under the terms and conditions of the Creative Commons Attribution (CC BY) license (<http://creativecommons.org/licenses/by/4.0/>).

## 7. Wissenschaftliche Beiträge

### Journal

*Wide Field Spectral Imaging with Shifted Excitation Raman Difference Spectroscopy Using the Nod and Shuffle Technique*

Florian Korinth, Elmar Schmäzlin, Clara Stiebing, Tanya Urrutia, Genoveva Micheva, Christer Sandin, André Müller, Martin Maiwald, Bernd Sumpf, Christoph Krafft, Günter Tränkle, Martin M. Roth, Jürgen Popp (2020)

*Sensors*, **20**: 6723, 1 – 19, <https://doi.org/10.3390/s20236723>.

*FLIm and Raman Spectroscopy for Investigating Biochemical Changes of Bovine Pericardium upon Genipin Cross-Linking*

Tanveer A. Shaik, Alba Alfonso-Garcia, Martin Richter, Florian Korinth, Christoph Krafft, Laura Marcu, Jürgen Popp (2020)

*Molecules*, **25**: 3857, 1 – 14, <https://doi.org/10.3390/molecules25173857>.

*New methodology to process shifted excitation Raman difference spectroscopy data: a case study of pollen classification*

Florian Korinth, Abdullah S. Mondol, Clara Stiebing, Iwan W. Schie, Christoph Krafft, Jürgen Popp (2020)

*Scientific Reports*, **10**(1): 11215, 1 – 12, <https://doi.org/10.1038/s41598-020-67897-4>.

*FLIm and Raman imaging for detecting micro-environmental changes in bovine pericardium upon genipin cross-linking (Conference Presentation)*

Tanveer A. Shaik, Alba Alfonso-Garcia, Martin Richter, Florian Korinth, Anne K. Haudenschild, James F. Mcmasters, Christoph Krafft, Jürgen Popp, Laura Marcu (2020)

*In Proceedings of the Imaging, Manipulation, and Analysis of Biomolecules, Cells, and Tissues XVIII*, Farkas, D.L., Leary, J.F., Tarnok, A., Eds.; SPIE: 49, <https://doi.org/10.1117/12.2544225>.



*Bildgebende Differenz-Raman-Spektroskopie mit "Nod and Shuffle" – Technik*

Elmar Schmäzlin, Tanya Urrutia, Florian Korinth, Clara Stiebing, Christoph Krafft, Jürgen Popp, Martin M. Roth (2019)

*In Proceedings of the 14. Dresdner Sensor-Symposium*; Dresden, Germany: 96–101, <https://doi.org/10.5162/14dss2019/6.4>.

*Evaluation of Shifted Excitation Raman Difference Spectroscopy and Comparison to Computational Background Correction Methods Applied to Biochemical Raman Spectra*

Eliana Cordero\*, Florian Korinth\*, Clara Stiebing, Christoph Krafft, Iwan W. Schie, Jürgen Popp (2017)

*Sensors*, **17**: 1724, 1 – 17, <https://doi.org/10.3390/s17081724>.

\* geteilte Erstautorenschaft

## Forschungsaufenthalt

03/2020      **Forschungsaufenthalt in der Gruppe von Laura Marcu**, Marcu Laboratory, Optical Spectroscopy and Ultrasound for disease diagnosis, Davis, Kalifornien, Vereinigte Staaten von Amerika  
Investigation of breast cancer patient samples using FLIm and Raman Imaging

## Vorträge

05/2019      **Bunsentagung 2019**, Jena, Deutschland  
Classification of different pollen samples using Raman difference spectra

02/2019      **Doktorandenseminar 2019**, Dornburg, Deutschland  
Shifted Excitation Raman Difference Spectroscopy and Imaging

09/2017      **DokDok 2017**, Suhl, Deutschland  
Evaluation of Shifted Excitation Raman Difference Spectroscopy for tissue imaging and comparison with Extended Multiplicative Scatter Correction

## Posterpräsentationen

- 02/2020      **Doktorandenseminar 2020**, Dornburg, Deutschland  
Shifted Excitation Raman Difference Spectroscopy (SERDS) Imaging Utilizing  
the Nod & Shuffle Technique with very short Acquisition Intervals
- 06/2018      **SPEC 2018**, Glasgow, Vereinigtes Königreich  
SERDS and EMSC for Fluorescence Background Removal in Raman Images
- 02/2018      **Doktorandenseminar 2018**, Dornburg, Deutschland  
Fiber optic Raman imaging of tissue using shifted excitation Raman difference  
spectroscopy (SERDS)
- 02/2017      **Doktorandenseminar 2017**, Dornburg, Deutschland  
Fiber optic Raman imaging of tissue using shifted excitation Raman difference  
spectroscopy (SERDS)

## Danksagung

Ich möchte an dieser Stelle allen danken, die mich während meiner Promotion unterstützt haben. Zuallererst möchte ich mich bei Prof. Dr. Jürgen Popp für seine Unterstützung und die Betreuung während der Promotion bedanken. Dein strategischer Weitblick und deine wissenschaftlichen Visionen sind inspirierend. Ich danke außerdem PD. Dr. Christoph Krafft für seinen wissenschaftlichen Input und die gemeinsamen Diskussionen. Ich habe von dir eine Menge über Raman-Spektroskopie und wissenschaftliches Schreiben gelernt. Ferner gilt mein Dank Dr. Clara Stiebing für ihr produktives Feedback, ihr stets offenes Ohr und ihre wissenschaftliche Expertise. Deine Korrekturen waren immer auf den Punkt, du hast dir immer für mich Zeit genommen und standst mir mit Rat und Tat zur Seite.

Ich danke allen Kooperationspartnern des HYPERAM-Projektes vom Ferdinand-Braun-Institut und vom Leibniz-Institut für Astrophysik Potsdam für die gemeinsame, wissenschaftliche Arbeit und im Speziellen Dr. Elmar Schmäzlin. Ich habe die gemeinsamen Messkampagnen in Potsdam sehr genossen. Prof. Dr. Iwan W. Schie und Dr. Claudia Beletes möchte ich für den wissenschaftlichen Austausch und die vielen Gespräche über meine wissenschaftliche Arbeit danken. Ihr habt immer versucht, euch Zeit zu nehmen und euch in meine wissenschaftliche Arbeit einzudenken. Dr. Jan Rüger, Dr. Roman Kiselev und Dr. Claudia Beletes danke ich für die Unterstützung und Einarbeitung in die Chemometrie und R.

Mein Dank geht auch an meine lieben Freunde und Kollegen Saif, Mo, Tanveer, Wei und Christina. Die gemeinsamen Unternehmungen und Gespräche, die gegenseitige moralische Unterstützung und das gute Essen haben die schwierigen Phasen leichter gemacht. Insgesamt möchte ich allen Kollegen aus der FA1.04 and FA1.10 für die gute Arbeitsatmosphäre und die schöne gemeinsame Zeit danken. Ich werde die Group Fun Time vermissen.

Ich danke auch allen meinen Freunden, die immer wieder für mich da waren, meine Stimmungen abbekommen haben und mir immer eine Stütze waren. Bitte entschuldigt, dass ich euch nicht alle namentlich erwähne. Ich möchte keinen aus Versehen vergessen. Ich hoffe, dass wir noch viele entspannte Stunden und angeregte Gespräche haben und noch viele Abenteuer zusammen erleben werden.

Ich danke Tamara für ihr offenes Ohr, ihre mahnenden Worte und ihre ehrliche Meinung. Du hast nie an mir gezweifelt. Deine Besuche haben mich immer alles andere vergessen lassen. Ich habe es genossen, dir Berlin zu zeigen, auch wenn ich noch nie so viel durch diese Stadt gelaufen bin wie mit dir.

Vielen Dank an Luise. Du warst immer da für mich, hast immer versucht mir zu helfen und mir einen Ausweg aus den Sackgassen aufzuzeigen. Ich hoffe, dass wir gemeinsam noch viele tolle Gespräche führen, Puzzle lösen, Serien schauen, Urlaube verbringen und irgendwann der Traum vom Garten wahr wird.

Zu guter Letzt möchte ich meiner gesamten Familie, im Besonderen meiner Mutter, meinem Bruder Dominik und meinem Onkel Mike für die Unterstützung danken. Mutter, du hast immer meinen Drang nach Wissen gestärkt und mich unterstützt, was der Grundstein für alles war. Uncle Mike, the many walks we took together to discuss any topic were a huge impetus for me to not only ask questions but look for answers. Dominik, du bist eine große Hilfe und ein enger Freund. Die vielen Fahrten nach Essen und der Roadtrip durch Rumänien werden mir immer in Erinnerung bleiben.

An meinen Vater, meinen Opa Rudi und meine Oma Erika: ihr werdet immer in meinem Herzen sein. Danke für alles.

## Erklärungen

### **Selbständigkeitserklärung**

Ich erkläre, dass ich die vorliegende Arbeit selbständig und unter Verwendung der angegebenen Hilfsmittel, persönlichen Mitteilungen und Quellen angefertigt habe.

Jena, den 26.11.2020

Florian Korinth

### **Erklärung zu den Eigenanteilen des Promovenden sowie der weiteren Doktorandinnen/ Doktoranden als Co-Autorinnen/-Autoren an den Publikationen und Zweitpublikationsrechten bei einer kumulativen Dissertation**

Für alle in dieser kumulativen Dissertation verwendeten Manuskripte liegen die notwendigen Genehmigungen der Verlage („Reprint permissions“) für die Zweitpublikation vor.

Die Co-Autorinnen/-Autoren der in dieser kumulativen Dissertation verwendeten Manuskripte sind sowohl über die Nutzung, als auch über die oben angegebenen Eigenanteile der weiteren Doktorandinnen/Doktoranden als Co-Autorinnen/-Autoren an den Publikationen und Zweitpublikationsrechten bei einer kumulativen Dissertation informiert und stimmen dem zu.

Jena, den 26.11.2020

Florian Korinth

### **Einverständniserklärung des Betreuers**

Ich bin mit der Abfassung der Dissertation als publikationsbasiert, d.h. kumulativ, einverstanden und bestätige die vorstehenden Angaben. Eine entsprechend begründete Befürwortung mit Angabe des wissenschaftlichen Anteils des Doktoranden an den verwendeten Publikationen werde ich parallel an den Rat der Fakultät der Chemisch-Geowissenschaftlichen Fakultät richten.







Jena, den 26.11.2020

Prof. Dr. Jürgen Popp



Article

# Wide Field Spectral Imaging with Shifted Excitation Raman Difference Spectroscopy Using the Nod and Shuffle Technique

Florian Korinth <sup>1</sup>, Elmar Schmälzlin <sup>2</sup>, Clara Stiebing <sup>1</sup>, Tanya Urrutia <sup>2</sup> , Genoveva Micheva <sup>2</sup>, Christer Sandin <sup>3</sup>, André Müller <sup>4</sup>, Martin Maiwald <sup>4</sup> , Bernd Sumpf <sup>4</sup> , Christoph Krafft <sup>1,\*</sup> , Günther Tränkle <sup>4</sup>, Martin M. Roth <sup>2</sup>  and Jürgen Popp <sup>1,5</sup> 

- <sup>1</sup> Leibniz Institute of Photonic Technology (Leibniz IPHT), Research Alliance “Health Technologies”, Albert-Einstein-Straße 9, 07743 Jena, Germany; florian.korinth@leibniz-ipht.de (F.K.); clara.stiebing@leibniz-ipht.de (C.S.); juergen.popp@leibniz-ipht.de (J.P.)
  - <sup>2</sup> Leibniz Institute for Astrophysics Potsdam (AIP), Research Alliance “Health Technologies”, An der Sternwarte 16, 14482 Potsdam, Germany; eschmaelzlin@aip.de (E.S.); turrutia@aip.de (T.U.); gmicheva@aip.de (G.M.); mmroth@aip.de (M.M.R.)
  - <sup>3</sup> Sandin Advanced Visualization, Tylögränd 14, 12156 Johanneshov, Sweden; christersandin@yahoo.se
  - <sup>4</sup> Ferdinand-Braun-Institut, Leibniz-Institut für Höchstfrequenztechnik, Research Alliance “Health Technologies”, Gustav-Kirchhoff-Str. 4, 12489 Berlin, Germany; andre.mueller@fbh-berlin.de (A.M.); martin.maiwald@fbh-Berlin.de (M.M.); bernd.sumpf@fbh-berlin.de (B.S.); guenther.traenkle@fbh-berlin.de (G.T.)
  - <sup>5</sup> Institute of Physical Chemistry and Abbe Center of Photonics, Friedrich Schiller University Jena, Helmholtzweg 4, 07743 Jena, Germany
- \* Correspondence: christoph.krafft@leibniz-ipht.de

Received: 6 October 2020; Accepted: 19 November 2020; Published: 24 November 2020



**Abstract:** Wide field Raman imaging using the integral field spectroscopy approach was used as a fast, one shot imaging method for the simultaneous collection of all spectra composing a Raman image. For the suppression of autofluorescence and background signals such as room light, shifted excitation Raman difference spectroscopy (SERDS) was applied to remove background artifacts in Raman spectra. To reduce acquisition times in wide field SERDS imaging, we adapted the nod and shuffle technique from astrophysics and implemented it into a wide field SERDS imaging setup. In our adapted version, the nod corresponds to the change in excitation wavelength, whereas the shuffle corresponds to the shifting of charges up and down on a Charge-Coupled Device (CCD) chip synchronous to the change in excitation wavelength. We coupled this improved wide field SERDS imaging setup to diode lasers with 784.4/785.5 and 457.7/458.9 nm excitation and applied it to samples such as paracetamol and aspirin tablets, polystyrene and polymethyl methacrylate beads, as well as pork meat using multiple accumulations with acquisition times in the range of 50 to 200 ms. The results tackle two main challenges of SERDS imaging: gradual photobleaching changes the autofluorescence background, and multiple readouts of CCD detector prolong the acquisition time.

**Keywords:** Raman spectroscopy; SERDS; wide field imaging; nod and shuffle; photobleaching; autofluorescence; integral field spectroscopy; background suppression; diode lasers

## 1. Introduction

Raman spectroscopy provides a label-free, non-destructive insight into the biochemical composition of a sample. It can be used for the pathological assessment of biological samples such as cells and tissues [1–5]. Although the majority of biomolecules such as nucleic acids, proteins,

lipids, and carbohydrates do not fluoresce at visible excitation, autofluorescence is often excited along with Raman scattering in biological samples [6]. Since the fluorescence absorption cross-section is much larger than the Raman scattering cross-section, even trace amounts of autofluorescent molecules often result in high-intensity spectral backgrounds. This high background can mask the Raman fingerprint information and increases the shot noise in spectra [7].

Approaches to solve this challenge can be divided into computational and instrumental methods [8]. Computational methods correct Raman spectra for their background using mathematical algorithms such as extended multiplicative scatter correction (EMSC) [9,10], rubberband [11,12], sensitive nonlinear iterative peak (SNIP) [13,14], and polynomial fittings [15]. Examples for the application of polynomial fitting are the correction during *in vivo* Raman studies of colorectal tissue [16] and brain cancer [17]. EMSC was used for the autofluorescence correction of Raman spectra of bladder biopsies [18]. Depending on the complexity of the algorithm, the computational data processing can be time consuming.

Instrumental methods for autofluorescence suppression enable less time consuming data processing, but they usually require more complex experimental setups. Examples for these methods are time-gated methods [19,20], phase or wavelength modulation techniques [21–24], and shifted excitation Raman difference spectroscopy (SERDS) [25]. For SERDS, two Raman spectra are measured at the same spatial position with two slightly shifted excitation wavelengths. Raman bands, which are a function of the exciting laser light, follow the shift in excitation wavelength. The background, a function of the instrument (filters, optics, and detection system), the sample's autofluorescence, room light, and other background components, does not shift. The two spectra are subtracted from each other, ideally resulting in a background-free difference spectrum with a first derivative-like appearance. For a proper reconstruction of the Raman spectrum from the difference spectrum, the shift in excitation wavelength, and therefore also the shift in relative wavenumbers, should be selected in accordance with the band widths of the expected Raman spectra. The target classification can be derived directly from the SERDS spectra, which was demonstrated for pollen [26], or from algorithm-based reconstructed Raman spectra, which was demonstrated for formalin fixed patient samples of breast tumors [27]. Further studies have already been published on biological samples using the SERDS technique. The investigated samples were molar tooth slices and *in vivo* human skin [28], algae produced complex polysaccharides [29], tissues from different animals [30–32], *ex vivo* oral squamous cell carcinoma biopsies [33], and spores of *Aspergillus nidulans* conidia [34].

There are only few examples of SERDS imaging so far, in which each point of the image corresponds to a difference spectrum. In the first implementation, such images were collected by performing a point-by-point raster scan of the sample, measuring each point twice with two different wavelengths. Cordero et al. [7] measured a beef steak in this fashion. After clustering the mean spectra of each cluster and assigning them to two different types of proteins and lipid, they compared the results of different wavelength shifts for SERDS with results based on EMSC and the 1st derivative of the EMSC corrected spectra. A second implementation applied a so-called integral field spectroscopy (IFS) approach [35,36], which belongs to the wide field imaging techniques. Whereas point scanning or line mapping approaches move the laser spot or line across the sample to sequentially collect a Raman image, wide field imaging instruments project the sample onto a multichannel detector such as a Charge-Coupled Device (CCD) chip and acquire the full Raman image simultaneously [37]. The spectral information can be obtained by fixed wavelength or tunable filters. In the context of light sheet Raman imaging, an interferometric detection scheme was developed [38]. More than 1000 Raman images were registered within minutes from which the Raman spectra were calculated via Fourier transformation. Another group of Raman imaging techniques generates several laser foci spots on the sample simultaneously by using fiber arrays, micro lens arrays, galvomirrors, or spatial modulators (such as liquid-crystal spatial modulators or digital micromirror devices). Then, the spectra from all foci are imaged on a CCD either by the use of integral field spectrographs or by producing several pinholes using the spatial modulators [39].



In astronomical observatories, integral field spectroscopy (IFS) [40] is used to create a complete spectral image of cosmic objects in one shot without raster scanning the object, which saves valuable and rare observation time. For this one shot imaging, the image is optically dissected by a so-called integral field unit (IFU). The sections (e.g., slices, spots, squares, hexagons) are re-arranged in front of the rather large entrance slit of a wide field spectrograph or even several such spectrographs. One of the options to realize an IFU is using a fiber bundle that is arranged in a two-dimensional array on the side facing the sample and in a row-like fashion on the side facing the spectrograph. The row of fiber front surfaces acts as long pseudo-slit at the entrance side of the spectrograph. If the fibers of the bundle have round cores, the image will be dissected into round spots. At the spectrograph, the dispersed signals emerging from the fibers are collected by a large area detector. Each signal trace correlates to a specific image location. The spectrograph is designed in a way that signal traces originating from light at the ends of the entrance slit show nearly the same quality as light traces originating from the slit's center, meaning the spectrograph works over a "wide field" with regard to signal position at the entrance. The raw signal is processed into a data cube that contains the full spectral and lateral information. So far, the most powerful IFS spectrograph developed for astronomy is M.U.S.E. (Multi Unit Spectroscopic Explorer) [41] at the Very Large Telescope Observatory, Paranal, Chile. It consists of 24 IFUs, each with its own attached spectrograph, and it detects a total of 90,000 spectra (and therefore image pixels called "spaxels") with a spectral resolution of 0.25 nm in the range of 465 to 930 nm in one exposure simultaneously. An IFS spectrograph with 400 spaxels, built as a clone of a M.U.S.E. spectrograph module, was successfully used for Raman and SERDS imaging [35,36]. A custom-made probe head focuses the excitation laser in 400 measuring spots on the sample and guides the backscattered Raman signal into the IFS spectrograph. This setup was used by Schmäzlin et al. [36] for Raman and SERDS imaging of different samples, e.g., a cross-section of a pig ear, skin, and a dissolving brown sugar cube.

Another technique from astrophysics that could be translated to wide field SERDS imaging is the nod and shuffle concept [42–44]. This concept was originally developed to measure deep spectra of very faint galaxies whose surface brightness is usually a fraction of the night sky brightness, sometimes orders of magnitude fainter than the sky. In order to overcome the systematic errors introduced by atmospheric background intensity fluctuations, it is necessary to employ a technique called beam switching, which essentially means to measure pairs of (object + sky) and (sky) in rapid succession. While fast readout detectors such as infrared arrays have no problem to accomplish this in real time, Charge-Coupled Devices (CCD) in the optical wavelength domain incur substantial readout times per image. To accommodate beam switching with CCDs, the original nod and shuffle technique allows for a "nod" as a small offset of the telescope to switch its focus between the target and the neighboring background night sky. The "shuffle" stands for shifting charges on a frame transfer CCD from an active exposure area into one of two storage areas: one for (object + sky), another one for (sky). By synchronizing the nod process with the charge shuffle on the chip, it is possible to create the beam switching short exposure pairs that are necessary to eliminate the rapid sky brightness fluctuations without having to read out the CCD every time. After a sufficiently high total exposure time has been acquired by a series of many nod–shuffles (of order several tens), the exposure is stopped, and the entire CCD is read out. This technique works particularly well with fiber-coupled spectrographs, where the spacing of fibers on the entrance slit provides gaps between spectral traces on the detector and the gaps are wide enough to accommodate an extra trace between two adjacent spectral traces in an interlaced fashion. A virtue of this technique lies in the ability to subtract (object + sky) and (sky) on a pixel-by-pixel basis, thus avoiding further systematic errors that occur in the process of data reduction, specifically optimal extraction of the spectral traces: the illumination of each pair of pixels in the (object + sky) and (sky) storage areas has occurred under (almost) exactly the same circumstances.

In this work, the nod and shuffle technique from astrophysics is adapted and implemented into a wide field SERDS imaging setup. As a result, this concept addresses the two main challenges of SERDS imaging. First, photobleaching between consecutive Raman spectra at two excitation wavelengths reduces the auto-fluorescent background and causes a residual background slope in the difference

spectrum. Second, short exposure times in the millisecond range can be applied to minimize the photobleaching effect that results in low signal to noise ratios or long total acquisition times for hundreds of single spectra. Since the CCD chip has to be read out in a traditional setup after each acquisition and readout time can take up to a minute or more in particular for large CCDs, the strategy of very short acquisitions and multiple readouts would increase the overall measurement time tremendously. The nod and shuffle technique can be adapted to support SERDS imaging and overcome these challenges of SERDS imaging. The nod corresponds to the shift in excitation wavelength at the same spatial position, whereas the shuffle remains the shuffling of the charges on the CCD, saving, and accumulating both signals on the same CCD until numerous cycles revealed to sufficiently high signal to noise ratio. For a single channel setup with a rectangle CCD chip ( $1024 \times 256$  pixels), this was previously demonstrated by Sowoidnich et al. [45,46] as a Charge-Shifting Charge-Coupled Device, based on the previous works of Heming et al. [47].

In comparison to a previous conference proceeding paper [48], this publication provides more details of the nod and shuffle approach and the laser diode development, and it demonstrates wide field spectral imaging with nod and shuffle SERDS for a tissue specimen for the first time.

## 2. Materials and Methods

### 2.1. Wide Field SERDS Setup

In the experiments, an IFS spectrograph unit of the M.U.S.E. system (Winlight System, Pertuis, France) with a large area  $4096 \times 4096$  CCD chip (CCD231, Teledyne e2v, UK) was used. A detailed description of the spectrograph and detector system can be found in [49] and [50]. Two different laser sources were used during the presented experiments. They were selected for their shift in their emitted wavelength, which should correlate to the expected band widths of the Raman profiles of the samples (see below in Table 1).

1. A fiber-coupled near infrared (NIR) laser source LS 2-VBG, Ushio, Tokyo, Japan (formerly PD-LD, Pennington, USA) was used. The laser emits at 784.43 and 785.48 nm with a maximum laser power of 400 mW. This 1.05 nm shift ( $17 \text{ cm}^{-1}$ ) in excitation wavelength was the largest possible shift without a high loss of laser intensity due to the filters used in the setup. This small shift in wavenumbers was used for the investigation of two pharmaceutical pills, which show Raman spectra with narrow band profiles.
2. A custom-made laser source based on two external wavelength stabilized blue laser diodes with spatially overlapping laser emissions at 457.74 and 458.90 nm in a conduction cooled package mount with a  $25 \times 25 \text{ mm}^2$  footprint was designed and realized [51]. The diode lasers are wavelength stabilized at both target wavelengths with volume Bragg gratings with spectral bandwidths of  $<0.2 \text{ nm}$  ( $<10 \text{ cm}^{-1}$ ) and diffraction efficiencies of 15%. The spectral distance of 1.16 nm ( $55 \text{ cm}^{-1}$ ) is selected for SERDS with respect to the spectral resolution of the spectrometer with  $0.22 \text{ nm}$  ( $\approx 10.4 \text{ cm}^{-1}$ ) and for the investigation of biological tissue samples, since these samples have broader Raman band structures. For the spatial overlap of both laser emissions, using a high-reflection coated prism as well as a polarizing beam splitter, one laser is rotated by  $90^\circ$ . During the measurements, the laser was mounted on a heatsink (hsa-series, Ostech, Berlin, Germany), which was set to an operating temperature of  $40 \text{ }^\circ\text{C}$ . For the individual operation of both laser diodes, two laser drivers were used (ds-series, Ostech, Berlin, Germany). The optical output power at both wavelengths was 0.4 W at 0.5 A. Figure 1 shows the corresponding emission spectra.

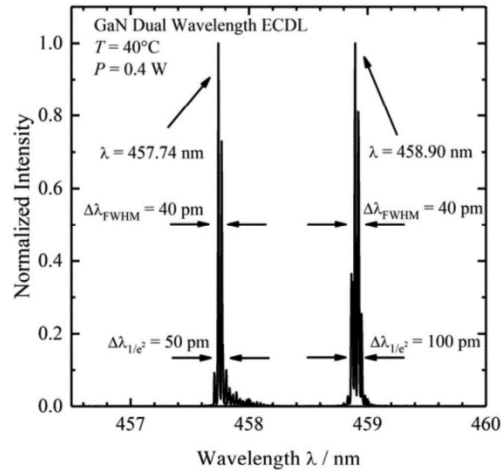


**Figure 1.** Emission spectra of the dual-wavelength GaN external cavity diode laser (ECDL) measured at an operating temperature of 40°C and an optical output power of 0.4 W.

The basic setup for Raman measurements was already reported in [36]. Briefly, 400 fibers of a bundle are arranged in a line at the spectrograph entrance to function as an IFU. On the sample side of the fiber bundle, the fibers form a 1 cm × 1 cm square, consisting of a 20 × 20 fiber matrix with a micro lens array (MLA) attached, so that the backscattered Raman signal can be efficiently coupled into the fibers. The laser light is guided via mirrors and filters on the sample. Two different probe head configurations were used: In the first configuration, another MLA focuses the laser light onto the sample by creating 400 foci (50 μm diameter; 0.5 mm center to center distance between focal spots) simultaneously while also collecting the Raman signal. This results in an imaging area of 1 cm<sup>2</sup>. The probe head in combination with the sample-side MLA was originally designed to measure thick skin samples with a low depth resolution. The low confocality is a consequence of 1 to 1 projection of 50 μm diameter foci onto 114 μm fiber cores to compensate alignment tolerances [52]. Due to the scattering, the achievable resolution was only 0.5 mm and, thus, a denser packing of the fibers was not useful. However, a far denser packing is possible and was already realized [53]. Figure 2 shows a schematic of the setup. The doublet lenses act as a telescope. They project the front surface of the sample onto the front surface of the fiber array. Furthermore, they project the exit pupil of the sample-side lens array to the entrance pupil of the fiber-side lens array. The second configuration with a field of view of approximately 0.02 cm<sup>2</sup> is used for smaller samples. Here, the MLA on the sample side is exchanged by an objective lens (Magnification = 10×, NA = 0.25). The two 50 mm doublet lenses are exchanged by a 200 mm tube lens. To implement the nod and shuffle technique, the wavelength axis has to be parallel to the readout register of the spectrograph, since the charge shuffle is only possible in the direction of the readout registers. Therefore the wavelength axis has to be orthogonal to the readout direction. In the original configuration of the spectrograph, this was not the case [36]; thus, the CCD chip had to be rotated by 90°. Unfortunately, a rotation of the existing CCD chip was not possible, since it had a graded index anti-reflection coating that was designed to maximize the throughput along the CCD chip's original wavelength axis. After the rotation, the profile of the anti-reflection coating would not match the wavelengths of the incident light anymore. Thus, a new CCD chip of the same type but with a uniform anti-reflection coating was purchased and built-in in the proper rotation. The loss of transmission caused by the simpler coating was insignificant. The camera control was changed to enable the shifting of the charges and the triggering of the lasers according to the settings in the user interface. For the generation of data cubes with single Raman spectra and difference spectra, the data reduction software also had to be adjusted to the new detector raw signal, which consisted of twice as many signal traces after the nod and shuffle changes.

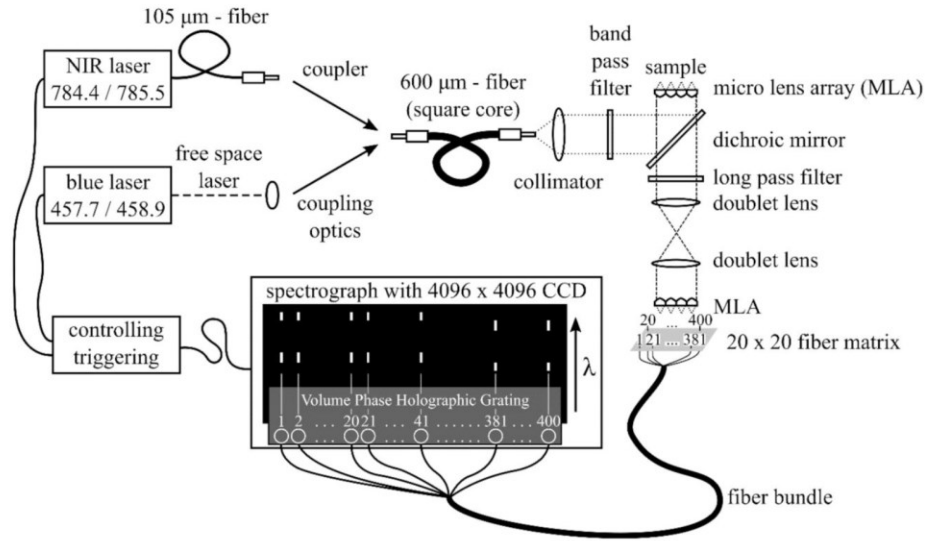


**Figure 2.** Wide field shifted excitation Raman difference spectroscopy (SERDS) imaging setup based on two micro lens arrays.

### 2.2. Nod and Shuffle

As briefly explained in the introduction the nod and shuffle technique for SERDS is a technique adapted from astrophysics. In SERDS, the nod corresponds to the change in excitation wavelength and the shuffle is, as in astronomy, the shift of charges on the CCD chip. In Figure 3, the interlaced nod and shuffle technique for SERDS is depicted.

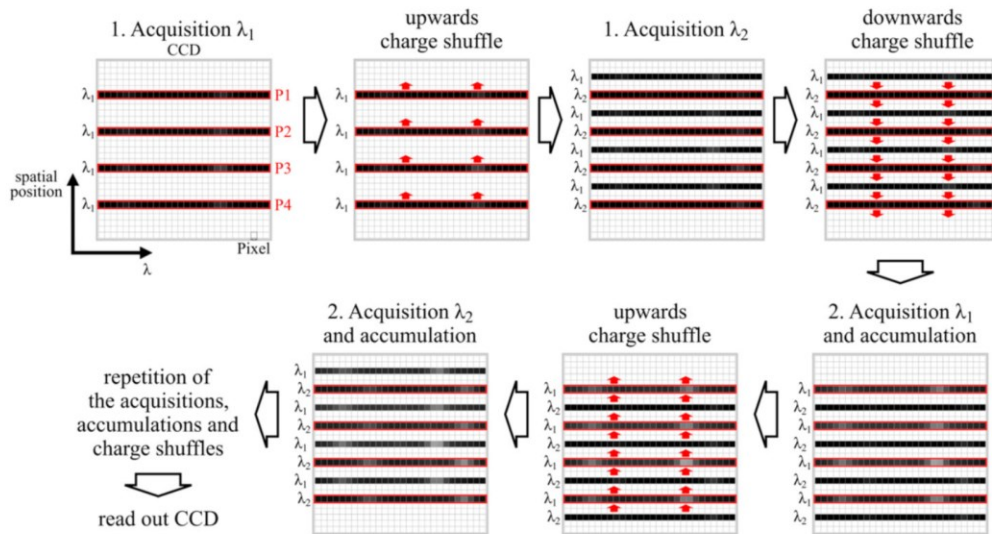


**Figure 3.** Illustration of the nod and shuffle technique by schematically showing the Charge-Coupled Device (CCD) chip (one square denotes one pixel on the CCD) and the shifting of charges (red arrows) after each acquisition and accumulation. The black lines symbolize the spectral signal traces with the corresponding excitation wavelengths to the left of them. The white spots inside the black lines display increasing signal strength, i.e., Raman bands that get more pronounced during the accumulation. The red boxes show the respective regions on the CCD, which are illuminated during the acquisition, where each box corresponds to the same spaxel (spatial Position P1, P2, P3, and P4) of the Raman image. For simplicity, only four spaxels of the Raman image are shown.

At first, a wide field Raman image of the sample is measured with the first excitation wavelength ( $\lambda_1$ ). Each signal trace corresponds to a full spectrum at a distinct spatial position. Then, all charges are shifted up by 5 pixels on the CCD, the excitation wavelength is changed to  $\lambda_2$ , and a new wide field Raman image of the sample is taken. A CCD consists of a light-sensitive area organized in vertical columns of electrodes. Four electrodes in series form a pixel in our case. They are separated horizontally by potential wells. Applying high or low voltage to the electrodes in a special scheme allows collecting electrons (charge) underneath. Clocking the electrodes with a dedicated voltage pattern moves the charge from electrode to electrode. All electrodes are equivalent and therefore charge transfer vertically up and down is possible. A shift of 5 pixels transfers the signal traces into the centers of the spaces in between their recording positions. A transfer to the centers minimizes the risk of crosstalk to the respective new recorded upper and lower signal traces. Then, all charges are shifted down by 5 pixels on the CCD, and the excitation wavelength is shifted back to  $\lambda_1$ . This ends the first acquisition cycle. By repeating these steps, several acquisitions with two different wavelengths can be accumulated without reading out the CCD chip in between measurements. The challenge of this technique is the high instrumental complexity and, in case of very intense signals, the danger of crosstalk due to the lower pixel distance between the signal traces. However, there are several advantages to this method:

1. Readout noise is only applied once to the complete set of data.
2. Readout time only factors into the complete measurement time once. As for a large CCD chip, the readout time can take up to a minute or more, the total measurement time is significantly increased, when reading out the CCD chip after every single measurement. In our case, a sample was measured with 200 accumulations for each wavelength before reading out the CCD once. If the CCD was read out after each acquisition, readout times alone would have taken 400 min instead of 1 min with nod and shuffle.
3. The technique allows measurements with very short acquisition times, which were accumulated with multiple iterations over a long time period using a wide field imaging setup. The accumulation of single measurements with very short acquisition times is favorable in the presence of signal fluctuations, e.g., photobleaching and fluctuating high-intensity background light (see Section 3.2.1).
4. Spectra measured at the same spatial position with different wavelengths are recorded on the same pixels of the CCD chip. Therefore, Raman images of both excitation wavelengths have the same artifacts originating from the sensitivity and noise variations of the CCD pixels.

### 2.3. Samples and Experimental Parameters

The samples used for the experiments were:

- Sample 1: Paracetamol tablet and a piece of an aspirin tablet were arranged on the large field of view probe head. Both samples show intense Raman bands.
- Sample 2: Polystyrene (PS) beads (50  $\mu\text{m}$  diameter) and polymethyl methacrylate (PMMA) beads (120  $\mu\text{m}$  diameter) were mixed and applied on a  $\text{CaF}_2$  window. Both samples show intense Raman bands and have diameters to demonstrate the lateral resolution.
- Sample 3: The lipid-rich part of a pork chop fresh from a butcher was placed on a  $\text{CaF}_2$  window. Pork tissue served as model for biological material with less intense Raman bands and elevated background.
- Sample 4: The transition region from meat to fat of a pork chop fresh from a butcher was placed on a  $\text{CaF}_2$  window.

The technical measurement conditions are shown in Table 1. The maximum acquisition time of 2 s for no. 3 and 4 gave the highest overall signal intensity on the CCD chip without crosstalk. This time was divided by the shortest achievable acquisition time of 50 ms for the laser system and resulted in 40 acquisitions. In the future, control of the lasers and the charge shift shuffling are improved to realize

even shorter acquisitions and systematic studies are planned to obtain a good signal-to-noise ratio and zero baseline at the same time.

**Table 1.** Overview over the technical measurement conditions shown by samples.

No.	Sample	Laser ( $\lambda_1/\lambda_2$ ) in nm	Intensity in W/mm <sup>2</sup>	Imaging Area in cm <sup>2</sup>	Acquisition Times <sup>1</sup>
1	Aspirin/Paracetamol	NIR (784.43/785.48)	0.004 <sup>2</sup>	1	200 × 200 ms
2	PS/PMMA	blue (457.74/458.90)	0.1	0.02	40 × 100 ms
3	Lipid-rich pork tissue	blue (457.74/458.90)	0.2	0.02	40 × 50 ms and 1 × 2000 ms
4	Pork tissue	blue (457.74/458.90)	0.2	0.02	40 × 50 ms

<sup>1</sup> Number of acquisitions × acquisition time for each excitation wavelength. Example: 40 × 50 ms results in a total acquisition time of 4 s for each excitation wavelength. The one-time final readout of the CCD takes 1 min. <sup>2</sup> The micro lens array (MLA) facing the sample generates 400 × 0.25 mm<sup>2</sup> laser foci with a power of approx. 1 mW each.

#### 2.4. Data Handling

The raw data were extracted, the wavelength was calibrated using a mercury (neon) lamp and an argon lamp (PenRay, Quantum Design Europe, Germany), and intensity was calibrated by a broad emission white light source. All of these preprocessing steps have been performed using the software p3d [54–56]. Afterwards, the data were further processed using the computer language R [57] and the following R packages: hyperSpec [58], FITSio [59], Ramancal [60], pracma [61], MALDIquant [62], and viridis [63].

In a first step, all spectra were cosmic spike corrected as well as corrected for pixel errors. As the MLAs were not exactly cut along the spaces in between the lenses, the MLAs were no more centrosymmetric. One outer horizontal and outer vertical lens row moved close to border of the holder aperture, which caused some shading of these rows. Consequently, the top spaxel row and/or the last spaxel row to the right were not usable and discarded for some images. Then, in order to obtain a SERDS image, the spatially corresponding spectra of the two Raman images were pairwise subtracted from one another, always subtracting the higher excitation wavelength spectra from the lower excitation wavelength spectra. A wavenumber calibration was performed on reconstructed spectra of paracetamol. For Sample 1 and Sample 4, a hierarchical cluster analysis (HCA) was performed using the SERDS spectra as input. For this analysis, the Pearson correlation distance between the SERDS spectra was first calculated and then clustered following Ward's minimum variance method [64]. The reconstruction of the Raman spectra was calculated by summation of the signal intensities over the wavenumber channels. Since this reconstruction method leads to an underlying background in the reconstructed Raman spectrum, the sensitive nonlinear iterative peak (SNIP) algorithm was implemented. The SERDS spectra of Sample 4 were normalized by a vector normalization before clustering. For better visualization purposes, the difference spectra of sample 1 were not normalized. The normalization would apparently amplify the residual room light and would give a poor signal-to-noise cluster.

### 3. Results and Discussion

#### 3.1. Wide-Field SERDS Imaging Using Nod and Shuffle and the Large Field of View (1 cm<sup>2</sup>) Probe Head

##### 3.1.1. Illustration of the Raw Wide-Field Raman Images on the CCD Chip Using Nod and Shuffle

To demonstrate the nod and shuffle technique, a Raman image of a paracetamol and an aspirin pill (sample 1) was measured with the large 1 cm<sup>2</sup> field of view probe head (Figure 4a) configuration for 200 ms with 200 acquisitions before reading out the CCD camera. Since the laser power per fiber was low for a NIR laser source, this long acquisition time was necessary to obtain strong Raman signals. The two pills did not cover the probe head completely (Figure 5a). This was done on purpose to show

that even room light directly shining into the detection system for a short period can be filtered out with this setup. One second after the measurement had started, the fluorescent lamp of room light was turned on for 3 s. In Figure 4a, a zoomed image of the CCD chip, which is turned by 90° compared to the schematic CCD chip in Figure 2, is shown for a better visualization. Higher signal intensity corresponds to higher brightness, and the horizontally arranged traces correspond to complete Raman spectra of two intertwined Raman images taken at two different excitation wavelengths  $\lambda_1$  and  $\lambda_2$ . The traces are arranged in blocks, where each block consists of 20 spectra of each excitation wavelength corresponding to an image pixel row of 20 spaxels on the probe head. The black square bracket marks one of these blocks in Figure 4a.

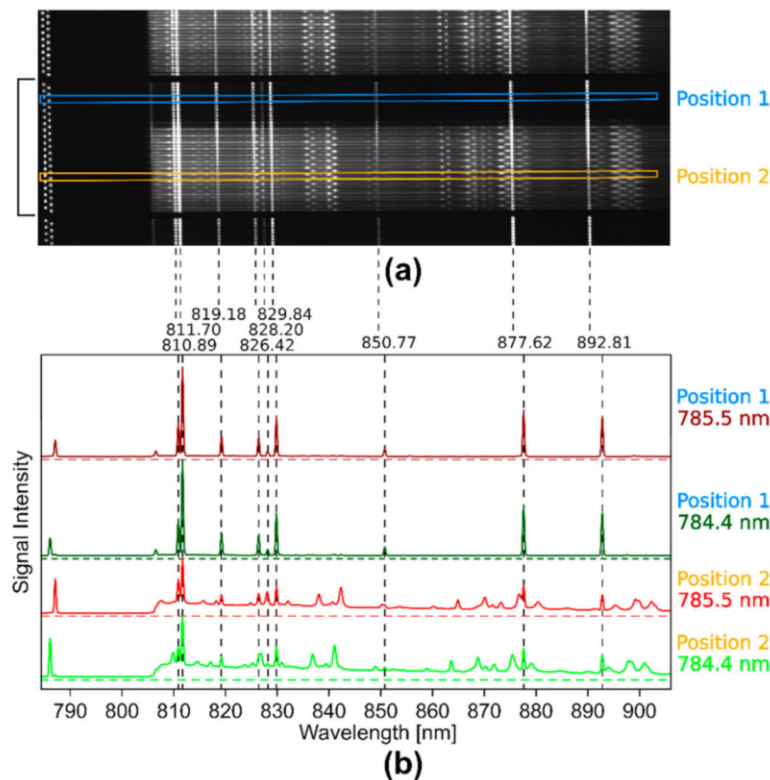


**Figure 4.** Illustration of the raw, wide field Raman data measured with two different excitation wavelengths ( $\lambda_1 = 784.4$  nm,  $\lambda_2 = 785.5$  nm) and the nod and shuffle technique: (a) zoomed view on a part of the CCD chip after acquisition for a closer look on the signal traces. Twenty spectra of each wavelength are always arranged in a block of traces (black square bracket), corresponding to one row of pixels in the Raman images. The upper blue box marks two intensity traces (Position 1) that correspond to a spaxel in the Raman image without a sample. The lower orange box marks two intensity traces (Position 2) that correspond to a spaxel on the Raman image with a paracetamol pill; (b) signal intensities of the two signal traces (in dark red and dark green) marked by the upper blue box in the CCD image showing only the room light spectra. In red ( $\lambda_1$ ) and green ( $\lambda_2$ ), the signal intensities of the two signal traces marked by the lower orange box in the CCD image are shown, which correspond to the paracetamol Raman spectra superposed by room light spectra. The dotted, vertical black lines indicate the position of the fluorescent lamp bands and above their spectral position in nm.

The two Raman images are shifted on the CCD by 5 pixels in the vertical direction. Therefore, every second trace belongs to the same excitation wavelength and hence the Raman image and each neighboring wavelength pair belong to the same spatial position on the probe head. The oscillating

dots on the left side of every trace correspond to the residual intensity of the excitation laser light that reached the detector in spite of the long-pass filter. The spots on the right of the laser signals correspond to Raman bands that shift with the excitation wavelength and to very intense, non-shifting signals of the fluorescent lamp. Figure 4b shows the profile plots of the four signal traces ( $\lambda_1$  in green and dark green;  $\lambda_2$  in red and dark red) inside the blue (Position 1) and orange (Position 2) boxes in Figure 4a. At the position of the blue box, there are fluorescent lamp bands only, whereas at the position of the orange box, the Raman signals are superposed with these bands that are shown by black vertical, dotted lines. Their positions were indicated on top in nm and coincide well with the emission bands of Krypton [65]. After comparison of the profiles, the Raman bands can be discriminated from the fluorescent lamp bands. Some Raman bands overlap with the fluorescent lamp bands after the shift of excitation wavelength (red spectrum), which would make it hard to correct for the fluorescent lamp contributions with computational methods. According to the position of the Raman bands and their profile, the selected Raman spectra belong to paracetamol. The image of the CCD chip also shows how close together all the signal traces are. If the signal intensities on the exposed pixels on the CCD are too high, the intensities cause crosstalk in the surrounding pixels and even in the neighboring shifted spectra. This is a limitation of the nod and shuffle approach, requiring careful monitoring of the overall intensity distribution between the spectra and the use of appropriately weighted extraction schemes such as optimal extraction [66].

### 3.1.2. Filtering Out Room Light by SERDS Imaging

A strength of SERDS is the capability to filter out room light or ambient light with a distinct band structure. This has been shown for single spectra before [67–69] but not for a complete Raman image or, in our case, a wide field Raman image. Since the room light bands do not shift with the change in excitation wavelength, the difference spectra of the SERDS image are ideally free of any room light bands. This advantage is demonstrated with help of the aforementioned samples (Section 3.1.1) of paracetamol and aspirin. The room light illumination time of a fluorescent tube was limited to 3 s to avoid overexposure of the CCD and the above-mentioned signal crosstalk. As shown before in Figure 4b, the room light bands are very dominant in the Raman spectra of the two Raman images. After subtraction, the room light bands vanish almost completely (Figure 5c). An HCA cluster analysis of the SERDS image using three clusters, one for paracetamol, one for aspirin, and one for empty space as the probe head, was not completely covered by the two pills. The resulting cluster map is depicted in Figure 5b and agrees well with the original bright field image (Figure 5a). In Figure 5c, the mean SERDS spectra and their respective standard deviation of the three clusters are shown. These clusters can be identified based on their SERDS spectra as paracetamol (cluster 1, black), empty space with residual room light (cluster 2, green), and aspirin (cluster 3, red). Residual traces of room light are still visible, which might be due to uneven exposure of one of the Raman images resulting in a higher room light intensity as the other, since the room light had to be turned off to avoid overexposure. Still, the strength of SERDS filtering out room light is obvious, which presents a huge advantage in operating theaters where room light needs to be switched on. Shorter acquisitions times will further reduce the interference of room light. However, the interface that was used to control a 784.43/785.48 nm laser source by polling the TTL (transistor-transistor-logic, square signal pulses that use +5 V for “1” or “high” and 0 V for “0” or “low”) trigger signals of the spectrograph with an USB digital input output device did not allow exposure times shorter than 200 ms.



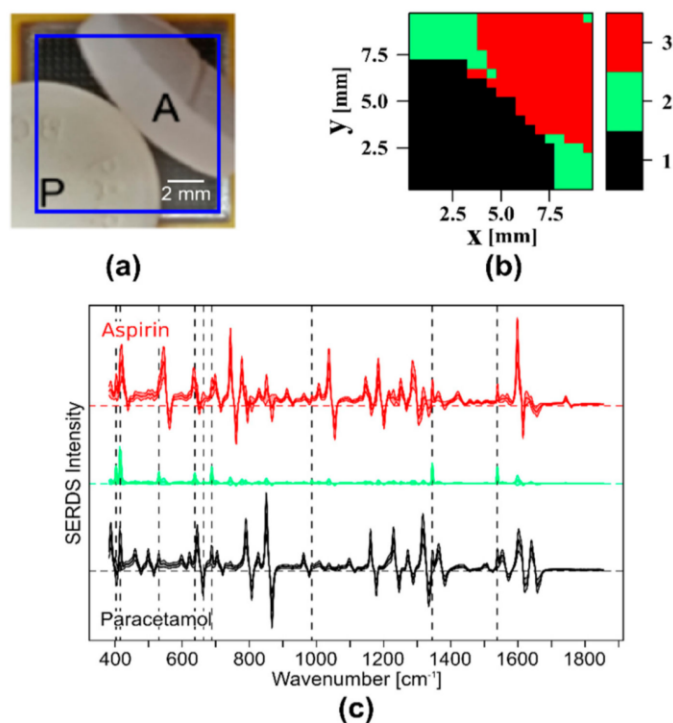


**Figure 5.** SERDS imaging using nod and shuffle of a paracetamol (P) and an aspirin (A) pill with an acquisition of 200 times 200 ms. (a) Picture of the sample on the probe head, the blue square corresponds to the field of view; (b) cluster map of the SERDS image; (c) clustered mean SERDS spectra and their standard deviation, cluster 1 = paracetamol (black), cluster 2 = no sample/residual room light (green), cluster 3 = aspirin (red); the dotted, vertical black lines indicate the position of the room light bands.

### 3.2. Wide-Field SERDS Imaging Using Nod and Shuffle, the Smaller Field of View Probe Head ( $0.02 \text{ cm}^2$ ), and the Rapidly Shifting Dual-Wavelength Blue Diode Laser Source

#### 3.2.1. Wide Field SERDS Imaging with Nod and Shuffle to Differentiate Different Polymer Beads

Since the spatial resolution of the larger field of view of  $1 \text{ cm}^2$  with 400 image points (1 spectrum per  $0.5 \text{ mm}$ ) is quite low for polymer beads, the setup was changed to a smaller field of view of  $0.02 \text{ cm}^2$ , resulting in approximately 1 spectrum per  $70 \mu\text{m}$ . To demonstrate the imaging capability and the higher lateral resolution of this setup, polystyrene (PS) and polymethyl methacrylate (PMMA) beads were distributed on a  $\text{CaF}_2$  slide and placed on the probe head. The Raman spectra were collected with the nod and shuffle technique with an acquisition time of 100 ms and 40 accumulations using the dual-wavelength blue diode laser light source ( $\lambda_1 = 457.7 \text{ nm}$ ,  $\lambda_2 = 458.9 \text{ nm}$ ). In the bright field camera image (Figure 6a), groups of small PS beads ( $50 \mu\text{m}$  diameter) and a region of bigger PMMA beads ( $120 \mu\text{m}$  diameter, red box) can be seen. To generate Raman intensity maps for PS and PMMA, specific marker bands of the reconstructed and baseline corrected Raman spectra were used. The PS intensity map (Figure 6b) shows the mean value of the aromatic ring breathing vibration  $999 \text{ cm}^{-1}$ , the ring stretching vibration at  $1590 \text{ cm}^{-1}$ , and the aromatic CH stretching vibration at  $3047 \text{ cm}^{-1}$ . To create the PMMA intensity map (Figure 6c), the mean value of the  $\text{CH}_3$  deformation vibration at  $1444 \text{ cm}^{-1}$ , the C=O stretching vibration at  $1718 \text{ cm}^{-1}$ , and the CH stretching vibration in  $\text{CH}_2$  and  $\text{CH}_3$  at  $2935 \text{ cm}^{-1}$  was calculated and mapped. A comparison of the bright field image with the two Raman intensity maps of PS and PMMA shows that the position of the PMMA beads and the PS beads corresponds to the Raman intensity maps very well. The squares on the intensity maps show regions of high intensity in the respective bands (green box for PS, blue box for PMMA).

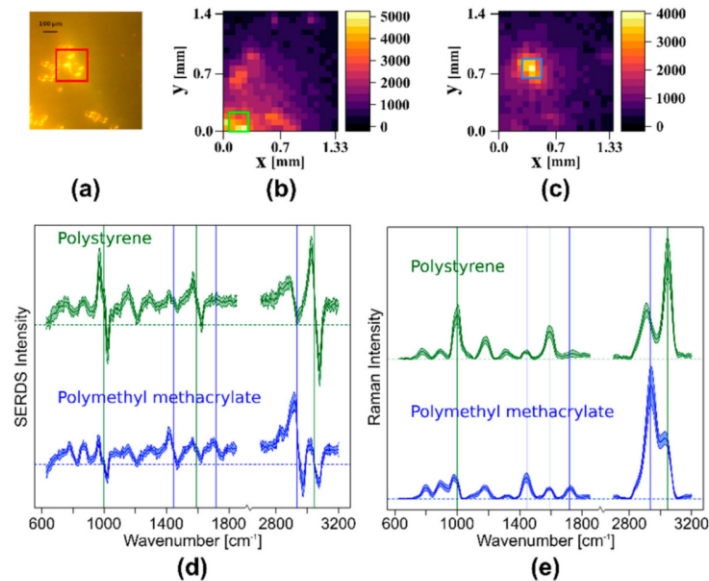


**Figure 6.** SERDS imaging of polystyrene and polymethyl methacrylate beads: (a) bright field image of the sample, red box shows a region of larger PMMA beads; (b) PS intensity map based on the intensity of three marker bands in the baseline corrected, reconstructed Raman spectra; (c) PMMA intensity map based on the intensity of three marker bands in the baseline corrected, reconstructed Raman spectra; (d) mean SERDS spectra and their standard deviation for nine spectra with the highest intensities for PMMA and PS marked by boxes (green for PS, blue for PMMA) in the corresponding intensity maps; (e) baseline corrected and reconstructed mean Raman spectra with standard deviation of the SERDS spectra shown in (d); The vertical lines in (d,e) indicate the marker bands (green for PS; blue for PMMA) that were used to create the intensity maps (b,c).

In Figure 6d, the mean SERDS spectra of these marked areas are shown in green (PS) and blue (PMMA). The vertical lines show the three marker bands for the intensity maps in the same colors. In Figure 6e, the mean and baseline corrected Raman spectra reconstructed from SERDS spectra of Figure 6d are plotted. The typical spectral profile of PS and PMMA are clearly visible, although the bands are rather broad. Since the laser was designed for the investigation of biological samples, the large spectral shift of approximately  $55\text{ cm}^{-1}$  is more appropriate for the SERDS investigation of tissue samples, which have a Raman profile with a larger band width. For the narrow-banded Raman profiles of polymers, this large shift results in the observed broadening during the integration in the reconstruction step and also yields a high risk of introducing artifacts into the reconstructed Raman spectra, since neighboring bands are shifted into one another.

### 3.2.2. Photobleaching Compensation in Wide Field SERDS Imaging by Very Fast Nod and Shuffle

A great challenge of SERDS is the variation in background intensities during the measurement, especially when the wavelength pair is affected differently. The main cause of changes in spectral background of biological samples is photobleaching of intrinsic fluorophores. Their generated autofluorescence gets bleached by the continuous laser radiation, which mainly causes a uniform decrease of the fluorescence. This leads to a SERDS spectrum with a background slope that needs further correction with some kind of computational solution such as normalization or optimization. Another possibility to deal with this challenge is to use very short acquisitions, thereby only allowing for minimal changes. Here, the nod and shuffle technique with fast switching between the wavelengths is promising, since the accumulation of multiple cycles allows for enough Raman signal collection, while equally distributing the photobleaching effect on the Raman measurements at both excitation

wavelengths. In combining this with wide field imaging and hence simultaneous irradiation of all image pixels, differences within one SERDS image can be eliminated.

Since the change in excitation wavelength was limited to 200 ms with the commercially available red laser system, the custom-built dual-wavelength blue diode laser system with the possibility for fast wavelength switching was used for the following experiments. A change from a NIR to a blue excitation will usually lead to a huge increase of the amount of fluorescence especially for biological samples. However, this drawback should be eliminated by the SERDS technique.

To demonstrate the compensation of photobleaching in wide field SERDS imaging using nod and shuffle, a piece of pork meat (Figure 7a) was imaged ( $\lambda_1 = 457.7$  nm,  $\lambda_2 = 458.9$  nm) with a total acquisition time of 2 s in two approaches:

1. Two Raman images were measured with a 50 ms acquisition time and 40 accumulations for each excitation wavelength before reading out the CCD chip once. Thus, the overall acquisition time was 2 s for each excitation wavelength.
2. Two Raman images were measured with a 2 s acquisition time and one accumulation for each excitation wavelength before reading out the CCD chip once. Thus, the total acquisition time was also 2 s for each excitation wavelength.

The two resulting Raman images of each measurement were subtracted. The SERDS spectra for the two SERDS images, with the mean difference spectra marked as dark colored lines (see Figure 7b), show the typical difference profile of lipid-rich tissue with bands at  $1446$   $\text{cm}^{-1}$ ,  $1650$   $\text{cm}^{-1}$ , and  $1740$   $\text{cm}^{-1}$ . While the SERDS bands have comparable absolute intensities, it is clearly visible that the difference spectra show a stronger residual background for the longer acquisition time (green spectra) due to the aforementioned photobleaching effect: At the beginning of the measurement at  $\lambda_1$ , the pork shows remarkable autofluorescence that significantly decreases during the 2 s measurement time. At the beginning of the measurement at  $\lambda_2$ , the autofluorescence is already decreased.

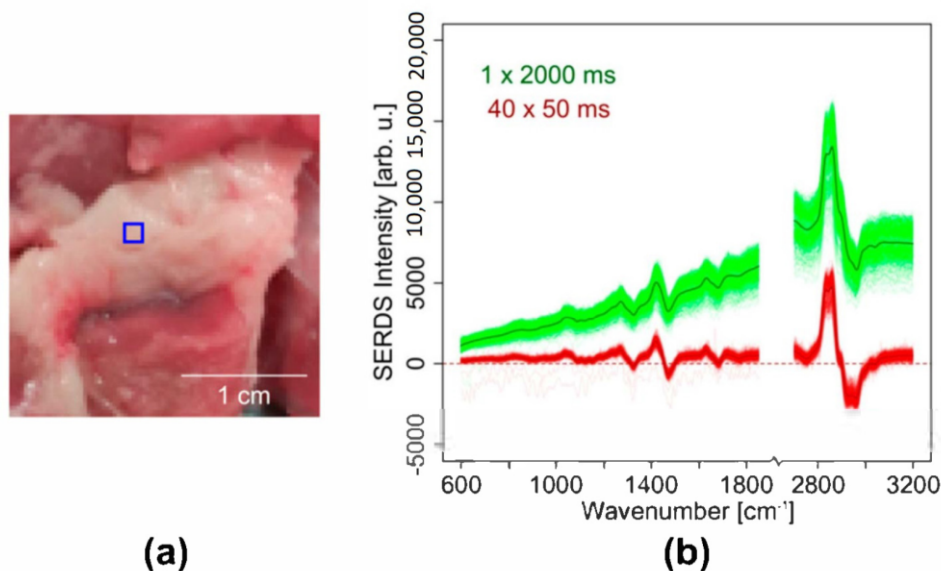


**Figure 7.** Compensation of photobleaching in SERDS imaging of the fat region of a pork chop using nod and shuffle: (a) image of the pork chop sample with measurement area marked by a blue square; (b) SERDS spectra of the SERDS image (red) with an acquisition time of 50 ms and 40 accumulations, SERDS spectra of the SERDS image (green) with an acquisition time of 2000 ms in a single accumulation. The darker lines (dark green and dark red, respectively) show the mean SERDS spectra of the respective SERDS image. The total exposure time is 4 s for each difference spectrum (2 s for each excitation wavelength).

Thus, the two measurement pairs show different backgrounds, leading to a non-zero baseline after the subtraction. For the short acquisition times, this residual background is not present, resulting in difference spectra almost on the zero line (red spectra). The reason for this effect is the equal distribution of the photobleaching on both measurements at  $\lambda_1$  and  $\lambda_2$ , when switching rapidly and repeatedly between the excitation wavelengths. Within a short 50 ms exposure time, the change of background signal is negligibly small. Each single measurement pair contains the same amount of background. When subtracting their sums, the background vanishes, and a zero baseline is obtained. This clearly demonstrates the advantage of the nod and shuffle technique in combination with wide field SERDS imaging and rapid switchable laser diodes. Even though the photobleaching must have been higher in the image with the short acquisition times, since it was recorded first, this setup configuration successfully circumvents this challenge and distributes the photobleaching equally on both excitation wavelengths.

### 3.2.3. Wide Field SERDS Imaging of Different Tissues in Pork Meat Using Nod and Shuffle

To test the introduced wide field SERDS setup on a heterogeneous biological sample, another piece of pork meat was imaged. As before, the custom made dual-wavelength blue diode laser source ( $\lambda_1 = 457.7$  nm,  $\lambda_2 = 458.9$  nm) and the smaller field of view probe head with the nod and shuffle technique was used to image a section including proteins and lipids. Figure 8a shows an intensity map of the SERDS spectra based on the intensity at  $2900\text{ cm}^{-1}$ .

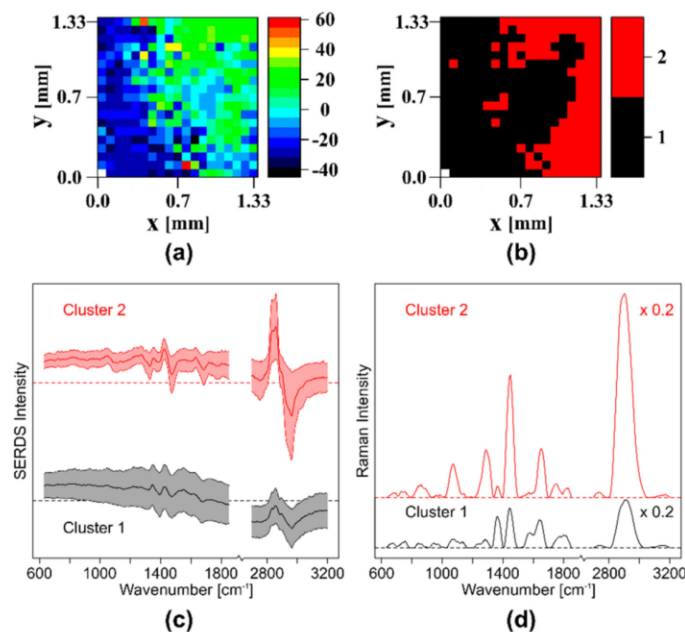


**Figure 8.** SERDS imaging of a piece of pork meat with protein and lipid-rich areas: (a) intensity map of the SERDS spectra at  $2900\text{ cm}^{-1}$ ; (b) cluster map of the SERDS spectra; (c) clustered normalized, mean SERDS spectra and their standard deviation; (d) reconstructed and baseline corrected mean Raman spectra of the two clusters shown in (c). The high wavenumber regions were multiplied by 0.2 for better visualization.

After hierarchical clustering, two clusters visualize the regions with protein and lipids in the cluster map (see Figure 8b). In Figure 8c, the normalized, mean difference spectra with standard deviation of the two clusters are shown. It is obvious that the intensity of cluster 2, the lipid cluster, is much higher than the intensity of cluster 1, the protein cluster. The larger standard deviation is a consequence of the lower intensity and the higher background in the protein cluster. For a better

visualization of the band positions, the reconstructed and baseline corrected mean Raman spectra of the two clusters can be seen in Figure 8d. Typical protein bands such as amide I at  $1638\text{ cm}^{-1}$ , amide III at  $1282\text{ cm}^{-1}$ , myoglobin at  $1363\text{ cm}^{-1}$  [32], tyrosine at  $858\text{ cm}^{-1}$ , tryptophane ( $754, 894\text{ cm}^{-1}$  and  $1587\text{ cm}^{-1}$ ), and CN ( $1075\text{ cm}^{-1}$ ,  $1099\text{ cm}^{-1}$  and  $1128\text{ cm}^{-1}$ ) classify cluster 1 as proteins, while cluster 2 shows lipid typical bands (carbonyl at  $1750\text{ cm}^{-1}$ , C=C  $1649\text{ cm}^{-1}$ ,  $\text{CH}_2$  and  $\text{CH}_3$  at  $1060\text{ cm}^{-1}$ ,  $1300\text{ cm}^{-1}$  and  $1450\text{ cm}^{-1}$ ) and can therefore be assigned to lipids. This also explains the already observed intensity differences between the two clusters, since lipids have a higher Raman scattering cross-section than proteins. In conclusion, with the chosen setup configuration, SERDS images of a biological sample can be recorded in one shot with small photobleaching effects, and the lipid and protein-rich regions can be easily identified.

#### 4. Conclusions

Using wide field Raman imaging, several spectra of an area can be recorded in a relatively short time, since all spectra are collected simultaneously. Consequently, the total acquisition time of a Raman image, in our case consisting of 400 spectra of a 20 by 20 fiber array, is orders of magnitude faster than in point-by-point Raman imaging. The fibers were arranged in a square probe head to image an area of  $10 \times 10\text{ mm}^2$  with  $0.5 \times 0.5\text{ mm}^2$  per pixel in standard mode or  $1.4 \times 1.4\text{ mm}^2$  with  $0.07 \times 0.07\text{ mm}^2$  per pixel in higher magnification mode. As the readout times of the usually employed, very large CCD chips are quite long, measurements in quick successions cannot be realized in this configuration. This is especially problematic for wide field SERDS imaging, where the accumulation of short measurements at two slightly different excitation wavelengths is favorable.

The presented wide field SERDS imaging approach using the nod and shuffle technique allows accumulating very short acquisition times before reading out the CCD chip. The structure of the signal traces on the CCD chip was presented. Since the signal traces on the CCD chip are closer together in the interlaced nod and shuffle approach, the risk of crosstalk from very high intensities into the neighboring spectra belonging to the other excitation wavelength can be problematic. For this reason, the signal intensity has to be monitored closely during the experiments.

Using the nod and shuffle approach, the advantages of SERDS and fast acquisition times was demonstrated for wide field SERDS imaging for the first time. As expected from previous single spectra measurements, room light filtering was one of these advantages, where the measurement was interfered by an external light source during the acquisition. This was compensated due to the SERDS technique and the fast acquisition times, which made it possible to filter out the room light, even when it directly shone into the detection system for a short period. If the sample covers the probe head completely, only stray light can enter the detection system. This will allow much longer acquisition times. The other demonstrated advantage of the fast acquisition times is the compensation of photobleaching resulting in minimal background in the SERDS spectra of the SERDS images. This compensation makes the usual normalization or optimization steps before the calculation of the SERDS spectra unnecessary and the whole SERDS approach faster and less computational.

It was demonstrated that structural differences can be resolved based on almost background free wide field SERDS images. The resulting reconstructed Raman spectra had to be baseline corrected, since the used quasi integration introduced a background into the reconstructed spectra. Especially for the investigation of the narrow band Raman profiles of polymers, the  $1.16\text{ nm}$  wavelength shift of the custom-made, dual-wavelength blue diode laser, which corresponds to a  $55\text{ cm}^{-1}$  shift of the Raman spectra, as well as the spectral broadening due to the reconstruction was quite large. For the investigation of biological samples, which was the targeted application for the blue diode laser, this large spectral shift is more appropriate.

The nod and shuffle technique will enable a compensation of the photobleaching and by directly using the difference spectra for a classification of the measured samples, no reconstruction will be necessary. This combination will streamline the wide field SERDS imaging and reduce the computational effort for this instrumental background correction method.

## 5. Patents

For results of the work, a patent application was filed at the German Patent and Trade Mark Office. Patent application no. DE 10 2018 130 582 A1.

**Author Contributions:** Conceptualization: M.M.R., E.S., C.K., J.P. Realizing of the setup: E.S. Performing the measurements: F.K., E.S. Upgrading of the data reduction software: C.S. (Christer Sandin). Data analysis and visualization: F.K., T.U., G.M. Evaluation and validation: C.S. (Clara Stiebing), C.K. Design and realization of dual wavelength (457.74 nm/458.90 nm) diode laser source: A.M., M.M., B.S., G.T. Supervision: C.S. (Clara Stiebing), C.K., J.P. Original draft preparation: F.K. Review and editing of the manuscript: all. All authors have read and agreed to the published version of the manuscript.

**Funding:** This research was funded by the Leibniz Association through the project HYPERAM (SAW-2016-IPHT-2). The publication of this article was funded by the Open Access Fund of the Leibniz Association.

**Acknowledgments:** This research has made use of the integral-field spectroscopy data-reduction software p3d, which is provided by the Leibniz-Institute for Astrophysics Potsdam (AIP) and maintained by Sandin Advanced Visualization (Stockholm). We thank Thomas Fechner from the AIP's electronics workshop for upgrading the spectrograph. Furthermore, we thank DECHEMA e.V. for the possibility to present results at the 14. Dresdner Sensor Symposium. Parts of the figures are adapted from the conference proceeding [32].

**Conflicts of Interest:** The authors declare no conflict of interest. The funders had no role in the design of the study; in the collection, analyses, or interpretation of data; in the writing of the manuscript, or in the decision to publish the results.

## References

1. Krafft, C.; Schie, I.W.; Meyer, T.; Schmitt, M.; Popp, J. Developments in spontaneous and coherent Raman scattering microscopic imaging for biomedical applications. *Chem. Soc. Rev.* **2016**, *45*, 1819–1849. [CrossRef] [PubMed]
2. Hubbard, T.J.E.; Shore, A.; Stone, N. Raman spectroscopy for rapid intra-operative margin analysis of surgically excised tumour specimens. *Analyst* **2019**, *144*, 6479–6496. [CrossRef] [PubMed]
3. Cheng, J.X.; Xie, X.S. Vibrational spectroscopic imaging of living systems: An emerging platform for biology and medicine. *Science* **2015**, *350*, 1–9. [CrossRef] [PubMed]
4. Krafft, C.; Schmitt, M.; Schie, I.W.; Cialla-May, D.; Matthäus, C.; Bocklitz, T.; Matthäus, C.; Bocklitz, T.; Popp, J. Label-free molecular imaging of biological cells and tissues by linear and non-linear Raman spectroscopic approaches. *Angew. Chem. Int. Ed.* **2017**, *4392*–4430. [CrossRef]
5. Butler, H.J.; Ashton, L.; Bird, B.; Cinque, G.; Curtis, K.; Dorney, J.; Esmonde-White, K.; Fullwood, N.J.; Gardner, B.; Martin-Hirsch, P.L.; et al. Using Raman spectroscopy to characterize biological materials. *Nat. Protoc.* **2016**, *11*, 664–687. [CrossRef]
6. Monici, M. Cell and tissue autofluorescence research and diagnostic applications. *Biotechnol. Annu. Rev.* **2005**, *11*, 227–256. [CrossRef]
7. Cordero, E.; Korinth, F.; Stiebing, C.; Krafft, C.; Schie, I.; Popp, J. Evaluation of Shifted Excitation Raman Difference Spectroscopy and Comparison to Computational Background Correction Methods Applied to Biochemical Raman Spectra. *Sensors* **2017**, *17*, 1724. [CrossRef]
8. Wei, D.; Chen, S.; Liu, Q. Review of Fluorescence Suppression Techniques in Raman Spectroscopy. *Appl. Spectrosc. Rev.* **2015**, *50*, 387–406. [CrossRef]
9. Afseth, N.K.; Kohler, A. Extended multiplicative signal correction in vibrational spectroscopy, a tutorial. *Chemom. Intell. Lab. Syst.* **2012**, *117*, 92–99. [CrossRef]
10. Martens, H.; Stark, E. Extended multiplicative signal correction and spectral interference subtraction: New preprocessing methods for near infrared spectroscopy. *J. Pharm. Biomed. Anal.* **1991**, *9*, 625–635. [CrossRef]
11. Pirzer, M.; Sawatzki, J. Method and Device for Correcting a Spectrum. U.S. Patent Application No. 2006/0211562 A1, 21 September 2006.
12. Kneen, M.A.; Annegarn, H.J. Algorithm for fitting XRF, SEM and PIXE X-ray spectra backgrounds. *Nucl. Instrum. Methods Phys. Res. Sect. B Beam Interact. Mater. Atoms* **1996**, *109–110*, 209–213. [CrossRef]
13. Morháč, M. An algorithm for determination of peak regions and baseline elimination in spectroscopic data. *Nucl. Instrum. Methods Phys. Res. Sect. A Accel. Spectrometers Detect. Assoc. Equip.* **2009**, *600*, 478–487. [CrossRef]

14. Morhác, M.; Matoušek, V. Peak clipping algorithms for background estimation in spectroscopic data. *Appl. Spectrosc.* **2008**, *62*, 91–106. [CrossRef] [PubMed]
15. Lieber, C.A.; Mahadevan-Jansen, A. Automated Method for Subtraction of Fluorescence from Biological Raman Spectra. *Appl. Spectrosc.* **2003**, *57*, 1363–1367. [CrossRef] [PubMed]
16. Bergholt, M.S.; Zheng, W.; Lin, K.; Wang, J.; Xu, H.; Ren, J.L.; Ho, K.Y.; Teh, M.; Yeoh, K.G.; Huang, Z. Characterizing variability of in vivo Raman spectroscopic properties of different anatomical sites of normal colorectal tissue towards cancer diagnosis at colonoscopy. *Anal. Chem.* **2015**, *87*, 960–966. [CrossRef]
17. Desroches, J.; Jermyn, M.; Pinto, M.; Picot, F.; Tremblay, M.A.; Obaid, S.; Marple, E.; Urmey, K.; Trudel, D.; Soulez, G.; et al. A new method using Raman spectroscopy for in vivo targeted brain cancer tissue biopsy. *Sci. Rep.* **2018**, *8*, 1–10. [CrossRef]
18. Cordero, E.; Rügler, J.; Marti, D.; Mondol, A.S.; Hasselager, T.; Mogensen, K.; Hermann, G.G.; Popp, J.; Schie, I.W. Bladder tissue characterization using probe-based Raman spectroscopy: Evaluation of tissue heterogeneity and influence on the model prediction. *J. Biophotonics* **2020**, *13*, 1–15. [CrossRef]
19. Ariese, F.; Meuzelaar, H.; Kerssens, M.M.; Buijs, J.B.; Gooijer, C. Picosecond Raman spectroscopy with a fast intensified CCD camera for depth analysis of diffusely scattering media. *Analyst* **2009**, *134*, 1192–1197. [CrossRef]
20. Kögler, M.; Heilala, B. Time-gated Raman spectroscopy—A review. *Meas. Sci. Technol.* **2020**, *32*, 1–17. [CrossRef]
21. De Luca, A.; Dholakia, K.; Mazilu, M. Modulated Raman Spectroscopy for Enhanced Cancer Diagnosis at the Cellular Level. *Sensors* **2015**, *15*, 13680–13704. [CrossRef]
22. Dochow, S.; Bergner, N.; Krafft, C.; Clement, J.; Mazilu, M.; Praveen, B.B.; Ashok, P.C.; Marchington, R.; Dholakia, K.; Popp, J. Classification of Raman spectra of single cells with autofluorescence suppression by wavelength modulated excitation. *Anal. Methods* **2013**, *5*, 4608–4614. [CrossRef]
23. Craig, D.; Mazilu, M.; Dholakia, K. Quantitative detection of pharmaceuticals using a combination of paper microfluidics and wavelength modulated Raman spectroscopy. *PLoS ONE* **2015**, *10*, e0123334. [CrossRef] [PubMed]
24. Wirth, M.J.; Chou, S.H. Comparison of Time and Frequency Domain Methods for Rejecting Fluorescence from Raman Spectra. *Anal. Chem.* **1988**, *60*, 1882–1886. [CrossRef]
25. Shreve, A.P.; Cherepy, N.J.; Mathies, R.A. Effective Rejection of Fluorescence Interference in Raman Spectroscopy Using a Shifted Excitation Difference Technique. *Appl. Spectrosc.* **1992**, *46*, 707–711. [CrossRef]
26. Korinith, F.; Mondol, A.S.; Stiebing, C.; Schie, I.W.; Krafft, C.; Popp, J. New methodology to process shifted excitation Raman difference spectroscopy data: A case study of pollen classification. *Sci. Rep.* **2020**, *10*, 11215. [CrossRef]
27. Gebrekidan, M.T.; Erber, R.; Hartmann, A.; Fasching, P.A.; Emons, J.; Beckmann, M.W.; Braeuer, A. Breast Tumor Analysis Using Shifted-Excitation Raman Difference Spectroscopy (SERDS). *Technol. Cancer Res. Treat.* **2018**, *17*. [CrossRef]
28. Martins, M.A.d.S.; Ribeiro, D.G.; Pereira dos Santos, E.A.; Martin, A.A.; Fontes, A.; da Silva Martinho, H. Shifted-excitation Raman difference spectroscopy for in vitro and in vivo biological samples analysis. *Biomed. Opt. Express* **2010**, *1*, 617–626. [CrossRef]
29. Noack, K.; Eskofier, B.; Kiefer, J.; Dilk, C.; Bilow, G.; Schirmer, M.; Buchholz, R.; Leipertz, A. Combined shifted-excitation Raman difference spectroscopy and support vector regression for monitoring the algal production of complex polysaccharides. *Analyst* **2013**, *138*, 5639–5646. [CrossRef]
30. Gebrekidan, M.T.; Knipfer, C.; Stelzle, F.; Popp, J.; Will, S.; Braeuer, A. A shifted-excitation Raman difference spectroscopy (SERDS) evaluation strategy for the efficient isolation of Raman spectra from extreme fluorescence interference. *J. Raman Spectrosc.* **2016**, *47*, 198–209. [CrossRef]
31. Sowoidnich, K.; Kronfeldt, H.-D. In-Situ Species Authentication of Frozen-Thawed Meat and Meat Juice Using Shifted Excitation Raman Difference Spectroscopy. In *Biophotonics: Photonic Solutions for Better Health Care VI, Proceedings of the SPIE Photonics Europe, Strasbourg, France, 22–26 April 2018*; Popp, J., Tuchin, V.V., Pavone, F.S., Eds.; International Society for Optics and Photonics: Bellingham, WA, USA, 2018; p. 106850.
32. Sowoidnich, K.; Kronfeldt, H.-D. Fluorescence Rejection by Shifted Excitation Raman Difference Spectroscopy at Multiple Wavelengths for the Investigation of Biological Samples. *ISRN Spectrosc.* **2012**, *2012*, 256326. [CrossRef]

33. Knipfer, C.; Motz, J.; Adler, W.; Brunner, K.; Gebrekidan, M.T.; Hankel, R.; Agaimy, A.; Will, S.; Braeuer, A.; Neukam, F.W.; et al. Raman difference spectroscopy: A non-invasive method for identification of oral squamous cell carcinoma. *Biomed. Opt. Express* **2014**, *5*, 3252–3265. [CrossRef] [PubMed]
34. Han, Z.; Strycker, B.D.; Commer, B.; Wang, K.; Shaw, B.D.; Scully, M.O.; Sokolov, A.V. Molecular origin of the Raman signal from *Aspergillus nidulans* conidia and observation of fluorescence vibrational structure at room temperature. *Sci. Rep.* **2020**, *10*, 5428. [CrossRef] [PubMed]
35. Schmäzlin, E.; Moralejo, B.; Rutowska, M.; Monreal-Ibero, A.; Sandin, C.; Tarcea, N.; Popp, J.; Roth, M.M. Raman imaging with a fiber-coupled multichannel spectrograph. *Sensors* **2014**, *14*, 21968–21980. [CrossRef] [PubMed]
36. Schmäzlin, E.; Moralejo, B.; Bodenmüller, D.; Darvin, M.E.; Thiede, G.; Roth, M.M. Ultrafast imaging Raman spectroscopy of large-area samples without stepwise scanning. *J. Sens. Sens. Syst.* **2016**, *5*, 261–271. [CrossRef]
37. Stewart, S.; Priore, R.J.; Nelson, M.P.; Treado, P.J. Raman Imaging. *Annu. Rev. Anal. Chem.* **2012**, *5*, 337–360. [CrossRef] [PubMed]
38. Müller, W.; Kielhorn, M.; Schmitt, M.; Popp, J.; Heintzmann, R. Light sheet Raman micro-spectroscopy. *Optica* **2016**, *3*, 452–457. [CrossRef]
39. Sinjab, F.; Liao, Z.; Notingher, I. Applications of Spatial Light Modulators in Raman Spectroscopy. *Appl. Spectrosc.* **2019**, *73*, 727–746. [CrossRef]
40. Allington-Smith, J. Basic principles of integral field spectroscopy. *New Astron. Rev.* **2006**, *50*, 244–251. [CrossRef]
41. Bacon, R.; Monnet, G. Recent Trends in Integral Field Spectroscopy. In *Optical 3D-Spectroscopy for Astronomy*; Wiley-VCH: Weinheim, Germany, 2017; pp. 115–128.
42. Glazebrook, K.; Bland-Hawthorn, J. Microslit Nod-Shuffle Spectroscopy: A Technique for Achieving Very High Densities of Spectra. *Publ. Astron. Soc. Pac.* **2002**, *113*, 197–214. [CrossRef]
43. Roth, M.M.; Cardiel, N.; Cenarro, J.; Schönberner, D.; Steffen, M. Nod & Shuffle 3D Spectroscopy. In *Scientific Detectors for Astronomy 2005*; Beletic, J.E., Beletic, J.W., Amico, P., Eds.; Springer: Dordrecht, The Netherlands, 2005; pp. 99–108.
44. Roth, M.M.; Fechner, T.; Wolter, D.; Kelz, A.; Becker, T. Ultra-Deep Optical Spectroscopy with PMAS. Using the Nod-and-Shuffle Technique. *Exp. Astron.* **2002**, *14*, 99–105. [CrossRef]
45. Sowoidnich, K.; Maiwald, M.; Sumpf, B.; Towrie, M.; Matousek, P. Charge-Shifting Optical Lock-In Detection with Shifted Excitation Raman Difference Spectroscopy for the Analysis of Fluorescent Heterogeneous Samples. In Proceedings of the Biomedical Vibrational Spectroscopy 2020: Advances in Research and Industry, San Francisco, CA, USA, 1–6 February 2020; p. 112360K.
46. Sowoidnich, K.; Towrie, M.; Maiwald, M.; Sumpf, B.; Matousek, P. Shifted Excitation Raman Difference Spectroscopy with Charge-Shifting Charge-Coupled Device (CCD) Lock-In Detection. *Appl. Spectrosc.* **2019**, *73*, 1265–1276. [CrossRef] [PubMed]
47. Heming, R.; Herzog, H.; Deckert, V. Optical CCD lock-in device for Raman difference spectroscopy. *DGAO Proc.* **2008**, *109*, 33.
48. Schmäzlin, E.; Urrutia, T.; Korinth, F.; Stiebing, C.; Krafft, C.; Popp, J.; Roth, M.M. Bildgebende Differenz-Raman-Spektroskopie mit “Nod and Shuffle“-Technik. In Proceedings of the 14th Dresdner Sensor-Symposium, Dresden, Germany, 2–4 December 2019; pp. 96–101. [CrossRef]
49. Moralejo, B.; Roth, M.M.; Godefroy, P.; Fechner, T.; Bauer, S.M.; Schmäzlin, E.; Kelz, A.; Haynes, R. The Potsdam MRS Spectrograph: Heritage of MUSE and the Impact of Cross-Innovation in the Process of Technology Transfer. In Proceedings of the SPIE Astronomical Telescopes + Instrumentation, Edinburgh, UK, 26 June–1 July 2016; p. 991222.
50. Moralejo, B.; Schmäzlin, E.; Bodenmüller, D.; Fechner, T.; Roth, M.M. Improving the frame rates of Raman image sequences recorded with integral field spectroscopy using windowing and binning methods. *J. Raman Spectrosc.* **2018**, *49*, 372–375. [CrossRef]
51. Sumpf, B.; Müller, A.; Maiwald, M. Tailored Diode Lasers: Enabling Raman Spectroscopy in the Presence of Disturbing Fluorescence and Background Light. In Proceedings of the SPIE BiOS, San Francisco, CA, USA, 2–7 February 2019; p. 1089411.



52. Schmäzlín, E.; Moralejo, B.; Gersonde, I.; Schleusener, J.; Darwin, M.E.; Thiede, G.; Roth, M.M. Nonscanning large-area Raman imaging for ex vivo/in vivo skin cancer discrimination. *J. Biomed. Opt.* **2018**, *23*, 1–11. [CrossRef] [PubMed]
53. Kelz, A.; Verheijen, M.A.W.; Roth, M.M.; Bauer, S.M.; Becker, T.; Paschke, J.; Popow, E.; Sánchez, S.F.; Laux, U. PMAS: The Potsdam Multi-Aperture Spectrophotometer. II. The Wide Integral Field Unit PPak. *Publ. Astron. Soc. Pac.* **2006**, *118*, 129–145. [CrossRef]
54. Sandin, C.; Becker, T.; Roth, M.M.; Gerssen, J.; Monreal-Ibero, A.; Böhm, P.; Weilbacher, P. p3D: A general data-reduction tool for fiber-fed integral-field spectrographs. *Astron. Astrophys.* **2010**, *515*, A35. [CrossRef]
55. Sandin, C.; Becker, T.; Roth, M.M.; Gerssen, J.; Monreal-Ibero, A.; Böhm, P.; Weilbacher, P. *p3d: General Data-Reduction Tool for Fiber-Fed Integral-Field Spectrographs*; Version 2.7; Astrophysics Source Code Library: Houghton, MI, USA, 2020; Available online: <http://ascl.net/1205.002> (accessed on 20 November 2020).
56. p3d a General Data-Reduction Tool for Fiber-Fed Integral-Field Spectrographs. Available online: <https://p3d.sourceforge.io/> (accessed on 20 November 2020).
57. R Core Team. *R: A Language and Environment for Statistical Computing*; R Foundation for Statistical Computing: Vienna, Austria, 2018.
58. Beleites, C.; Sergio, V. hyperSpec: A Package to Handle Hyperspectral Data Sets in R. Available online: <https://CRAN.R-project.org/package=hyperSpec> (accessed on 23 November 2020).
59. Harris, A. FITSio: FITS (Flexible Image Transport System) Utilities. Available online: <https://rdr.io/cran/FITSio/> (accessed on 23 November 2020).
60. Beleites, C. Software Package for R-Ramancal: Calibration Routines for Raman Spectrometers. 2013.
61. Borchers, H.W. Pracma: Practical Numerical Math Functions. Available online: <https://rdr.io/rforge/pracma/> (accessed on 23 November 2020).
62. Gibb, S.; Strimmer, K. MALDIquant: A versatile R package for the analysis of mass spectrometry data. *Bioinformatics* **2012**, *28*, 2270–2271. [CrossRef]
63. Garnier, S. Viridis: Default Color Maps from “Matplotlib”. Available online: <https://rdr.io/cran/viridis/> (accessed on 23 November 2020).
64. Bonifacio, A.; Beleites, C.; Sergio, V. Application of R-mode analysis to Raman maps: A different way of looking at vibrational hyperspectral data. *Anal. Bioanal. Chem.* **2015**, *407*, 1089–1095. [CrossRef]
65. Arc Line Lamps on the Website of W. M. Keck Observatory. Available online: [https://www2.keck.hawaii.edu/inst/lris/arc\\_calibrations.html](https://www2.keck.hawaii.edu/inst/lris/arc_calibrations.html) (accessed on 20 November 2020).
66. Horne, K. An optimal extraction algorithm for CCD spectroscopy. *Publ. Astron. Soc. Pac.* **1986**, *98*, 609. [CrossRef]
67. Dochow, S.; Bergner, N.; Matthäus, C.; Praveen, B.B.; Ashok, P.C.; Mazilu, M.; Krafft, C.; Dholakia, K.; Popp, J. Etaloning, fluorescence and ambient light suppression by modulated wavelength Raman spectroscopy. *Biomed. Spectrosc. Imaging* **2012**, *1*, 383–389. [CrossRef]
68. Maiwald, M.; Müller, A.; Sumpf, B.; Tränkle, G. A portable shifted excitation Raman difference spectroscopy system: Device and field demonstration. *J. Raman Spectrosc.* **2016**, *47*, 1180–1184. [CrossRef]
69. Sowoidnich, K.; Towrie, M.; Matousek, P. Lock-in detection in Raman spectroscopy with charge-shifting CCD for suppression of fast varying backgrounds. *J. Raman Spectrosc.* **2019**, *50*, 983–995. [CrossRef]

**Publisher’s Note:** MDPI stays neutral with regard to jurisdictional claims in published maps and institutional affiliations.



© 2020 by the authors. Licensee MDPI, Basel, Switzerland. This article is an open access article distributed under the terms and conditions of the Creative Commons Attribution (CC BY) license (<http://creativecommons.org/licenses/by/4.0/>).